ArcISo

LASTER, DESIGN OG OPERASJON AV FLYTERE I NORDOMRÅDENE (NORD ST20) 2019/313

Loads, Design and Operations of Floaters in the North

Petroleumstilsynet

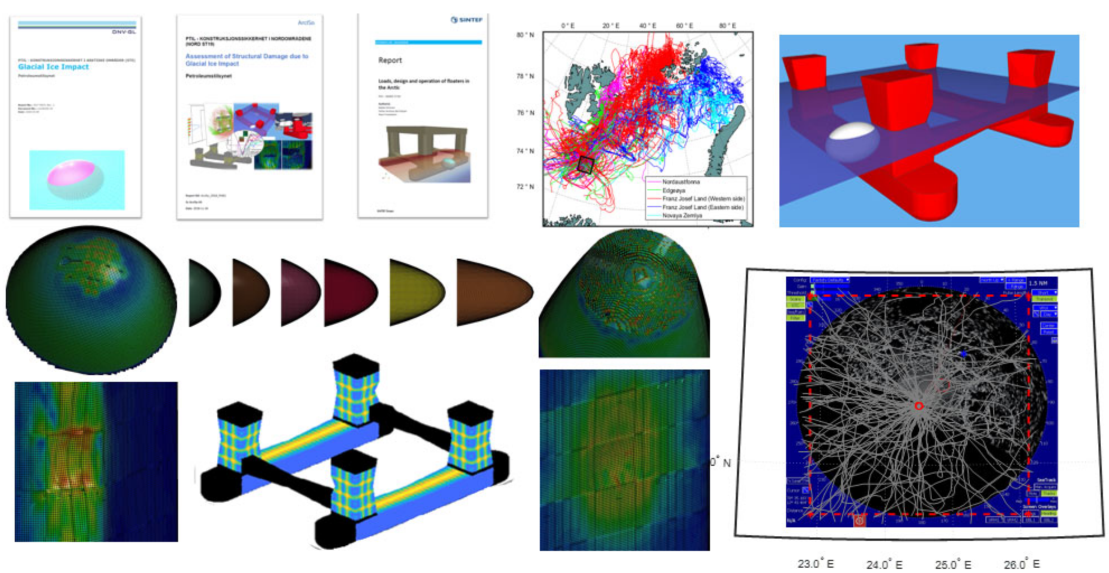

Report NO: ArcISo_2019_Ptil02

By ArcISo AS

Date: 28/10/2019

ArcISo
Arctic Integrated Solutions
 	
Address: NO-7034 Trondheim, Norway
Location: Gløshaugen Høgskolerigen 7A
Managing director: Raed Lubbad (+47 735 94 583)
Email: raed.lubbad@ntnu.no
Enterprise NO: 917100454
Website: https://arciso.com
		# ArcISo AS
		AUTHOR(S)
		Wenjun Lu, Zhaolong Yu, Marnix van den Berg, Dennis Monteban, Raed Lubbad, Vegard Hornnes, Jørgen Amdahl, Sveinung Løset, Ekaterina Kim	

TITLE LASTER, DESIGN OG OPERASJON AV FLYTERE I NORDOMRÅDENE (NORD ST20) 2019/313		CLIENT(S) Petroleumstilsynet (Petroleum Safety Authority Norway)	
CLASS. THIS PAGE Open	PROJECT MANAGER Wenjun Lu	PROJECT NO ST20_2019/313	NO OF PAGES 233
APPROVED BY Raed Lubbad (ArcISo Managing Director)		CHECKED BY Jørgen Amdahl Jørgen Amdahl Sveinung Løset Sveinung Løset Raed Lubbad Raed Lubbad	
REPORT NO ArcISo_2019_Ptil02	DATE 28.10.2019		

ABSTRACT

As a continuation of a series of projects related to the structural safety in the high North, this project performed the following four tasks:

- Task #1: Reviewing and making a synergy out of the results from previous projects (ST5, ST19, and ST20_2018)
- Task #2: Studying the statistical characteristics of drifting icebergs and determining the annual iceberg encounter frequency for structures with different sizes at a given location in the Barents Sea.
- Task #3: Performing structural damage assessment due to impact with glacial ice features of varying local sharpness at the contact zone.
- Task #4: Evaluating the lower limit of a glacial ice feature's size that can be detected by marine radar.

Among many insights gained through the projects and described in the report, major findings are summarised in the following:

- Throughout the years, quite consistent and gradually less conservative impact velocities and impact heights were calculated based on different methods in the different project on wave driven motion of a glacial ice feature. The results are encouraging but still can be improved. More thorough hydrodynamic analyses including physical model tests are recommended.
- Both large- and local- scale simulations of iceberg's drift and deterioration (including thermal and wave erosion) were performed. The results cover the Barents Sea domain and they include probabilities of iceberg intrusion, annual encounter frequencies, statistical distribution of mass and geometry, drift speed, etc. Quantitative results concerning a selected location, i.e., Block #7424 are also presented in the report.
- Three different methods were utilised to perform structural damage assessment from impacts with a glacial ice feature of varying local sharpness. The anticipated and mutually consistent results from all three methods yield a critical local geometry that leads to the maximum damage on a tested structural area. This local geometry is influenced by the structural dimensions; and its radius of curvature (a measure of sharpness) at the contact area is approximately 0.81 times of the stiffened panel length.
- Simulations performed on this local critical geometry using all three different methods indicate a maximum structural deformation of around 0.6 m. In addition, Simulator for Arctic Marine Structures (SAMS) effectively constructed a deformation or damage map showing that 90% of the impacted location has a deformation that is less than 0.36 m. This simulation example is based on glacial ice features with a characteristic length of 15 m, which has an impact energy of around 7.5 MJ in the simulated wave condition.
- The 15-m lower-limit for detectability was evaluated to be too optimistic given most of the concurrent marine radar's capability and challenges arise in high sea state scenarios. In that case, a doubling to about 30 m size seems more realistic. In addition, the recommended lower limit should be considered in conjunction with the type of the Arctic marine operations.

KEY WORDS: SAMS, Nonlinear FEM, Deformation/damage map, Damage assessment, Impact, Ice, Semi-submersible

Contents

1 Introduction

Bergy bits and growlers (i.e., small glacial ice features) travelling with waves and currents can pose great threats to offshore structure operating in the high North. As shall be discussed more in detail in this project, it is generally believed that these relatively small glacial ice features are more difficult to detect, monitor and to manage by concurrent ice management operations. Therefore, it is important to quantify the probabilities and consequences of the potential glacial ice impacts with the structure of interest. Technically, it is rather challenging to formulate and quantify the eventual structural safety associated with this complex and extensive interaction scenario (i.e., from ice mechanics, to hydrodynamics, to impact analysis, and to structural damage assessment). In efforts to ensure that involved petroleum industries maintain a high level of HSE and emergency preparedness, the Petroleum Safety Authority Norway (PSA) established a series of projects to study the structural safety in the high North (i.e., the central part of the Barents Sea). Through these projects, great insights into different aspects of this technical challenge have been achieved.

This project (i.e., NORD ST20_2019/313) is a follow-up project of three closely related preceding projects, namely, ST5 by Ekeberg et al. (2018) (going through the above-mentioned entire interaction process), ST19 by Lu et al. (2018) (with more detailed studies on impacts and damage assessments), and ST20_2018 by Ommani et al. (2018) (with more detailed studies on hydrodynamics and impacting bodies' motions in waves)[1]. As a continuation and further enrichments, in this project (ST20_2019), we intend to perform the following four main tasks:

- Assimilate and fuse knowledge generated over the previous projects (i.e., ST3, ST5, ST19, and ST20_2018). This task is presented in Chapter 4.
- Study the encounter frequency and statistical distribution of glacial ice features' geometry (i.e., size and parameterised shape) at the site of interest. This task is presented in Chapter 5.
- Establish local ice geometries and perform integrated analysis using Nonlinear Finite Element Methods (FEM) and the state-of-the-art *Simulator for Arctic Marine Structures* (SAMS). This means that the 'shared energy approach' shall be followed; and the structural damage assessment (i.e., internal mechanics) shall be carried out by Nonlinear FEM; and the impact energy map construction (i.e., external mechanics) shall be simulated with SAMS. In addition, SAMS has been upgraded to be able to simulate an 'deformation/damage map' around the structure directly. This feature shall be utilised as one of the methods (i.e., Method #2, shall be described later) to offer a more in-depth structural damage assessment. This task is presented in Chapter 6.
- Examine the assumption on the size of detectable small glacial ice features and construct a probability of detection curve with relevant parameters. This task is presented in Chapter 7.

Our deliverables from this project are:

- A review of the previous projects (ST5, ST19 and ST20_2018) and a synergy of their results. This manifested in distributions of velocity, location and probability of glacial ice feature impacts with a structure using an updated model.
- Probability of iceberg intrusions at any 100 by 100 km cell in Barents Sea (presented in terms of contours over the entire Barents Sea).

[1] In this report, for simplicity, we use the project numbers ST5, ST19, and ST20_2018 to refer to different projects without giving detailed project names and repeated citations to the project reports.

- Annual iceberg encounter frequency for structures with different sizes at a representative area in the Barents Sea (Block #7424 in the awards in predefined areas for petroleum activity)
- Statistical distributions of iceberg mass, geometry, residence time, and drift speed at any site in the Barents Sea.
- Introduction of two new methods for prediction of structural damage due to impact with glacial ice, i.e., Weakly-coupled and Fully-coupled.
- Deformation- or damage map on a structure: the weakly-coupled approach builds on the highly-accurate and efficient Simulator for Arctic Marine Structures (SAMS) and produces a deformation- or damage map around the structure showing critical locations susceptible to glacial impacts (this is an improvement comparing to the energy map simulated in ST19).
- A critical local geometry of glacial ice is identified with the help of the fully-coupled approach (Nonlinear Finite-Element Method (NLFEM) that is implemented in LSDYNA and calibrated against full-scale data).
- An assessment of marine radar's capabilities in detecting glacial ice features of various sizes under different environmental conditions and instrumentation set up.

2 Background

2.1 Glacial ice's life story

Glacial ice features of various sizes can pose a great threat to offshore structure in the Northern areas. According to the NORSOK N-003, presence of icebergs cannot be neglected in any part of the Barents Sea and the shelf of Jan Mayen. The probability of impact between structure and icebergs shall be estimated as a part of the design process and prior to operations in the Barents Sea. According to ISO 19906 (2019), the Barents Sea contains icebergs from the glaciers of Svalbard, Franz Josef Land and Novaya Zemlya. Figures 1.1 and 1.2 show several icebergs calved from these locations.

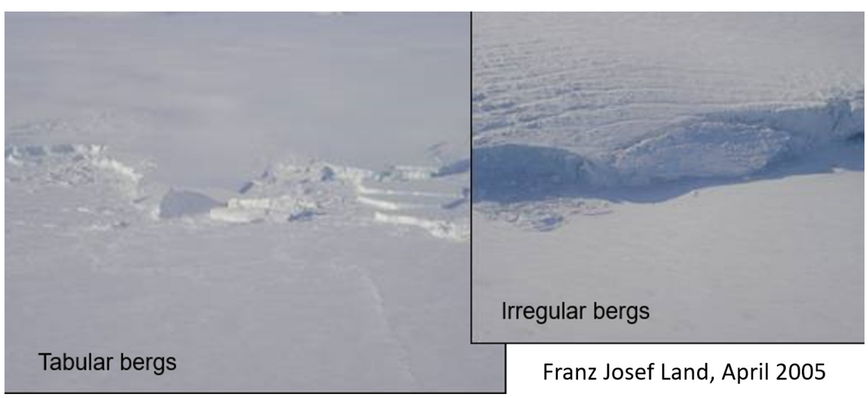

Figure 2.1. Icebergs of various shapes (tabular and irregular shapes) calved from the glaciers of Franz Josef Land, April 2015.

Figure 2.2. Icebergs calved from the glaciers of Novaya Zemlya.

The calved icebergs drift from the glaciers under the influence of the prevailing winds, waves, and ocean currents; and they can move large distances during their life span. It is possible to simulate the drifting track of icebergs from various origins. Figure 2.3 shows an example of the simulated icebergs' drift tracks in the Barents Sea, for clarity with reference to the blocks in the 23rd licensing round. We can see from this example that the northernmost Block A has a potential overlap with icebergs' drifting tracks.

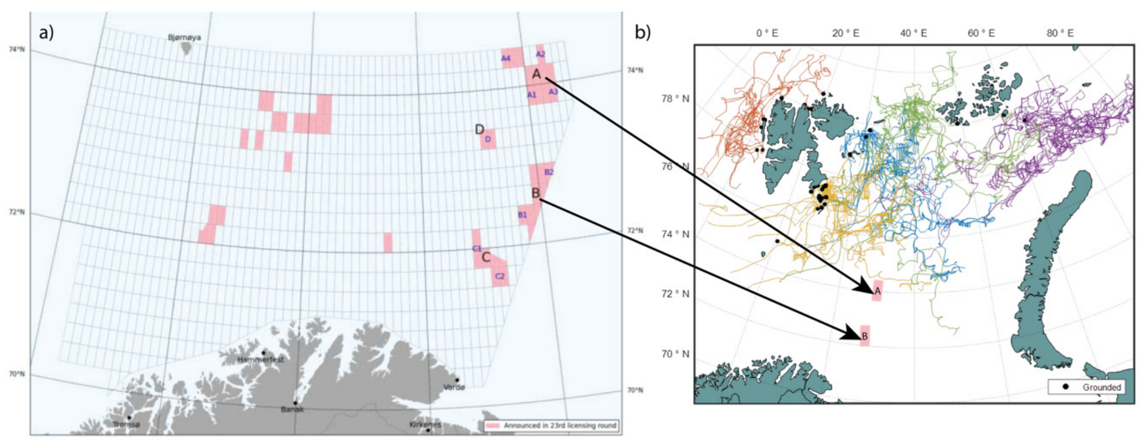

Figure 2.3. a) Blocks in the 23rd licencing round; b) a simulation example of icebergs' drift track (curvature lines) simulations and with rough locations of Blocks A and B from the 23rd licensing round.

Note that the southernly drifting icebergs undergo significant morphological changes due to thermal and wave erosions. Figure 2.4 exemplified such morphological transformation for a tubular iceberg (numerical modelling of the vertical cross-section, just right-half modelled) going through wave and thermal erosion after 40 and 150 days, respectively. We see from this example that the diameter of this iceberg shrinks from around 100 m to 80 m; and the total height shrinks from around 100 m to 80 m as well. Interestingly, an iceberg's inner mechanical properties are not changing too much in the course of thermal and wave erosion.

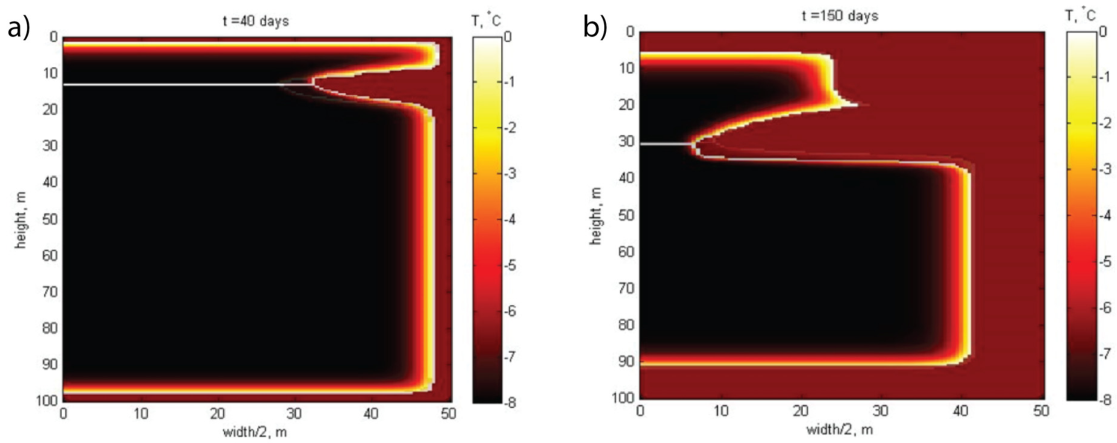

Figure 2.4. An example of thermal and wave erosions of an originally tubular iceberg after 40 days and 150 days (waterline is labelled with the 'white horizontal line') (Løset, 1993, Løset, 2018)

Eventually, when the icebergs drift to the sites of interests, they are relatively small and with a largely transformed global geometry. See e.g., Figure 2.5, where we tracked an iceberg drifting south of Bjørnøya. The effect of the wave washing of the iceberg is illustrated in Figure 2.5. The figure shows a part of an iceberg with the edge to sea water or sea ice at the lower right corner and a pool, which is likely to be formed by leftover water due to wave washing. Clear erosion marks, caused by wave washing, are seen diagonally from upper left towards the sea in lower left corner.

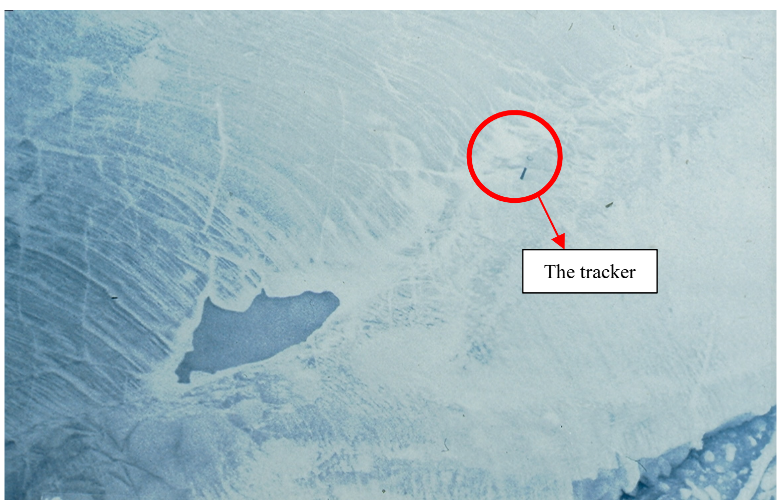

Figure 2.5. Iceberg with position tracker just south of Bjørnøya (Løset, 2018).

Larger icebergs can be detected, and corresponding ice management may be applied, e.g., by towing or deflecting them away from our assets. However, it is those small glacial ice features that can escape from concurrent ice surveillance system that are of great concern in this project.

Both ST5 and ST19 took for granted the occurrence of impact between the structure of interests and a glacial ice feature of a certain geometry. Given the background about glacial ice features' life story and in order to understand the structural safety in relation to a potential glacial ice's impact, it is important to investigate the annual encounter frequency of icebergs at a site of interests. In addition, thermal and wave erosions must be incorporated into the ice drifting models to obtain the statistical information of the encountered glacial ice features' size (mass). For small glacial ice features, which can slip through the ice surveillance system (e.g., marine radars) due to their limited size, impact analysis and structural damage assessment should be carried out.

2.2 Impact analysis

Small glacial ice features travelling with wave and currents can pose threats to offshore structures. The coupled motion of the glacial ice features and the offshore structure largely determine the location and velocity of impacts. Figure 2.6 illustrates the motion calculations of different shapes of the glacial ice feature in waves from ST20_2018. Figure 2.7 shows the impact velocity and their associated impact probability at different heights of the structure. The results in Figure 2.7 are derived from ST19, in which, the motion of the glacial ice in waves did not consider nonlinearities in the vertical direction.

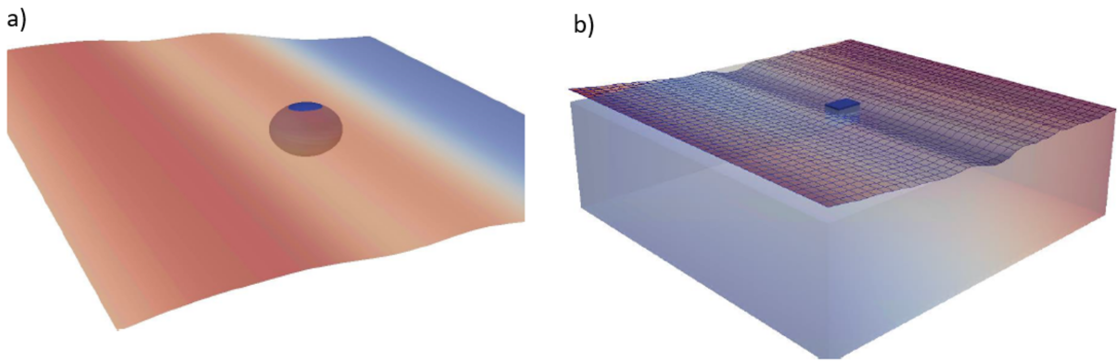

Figure 2.6. Glacial ice features' motions in waves by introducing nonlinear Froude-Krylov forces (from ST20_2018).

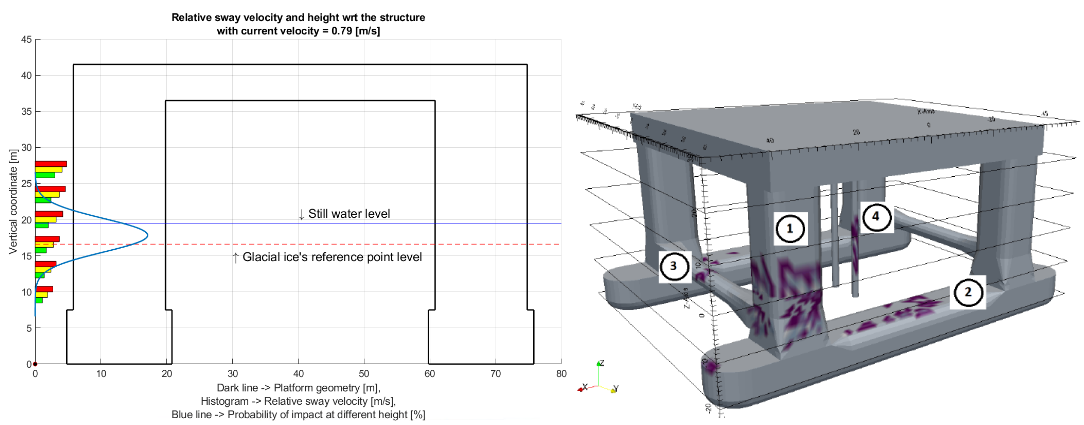

Figure 2.7. Left: impact velocity and the associated impact probability at different heights of the structure (from ST19) based on wave induced linear motion analysis; right: 'limited' high resolution simulations (from ST20) indicating impact location and impact velocities.

With known impact velocities and locations, external mechanics can be solved to obtain an 'impact energy map' around the structure (see Figure 2.8). The calculation of this 'impact energy' needs to take into account the dynamics of both the glacial ice feature and the offshore structure; and also, the local contact geometry of the glacial ice feature. This map essentially shows critical locations that can be selected for detailed structural damage assessment. To this point, it is shown that the methods and results from ST19 are complementary with ST20_2018 in many ways. It is important to assimilate and incorporate results from both the preceding projects; and to re-evaluate the impact analysis taking into account the glacial ice's nonlinear motions in waves.

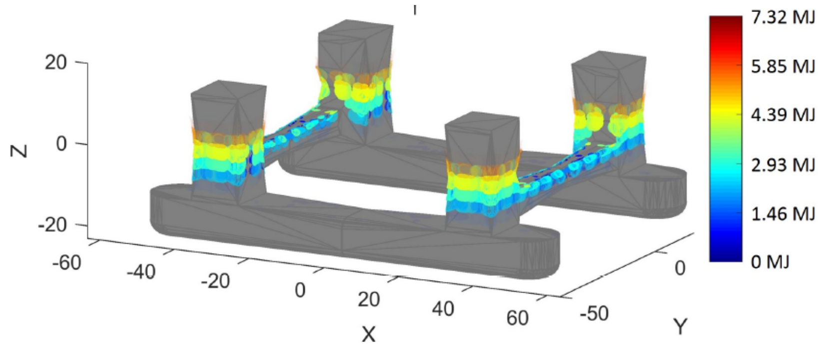

Figure 2.8. Impact energy map (results from ST19).

2.3 Structural damage assessment

For structural damage assessment, the '<u>shared energy approach</u>' should be adopted (Kim, 2014). It means that the impact energy should be dissipated both by the crushing of the glacial ice feature and the deformation of the structure. However, depending on the model assumptions, the shared energy approach can be realised with different levels of sophistication. In this project, we are presenting three different methods to perform damage assessment. Each of these methods has its own advantage and range of applicability. These are:

- **Method #1**: Integrated Simulations using SAMS and LS-DYNA (same method used in ST19)

For the integrated approach adopted in ST19, we first simulate separately two limiting scenarios, i.e., crushable ice + rigid structure simulation with SAMS; and rigid ice + deformable structure using NLFEM. Then the results are integrated by a joint force-displacement plot following the 'shared energy approach' allowing impact energy to flow both into the structure and the ice.

- **Method #2**: Weakly-coupled Simulations using SAMS (an improvement to ST19)

As an improvement to the integrated approach, it is possible to pre-run extensive NLFEM analysis to extract the Force – Deformation (F-D) curves at different locations of the structure. With these F-D curves available, the 'shared energy approach' can be directly and explicitly simulated within SAMS in a weakly-coupled manner. This is a technical advancement compared to Method #1 as used in ST19. This is to say, in ST19, we used Method #1 and simulated 1800 impact cases using SAMS, whereas only 7 critical locations were simulated with NLFEM using LS-DYNA. With this weakly-coupled approach, around the same amount of simulations (i.e., in the order of tens of hundreds) including structural deformation can be directly simulated and effectively performed by SAMS. Hundreds of structural locations' deformation/damage can be simulated and thereby creating a '<u>deformation/damage map'</u> around the structure. This offers a better insight on the local structural deformation and safety in different impact scenarios.

- **Method #3**: Fully-coupled NLFEM analysis using LS-DYNA

This method was originally developed by Liu, Amdahl and Løset (2011) and applied in ship and iceberg collision studies. An ice material model needs to be introduced in the NLFEM analysis to simulate the crushing of sea ice. The shared energy approach is simulated with NLFEM in a fully-coupled manner in LS-DYNA. We will introduce this method in this project to make damage assessment for selected cases (particularly for glacial ice features with rather sharp local geometry).

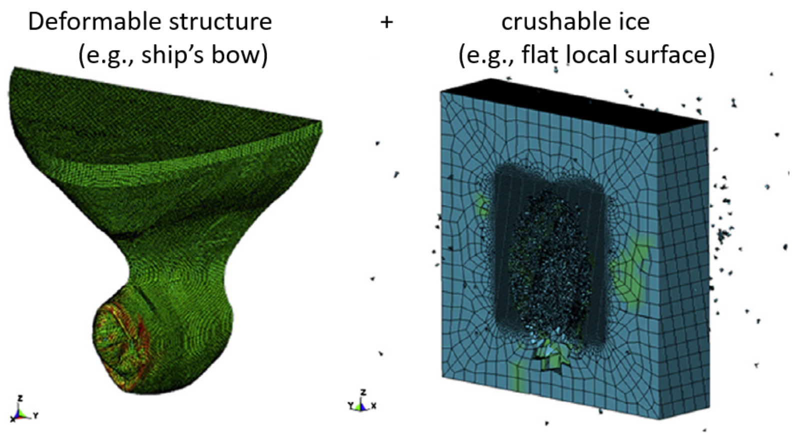

Figure 2.9. Fully-coupled NLFEM analysis between a deformable structure and a crushable ice by Liu et al. (2011).

2.4 Shape of glacial ice features

The damage caused by impacts from ice features depends on both the global geometry and the local geometry as illustrated in Figure 2.10. The global geometry determines how much of the kinetic energy that must be dissipated by deformation and crushing of the structure and the ice, while the local geometry (refer hatched areas in Figure 2.10) has a strong impact on the share of the deformation energy between the structure and the ice feature.

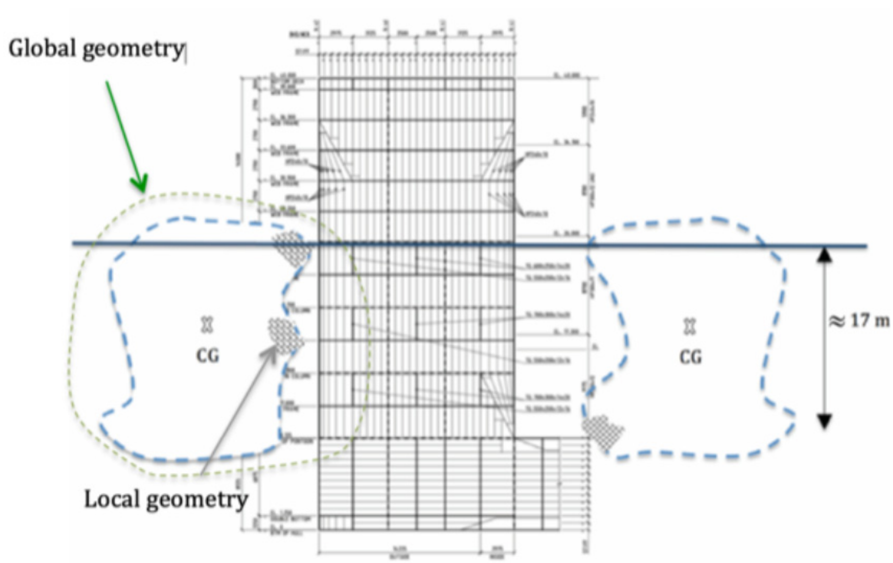

Figure 2.10. Illustration of local and global geometry.

The local geometry concerns the shape of the ice in a small area i.e. from the range of < 1 m^2 to a few m^2. Quantitative information of ice geometry on this local scale is scarce. On the other hand, the ice local geometry should not be considered independent of the structural configuration in the impact area.

Obviously, ice features with protruding parts may cause penetration of the side plating and inner panels and represent the largest damage potential. However, sharp sections are prone to crushing and by this the ice local geometry becomes smoother, see Figure 2.11. The sketch shows a horizontal section of the ice and the side structure in the impact area. The side plate is supported by vertical web frames. The "sharp" ice protrusion indicated by the dotted line is not strong enough to deform the side plating and will be crushed. The full line shows a shape that is strong enough to deform the plating and the web frame with (relatively) moderate deformation and modification of the ice shape.

What is the critical shape that must be considered for a given structural lay-out? This will be assessed in this project. The work will take into consideration both the ice crushing strength characteristics as well as structural resistance of the plate between stiffeners, stiffeners between frames and stringers as well as the resistance of a stiffened panel.

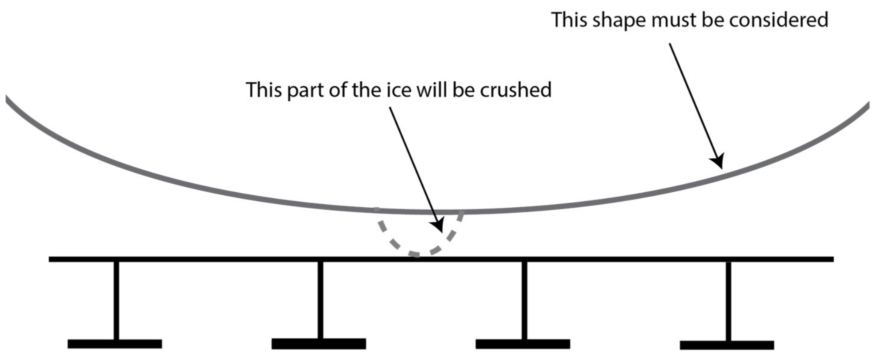

Figure 2.11. A simple illustration of the ice shape relative to the structural configuration.

3 Objectives of this project

Given the background of the task, this project comprises the following objectives:

- Review and make a synergy out of the results from ST5, ST19, and ST20_2018:
    1. Evaluation of the motion simulations using nonlinear hydrodynamic analysis in ST20_2019 and identifying important nonlinearities when conducting pre-impact motion analysis.
    2. Incorporate important nonlinearities into the impact sampling method (Fylling, 1994) utilised in ST19 by developing a new pre-impact motion analysis model (i.e., ST20_2019 model).
    3. Re-examine pre-impact motion analyses results from all the calculations from ST5, ST19, ST20_2018 and ST20_2019.

- Establish the annual iceberg encounter frequency for structures with different sizes at a given location and establish statistical distributions of iceberg mass, geometry, residence time, and drift speed at that location.
    1. Large-scale glacial ice feature's drifting track simulations in the Barents Sea taking into account wind, wave, current and Coriolis forces as well as effects of possible adjacent sea ice.
    2. Incorporate a thermo- and wave- erosion model in the drifting model to account for the morphological change of the drifting glacial ice (this provides information for the consideration of glacial ice's local geometry used for damage assessment).
    3. The influence of potential climate change scenarios on the results shall be investigated.
    4. In a selected local site, simulation with higher resolution is to be performed to derive the residence time and average drifting speed of a glacial ice feature. The annual probability of iceberg encounters can be obtained.

- Assessment of structural damage due to impact with a glacial ice feature with different reasonable local geometries established in the project. Both the exposed area of the semi-submersible structure and the un-strengthened structural members (e.g., pontoons) are analysed. This will be performed using more advanced methods (compared to those in ST19) following the 'shared energy approach'.
    1. Assess critical and reasonable local ice geometries.
    2. Integrate SAMS and NLFEM (following the procedure adopted in ST19) to perform external and internal mechanics analysis in order to construct the impact energy map and the amount of local structural damage.
    3. With improvement to ST19, weakly-coupled simulations with SAMS for damage assessment are performed within SAMS.
    4. Perform fully-coupled impact analysis involving ice material and structural material modelling within NLFEM for a few selected critical cases. This approach is more computationally demanding and is utilised to identify the critical glacial ice geometry.

4 Task #1: Review of ST5, ST19, and ST20_2018

Under the umbrella of the project 'Structural Safety in the High North', three closely related preceding projects were carried out with initiatives from the Petroleum Safety Authority Norway (PSA) (see Figure 4.1), and they are:

- ST5: Glacial Ice Impact, by DNV GL in 2018;
- ST19: Assessment of Structural Damage due to Glacial Ice Impact, by ArcISo in 2018;
- ST20_2018: Load, Design and Operation of Floaters in the Arctic, by SINTEF in 2018.

Figure 4.1 Reports' covers of the ST5, ST19, and ST20_2018 reports.

The ST5 report provided comprehensive analyses of the topic of glacial ice impact on structures, starting from analysing the motion of glacial ice features in waves and ending with performing structural damage assessment. ST5 started with a wide and extensive scope of work. Later, many simplifications were introduced given the time constrains in the project. These simplifications and the resulted shortcomings were further addressed in the follow-up projects: ST19 and ST20_2018. In this chapter, we will systematically go through all these related projects and identify their coherence, differences, shortcomings, and potential improvements that can be obtained. More precisely, we thoroughly examine the answers from the 3 projects to the following questions:

- When a small glacial ice feature impacts a platform, what would be the expected impact velocity and impact location (height range) given a certain sea state? This question is answered in the 3 projects through hydrodynamic analysis.
- Upon impact, what is the expected critical impact energy and what would be the consequent structural damage? This is answered in ST5 and ST19 through impact analysis and structural damage assessment.

4.1 Review of ST5[2]

The work carried out in ST5 can be largely separated into two parts. The first part focused on the hydrodynamic analysis and the second part dealt with impact simulations and damage assessment. The

[2] A more thorough review of ST5 was presented in the ST19 report. Here, only the key points of ST5 are re-summarised. Table and figure numbers used in this section are from the original report of ST5.

hydrodynamic analysis was mainly to study the relative motion of a glacial ice feature and a structure in different sea states. The relative motions were further interpreted as potential impact heights and velocities between the two objects. The structural analysis part focused on the local damage assessment given the impact energies that were derived from the results of the relative motion studies. The major findings from ST5 are summarised herein:

1. Though all facilities operating on the Norwegian continental shelf are designed for ship impact, but this might not be applicable/relevant to impacts for sea ice and ice features with respect to the impact locations and energy levels.
2. Due to potential severe wave conditions, the vertical extent of impacts on the semi-submersible structure can be beyond ship impact regions (e.g., Table 7 shows the impact range -10.8 m to +10.8 m from the reference point of the spheroidal ice feature).
3. The ice feature can protrude and collide with the structure elements which are not re-enforced for ship impact (Figure 23).
4. More than 1.5 m horizontal penetration may result from impacts with ice features (Table 15).
5. Uncertainties related to the pressure-area formulation that is used to estimate the load of the ice feature should be considered.

The preceding conclusions are based on the separate hydrodynamic analysis, impact analysis and damage assessment. Some critical points on these analyses are summarised below:

4.1.1 Hydrodynamic Analysis in ST5

ST5 mainly investigated the first order wave induced relative motion and velocity between a glacial ice feature and a structural column, but discussed the relation between impact velocity, drift velocity and impact location (vertical extent) only quite briefly. The major results presented (i.e., impact height and impact velocities) were obtained from frequency domain analysis, therefore such information was not correlated and often lead to conservative conclusions. This is to say, the dependence between impact velocity and impact height were not elucidated in ST5. In ST5, there was no information about mean drift velocity (mainly due to current and second order wave drift forces) for the ice feature studied. As considered for drifting vessels (Fylling, 1994) the ice feature needs to have a mean drift velocity to approach the structure, and the impact velocity distribution is largely influenced by the instantaneous drift velocity that is influenced by the oscillatory wave induced motion.

4.1.2 Impact Energy in ST5

For the velocity calculated in ST5, Eqs. (4-1) and (4-2) were utilised to calculate the impact energy. Eq. (4-2) that is based on DNV GL-RP-C204 (DNVGL, 2018), accounts for the fact that only a part of the kinetic energy E_i (from the glacial ice with a mass m_i, added mass a_i, and impact velocity v_i) contributes to the impact energy given by Eq.(4-1). A fraction of the kinetic energy E_i is transferred into other motion components of the platform.

$$E_i = \frac{1}{2}(m_i + a_i)v_i^2 \tag{4-1}$$

$$E_{impact} = E_i \frac{(1-\frac{v_s}{v_i})^2}{1+\frac{m_i + a_i}{m_s + a_s}} \tag{4-2}$$

4.1.3 Damage Assessment in ST5

NLFEM analysis was conducted for a vertical column of a given structure designed for operation in the Barents Sea. The column was subjected to impact from rigid, spheroidal ice features of varying sizes. Thus, crushing of the ice was neglected, but the interface pressure from the simulations (that was governed by the structural resistance) was compared with the pressure-area relationships given in ISO 19906 (2019). It was found that for small indentations/contact areas the ice crushing pressure exceeded by far the structural resistance, but for larger indentations/contact areas the structural resistance could exceed the crushing pressure especially for larger ice spheroids, thus forcing the ice to deform and dissipate energy. This was neglected in the analysis, partly because of the uncertainties in the pressure-area characteristics. The approach adopted was conservative and sometimes very conservative; once the ice starts to crush, the contact area increases, and the structure becomes even stronger.

In view of the complexities of the problem addressed but not fully resolved in ST5; and considering the recommendations of ST5 for further work, PSA commissioned two follow-up projects (ST19 and ST20_2018), which were executed simultaneously during the same time period in 2018.

4.2 Review of ST19[3]

ST19 mainly focused on advanced structural damage assessment. In addition, a more detailed analysis, of impact velocities, impact energies and impact height distribution were conducted. In all, three related tasks were performed: 1) Analysis of impact energies, including the effect of relative motion analysis between the glacial ice feature and the platform; 2) Impact simulation using the Simulator for Arctic Marine Structures (SAMS); and 3) Structural damage assessment following the shared energy approach. Among many findings, the major findings from ST19 are summarised in the following:

1. The relative impact velocity increases with impact height (presented in Figure 3.13).
2. The most probable horizontal impact takes place around the tip of the analysed ellipsoidal glacial ice feature around the Still Water Level (SWL).
3. Impacts occur mainly on the semi-submersible's column structure; only 0.6% impact takes place on the pontoon in the given 100-year return period wave condition.
4. In the selected 100-year return period wave condition, the maximum impact energy obtained from SAMS simulation is around 7.32 MJ, however, with a very low conditional probability. 90% of the impact events lead to impact energies less than 4.3 MJ.
5. Damage assessment was carried out using integrated analysis of SAMS simulation plus NLFEM analysis following the shared-energy approach. For the given ellipsoidal glacial ice feature the structure and ice dissipate an appreciable amount of the impact energy.
6. The structural indentation for 7.5 MJ impact energy vary from 0.25 m to 0.55 m. Considering that outer shell rupture is predicted to occur at about 0.6 – 0.9 m indentation the structure is considered safe from compartment flooding.

[3] Referred table and figure numbers are in their original numbering in the ST19 report.

4.2.1 Hydrodynamic Analysis in ST19

The hydrodynamic analysis in ST19 was a further extension of the work carried out in ST5. The main purpose was to establish correlated impact heights and impact velocities, such that the spatial distribution of impact events in the vertical extent could be obtained.

In ST19 the Response Amplitude Operators (RAOs) in ST5 were converted into time domain histories of coupled glacial ice feature and platform motions. Fylling's method (1994) was adopted to sample a large quantity of impact events (in the order of 1 million) for statistical purpose.

One of the shortcomings of ST19's hydrodynamic analysis is that only the linear wave theories were applied. Important phenomena such as nonlinearity of the vertical restoring force for a small glacial ice feature was not accounted for (see Figure 4.2).

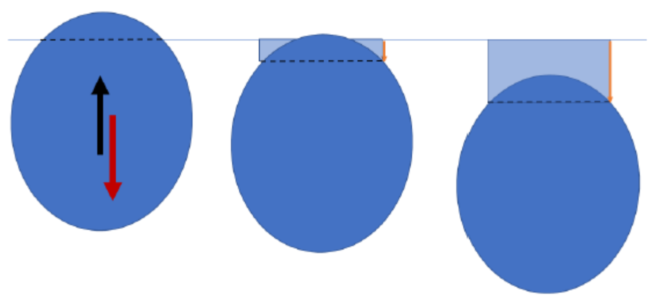

Figure 4.2 Nonlinear vertical restoring force of a small glacial ice feature due to its varying waterplane area leading to potential submergence (originally from Figure 9 of ST20_2018 report).

In addition, advanced but important 'near field' hydrodynamic effects (Sayeed et al., 2017) such as:

- Negative drift force on the glacial ice feature
- Velocity reduction as the glacial ice feature approaches the structure
- Fluid cushioning and shadowing
- The increase of the added mass of the ice

were not 'intended' to be studied in ST19. The consequence of neglecting these 'slowing down' hydrodynamic effects is that impact velocities calculated from ST19 and ST5 are most likely conservative. However, it should be noted here that the added mass will increase when the ice feature approaches the structure. So, it is difficult to say the overall impact energy is conservative or not when these important near field hydrodynamic effects are considered.

Similarly, due to the adoption of linear wave theories, wave drift forces were not included in the motion calculations in ST19. Alternatively, a current velocity of 0.79 m/s (Dezecot and Eik, 2015), corresponding to 100-year return period, was added to the wave induced oscillatory motion.

4.2.2 Impact Energy in ST19

ST19 comprised extensive analyses of ice impact and associated damage assessment. With respect to the impact energy calculation, extensive simulations (i.e., 1800 impact scenarios) with SAMS were performed to construct an 'energy map' characterising the distribution of the impact energy E_i around the structure. This is a much more informative approach compared to the one parameter E_i obtained through Eq. (4-2) in ST5. From this energy map, it was observed that for the given 100-year return wave period most impact events (90%) had an impact energy less than 4.3 MJ and the maximum impact energy 7.32 MJ was for hits on the column corners.

4.2.3 Damage Assessment in ST19

Compared to the damage assessment approach in ST5, ST19 adopted the more advanced (and less conservative) shared energy approach, in which, the impact energy was dissipated both in the structure and in the ice. Further to characterise the ice strength during the crushing process ST5 used the local design Pressure Area relationship (see Eq. (4-3) from ISO 19906 (2019)), while ST19 adopted the so-called process P-A curve (see Eq. (4-4)). The latter has significantly smaller pressures for small contact areas, but larger pressures for contact areas > 4 m^2. It was argued that it is physically more plausible to use the process P-A curve in damage assessment in the accidental limit state (ALS); generally, the deformations are not related to a single plate or a single stiffener (where Eq. (4-3) would be appropriate) but comprises larger stiffened panels with areas > 4 m^2. In summary, both the more advanced shared energy approach and more physically plausible P-A curves made ST19's damage assessment much less conservative than that was performed in ST5 for most of impact scenarios (especially for those with contact areas < 4 m^2).

$$p = 7.4A^{-0.7} \tag{4-3}$$

$$p = 3.2A^{-0.1} \tag{4-4}$$

4.3 Review of ST20_2018[4]

ST20_2018 focused on the hydrodynamic aspects of the interaction between a glacial ice feature and a platform. Three tasks were performed: 1) Linear model frequency domain analysis; 2) Development and calibration of a Nonlinear Froude-Krylov (FK) force model; 3) (Pre-) impact simulations.

After reviewing the ST20_2018 report, we consider the major clear findings to be:

- For the investigated case, when the distance between the glacial ice feature and the platform is approximately of the same size as ice, the added mass increases 47% and 10% in the sway and heave direction, respectively.
- Compared to the linear model, the inclusion of the nonlinear FK force improves the prediction of vertical force components on the glacial ice.
- Being not emphasized in the original report, but interestingly indicated by one simulation; the near-field change of the added mass (via the equation in Section 7.1.2) can reduce the horizontal impact velocity to only 60% of its original value (see Tables 18 and 19). However, the opposite trend was observed in a different simulation.

4.3.1 Hydrodynamic analysis in ST20_2018

The hydrodynamic analysis constituted the main bulk of the work carried out in ST20_2018. The report started with an extensive review of the different hydrodynamic aspects that are of interest to the

[4] Referred table and figure numbers are in their original numbering in the ST20 report.

engineering problem at hand; and it was indicated that it was the near-field wave driven hydrodynamic effects that were of interest for this project (ST20_2018).

Extensive linear frequency domain analysis was performed using WAMIT to derive the hydrodynamic coefficients, e.g., added mass, as a function of the position of the glacial ice feature relative to the platform. However, such information was not fully exploited in the remaining of the work, i.e., in simulating the impact between the glacial ice and the platform. For example, out of the 23 simulation cases presented in the report concerning column impacts, added mass variations were considered only in a very limited number of cases (i.e., Cases #21, #22 and #23). Moreover, in these 3 cases where the added mass variations were considered, ST20_2018 simplified the problem considerably by adopting the following strong assumptions:

- Added mass variation is only considered in translational modes.
- Convolution integrals were replaced by zero-frequency added mass, and memory effects were neglected in these impact simulations.

The authors of the ST20_20018 report acknowledges the significance of the above assumptions, and they wrote the following in their recommendations for future work:

- *The repelling or attraction forces due to variation of zero-frequency added mass, as ice approaches the platform, are studied briefly here, only for translational motions of ice. A more detailed investigation and validation of the implemented model is needed, since these forces may play an important role on determining the velocity of ice at the time of impact.*
- *Wave tank model experiments including both the ice mass and platform should be carried out to validate the numerical analysis results. Hydrodynamic tests should be carried out on the glacial ice with and without the platform present.*

In most of their simulation cases, i.e., Cases # 1 – 17, the only major improvement compared to the hydrodynamic analysis performed in ST19 (see Section 4.2.1) is the inclusion of the Nonlinear Froude-Krylov force (NLFK). Major conclusions concerning impact velocity and impact energy were based on this NLFK analysis, in which, potential repellent or attraction force was in fact not considered. In addition, according to the description in the first paragraph in page 41 of the ST20_2018 report, the implemented Froude-Krylov model introduced in ST20_2018 utilised the incident wave pressure field (not the total pressure field introduced by the platform) to calculate the forces. In other words, the effect of the wave pressure field's variation caused by the presence of the platform was not included in their analysis.

As ST20_2018 pointed out in one of their reviewed papers, that Isaacson and McTaggart (1990) through simulation and model experiments, found that small ice features with diameters less than 50% of the structure's dimension may lead to significant reduction in impact velocity and even no collision at all. This important phenomenon, which potentially can lead to less conservative impact energy estimates, requires further studies, as indicated in ST20_2018. It is therefore also ST20_2019's recommendation that this interesting and important phenomenon should be studied in the future.

4.3.2 Impact Energy in ST20_2018

Because ST20_2018 mainly focused on hydrodynamic studies, the impact energy was calculated via Eq. (4-1) in a simplified fashion. As commented before, the energy calculated from this equation additionally includes energies that lead to body motions and only a portion of this value is the so-called 'impact energy', which is supposed to be dissipated by structural deformation and ice crushing. In general, this overestimates the impact energy compared to Eq. (4-2) utilised in ST5 by about 2% - 6% (Ekeberg et al., 2018). In addition, the impact energy calculated in ST20_2018 were limited by the maximum amount of impact scenarios (in the order of 20-30 scenarios, see the case IDs in Table 5) that were simulated; whereas in ST19, hundreds of impact events were simulated efficiently by SAMS which leads to the construction of an impact energy map around the structure.

4.4 ST20_2019 model: A simplified nonlinear model for wave induced glacial ice motion

Building on the previous studies (i.e., ST5, ST19 and ST20_2018), we develop in this section a simplified but improved numerical model to predict the nonlinear motion of a glacial ice feature in waves.

4.4.1 Model description

The aim is to calculate the relative motion between the glacial ice feature and the platform taking into account the involved nonlinearities (i.e., nonlinear vertical restoring force, and slow drift force). The coordinate system of the studied problem is shown in Figure 4.3.

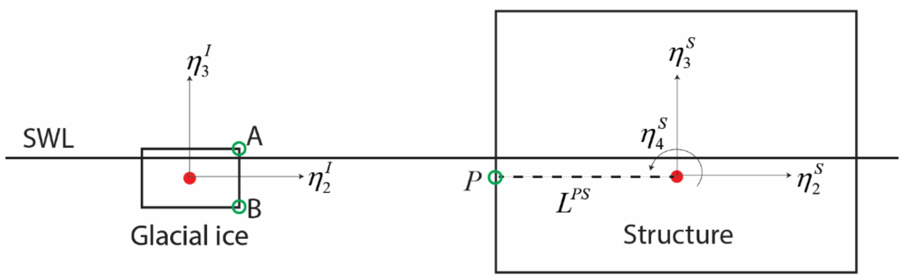

Figure 4.3 Coordinate system of the studied problem.

The motion of the glacial ice feature and the platform are calculated separately. As the platform is quite large, the same linear wave theory as applied in ST19 is adopted. Nonlinearities concerning potential full submergence and slow drift force are accounted for in the motion calculations of the small glacial ice feature.

When formulating the simplified nonlinear model, the following assumptions are made:

- The Froude-Krylov force component is calculated by integrating the incident wave pressure without considering the presence of the platform. This appears to be the same assumption implicitly mentioned in ST20_2019 (see Section 4.3.1).
- Constant added mass and added damping coefficients are adopted. This assumption is utilised in most of the simulation cases (e.g., 20 out of 23 cases for the column impact scenario) in ST20_2019. However, these parameters are dependent upon the wave frequency and the relative distance between the ice and the structure. Further studies on these parameters' influences are needed.
- For the wave diffraction force components, simplified formulation based on long wave theory is adopted. This formulation might become inaccurate when dealing with relatively short-wave

components. However, considering the relatively limited size (around 15 m) of the glacial ice feature we are studying, this assumption is considered reasonable.

- For a given wave spectrum, wave drift force is calculated based on existing nondimensionalised results.

For the wave introduced oscillatory motion, and considering the above-mentioned assumptions, the motion of a glacial ice feature may be described as in Eq. (4-5),

$$(A_{ij} + M)\ddot{\eta}_i + B_{ij}\dot{\eta}_i = F_i^W + F_i^R \tag{4-5}$$

in which, M is the mass of the glacial ice feature. η_i is the displacement of the glacial ice feature in i direction. For our problem, we consider that the glacial ice feature has only two degrees-of-freedom (2 DoF), i.e., in the sway (i=2) and heave (i=3) directions. The 'dot' represents derivative with respect to time, which leads to $\ddot{\eta}_i$ and $\dot{\eta}_i$ being the acceleration and velocity of the glacial ice, respectively. A_{ij} and B_{ij} are the added mass and added damping of the glacial ice; together with the restoring force component F_i^R, which corresponds to the so-called radiation force components. On the right-hand side of Eq. (4-5), F_i^W is the wave excitation force. To calculate the motion η of a glacial ice in waves, the formulation of each force component is described below.

We first assume that the scenario is a small volume body in waves. This means that the characteristic body size L and the wave length λ should satisfy the relationship of $\lambda / L > 5$ (Faltinsen, 1993). Given the limited size of the glacial ice we are studying, i.e., $L \leq 15\,\text{m}$, this condition is satisfied for most wave components in a typical wave spectrum. We can thereby write the generalised wave excitation force $\mathbf{F}^W$ as in Eq. (4-6),

$$F_i^W = F_i^{FK} + F_i^{Diff} = -\iint_S p n_i ds + A_{i1}a_1 + A_{i2}a_2 + A_{i3}a_3 \tag{4-6}$$

Eq. (4-6) shows that the wave excitation force consists of two parts: the Froude-Krylov force (see Eq.(4-7)); and the diffraction force. In Eq. (4-7), ds is a small portion of the instantaneous wetted surface area of the ice feature, S. Moreover, p is the local pressure acting on ds, n is a unit vector on ds, and n_i is the component of n in the i direction. p can be calculated as shown in Eq. (4-8) assuming infinite water depth. The formulation in Eq. (4-8) is the incident wave pressure without the influence of the platform presence. We believe this is same formulation of pressure as used in ST20_2018 (see comment in Section 4.3.1).

$$F_i^{FK} = -\iint_S p n_i ds \tag{4-7}$$

$$p = \begin{cases} \frac{\rho g \zeta_a}{\omega} e^{kz} \sin(\omega t - kx) & z \le 0 \\ \frac{\rho g \zeta_a}{\omega} \sin(\omega t - kx) & z > 0 \end{cases} \quad (4\text{-}8)$$

where,

ρ	is the water density, 1020 kg/m^3;
g	is the gravitational acceleration, 9.8 m/s^2;
ζ_a	is the wave amplitude, in [m];
z	is the water depth calculated from the mean Still Water Level (SWL), in [m];
ω	is the wave frequency, in [rad/s];
k	is the wave number and can be expressed as $k = 2\pi/\lambda$.

For the general diffraction force expression F_i^{Diff} in Eq. (4-9), $A_{22}, A_{33}, A_{23}, A_{32}$, are the added mass coefficients of the glacial ice feature in sway, heave, sway/heave and heave/sway directions, respectively; whereas a_2 and a_3 are the undisturbed fluid particle acceleration at the geometric centre of the wetted volume in sway and heave directions, respectively (Faltinsen, 1993).

$$F_i^{Diff} = A_{i2} a_2 + A_{i3} a_3 \quad (4\text{-}9)$$

In Eq. (4-5), the restoring force F_i^R , by only considering the vertical direction motion η_3, can be formulated as in Eq. (4-10), in which, $D(S)$ is the distance from the centre of area ds to SWL. At the static equilibrium in absence of wave motion (i.e., $\eta_3 = 0$), it follows that, equivalently, $\rho g \int D(S) ds = Mg$, $F_3^R = 0$, and $(\rho g \int D(S) ds) / A_W =$ mean draft of the glacial ice, in which, A_W is the waterplane area of the glacial ice at SWL. Notably, with changing vertical motion η_3 of the glacial ice, Eq. (4-10) takes into account the nonlinearities due to waterplane area change and the scenario when the entire glacial ice is fully submerged.

$$F_3^R = \rho g (\int D(s) ds - \eta_3) - Mg \quad (4\text{-}10)$$

Eqs. (4-5) to (4-10) are formulated in the time domain and the external forces, i.e., $F(\eta)$ on the right hand side of Eq. (4-5), are dependent on the instantaneous position/solution η . The Partial Differential Equation (PDE) system in Eq. (4-5) is solved with an explicit numerical scheme (Cook et al., 2007).

Solving Eqs. (4-5) to (4-10) yields the oscillatory motion of the glacial ice. In addition, we capture just a small portion of the drift motion mostly because we integrate on the instantaneous wetted surface when calculating the Froude-Krylov and the restoring forces, see Eqs. (4-7) to (4-10). Other contributions to drift motion are not captured in the above model and thus only the oscillatory part motion from the solutions to Eqs. (4-5) to (4-10) are trust worthy. To overcome this shortcoming, we filter away the drift motion calculated from Eqs. (4-5) to (4-10) and apply a different method to calculate the wave drift motion of the glacial ice.

The wave drift force can be formulated as in Eq. (4-11), in witch, A_R is the reflected wave height. In Fig. 5.5 of the text book *Sea Loads* (Faltinsen, 1993), the normalised wave drift force α (see Eq. (4-11)) are plotted for a wide range of wave periods/frequencies for a two dimensional (2D) free-surface piercing rectangular body. For a given wave spectrum, we shall adopt the nondimensionalised drift force to approximate the wave drift force on our glacial ice feature.

$$\bar{F} = \frac{\rho g}{2} A_R^2 = \alpha \rho g \zeta_a^2$$
$$\alpha = \frac{1}{2}\frac{A_R^2}{\zeta_a^2} = \frac{\bar{F}}{\rho g \zeta_a^2} \tag{4-11}$$

This numerical model was implemented as code package. This numerical model was utilised to qualitatively review some of the results in ST5 and ST20_2018.

4.4.2 Validation against ST5 results

The glacial ice feature motion analyses in ST5 were based on linear wave theory. The Response Amplitude Operators (RAOs) were presented for the glacial ice feature of various shapes and distance from the platform. The simplified nonlinear model should be able to reproduce these linear RAOs results of a stand-alone glacial ice feature if we introduce the small-amplitude wave conditions (i.e., no submergence effects).

In this section, we present the validation of the ST20_2019 model against the heave and sway RAOs from the ST5 report for the cuboidal glacial ice feature in Figure 4.4 and Figure 4.5, respectively.

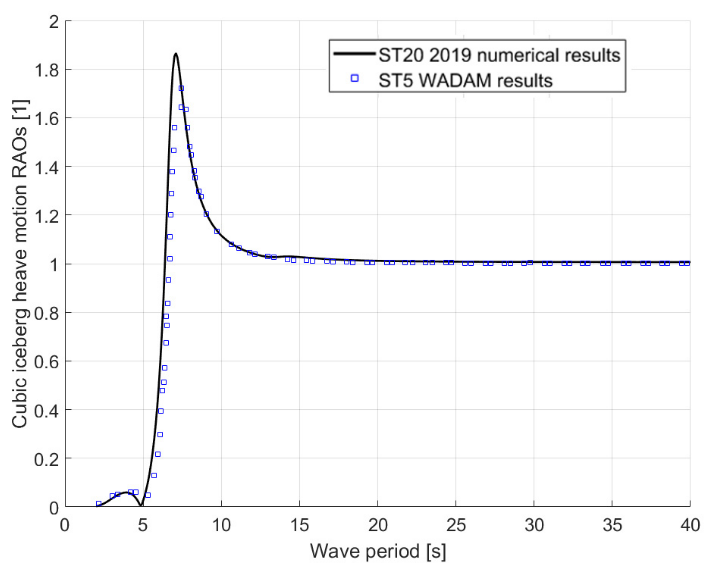

Figure 4.4 Comparison of the heave RAOs of the cuboidal glacial ice feature (Original results are from Figure 10 of the ST5 report).

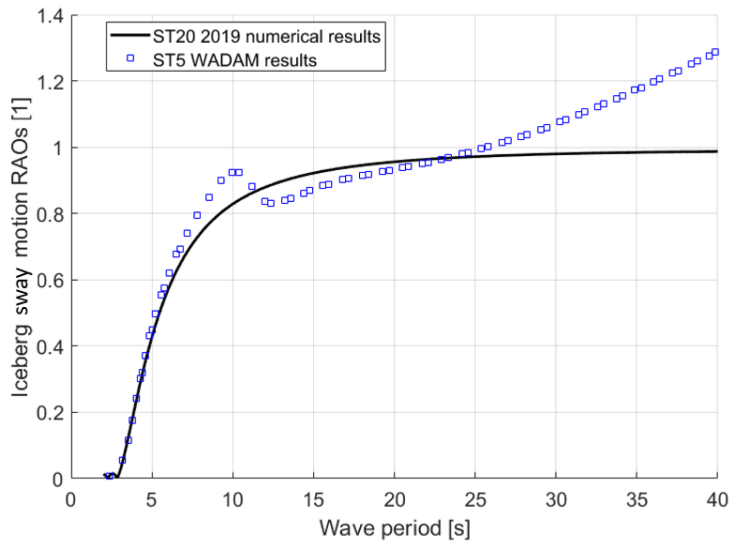

Figure 4.5 Comparison of the sway RAOs of the cuboidal glacial ice feature (Original results are from Figure 10 of the ST5 report).

From Figure 4.4 and Figure 4.5 we see that the results of the ST20_2019 numerical model agree well with the WADAM simulations performed in ST5. In Figure 4.5, there are small discrepancies between the sway direction RAOs in the wave period ranges of around 10 s and beyond 25 s. Concerning the discrepancies around 10 s wave period, it is possible that this is due to the neglection of the roll motion in the simplified model. It is speculated whether the deviation for wave period larger than 25 s, could be due to 'limited water depth setting' in WADAM simulations such that their results are not converging to 1 as it should be theoretically. This non-converging but increasing RAOs in the sway direction in long wave periods exist in both ST5 and ST20_2018 (e.g., see Figures 4 and 5 in ST20_2018 report). However, this discrepancy is considered as a minor issue as most wave components in a typical irregular wave condition are less than 25 s, which corresponds to a wave length of approximately 1 km.

In summary, with this quantitative probe, it confirms that the RAOs results from both ST5 and ST20_2018 are solid and trustworthy. These results were also the basis for the glacial ice motion analysis performed in ST19; and in turn, such validation also corroborates the validity of our developed simplified nonlinear model.

4.4.3 Validation the ST20_2018 results against the ST20_2019 results

ST20_2018 developed the Froude-Krylov (FK) model to account for the nonlinear motion of the floating glacial ice feature in waves. After the implementation of the FK model, ST20_2018 calibrated their model against Computational Fluid Dynamic (CFD) simulation results. Coefficients were introduced and calibrated such that the FK model (together with a Morrison-type element for drag force calculation) yielded similar results. Two calibration cases were performed: a fixed- and floating- ice cube in a regular wave.

The model set-up for the tests cases is illustrated in Figure 4.6. An ice cube with the size of (15 m × 10.3 m × 10.3 m) was constrained by four horizontal mooring lines. For the fixed ice cube case, the motion of the ice cube was set to zero (the mooring lines had no effect or had infinite stiffness). For the floating ice cube case, each mooring line was giving a stiffness of 4 kN/m. With the mooring line arrangement in Figure 4.6, it leads to a total horizontal mooring stiffness of $4\sqrt{2}$ kN/m.

For the wave condition, a regular wave with a height of 9.8 m and a period of 14.8 s was utilised. Comparing the size of the ice cube (L = 15 m) with the wave length ($\lambda = 342\,\mathrm{m}$), it was a long wave scenario that was tested. In this section, our developed ST20_2019 numerical model will be employed to quantitatively review these ST20_2018 results.

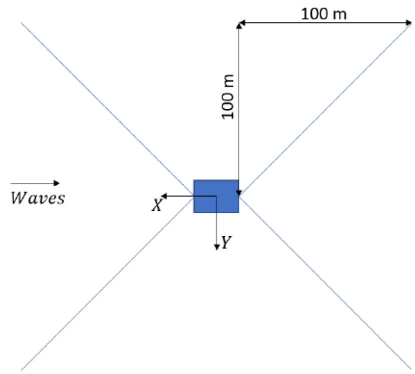

Figure 4.6 Model set-up in ST20_2018 for calibration of the NLFK and drag force (originally from Figure 16 of the ST20_2018 report).

4.4.3.1 Fixed ice cube

A fixed ice cube exposed to the action of a regular long wave, it is constantly submerged when wave peaks arrive. This is a nonlinear effect that is disregarded in linear wave theory. In this section, we shall present the validation of the vertical force in this test set-up.

In the original report of ST20_2018, the authors first compared the vertical force against the CFD simulation results. At this stage, the vertical force includes the Nonlinear Froude-Krylov (NLFK) force but was without the 'Morrison type drag force'. Their results were reproduced and presented in Figure 4.7 together with the prediction from the ST20_2019 model. We see that our ST20_2019 numerical results agree well with the ST20_2018 results when it comes to the vertical force component excluding the drag term. The nonlinear submergence behaviour at wave peaks is captured by both the ST20_2018 (blue circle markers) and ST20_2019 (red curve) results. However, there is a discrepancy with respect to the CFD simulation results.

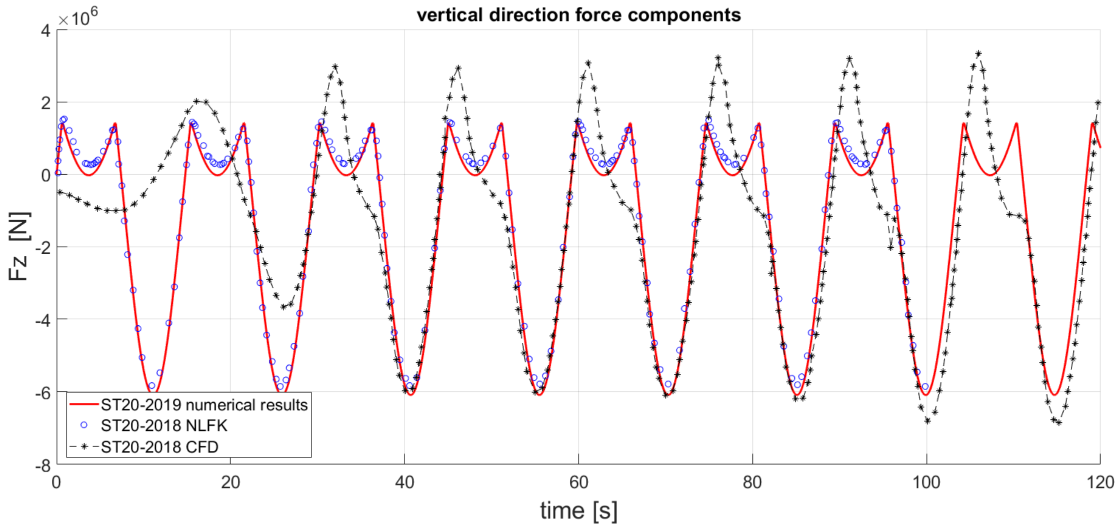

Figure 4.7 Comparison of vertical force components among different methods for the fixed ice cube in a long regular wave.

In the report of ST20_2018, such discrepancy with the CFD simulation results are considered due to the missing 'drag term'. Accordingly, they introduced in ST20_2018 the '*Morrison-type viscous force with a constant drag coefficient*'. Similarly, we may use Eq. (4-12) to account for the drag term in the vertical direction. Via Eq. (4-12), we can calibrate different drag coefficient values such that we can approximate the CFD simulation results.

$$F_{drag3} = \frac{1}{2}\rho C_D A_w v_3^2 \tag{4-12}$$

Eventually, it is found that only with a drag coefficient of around $C_D = 6.7$, can we approximate the CFD results well as in Figure 4.8. This drag coefficient is considered unrealistically large. It is almost 10 times larger than a typical drag coefficient that is normally encountered (e.g., from 0.66 to 0.81 according to Isaacson and McTaggart (1990)). In the ST20_2018 report, the exact value of the drag coefficient that was utilised to calibrate the model to match the CFD results was not mentioned. However, based on the above results, we believe that a large drag coefficient of around 7 was utilised in the ST20_2018 project. The consequence of this is that almost 10 times larger than normal drag force have been included in the ST20_2018 calculations.

Surprisingly, this is not influencing the eventual results (i.e., impact velocity and impact height) significantly. This will be discussed in the next section and be demonstrated in detail in Section 4.5.2.

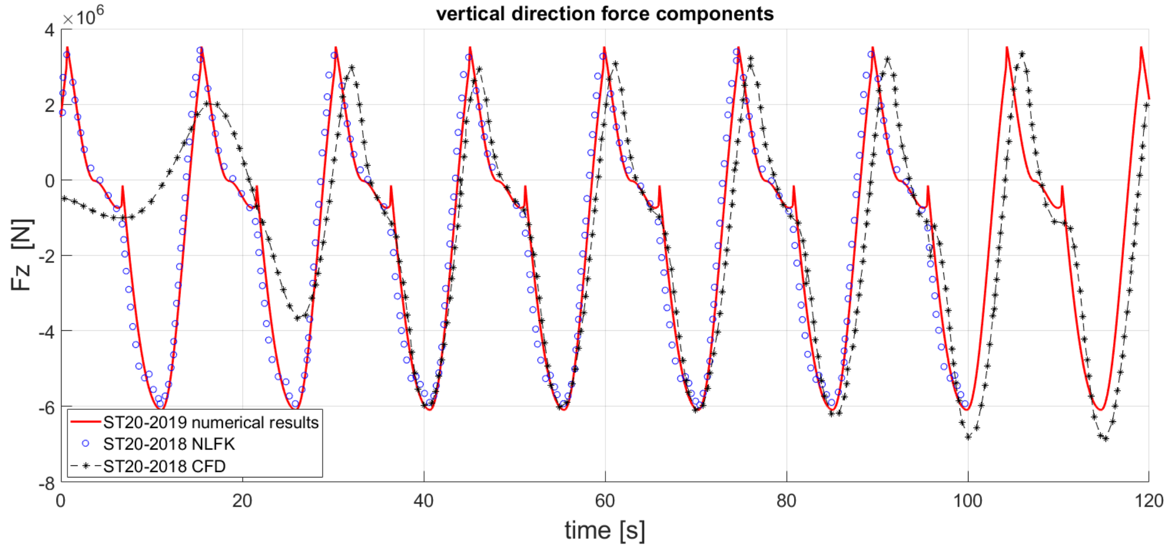

Figure 4.8 Comparison of vertical force components with the inclusion of a drag term together with a constant drag coefficient of $C_d = 6.7$.

4.4.3.2 Moving ice cube

A moving/floating ice cube in a long regular wave condition was simulated in ST20_2018. The vertical and horizontal motion histories of the glacial ice are presented in Figure 4.9.

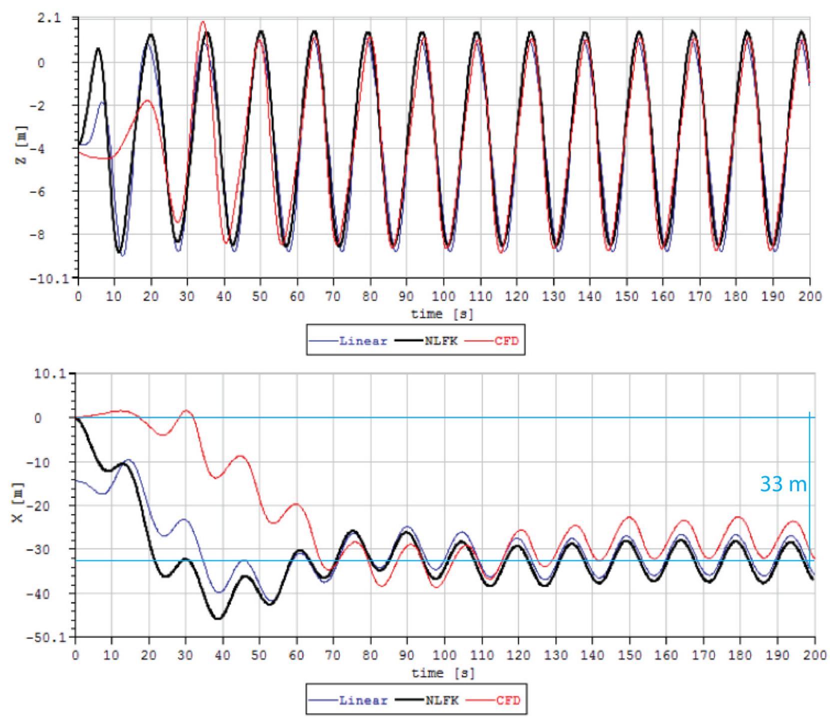

Figure 4.9 Vertical and horizontal motion histories of the glacial ice feature simulated by different methods (originally from Figure 20 of the ST20_2018 report).

Recall, that the floating ice cube case shown in Figure 4.9 represents a scenario of a small floating body in a regular long wave condition. According to Lever and Sen (1987), when the wave length and glacial ice feature's size ratio λ / L is larger than 13, the floating ice cube is supposed to behave like wave particles. The ratio for the ice cube in Figure 4.9 is $\lambda / L = 342/15 \approx 23$, which indicates that the floating ice cube should follow the wave profile in both vertical and horizontal direction.

According to the upper plot of Figure 4.9, the ice cube follows the wave profile rather well in the vertical direction as expected (i.e., linear wave solution curve and the NLFK curve coincide with each other). However, in the horizontal direction (lower plot of Figure 4.9), there is an obvious drift of about 33 m, which is hard to explain. This is equivalent to a drift force of 187 kN whereas almost 0 N drift force is expected according to Fig. 5.5 in Page 140 of the book *Sea Loads* by Faltinsen (1993).

In addition, the ST20_2018 report writes:

"The comparisons for vertical motions are better than horizontal motions. CFD predicts 10 times larger mean drift force comparing to two other methods. The reason for this discrepancy is unclear. Possible viscous effects in the splash zone steepening the waves in the CFD domain could be among the reasons. Nevertheless, a relatively good comparison between the horizontal motions are obtained simply by adjusting the mean forces in the SIMO simulations according to CFD."

It appears that the drift force in the model developed in ST20_2018 has been increased by 10 times in order to match the CFD results. However, as will be shown in a later section, the ST20_2018 results concerning the impact velocities and impact heights are very close to the prediction by the newly developed simplified nonlinear model in ST20_2019, which comparatively has 10 times less drag coefficient and 10 times less drift force. It is therefore speculated that the 10 times increase in drag force in Section 4.4.3.1 and 10 time increase in the mean drift force in Section 4.4.3.2 counterbalance each other in ST20_2018; and their final results concerning the impact velocities and impact heights are still valid (to be presented).

4.5 Synergy of ST5, ST19, and ST20_2018

So far, we have introduced the simplified nonlinear model (i.e., ST20_2019 model), with which we have performed validations against important results of previous projects. In this section, we shall develop a synergy between relevant methods and important results from the previous projects (i.e., ST5, ST19, and ST20_2018) and the new analysis of ST20_2019 to answer the important questions of 'impact velocity' and 'impact location' in this engineering problem.

This section gives more weight to the calculations of glacial ice feature's motion in waves, i.e., pre-impact hydrodynamic analysis. When it comes to damage assessment, it is recommended to directly consult results from Chapter 5 of the ST19 report and Chapter 6 of the ST20_2019 report, which are based on more advanced damage assessment method.

In order to make a synergy between the results, we must first identify comparable results with similar inputs from these different projects. In ST5, the simulation set-up for the pre-impact relative motion study is presented in Figure 4.10. Glacial ice features of various sizes and geometries (including the cuboidal shape) were positioned at a pre-defined and fixed distance. For the 15 m long cuboidal glacial ice feature, all wave conditions, including the 1-year, 10-year and 100-year return periods wave conditions were simulated in their linear frequency domain analysis. We shall mainly use results from this set of simulations (see Table 9 of the ST5 report).

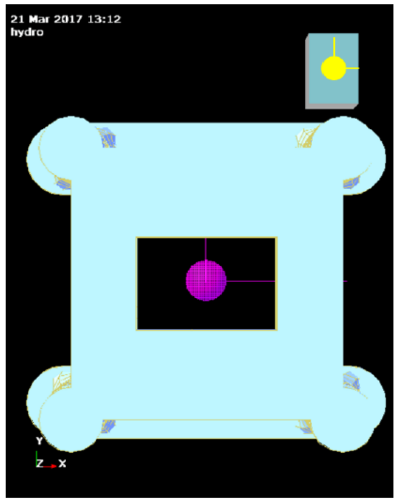

Figure 4.10 Numerical set-up to study the relative motions via linear frequency domain analysis by WADAM (originally from Figure 8 of the ST5 report).

For ST19, the authors conducted time-domain analysis based on the frequency domain RAOs results from ST5. The numerical set-up is illustrated Figure 4.11. As shown in the figure, the analysis comprised a two-dimensional simulation with only the spheroidal glacial ice feature in the 100-year return period wave condition. Therefore, the results from ST19 are not strictly comparable with other projects because of a different geometry. Nevertheless, the relevant results from ST19 are still presented in the comparison to give a flavour of the geometrical influences on the pre-impact hydrodynamic analysis.

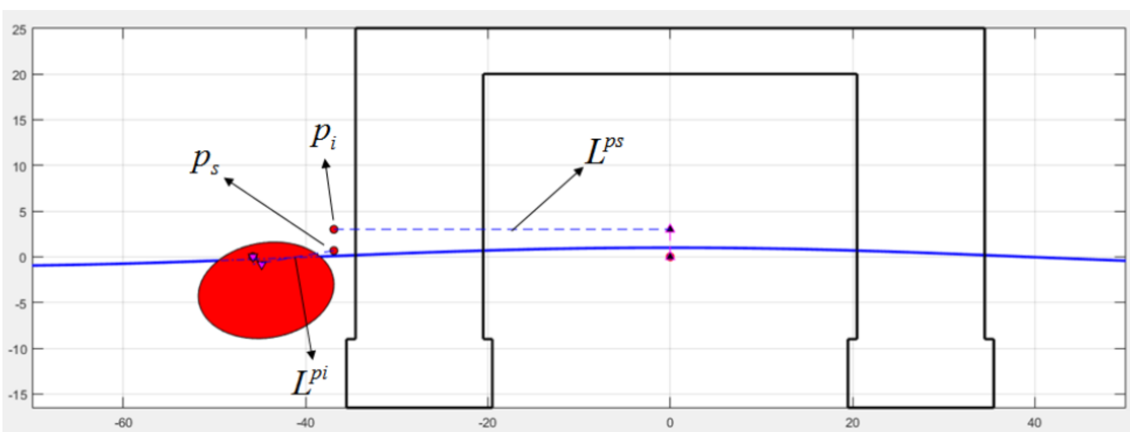

Figure 4.11 Numerical set-up to study the relative motions via linear time domain analysis (originally from Figure 3.4 of the ST19 report).

For ST20_2018, most of the simulations were conducted on the cuboidal glacial ice feature in the 1-year return period wave condition. The initial locations and orientations of the glacial ice feature were varied in different simulations. Figure 4.12 presents 10 different scenarios in terms of the Location IDs (LID). For each LID, three wave conditions with a return period of 1 year were simulated. For inter comparison purpose, we mainly focus on the results from LID #3, #4, and #9, in which, impacting with the column of the structure is of concern.

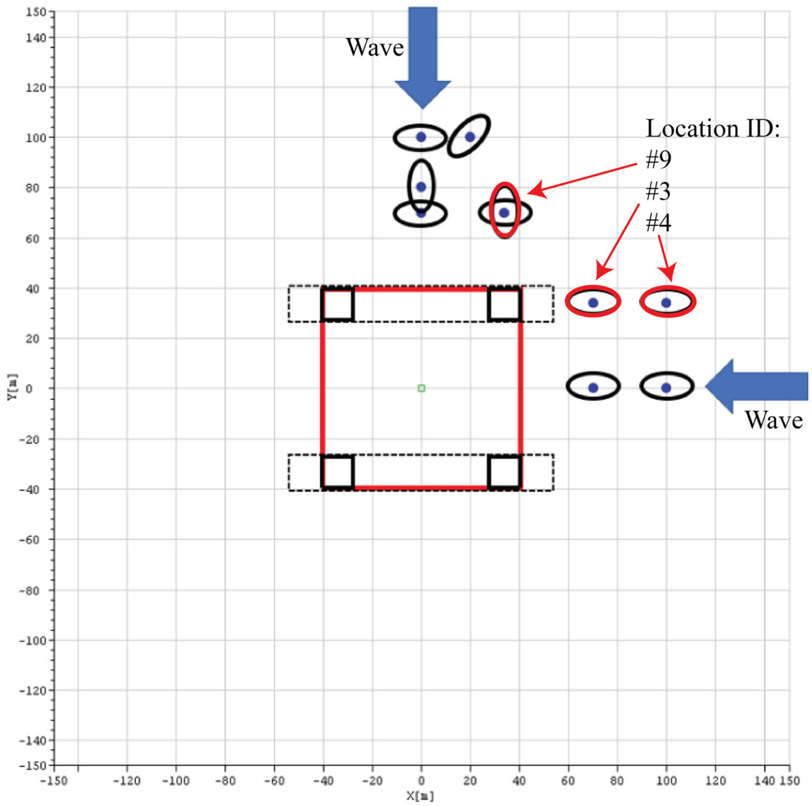

Figure 4.12 Location and orientation variations in ST20_2018's simulations (comparable cases: impacts with the column were labelled by red colours. Note that although ellipsoids were utilised in this figure to represent the glacial ice feature, most of the simulated glacial ice features are actually in the cuboidal shape. This figure is originally from Figure 31 of the ST20_2018 report).

After reviewing all the cases that were simulated in the previous projects, we find that the common comparable cases are:

- Cuboidal glacial ice feature with a geometry of 15 m × 10.3 m × 10.3 m (see Figure 4b and Figure 2 in ST5 and ST20 reports respectively).
- 1-year return period wave conditions (see Table 9 and Table 3 in ST5 and ST20 reports, respectively).
- Impacts with the platform's column structure.

In the next section, the newly developed simplified nonlinear model (ST20_2019 model) is utilised to simulate the above comparable cases and shed light on the impact velocity, impact height and their distributions. To date, all projects have developed their own methods to calculate these important values. It is beneficial to summarise the characteristics of these different methods in Table 4.1. Although with several simplifications in the newly developed nonlinear model in ST20_2019 (see Section 4.1.1) , the major advantage of this method is that it enables a significant amount of impact events' sampling, leading to smoother and converged statistical distributions of the pursued values. The re-simulation results are presented in the next section.

Table 4.1: Overview of the different methods utilised to calculate the pre-impact relative motions of the glacial ice feature in different projects.

	ST5*	ST19	ST20_2018	ST20_2019
Simulation domain	Frequency	Time domain	Time domain	Time domain
DoFs	Heave, Roll and Sway	Heave, Roll and Sway	all 6 DoFs	Heave and Sway for glacial ice; Heave, Roll and Sway for the structure
Wave theory	Linear	Linear	Nonlinear effect (FK force, drag force, drift force)	Nonlinear effect (FK force, drag force, drift force)
Added mass variation	Constant	Constant	Most cases with constant added mass, a few cases with varying added mass	Constant
Amount of impact events	1	1 million	Most cases with 20 impacts; some with 40, or 120 impacts	Each case with around 500,000 impacts
Velocity distributions at various heights	NA	YES	NA	YES

* ST5 also conducted some nonlinear analysis. However, most of their analysis were based on the linear frequency domain analysis as illustrated in this table.

4.5.1 Re-examination of glacial ice feature's motion in waves

This section sets up comparable simulation cases and adopts the newly developed nonlinear model in ST20_2019 to make re-calculations. The glacial ice feature is chosen to be the cuboidal ice with the dimension of 15 m × 10.3 m × 10.3 m. The detailed wave conditions are summarised in Table 4.2.

Table 4.2: Simulated wave conditions for inter-comparison purpose.

Wave condition	Return period of sea state [Year]	*Hs* [m]	*Tp* [s]	γ
#1	1	4.9	6.5	5
#2	1	8.6	12	2.9
#3	1	9.8	14.8	1.4
#4	100	13.8	18	1.2

In the new model, wave drift force and oscillatory motions are calculated separately. The drift velocity is calculated utilising Eq. (4-11) to equate the drag force term for each wave component sampled from the JONSWAP wave spectrum based on information of significant wave height and peak periods given in Table 4.2. The calculated drift velocities for these wave conditions are presented in Table 4.3.

Table 4.3: Drift velocity calculated in different wave conditions.

Wave condition	Return period of sea state [Year]	*Hs* [m]	*Tp* [s]	Drift velocity calculated in ST20_2019 [m/s]
#1	1	4.9	6.5	1.62
#2	1	8.6	12	1.1
#3	1	9.8	14.8	0.98
#4	100	13.8	18	0.96

In ST5, there was no drift velocity (or drift velocity = 0 m/s); in ST19, a 100-year return current velocity of 0.79 m/s was introduced to facilitate simulation of impact events. Table 4.3 shows that most of the calculated drift velocities are slightly larger than this chosen current velocity. In addition, as expected, with shorter waves, higher drift velocity is attained. This drift velocity shall be added to the wave induced oscillatory velocities when calculating the total relative impact velocities.

Except for the method to calculate the motion of the glacial ice feature, as described in Section 4.4.1, the procedures to calculate the relative motions between the ice and the semi-submersible are the same as in the ST19 report and an associated paper (Lu and Amdahl, 2019). The detailed procedure will not be repeated, and the results are directly presented herein. For the purpose of illustration, we select the case with significant wave height *Hs* = 9.8 m, wave period *Tp* = 14.8 s as an example.

With known relative motion histories between the ice and the platform, Fylling's (1994) method was utilised to sample the impact events. The sampled 50,000 impact events for the selected case are visualised in Figure 4.13.

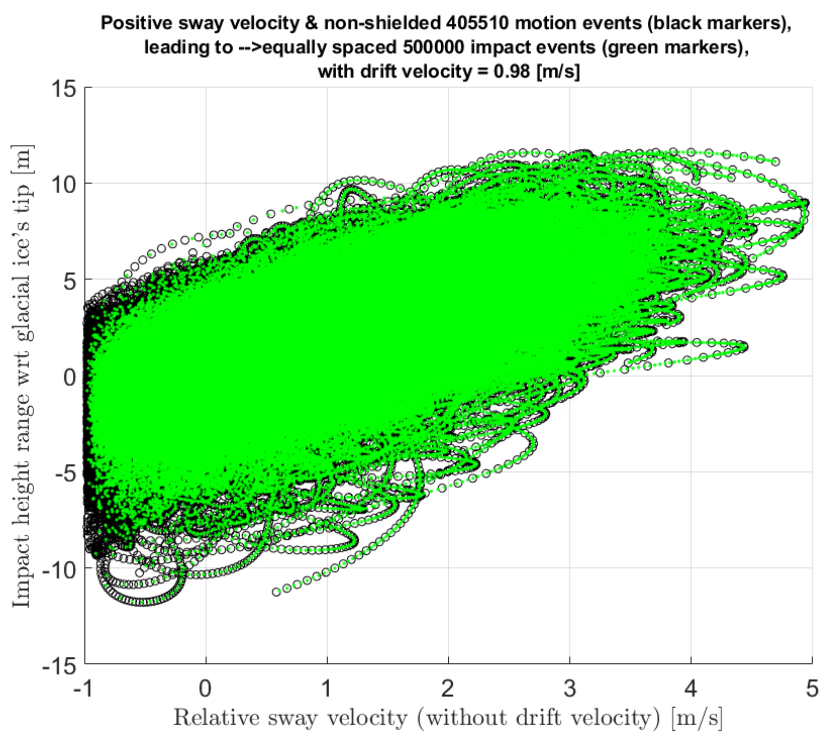

Figure 4.13 Impact height versus impact velocity for the sampled impact events (green dots) for the case with *Hs* = 9.8 m and *Tp* = 14.8 s (a long wave).

Out of these 50,000 sampled impact events, the overall impact velocity and impact height distributions can be obtained as shown in Figure 4.14 and Figure 4.15, respectively. Similar to ST19, the impact velocity fits best to the two parameter Weibull distribution whereas the impact height fits best to the Normal distribution. In ST20_2018, the chosen Gumbel fit did not converge to their simulation results due to limited impact events studied there. As mentioned in Table 4.1, the method adopted in ST19 and ST20_2019 enables a much smoother statistical fitting as shown in Figure 4.14 and Figure 4.15.

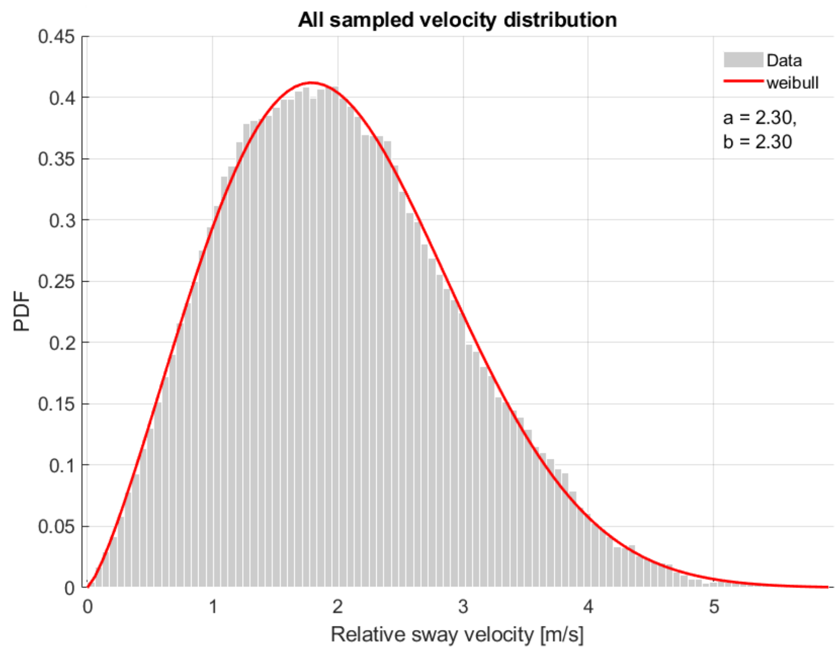

Figure 4.14 Overall impact velocity's distribution for the sampled impact events (green dots) for the case with *Hs* = 9.8 m and *Tp* = 14.8 s (a long wave).

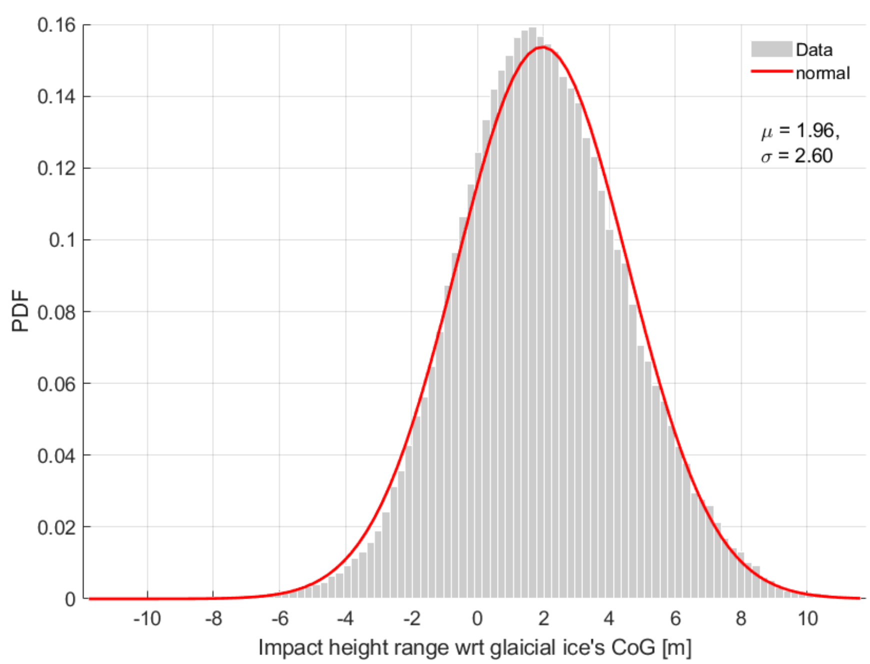

Figure 4.15 Overall impact height's distribution for the sampled impact events (green dots) for the case with *Hs* = 9.8 m and *Tp* = 14.8 s (a long wave).

Table 4.4 summarises the parameters of the respective best-fit distribution functions for the overall impact velocity and impact height for all re-simulated cases.

Table 4.4: Overall impact velocity and impact height distributions*.

Return period of sea state [Year]	*Hs* [m]	*Tp* [s]	Weibull distribution of the overall impact velocity [m/s]	Normal distribution of the impact height wrt CoG of glacial ice [m]
1	4.9	6.5	$a = 2.20$; $b = 2.99$	$\mu = -0.17$; $\sigma = 0.81$
1	8.6	12	$a = 2.29$; $b = 2.32$	$\mu = 1.40$; $\sigma = 2.34$
1	9.8	14.8	$a = 2.30$; $b = 2.30$	$\mu = 1.96$; $\sigma = 2.60$
100	13.8	18	$a = 2.87$; $b = 2.23$	$\mu = 3.39$; $\sigma = 3.79$

* a and b are the scale and shape parameters for the Weibull distribution respectively; μ and σ are the mean and the standard deviation for the Normal distribution respectively.

In addition to the overall statistical distributions, the impact velocity and impact height are correlated in the time-domain simulations. The statistical distribution of the impact velocity at different heights can therefore be extracted and the results are presented in Figure 4.16. The same trend as in the ST19 case is observed here as well: a larger impact velocity is expected at a higher location.

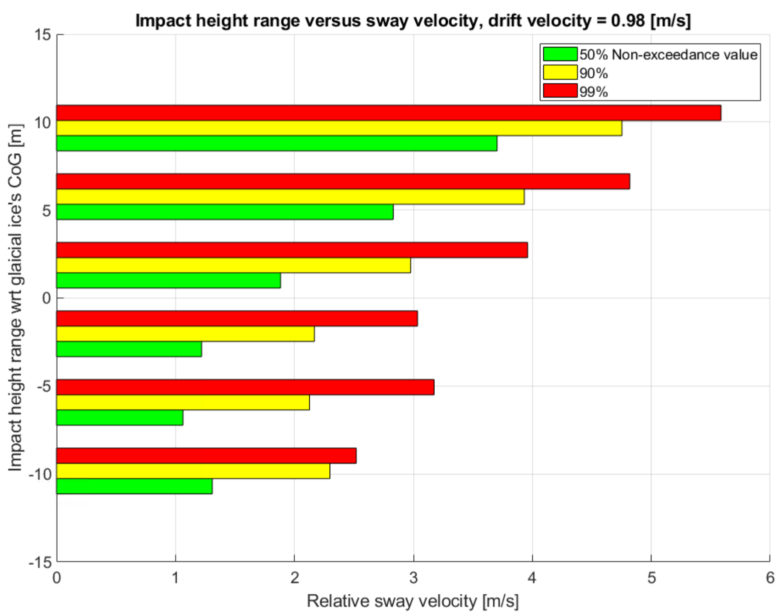

Figure 4.16 Impact velocities at different heights for the glacial ice feature for the case with *Hs* = 9.8 m and *Tp* = 14.8 s (a long wave).

Summarising both the impact velocity's distribution at different heights and the impact probability distribution, we can plot them with reference to the structure at the SWL as shown in Figure 4.17 and Figure 4.18 for different wave conditions (i.e., a long wave and a relatively short wave conditions). These two plots show that for long wave conditions, the impact range is more spread whereas the impact range is more concentrated for relatively short-wave conditions. This is also reflected by the standard deviation of the impact height σ in Table 4.4, i.e., a larger standard deviation is obtained for longer waves. This is understandable as longer waves often mean larger significant wave heights, which excite the glacial ice feature and the platform to oscillate in a much larger vertical range.

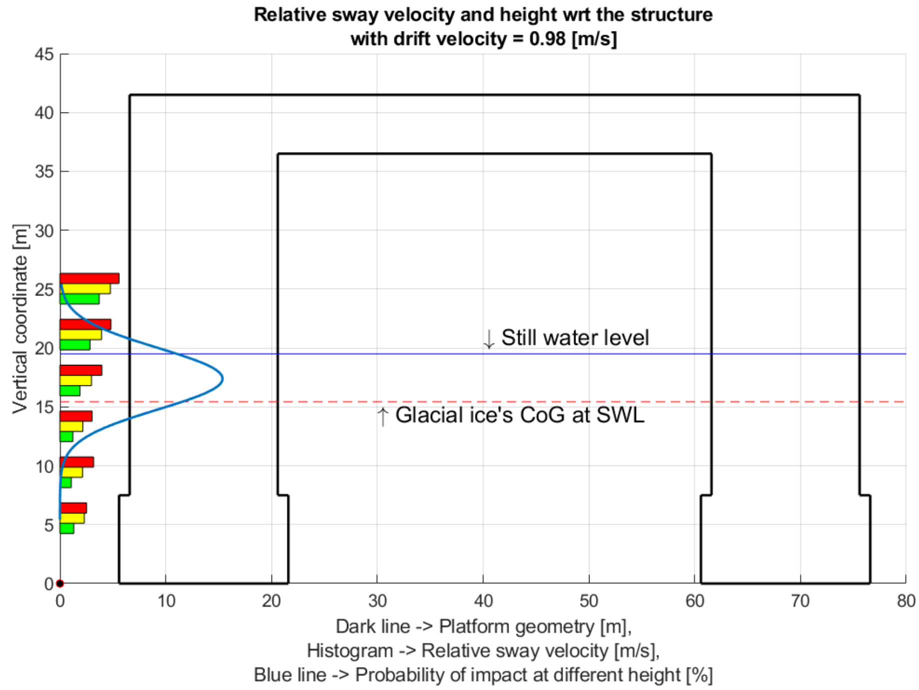

Figure 4.17 Impact velocities distribution and impact probability at different height of the structure for the case with *Hs* = 9.8 m and *Tp* = 14.8 s (i.e. long waves).

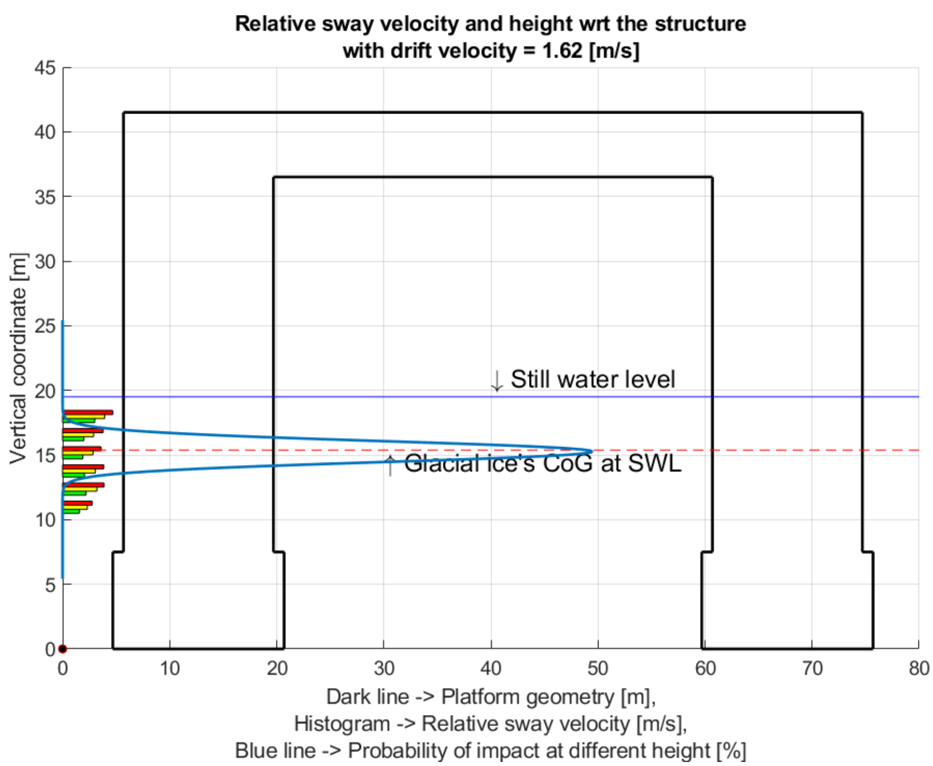

Figure 4.18 Impact velocities distribution and impact probability at different height of the structure for the case with *Hs* = 4.9 m and *Tp* = 6.5 s (i.e. short waves).

The distribution of impact velocity over the height shows a similar trend, i.e., in long waves the velocity is more spread whereas in short waves it is more concentrated. Visually, for the same exceedance level, the difference between the largest and the smallest impact velocity in Figure 4.17 is more significant than in Figure 4.18. Quantitatively, in Table 4.4, the scale parameter *a*, which characterises the 'spreading level' increases with longer waves. In addition, the most probable impact height in Figure 4.18 is much lower than in the other wave conditions. This is because the ice is more often submerged with shorter wave conditions. These features were anticipated and are well captured by the newly developed nonlinear model.

4.5.2 Quantitative comparisons of impact velocities predicted in different projects

In the previous sections, we utilised the new, nonlinear model (ST20_2019 model) to re-examine important results such as the impact velocity and impact height from previous projects. The results from different projects are summarised in Table 4.5 and Table 4.6.

Table 4.5: Overall impact velocity calculated from different projects.

Wave condition	Impact Velocity [m/s]							
	ST5		ST19		ST20_2018		ST20_2019	
	Mean	90%	Mean	90%	Mean	90%	Mean	90%
#1	2.6	2.9	NA	NA	2	3.55	1.92	2.91
#2	3.5	4	NA	NA	2.25	4.01	1.95	3.27
#3	3.4	3.8	NA	NA	1.66	3.13	1.96	3.30
#4	3.9	4.4	1.8*	3*	NA	NA	2.44	4.18

* Results from ST19 are calculated based on a much smaller ellipsoidal glacial ice feature whereas the rest are based on the cuboidal glacial ice feature.

Table 4.6: Overall impact height calculated from different projects.

Wave condition	Impact Height calculated from SWL (positive upward) [m]							
	ST5		ST19*		ST20_2018**		ST20_2019	
	Mean	90%	Mean	90%	Mean	90%	Mean	90%
#1	[-7.22 -1.02]	[-7.62 -0.62]	NA	NA	-3.58	2.29	[-4.67 -3.57]	[-6.23 -2.01]
#2	[-8.42 0.18]	[-8.92 0.68]	NA	NA	-2.6	4.11	[-6.0 -2.24]	[-8.62 0.38]
#3	[-9.22 0.98]	[-9.82 1.58]	NA	NA	-4.39	2.54	[-6.41 -1.83]	[-9.45 1.21]
#4	[-13.12 4.88]	[-14.32 6.08]	[-4.68 -1.08]	[-7.28 1.52]	NA	NA	[-7.81 -0.43]	[-12.4 8.11]

* Results from ST19 are calculations based on a much smaller ellipsoidal glacial ice feature whereas the rest are based on the cuboidal glacial ice feature.

** The impact range in ST20_2018 was not presented. Instead, a single value was derived from the limited amount of impact height statistics. Therefore, the mean value can be interpreted as the most probable (MP) impact location; the 90% value can be understood as 90% of the impacts happened below this height.

It is rather encouraging to notice that the results from the different projects are quite close to each other, although they are based on different methods. In addition, it appears that from ST5 to ST20_2019, that the predictions of both the impact velocities and the impact height ranges become less and less conservative.

4.6 Summary of Task #1

In this task, reviewing and making synergy of previous projects were performed. In this process, a dedicated simplified nonlinear model was developed to re-examine important results achieved in previous projects. In the end, important results regarding impact velocities and impact heights were summarised and re-examined. The findings are summarised as follows:

- In total, the important results regarding impact velocities and impact heights from different projects are rather consistent. This is encouraging as these results were obtained by quite different methods.
- The overall trend of impact velocities and impact height is that these values are getting less conservative over time.
- The most recent analyses in this project (ST20_2019), show that:
  a) The impact velocity increases with increasing impact height
  b) The relative impact velocity increases with higher sea states
  c) In longer/higher wave conditions, the impact height range is more spread whereas a more concentrated impact range is calculated for shorter wave conditions
  d) In shorter wave conditions, the most probable impact height is below the CoG of the glacial ice feature in still water, indicating that submergence of the ice is taking place more frequently in shorter waves than in longer wave conditions.

Nevertheless, it is believed that the near field hydrodynamic effects of a small glacial ice feature approaching a structure/platform is not sufficiently investigated. According to the literature (see e.g., the paper by Isaacson and McTaggart (1990)), a small glacial ice feature can be re-directed from its collision course with the platform such that no impact shall happen at all. In the ST20_2018 report, limited impact analyses were conducted with increasing added mass when the ice approached the platform. They obtained quite mixed results. For the scenario of collision with the column structure (i.e., Case ID #21 in ST20_2018), an obvious reduction of the impact velocity of almost 50%, was observed (see Table 19 of the ST20_2018 report). However, in the case of collision with the pontoon (i.e., Case ID #22 and #23 in ST20_2018), an increasing impact velocity was calculated (see Table 21 of the ST20_2018 report). It is therefore recommended that more thorough near-field hydrodynamic analyses should be carried out in the future. It is expected that with the inclusion of near-field repellent force, the impact velocity in Table 4.5 should be even smaller than those calculated here, or it may even happen that there is no impact at all?

5 Task #2: Iceberg encounter probability

This chapter reviews all available information on icebergs in the Barents Sea. Then, it presents a numerical model for icebergs' drift for the entire Barents Sea. The model is then used to calculate the probability of iceberg intrusions into a representative area in the Barents Sea and the results are presented herein. The selected location for this study is chosen in agreement with the Petroleum Safety Authority Norway (PSA) to be the centre of Block #7424 in the awards in predefined areas for petroleum activity.

Furthermore, a numerical model for Block #7424, which also includes tidal currents (higher temporal resolution), is used to estimate the annual iceberg encounter frequency at Block #7424. The model results are presented in this chapter and checked against results from other calculation methods as in ISO 19906 (2019). Distributions of iceberg sizes at the Block #7424 are derived from the results of the numerical models and are presented herein. Moreover, we demonstrate the potential of using remote-sensing data, especially the optical Sentinel-2 imagery, to reduce the uncertainty in important model-input parameters like the number of icebergs produced per year from the different sources and their size distributions. Finally, we discuss the possible effects of climate change on our predictions and propose a methodology to account for these possible changes.

5.1 Review of available information on icebergs in the Barents Sea

5.1.1 Formation of icebergs

The amount of iceberg-producing calving from an ice margin is influenced by the mass balance of the glacier, the crevassing within the glacier, by the rate of glacier flow, by whether the glacier terminus is grounded or afloat, and therefore by the depth of water fronting the ice. The principle is sketched in Figure 5.1 and Figure 5.2.

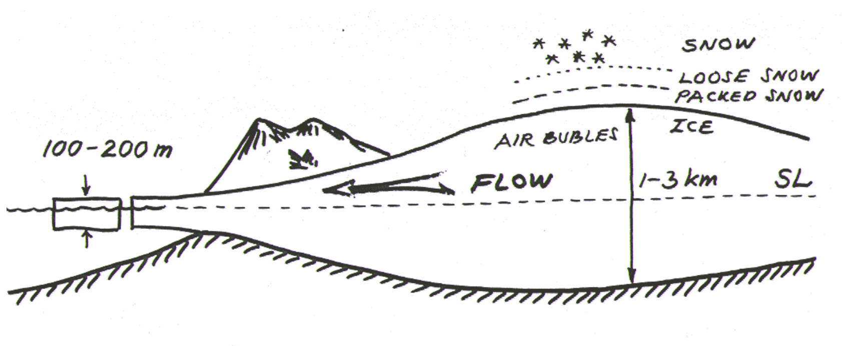

Figure 5.1. Principle sketch of the formation process of glaciers and icebergs (Løset et al., 2006).

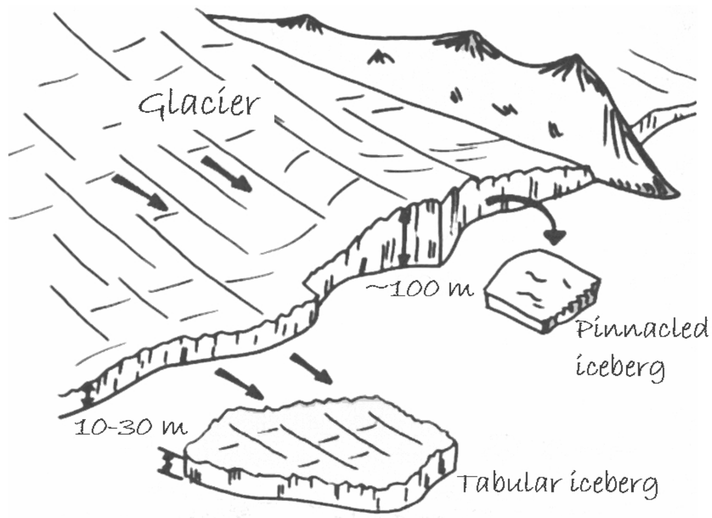

Figure 5.2. Sketch of the formation process of tabular and irregular icebergs from an ice cliff (Løset et al., 2006).

5.1.2 Physical properties of glacial ice

The transformation from snow to ice is demonstrated in Figure 5.3a with associated air bubbles depicted in Figure 5.3b. Glacier ice develops from successive snowfalls of pure freshwater snow which compresses under its own weight until they become solid ice. The initial density of freshly precipitated snow is very low, about 400 kg/m^3, but the density increases systematically with depth and overburden pressure, reaching about 600 kg/m^3, at depth 10 m below surface (Sanderson, 1988). At depth 50 m the density reaches about 820 kg/m^3.

(a) (b)

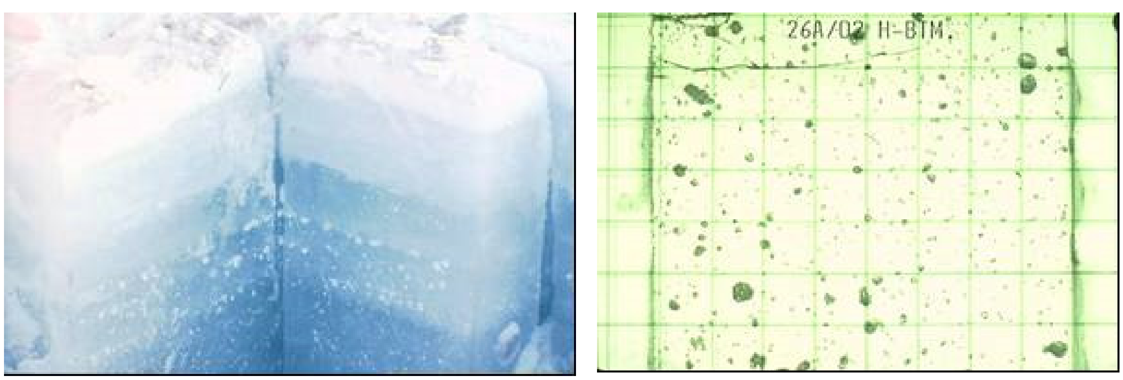

Figure 5.3. a) Picture showing transformation from snow to ice; b) air bubbles in glacial ice (grid size: 10 mm) (Løset et al., 2006).

Calculations using a two-dimensional numerical model which simulates the heat balance and temperature distribution of icebergs show that the ice temperature in the central region of an iceberg is almost unaffected by the thermal conditions imposed on its boundary. Hence the original temperature of the iceberg at the time of calving is retained in its core, owing to the insulation quality of the ice. With the assumption of heat conduction, simulations show that with a tolerance of 0.4°C the temperature is virtually free of any thermal boundary influence only 12 m into the ice throughout the whole year

(Løset, 1993). When correlated with glacioclimatic conditions, this temperature conservation may be used to backtrack an iceberg to its parent ice cliff (Løset, 1993).

Prior to 1987, data on icebergs for the Western Barents Sea was sparse and not very systematic. An overview of iceberg sightings is given in Abramov and Tunik (1996), and in Løset and Carstens (1996).

5.1.3 Iceberg mapping – ICEBASE

The first well documented sea ice and iceberg study in the Barents Sea was the multi-sensor ice data acquisition programme ICEBASE (Sea Ice Investigations in the Barents Sea) established in 1987, funded by BP Norway, Esso Norway and Mobil Exploration Norway. ICEBASE was executed during the mid-winter and fall campaigns of 1987 (Løset and Carstens, 1996). The main purpose of the research programme was to obtain comprehensive information about sea ice and icebergs in the western Barents Sea. The specific elements of the mapping were satellite imaginary, precision stereo aerial photography, airborne synthetic aperture radar (SAR), helicopter-borne impulse radar and three ground truthing field campaigns. Field Survey 1 employed the Norwegian Coast Guard vessel K/V "Nordkapp" from 24th February to 10th March 1987, a second field survey (late March to early April 1987) used aircrafts and helicopters as platform from Longyearbyen Airport on Spitsbergen. Finally, Ship Survey 2, with the Norwegian Coast Guard vessel K/V "Senja", was conducted in the period 13th October to 25 October 1987 (Carstens et al., 1988).

The programme of 1987 was the only viable source of much-needed data and was also seen as a model for future investigations in the Barents Sea. Thus, it was important to compare the various observation methods, both their field performance, data catch and the overlapping output. ICEBASE became a model for its successor IDAP ("Ice Data Acquisition Program") conducted by OKN ("Operator Committee North of 62°N") through the years 1988-1992 (Spring et al., 1993, Spring, 1994).

The different campaigns of ICEBASE aimed at mapping the population and characteristics of icebergs, and sightings were made as indicated in Figure 5.4. In total the programme observed 180 icebergs, of which 105 were made from stereo photos made by a fixed wing aircraft. All pictures taken from the aircraft were stereographic with 60 % overlap. The advantage of the stereo photos is the high resolution (in the order of 0.1 m) and that it yields vertical dimensions. The stereo photos were acquired at two different scales, 1:2000 and 1:6000. The total areal coverage of these photos, excluding overlaps, was about 160 km^2.

The stereo technique was used to obtain above water volume, maximum sail height, maximum length, and other geometric parameters of 52 icebergs (43 in the 1:2000 scale photos and 9 in the 1:6000 scale photos). Of these icebergs, 37 were located in Storfjorden, 14 icebergs around the northern tip of Hopen Island, and one tabular iceberg just South of Svenskøya. Table 5.1 reports the observation methods of the total iceberg sightings. Overlaps are excluded.

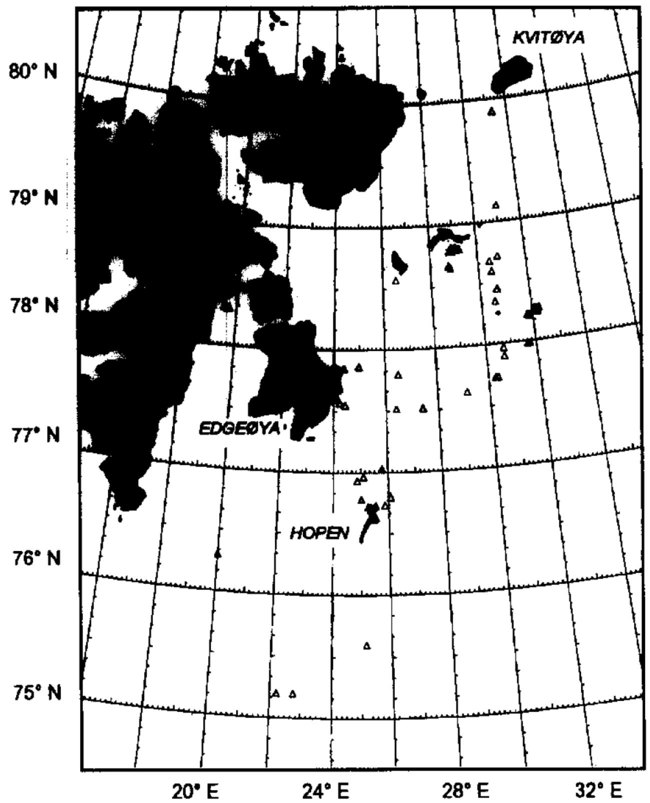

Figure 5.4. Location of iceberg sightings made of ICEBASE (Løset and Carstens, 1996).

Table 5.1: Iceberg sightings of ICEBASE.

Observation method	Number of icebergs
Stereo photos (scale 1:2000)	44
Stereo photos (scale 1:6000)	61
Survey 1 (helicopter flights; visual)	10
Survey 2 (helicopter flights; visual)	65

Statistical data were obtained for the 52 digitized images. The geometrical form of an iceberg at the waterline can be expressed by a shape factor (S_{peri})

$$S_{peri} = \frac{4\pi A}{p^2} \tag{5.1}$$

where A is the cross–sectional area at the waterline plane and p is the perimeter at the waterline. It is worth noticing that $S_{peri} = 1$ for a circle, 0.785 for a square and decreases for elongated shapes.

In a similar way the geometrical shape of the iceberg sail may be expressed by a sail volume shape factor (S_{sail}).

$$S_{sail} = \frac{V_{sail}}{H_{\max} L_{\max} W_{\max}} \tag{5.2}$$

where V_{sail} is the above sea level volume, H_{max} the maximum sail height, L_{max} the maximum length. The maximum width (W_{max}) of an iceberg is measured perpendicular to L_{max}. The total iceberg mass is estimated from the above sea level volume by using Archimedes Law (ice density: 900 kgm^{-3}, sea water density: 1027 kgm^{-3}).

A significant sighting of ICEBASE was a tabular iceberg in position 78°34'N 26°32'E, just south of Svenskøya. The estimated mass was 6.35 million tonnes; H_{max} = 12 m, L_{max} = 499 m and W_{max} =253 m.

Table 5.2 summarises the key iceberg data from the photo analysis of the 52 digitized images.

Table 5.2: Key iceberg parameters from the aerial stereo photo analysis of ICEBASE (mean value and the empirical standard deviation, σ).

Key parameters	Mean values; ± σ
Max. iceberg sail height, H_{max} (m)	15.4 ± 8.0
Max. iceberg length, L_{max} (m)	117.9 ± 97.5
Max. iceberg width, W_{max} (m)	80.9 ± 65.1
Shape factor, S_{peri}	0.78 ± 0.09
Sail shape factor, S_{sail}	0.32 ± 0.10
Total iceberg mass (1000 tonnes)	847 ± 2173

The most important parameters of the icebergs are fitted to a 3-parameter Weibull probability distribution given by:

$$f(x) = \frac{\gamma}{\theta}\left(\frac{x-\varepsilon}{\theta}\right)^{\gamma-1} \exp\left[-\left(\frac{x-\varepsilon}{\theta}\right)^{\gamma}\right] \tag{5.3}$$

Where $x(>\varepsilon)$ is the statistical variable, ε the location parameter, $\theta > 0$ the scale parameter and $\gamma > 0$ the shape parameter. The corresponding cumulative function is given by:

$$F(x) = 1 - \exp\left[-\left(\frac{x-\varepsilon}{\theta}\right)^{\gamma}\right] \tag{5.4}$$

The method of moments is used to provide estimators for the location-, scale- and shape parameters of the Weibull distribution. The values of these parameters are shown in Table 5.3.

Table 5.3: Estimator values for the Weibull parameters (Løset and Carstens, 1996).

Parameter	Location, ε	Scale, θ	Shape, γ
H_{max}	4.5	13.0	1.45
L_{max}	44.9	74.4	0.83

5.1.4 Iceberg mapping – IDAP

It is interesting to compare the sightings of ICEBASE with its successor IDAP; conducted by OKN through the years 1988-92. IDAP gathered data on icebergs showing a substantial variation both in number and masses over the five-year period 1988-92.

Table 5.4 shows summarized iceberg data from the aerial stereo photo analysis in a similar way as done in ICEBASE (Løvås et al., 1993). The table clearly shows that 1988 (the year following the ICEBASE investigations) was the most severe year in this period with a total of 17 icebergs with mass exceeding 1 million tonnes.

Table 5.4: Key iceberg parameters from the aerial stereo photo analysis of IDAP, 1988-92 (mean values ± indicating the empirical standard deviation, σ) (Løset and Carstens, 1996).

Year	Number of bergs	Max. iceberg sail height (m)	Max. iceberg length (m)	Total iceberg mass (1000 tonnes)
1988	109	17.8 ± 7.1	101.8 ± 60.3	453.3 ± 738.8
1989	68	17.5 ± 7.2	83.4 ± 39.8	276.7 ± 306.7
1990	89	13.3 ± 6.1	84.9 ± 46.6	196.6 ± 244.3
1991	41	13.2 ± 5.0	83.1 ± 61.9	284.3 ± 516.9
1992	23	10.2 ± 3.8	104.2 ± 48.8	221.2 ± 219.4
1988-92	330	15.4 ± 6.9	92.3 ± 52.9	311.2 ± 512.2

5.1.5 Origin and release of glacial ice in the Barents Sea

The dominant source of icebergs in the Barents Sea is calving from the ice cliffs of Franz Josef Land. This archipelago consists of about 2600 km of tidewater ice cliffs (Løset, 1993). The fjords and adjacent waters are rather deep, typically 100 – 200 m deep, which may allow large icebergs to escape from the glacier terminus. Most calving occurs in the late summer and autumn (June through September), when ocean wave excitation reaches the calving ice cliffs. This observation is also supported by Kubyshkin et al. (2006). Even though winter iceberg movement is observed in these waters, drift is very restricted by the sea ice. Thus, the number of icebergs close to the calving sources is higher in winter than in summer. Icebergs which have not escaped from the ice cliff before the presence of landfast ice will normally be trapped in the ice until the breakup of the fast ice in the coming spring (Løset et al., 2006).

Figure 5.5 shows the major sources of icebergs in the Barents Sea. The main ocean currents are also indicated in the figure with red indicating relatively warm water, grey indicating slightly colder water, and blue for cold Arctic water.

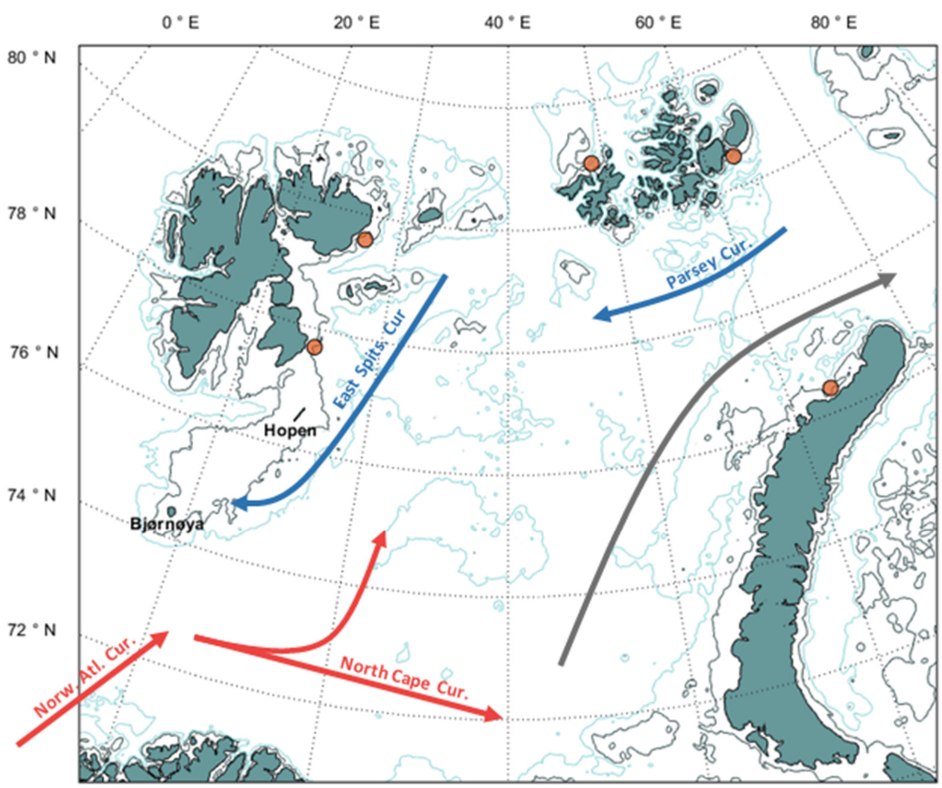

Figure 5.5. Major sources of iceberg production in the Barents Sea (orange-filled circles) and the main ocean currents. Light and green contour lines are the isobaths at 100 and 200 m, respectively.

Table 5.5 provides the annual discharge rate from these sources. This data is based on observations and precipitation studies.

Table 5.5: Major iceberg calving locations and rates in the Barents Sea.

Geographical area	Calving location	Discharge rate ($km^3\ yr^{-1}$)	Data source
Franz Josef Land (Eastern side)	80.5°N/62.8°E	2.64	(Kubyshkin et al. 2006)
Franz Josef Land (Western side)	81.0°N/48.7°E	1.76	(Kubyshkin et al. 2006)
Nordaustfonna	79.6°N/27.0°E	2.7	(Dowdeswell et al., 2008)
Edgeøya	77.7°N/25.0°E	0.6	(Hagen et al., 2003)
Novaya Zemlya	76.4°N/63.0°E	1.0	Kubyshkin et al. (2006)

The challenge is to estimate the iceberg production rate from the potential sources, the release time and the discharge rate. The photo in Figure 5.6 clearly shows how a large part of a glacier may collapse at the front and just produce growlers and bergy-bits. In particular, this is the case for a glacier ice front that rests on the sea bed. We believe this is the case for three of the sources we consider as iceberg producers; Novaya Zemlya, Nordaustfonna, and Stonebreen on Edgeøya.

(a) (b)

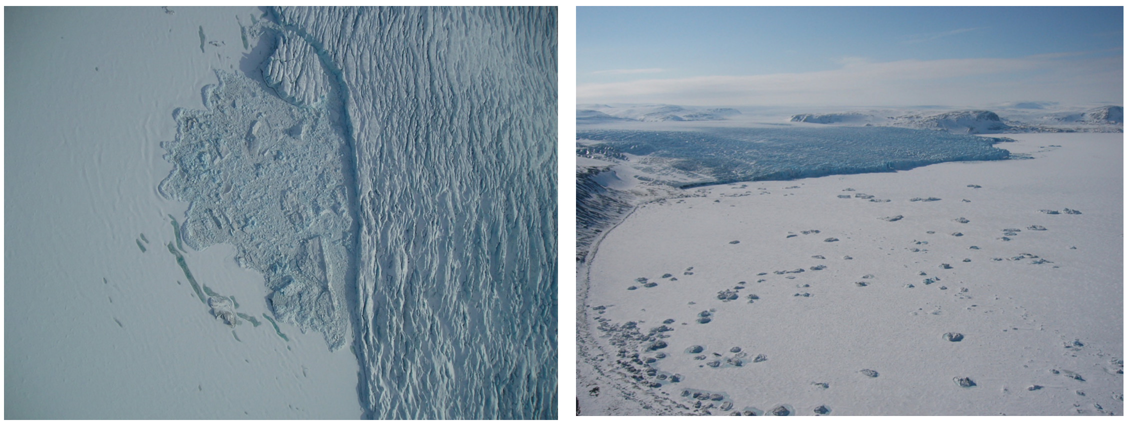

Figure 5.6. Glacier at Novaya Zemlya, April 2005: a) Bird's view of ice cliff, b) bergy-bits off the glacier. (Photo: A. Marchenko).

Figure 5.7 - Figure 5.11 provide locations and typical observations from the major glacier outlets in the Barents Sea; namely that a substantial part of the glaciers does not produce icebergs; rather bergy bits and growlers. Based on observations and experience from these waters, our *best guesstimate* of the number of icebergs released per year from the five sources is presented in Table 5.6.

There is currently no data available based on which the discharge rate of the glaciers can be linked to the number and size of icebergs produced. This is the main source of uncertainty in the modelling results presented in this chapter. In order to obtain more information on the size, shape and number of icebergs produced by the potential iceberg sources, high resolution satellite images are processed in Section 5.4. The performed analysis shows that the processing of satellite images is a promising method to obtain more information on iceberg production by glaciers. However, the time range covered by the image processing performed for this report is currently insufficient to significantly improve the estimates based in expert judgement and aerial surveys presented in Table 5.6. The number of satellite images that could be processed was limited because the processing method used relied mainly on manual image analysis. If the image processing could be reliably automated, then a broader time range could be analysed.

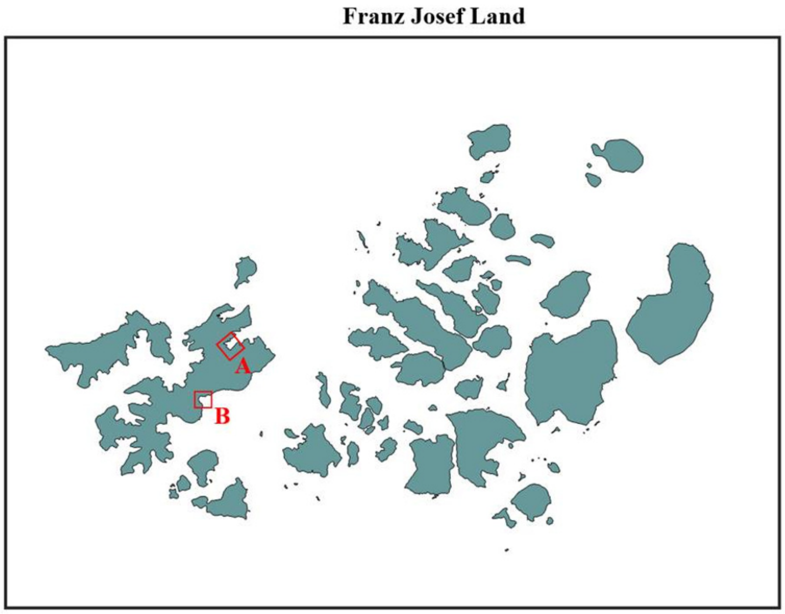

Figure 5.7. Location of two calving glaciers at Franz Josef Land; A - Franz Josef Land East (80.5°N/62.8°E); B - Franz Josef Land West (81.0°N/48.7°E).

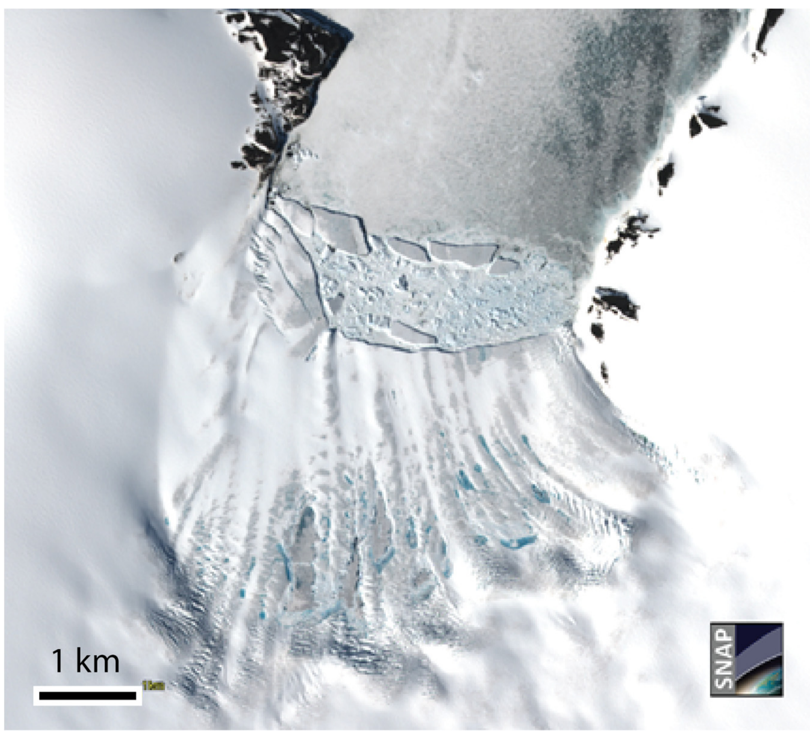

Figure 5.8 Satellite image from Franz Josef Land, Location A, 19.06.2018. (Source: Sentinel 2, resolution 10 m).

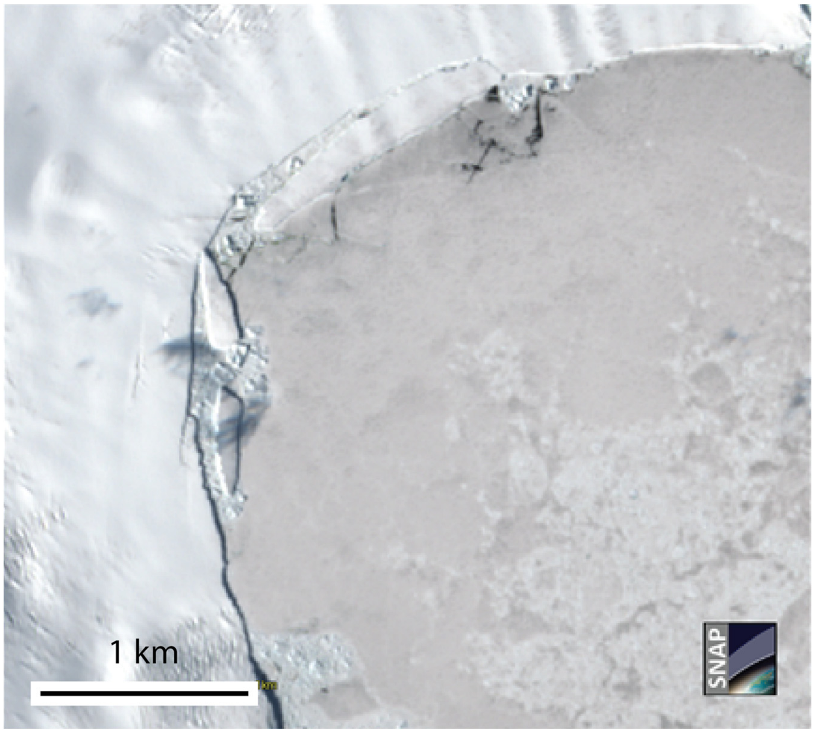

Figure 5.9. Satellite image from Franz Josef Land, Location B, 19.06.2018. (Source: Sentinel 2).

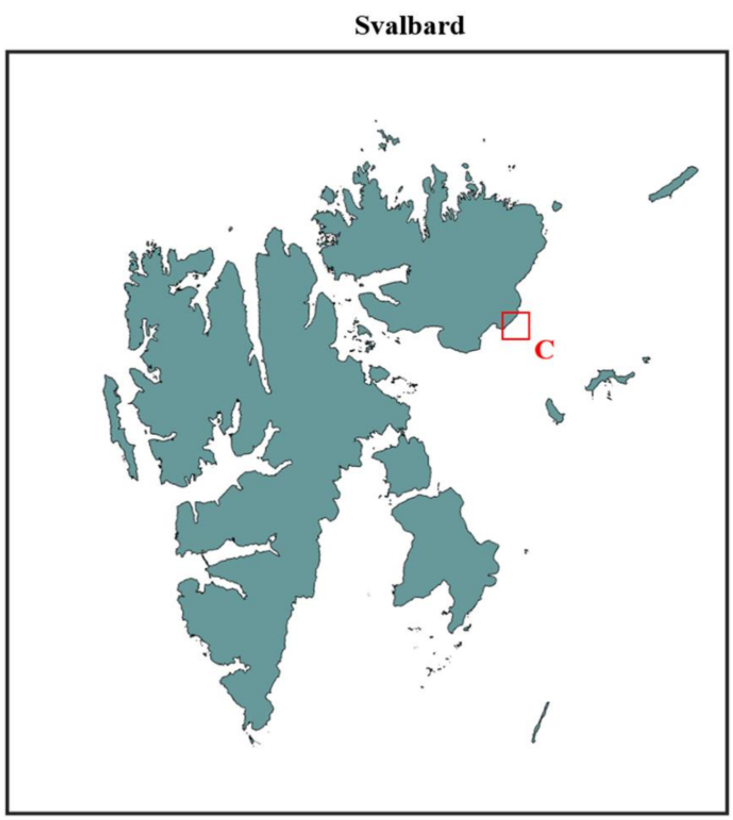

Figure 5.10. Location C (79.6°N/27.0°E), the calving part of Nordaustfonna.

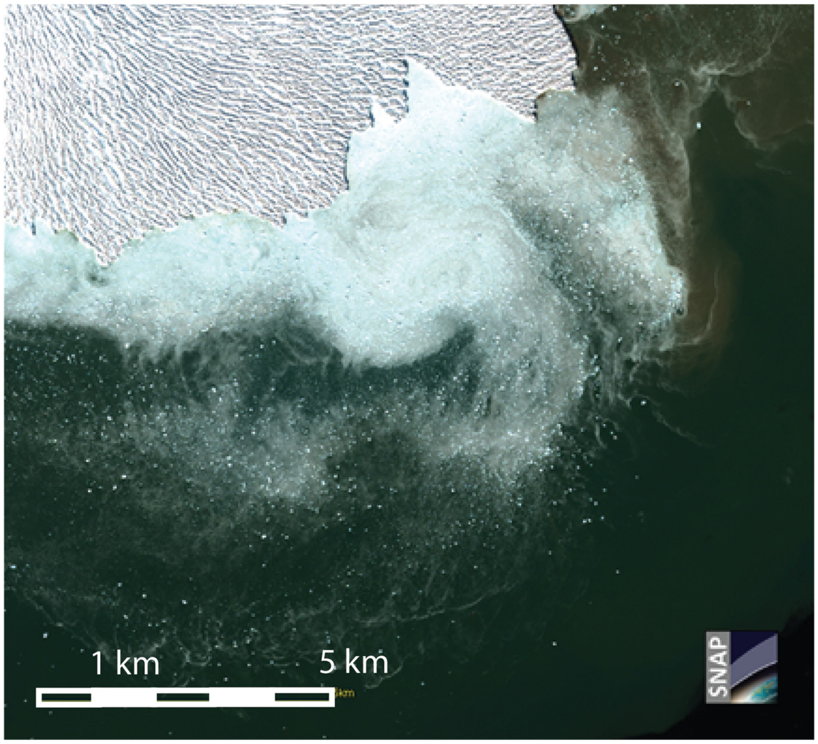

Figure 5.11. Satellite image from Nordaustfonna, Location C, 24.08.2018. (Source: Sentinel 2).

Figure 5.12 shows the maximum number of icebergs observed (mostly from aerial surveys, see Section 5.1.8) within a one-year period in cells of 2°N × 5°E in size. This figure is taken from Dezecot and Eik (2015) based on AARI (2005) and Abramov and Tunik (1996). For each of the five sources, we use information from the closest cell in Figure 5.12 to determine the maximum number of icebergs released per year from each source. Assuming that the five sources will have a simultaneous maximum production rate, we develop a *conservative estimate* of the number of icebergs released per year from the five sources. This conservative estimate is also shown in Table 5.6. Finally, we assume a uniform release rate during the months July – November (5 months) and no release for the rest of the year.

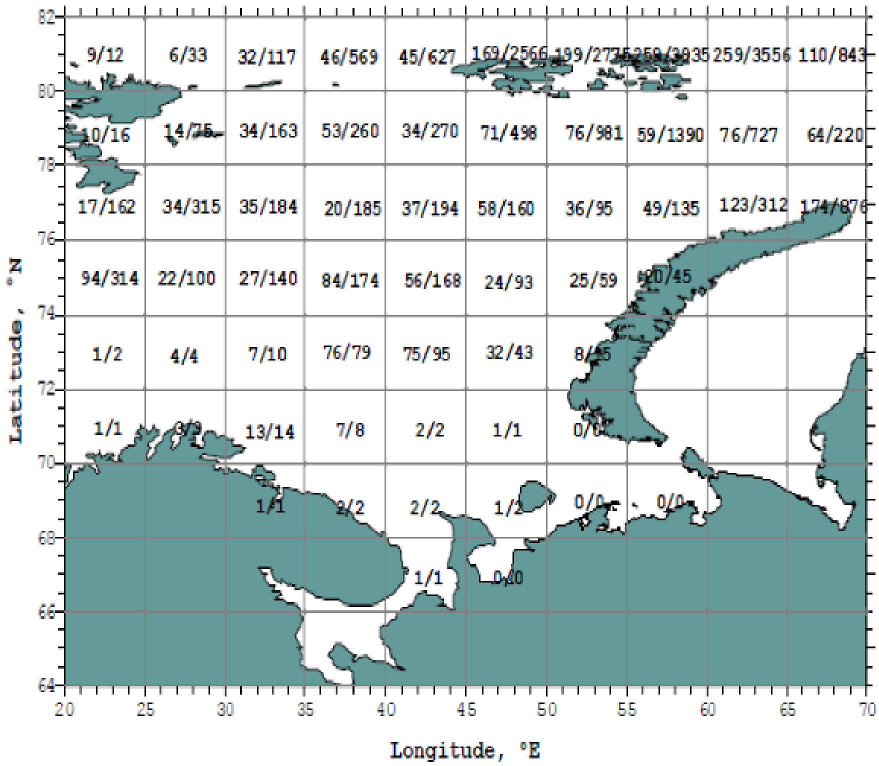

Figure 5.12. Number of iceberg observations within cells of 2°N x 5°E in size. The numerator characterizing each of the squares is the maximal number of icebergs registered within a one year period, while the denominator represents the total number of registrations made within the entire period of observations (from Dezecot and Eik (2015) based on AARI (2005) & Abramov and Tunik (1996).

Table 5.6: Major iceberg calving locations and average iceberg production rates in the Barents Sea.

Geographical area	Calving location	Number of icebergs released/year (***Best guesstimate***)	Number of icebergs released/year (***Conservative estimate***)
Franz Josef Land (East)	80.5°N/62.8°E	65	76
Franz Josef Land (West)	81.0°N/48.7°E	111	169
Nordaustfonna	79.6°N/27.0°E	10	14
Edgeøya	77.7°N/25.0°E	5	17
Novaya Zemlya	76.4°N/63.0°E	9	49
Total		200	325

5.1.6 Strength of ice from icebergs in the Barents Sea

The strength of glacial ice in the ocean is of importance for studies of iceberg-structure impacts. The strength of iceberg ice has been measured in just a few occasions in the Barents Sea. The uniaxial compressive strength is the ice property measured most. Most measurements were performed at a strain rate of $10^{-3}s^{-1}$. The IDAP laboratory testing from 1988 provided a mean value for σ_c of 5.4 MPa and a range from 2.3 MPa to 7.3 MPa for 16 tests at -10°C (Spring et al., 1993). Additional data, taken in 1990, had a mean of 2.3 MPa and a range from 1.6 MPa to 3.8 MPa for 7 tests at -4°C.

More recently, in-situ tests have been performed. Table 5.7 shows results from such an in-situ test from a relatively small pinnacle iceberg (about 40 m across and 7 m sail height) located at about 77°N, 29°E North-East of Hopen in May 2009 (UNIS, 2009). As can be seen, the ice temperature was relatively high, and the tests yielded an average strength of 2.8 MPa. For larger icebergs in a melting stage, Løset (1993) has shown that the iceberg temperature at about 2.5-3 m inward from the ice surface will reflect the core temperature of the iceberg. This means that colder ice can be expected further into the ice which again increases the strength of the iceberg ice and may switch the failure mode from ductile to brittle failure of the ice. This information is relevant to studies of impacts between glacial ice features and structures.

Table 5.7: Strain rate $10^{-3}s^{-1}$. Uniaxial compressive strength (σ_c).

Depth from the top iceberg surface (cm)	Temperature (°C)	Uniaxial compressive strength (σ_c) (MPa)
23-49	-2.1	
131-169	-1.9	1.2
169-189	-3.3	2.3
189-210	-1.4	5.5
210-240	-1.3	4.1
292-325	-3.5	1.0

5.1.7 Iceberg tracks

5.1.7.1 Pioneering data

Over the years quite some icebergs in the Barents Sea have been tracked by different kinds of positioning buoys. At first ARGOS positioning buoys were used, while after the millennium GPS positioning came into use. As far as known to the authors, the first iceberg reported being tracked in the Barents Sea was Iceberg #3057 (Løset and Carstens, 1996). The iceberg had a pinnacle shape with a length and width of 95m × 80 m and with a mean height of 11 m. The maximum sail height was 15 m and based on the actual surface dimensions the maximum draft was estimated to 60-90 m (see Figure 5.13).

Figure 5.13. Photo of Iceberg #3057 (78°13'N 31°51'E, 20th October 1987). The tracker was deployed at the top surface centre of the iceberg.

Six icebergs that clearly had been fragmented from one large iceberg were visited by a helicopter flight towards North from K/V Senja. A tracker was deployed on the northernmost of these icebergs (the tracker indicated by a circle in Figure 5.14). Iceberg #3056 was a tabular berg with a tilt of about 20°. The berg was 100 m × 75 m with a sail of about 12 m. The original positions and drift tracks of the two bergs are shown in Figure 5.15.

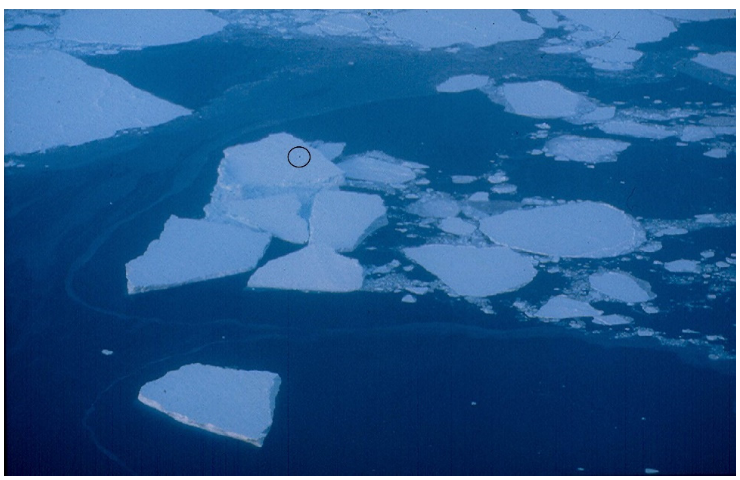

Figure 5.14. Photo of Iceberg #3056 (79°543'N 31°18'E, 22nd October 1987). The tracker is indicated by the dark circle on the northernmost iceberg.

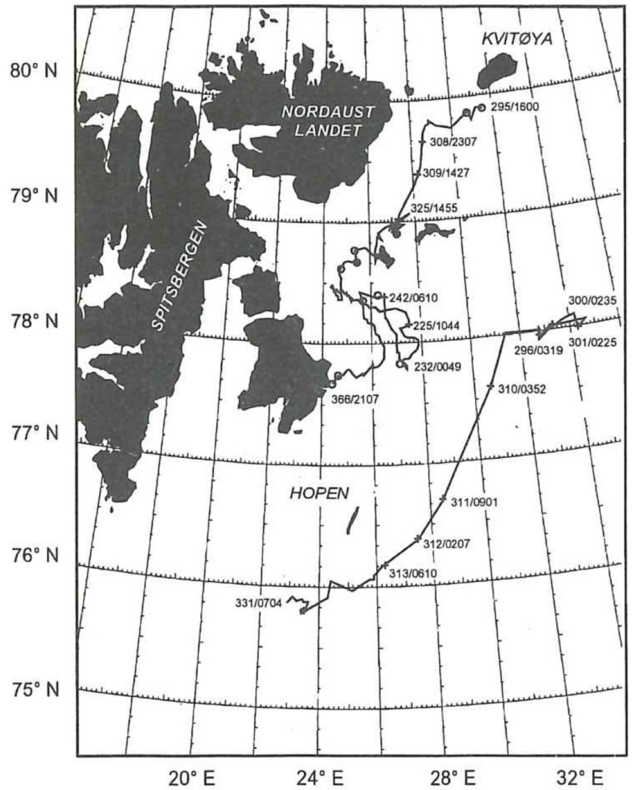

Figure 5.15. Drift trajectories of Icebergs #3057 and #3056, 1987. Grounded periods are encircled (Løset and Carstens, 1996).

For the period Julian days 293-335 (20.10.1987 – 01.12.1987), the average drift speed of the pinnacle iceberg (Iceberg #3057) was 0.25 m/s with a standard deviation (σ) of 0.22 m/s. For the same period the average drift speed of the tabular iceberg (Iceberg #3056) was 0.28 m/s (σ= 0.20 m/s).

As reported by Løset and Carstens (1996), a special event in the drifting of the two icebergs took place during Julian days 308-311 (4th-7th November 1987). There was a sudden increase in the speed for both icebergs. From 3 a.m. on the 5th of November, Iceberg #3057 drifted with an average speed of 1.13 m/s (σ= 0.12 m/s) for 31 hours. A maximum speed of 1.38 m/s was achieved towards the end of this period (8 a.m. on the 6th of November). A possible reason for these extreme drift speeds was strong tail winds aligning with the current in these waters. An explanation of this record high drift speed is discussed by Løset and Carstens (1996).

5.1.7.2 Southernmost iceberg tracking

Løset et al. (1989) report on tracking of an iceberg that was drifting south of Bjørnøya. The track is shown in Figure 5.16. The iceberg headed south on the west side of Bjørnøya before reaching south to the 74°N latitude. Thereafter it drifted back north again on the west side of Bjørnøya. The picture in Figure 5.17 at about 74°N, shows the ongoing deterioration of the iceberg. The ARGOS buoy on the upper right side reveals an erosion of about 0.5 m during this drift period. The buoy was drilled 1.0 m into the iceberg. The transmitter stayed in place, so the iceberg had not capsized at this stage of the drift.

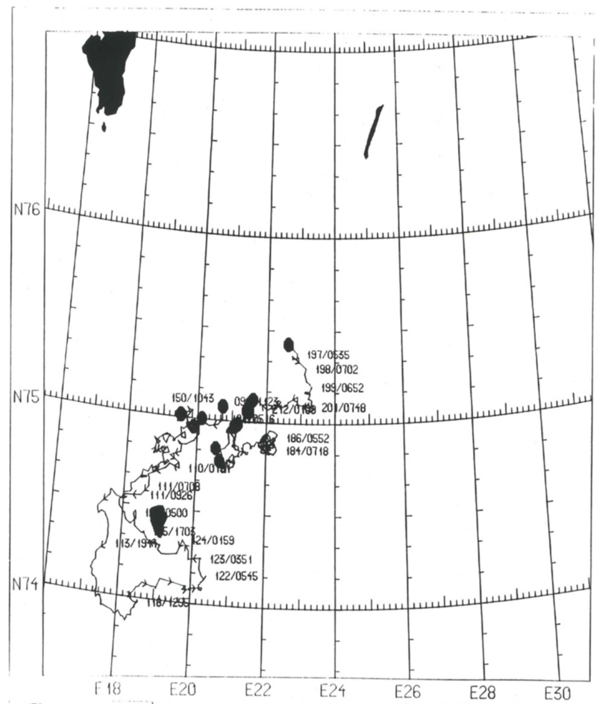

Figure 5.16. Tracking of 3 icebergs (PTTs 3105, 3106, 3109 deployed by helicopter on the R/V Lance Survey in late March 2018. Black dots show grounding of the icebergs. One iceberg drifted south of Bjørnøya and the 74°N latitude (Løset et al., 1989).

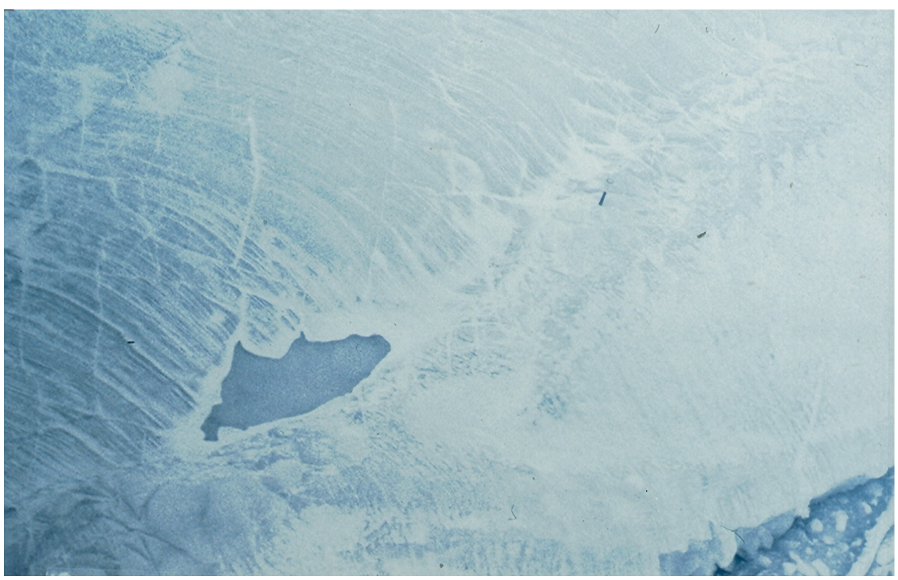

Figure 5.17. Picture of the iceberg that was tracked south of Bjørnøya with the PTT shown in the upper-right part of the eroded iceberg.

5.1.8 Arctic Iceberg Atlas

The Atlas of Arctic Icebergs (Abramov and Tunik, 1996) is a useful source of information on iceberg distribution in the Arctic seas. It provides a summary of existing data and it is usually helpful for early evaluation of iceberg presence. The main bulk of the Atlas data is from aerial surveys (around 96% of the iceberg data were obtained from ice reconnaissance flights; around 4% from shipboard observations; and less than 0.1% were obtained by other means, e.g., observations at coastal polar stations, satellite observations). Different Arctic seas had different duration of iceberg observations and the longest history of observations was in the Barents Sea.

The Abramov Atlas provides charts of iceberg distributions. In order to develop these charts, the Atlas assumes uniform distribution of icebergs within the region of observation and expands the estimate of the frequency of icebergs along the flight route into 100 × 100 km cells. By sorting the observations in each cell per month and accumulating the observations over years, the Atlas provides charts for monthly and annual occurrence probabilities. The Atlas calculates the probability of iceberg occurrence as:

$$P = \frac{100m}{n} \tag{5.5}$$

where *P* is the probability of iceberg occurrence (%), *m* is the number of years where icebergs occurred in the given cell in the given period of time, and *n* is the total number of years of observations for the given cell in the given period of time. Figure 5.18 shows the chart of annual probability of occurrence of icebergs as presented in the Atlas.

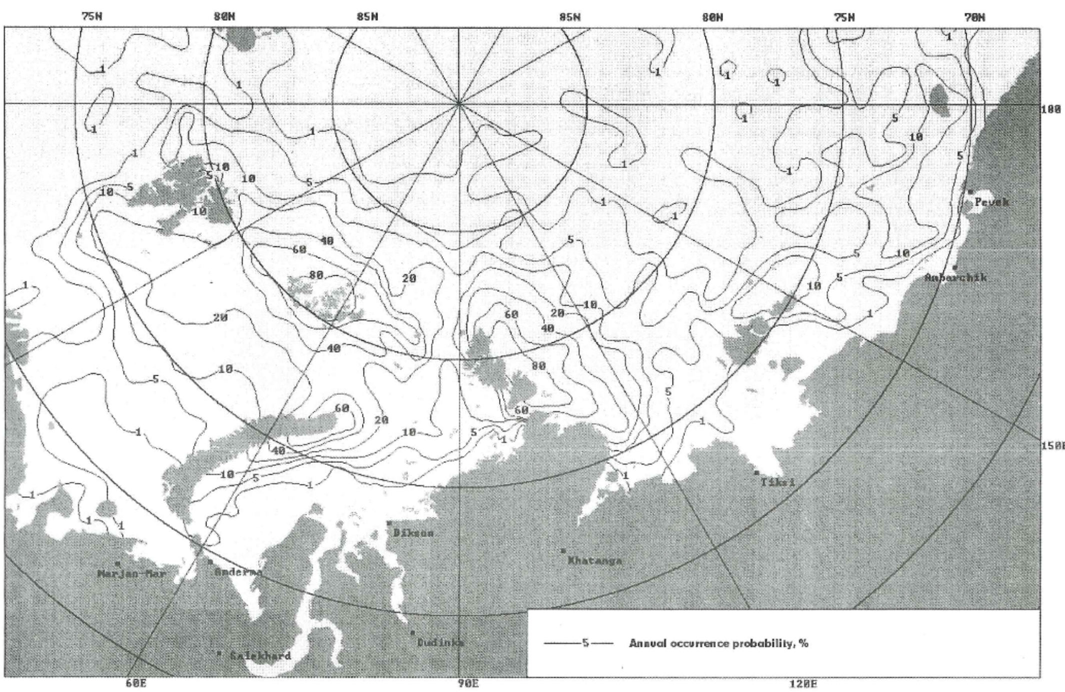

Figure 5.18 Annual probability of occurrence of icebergs, from The Atlas of Arctic Icebergs (Abramov and Tunik, 1996).

5.2 Probability of iceberg intrusions into Block # 7424

The task is to estimate the probability of iceberg intrusions into Block #7424. For this purpose, we developed a numerical model for simulating icebergs' drift and deterioration over large spatial and temporal scales (the computational domain includes the entire Barents Sea and it spans over a duration of 27 years). The model includes the dominant sources of icebergs in the Barents Sea that are of relevance to the Block #7424, i.e., Franz Josef Land (Eastern and Western sides), Nordaustlandet, Edgeøya, and Novaya Zemlya. The annual iceberg production rates from these sources are estimated based on theoretical calculations of precipitation rates and are adjusted based on observations/experience from the region. The icebergs are released randomly in time and space following uniform distributions. In time, they are released randomly from July 1st until November 30th every year. In space, they are distributed randomly in polygonal areas along the sources. The geometrical form and the thermomechanical properties of the released icebergs are derived based on statistical data from the ICEBASE and IDAP measurement programmes. The numerical model uses relatively high-resolution bathymetric data (2.5 km) and best-available metocean data (from state-of-the-art reanalysis products) that include, wind, current, wave, sea-ice and temperature.

The results of the numerical model are processed to create contour lines on a map of the Barents Sea showing the annual probability of occurrence of icebergs in a domain of 100 × 100 km. These contour lines are compared with the contour lines in the Abramov Atlas (Abramov and Tunik, 1996). Finally, the annual probability of icebergs at Block #7424 is estimated.

5.2.1 Model description

5.2.1.1 Drift equations

The equation for iceberg drift motion, is given by:

$$m \cdot (1 + C_m) \frac{dV_i}{dt} = F_a + F_w + F_c + F_{wd} + F_{si} \tag{5.6}$$

where m is the iceberg mass, C_m is the added mass coefficient, V_i is the iceberg velocity, F_a and F_w are the air and current form drag, respectively, F_c is the Coriolis force, F_{wd} is the mean wave drift force and F_{si} is forcing from sea ice. Note that forces due to ocean tilt are assumed marginal in this large-scale model and thus neglected. All the force terms are defined in the following and they are based on Eik (2009) and references therein, unless stated otherwise. The added mass is set to zero in this study due to the lack of data and due to the considerable uncertainty in the available estimates of icebergs' mass.

The drag forces due to currents are expressed as:

$$F_w = \frac{1}{2} \cdot \rho_w \cdot C_w \cdot A_w \cdot |V_w - V_i|(V_w - V_i) \tag{5.7}$$

where ρ_w is the density of the sea water, C_w the current form drag coefficient, V_w is the current speed and A_w is the cross-sectional area on which the current velocity acts. We adopt the approach of Wagner et al. (2017) and define A_w as:

$$A_w = \frac{\rho_i}{\rho_w} \cdot \frac{2}{\pi} \cdot (L_i + W_i) \cdot H_i \tag{5.8}$$

where ρ_i is the density of glacier ice. L_i, W_i and H_i are the iceberg length, width and total height (sail plus keel), respectively.

The drag forces due to the wind are expressed as:

$$F_a = \frac{1}{2} \cdot \rho_a \cdot C_a \cdot A_a \cdot |V_a - V_i|(V_a - V_i) \tag{5.9}$$

where ρ_a is the density of the air, C_a the air form drag coefficient, V_a the wind velocity and A_a the cross-sectional area on which the wind velocity acts. This area A_a is defined as (Wagner et al., 2017):

$$A_a = \frac{\rho_w - \rho_i}{\rho_i} \cdot A_w \tag{5.10}$$

The Coriolis force reads:

$$F_{cor} = -m \cdot f \times V_i \tag{5.11}$$

where f is the Coriolis parameter, which can be written as:

$$f = 1.45 \cdot 10^{-4} \cdot \sin(\varphi)\ \mathrm{k} \tag{5.12}$$

where φ is the geographic latitude position, and k is a unit vector in the vertical (up) direction. Note that the iceberg velocity, V_i, has two components, i.e., east and north.

The expression for the wave drift force is

$$F_{wd} = 0.25 \cdot \rho_w \cdot g \cdot a^2 \cdot L_i \cdot \frac{V_{wa}}{|V_{wa}|} \tag{5.13}$$

where a is the wave amplitude ($a = 0.5 \cdot H_s$, where H_s is the significant wave heigth) and $\frac{V_{wa}}{|V_{wa}|}$ is the wave direction.

And finally, the expression for the sea ice forces is

$$\begin{aligned} F_{si} &= 0 && : C_i \leq 0.15 \\ F_{si} &= 0.5 \cdot \rho_{si} \cdot C_{si} \cdot A_{si} \cdot |V_{si} - V_i| \cdot (V_{si} - V_i) && : 0.15 \leq C_i \leq 0.9 \\ F_{si} &= -(F_a + F_w + F_{cor}) && : C_i \geq 0.9\ \&\ h > h_{min} \end{aligned} \tag{5.14}$$

where ρ_{si} is the density of sea ice, C_{si} the sea ice drag coefficient, V_{si} the sea ice drift, C_i the ice concentration, h the sea ice thickness, h_{min} is the minimum sea ice thickness to lock an iceberg in the sea ice and A_{si} is the cross-sectional area on which the sea ice acts and is defined as:

$$A_{si} = \frac{2}{\pi} \cdot (L_i + W_i) \cdot h \tag{5.15}$$

The minimum sea ice thickness (h_{min}) reads:

$$h_{min} = \frac{P}{P^* \cdot exp(-20 \cdot (1 - C_i))} \tag{5.16}$$

where P is the sea ice strength and P^* is a sea ice coefficient.

5.2.1.2 Deterioration equations

The iceberg length, width and total height deteriorate with the following rates:

$$\frac{d(L_i)}{dt} = \frac{d(W_i)}{dt} = -(M_e + M_v) \tag{5.17}$$

$$\frac{d(H_i)}{dt} = -M_b \tag{5.18}$$

It is considered that the melt and erosion of an iceberg is mainly driven by wave erosion M_e, bottom melt M_b and buoyant convection at the side walls M_v. In the following, we summarize the formulation of these three terms. All the melt terms given here have units of metres per day. Further details and references can be found in the paper by Martin and Adcroft (2010). Wave erosion is given by:

$$M_e = \frac{1}{12} S_s \left(1 + cos\left(\pi A_i^3\right)\right)\left(\tilde{T}_o + 2\right) \tag{5.19}$$

where S_s is the sea state, A_i is the fractional sea ice cover and $\tilde{T}_o$ is the sea surface temperature. Sea state S_s is estimated by a fit to the Beaufort scale:

$$S_s = \frac{3}{2}|V_a - V_w|^{1/2} + \frac{1}{10}|V_a - V_w| \tag{5.20}$$

Melt rate at the base of the iceberg due to the turbulence created by the relative motion of water passing the iceberg is given by:

$$M_b = 0.58|V_i - V_w|^{0.8} \frac{\tilde{T}_o - \tilde{T}}{L_i^{0.2}} \tag{5.21}$$

where $\tilde{T}$ is the effective iceberg temperature assumed to be constantly at -4 °C.

The melt rate due to buoyant convection along the side walls of the iceberg caused by the temperature contrast between the iceberg and the ocean. This melt is given by:

$$M_v = 7.62 \cdot 10^{-3}\tilde{T}_o + 1.29 \cdot 10^{-3}\tilde{T}_o^2 \tag{5.22}$$

Finally, hydrostatic stability of the iceberg is considered by allowing for icebergs to capsize when the width-to-height ratio $\varepsilon \equiv W_i/H_i$ falls below a critical value ε_c. The criteria for the critical value is derived as:

$$\varepsilon_c = \sqrt{6\frac{\rho_i}{\rho_w}\left(1 - \frac{\rho_i}{\rho_w}\right)} \tag{5.23}$$

5.2.1.3 Sources and size distribution icebergs

Icebergs are generated at the five dominant sources in the Barents Sea. At each of these locations, a polygon is defined, and icebergs are generated at random positions within this polygon. Icebergs are released randomly in time (following a uniform distribution) from the beginning of July to the end of November for the period from 1991 to 2017. The 5 dominant sources, together with their polygons are plotted in Figure 5.19. In addition, the number of icebergs that are generated annually from each location is displayed in blue for the conservative scenario and red for the best guesstimate scenario. The total number of icebergs generated each year is 325 for the conservative scenario and 200 for the best guesstimate scenario. The details on the number of icebergs at each source are given in Section 5.1.5.

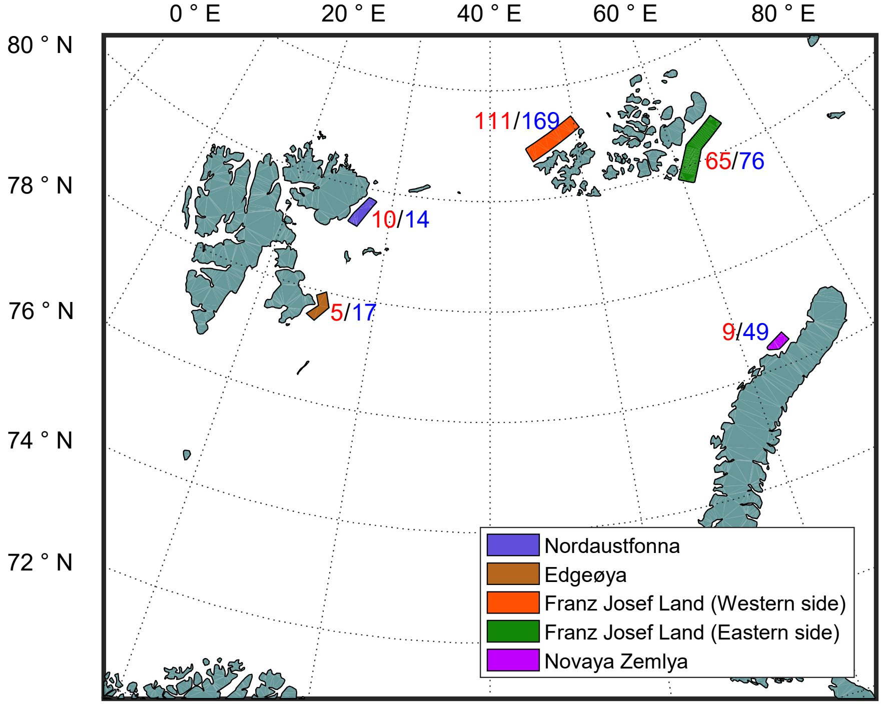

Figure 5.19. The five sources of icebergs in the global model together with the polygons where the icebergs are generated randomly. The numbers indicate the number of icebergs generated annually at each location for the *best guesstimate* in red and the *conservative estimate* in blue.

The initial length of the icebergs is generated from a Weibull distribution, which is based on in-situ data from the IDAP campaign. The width and the total height of the icebergs are defined as functions of the iceberg length. The Weibull parameters and the equations used to calculate the width and height of each generated iceberg are given in Table 5.8. The distribution of the initial dimensions of the generated icebergs are shown in Figure 5.20.

Table 5.8. Input dimensions for the generated icebergs.

Iceberg parameters		Input value			Data source
Length	L_i	Weibull distribution			IDAP
		Location	Scale	Shape	
		30.1	64.97	1.15	
Width	W_i	$W_i = 0.7 \cdot L_i \cdot \exp(-0.00062 \cdot L_i)$			Dezecot and Eik (2015)
Total height (sail + keel)	H_i	$H_i = 0.3 \cdot L_i \cdot \exp(-0.00062 \cdot L_i)$			Dezecot and Eik (2015)
Mass	M_i	$M_i = H_i \cdot L_i \cdot W_i \cdot \rho_i$			-

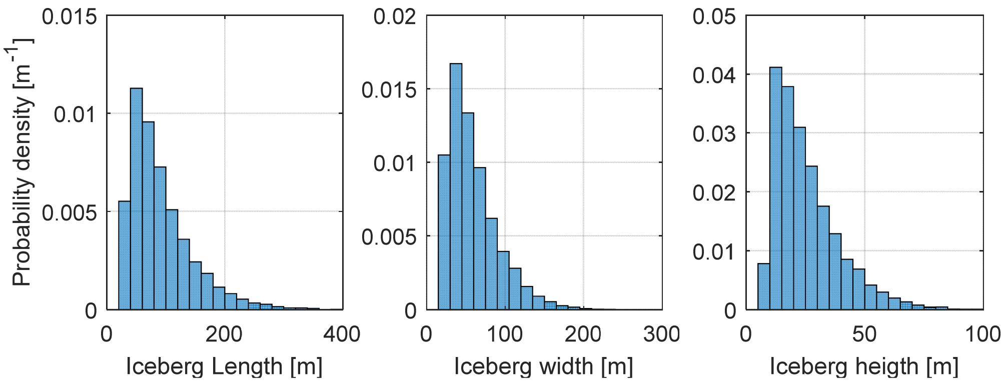

Figure 5.20. Distributions of the generated iceberg length, width and total height.

5.2.1.4 Meteorological data

The meteorological conditions, ice conditions and the bathymetry used as input to the model are summarized in Table 5.9**.** These input parameters and their sources are described in more detail below.

Table 5.9. Specifications of the used meteorological data and bathymetry.

Parameter	Spatial resolution	Temporal resolution	Model/ product name	Source data
Bathymetry	1 × 1 min	-	IBCAO	NOAA/NCEI
Wind	0.25 × 0.25 degree	2 hours	ERA 5	ECMWF
Waves	0.5 × 0.5 degree	2 hours	ERA 5	ECMWF
Currents	25 × 25 km	Daily	TOPAZ	Copernicus
Temperature	25 × 25 km	Daily	TOPAZ	Copernicus
Sea ice concentration	25 × 25 km	Daily	TOPAZ	Copernicus
Sea ice thickness	25 × 25 km	Daily	TOPAZ	Copernicus
Sea ice drift	25 × 25 km	Daily	TOPAZ	Copernicus

The bathymetry data are taken from the International Bathymetric Chart of the Arctic Ocean (Jakobsson et al., 2012), which are maintained by NOAA/NCEI. For this project, IBCAO version 1.0 is used, which can be downloaded freely from: https://www.ngdc.noaa.gov/mgg/bathymetry/arctic/arctic.html.

The wind and wave data are taken from the European Centre for Medium-range Weather Forecast (ECMWF) ERA 5 model. This is the fifth-generation atmospheric reanalysis of the global climate from 1979 to within three months of the present time. This model combines the laws of physics and assimilates large amounts of both in-situ and remote sensing observations into the model. The data are generated using the Copernicus Climate Change Service (2017) and can be downloaded from: https://cds.climate.copernicus.eu/cdsapp#!/dataset/reanalysis-era5-single-levels?tab=overview.

The currents, sea surface temperature, sea ice concentration, sea ice thickness and sea ice drift are obtained using the E.U. Copernicus Marine Service Information. The product *Arctic Ocean Physics Reanalysis* (TOPAZ) system was utilized. This reanalysis product is using the HYCOM ocean model and assimilates observations of sea level anomalies, sea surface temperature, salinity, ice concentration, drift and thickness. For more information regarding this reanalysis system, see Simonsen et al. (2018). The data are available at:

http://marine.copernicus.eu/servicesportfolio/accesstoproducts/?option=com_csw&view=details&product_id=ARCTIC_REANALYSIS_PHYS_002_003

5.2.1.5 Other input parameters

The remaining input parameters, constants and densities, needed in the global iceberg drift model are listed in the Table 5.10.

Table 5.10. Other input parameters used in the model including densities and constants.

Parameter		Input value	Data source
Iceberg density	ρ_i	850 kg m^{-3}	(Silva et al., 2006)
Sea water density	ρ_w	1027 kg m^{-3}	
Sea ice density	ρ_{si}	920 kg m^{-3}	(Timco and Weeks, 2010)
Density of air	ρ_a	1.225 kg m^{-3}	
Form drag coef. water	C_w	0.9	(Bigg et al., 1997)
Form drag coef. air	C_a	1.3	(Bigg et al., 1997)
Sea ice drag coefficient	C_{si}	1.0	(Lichey and Hellmer, 2001)
Added mass coefficient	C_m	0	
Sea ice strength	P	13000 N m^{-1}	(Lichey and Hellmer, 2001)
Sea ice coefficient	P^*	20000 N m^{-2}	(Lichey and Hellmer, 2001)

5.2.2 Results and discussions

This section describes the results of 27-years simulation (1991-2017) with 325 icebergs released each year from the 5 sources (i.e., the *conservative scenario* as described in Sections 5.1.5 and 5.2.1.3). The results from the *best guesstimate scenario* are shown in Appendix A. The simulations of the conservative scenario were repeated 3 times in order to assure the statistical validity of the results. The results from the 3 runs are shown in Appendix B. Moreover, we simulate the *conservative scenario* once with half the number of the released icebergs (*less conservative scenario*) and once with twice the number of the released icebergs (*overly conservative scenario*). This is done to study the sensitivity of the results from the conservative scenario on the assumed number of icebergs released. The results from this sensitivity analysis is shown in Appendix C.

For the conservative scenario, the total number of icebergs that entered Block #7424 (which is defined herein by a square of 100 × 100 km centred at 74° 14' 31.05" N 24° 30' 18.62" E) during the 27-years period were 264, 263, and 243 icebergs for Run #1 to Run #3, respectively. The variation between the results from the different runs is minor (see Appendix B), which indicates that simulations with this number of icebergs give stable results. For the remaining of this section, we examine only the results from simulation Run #1.

Figure 5.21 shows a map with total number of icebergs entering a box of 100 × 100 km. Here and in the upcoming figures, the red cross marks Block #7424 (74° 14' 31.05" N 24° 30' 18.62" E) and the red square around it has the dimensions of 100 × 100 km. The number on the side of Block # 7424 is the total number of icebergs entering the box at the Field during the 27-years simulations.

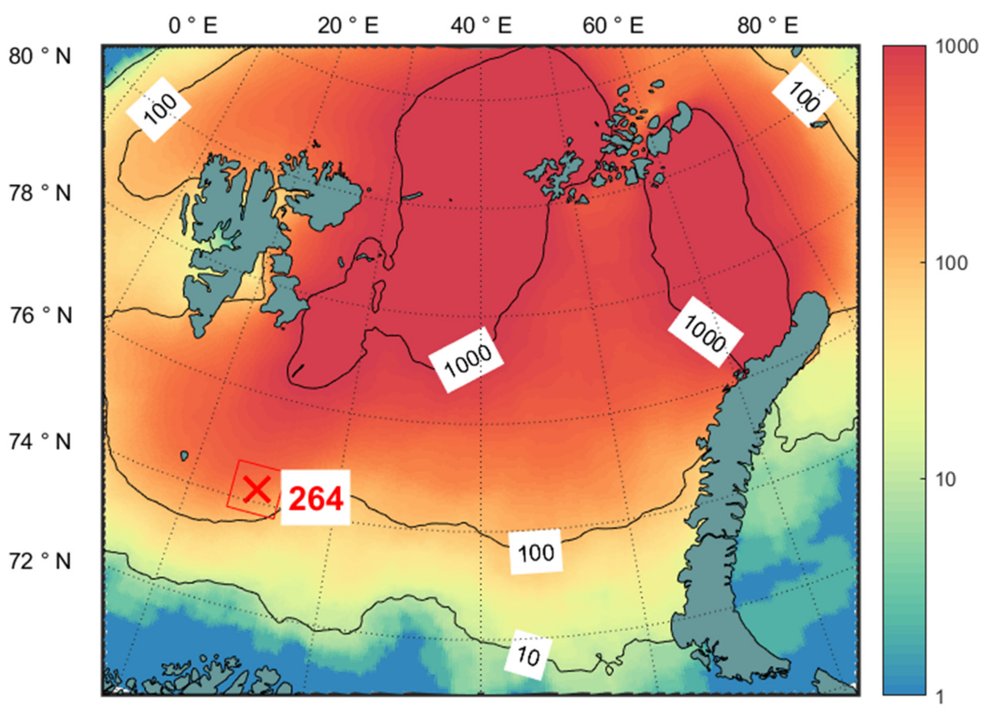

Figure 5.21. Total number of icebergs in a 100 × 100 km box during the simulated 27 years.

The number of icebergs per year in a 100 × 100 km box is shown in Figure 5.22. This is calculated by taking the results shown Figure 5.21 and dividing them by the total number of years that were simulated (i.e., 27 years). Figure 5.22 shows that the number of icebergs entering the 100 × 100 km box at Block #7424 per year is 9.78 icebergs.

.

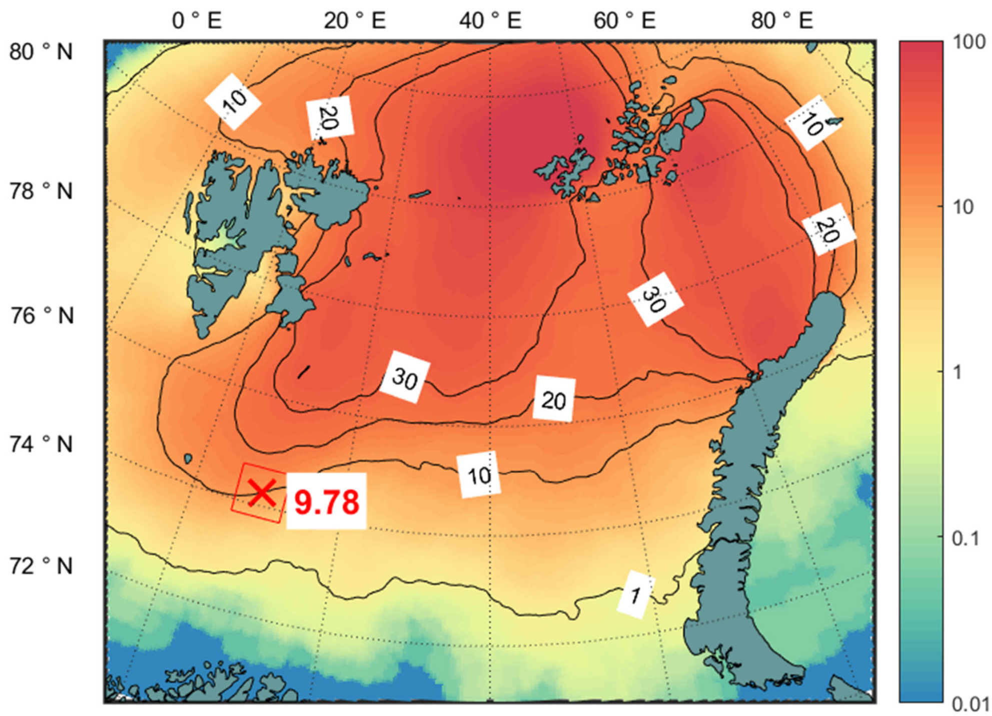

Figure 5.22. Expected number of icebergs per year in a 100 x 100 km box.

Figure 5.23 shows the number of icebergs that entered the 100 × 100 km box centred at Block #7424 each year during the 27-years that were simulated. From the figure, it is evident that icebergs entered Block #7424 only in 23 out of the 27 years. This gives a probability of (23/27 = 85.19%) that at least one iceberg will enter the 100 × 100 km at Block #7424. Performing a similar analysis to all other boxes, Figure 5.24 presents a map with probability of at least one iceberg entering a 100 × 100 km box.

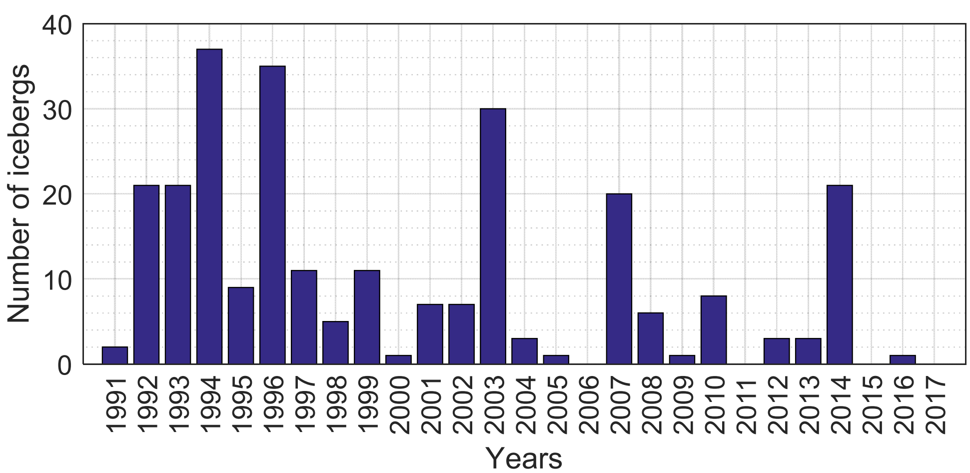

Figure 5.23. Number of icebergs entering the 100 × 100 km box at Block #7424.

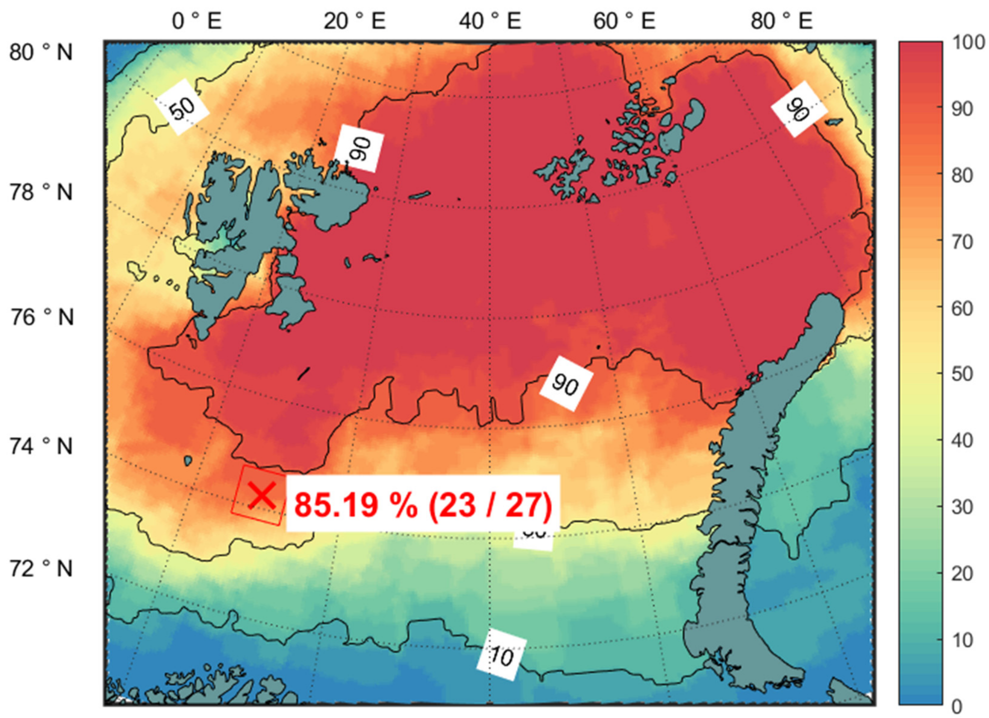

Figure 5.24. Yearly probability of iceberg occurrence in a 100 × 100 km box (i.e., at least one iceberg entering the box).

While the above figures show the number of icebergs entering Block #7424 (either the total number of icebergs in the 27-years or the number of icebergs per year), they do not provide information about that the areal density of icebergs at Block #7424, ρ_a, which can be defined as:

$$\rho_a = \frac{\sum_{i=0}^{\infty} i \cdot p_i}{A} \tag{5.24}$$

where p_i is the probability of having i icebergs at the same time inside Block #7424 of area A equals 100 × 100 km. Figure 5.25 shows the histogram of the number of icebergs that can be at the same time inside Block #7424, i.e., histogram of i. This histogram is estimated by counting the number of icebergs inside Block #7424 at each time step (i.e., each two hours period). Figure 5.25 shows, for example, that during $1.14794 \cdot 10^5$ timesteps out of the $1.18333 \cdot 10^5$ timesteps, there were zero icebergs inside Block #7424 (i.e., $p_o = 1.14794 \cdot 10^5 / 1.1833 \cdot 10^5 = 0.9701$). The figure shows also that the maximum number of icebergs that are at the same time inside Block #7424 box is 16. Table 5.11 summarizes the probabilities of having i icebergs at the same time inside the Block #7424 box.

Table 5.11. Probability of having *i* icebergs at the same time inside Block #7424.

	Number of icebergs that are at the same time inside the Block #7424 box (i)									
	0	1	2	3	4	5	6	7	8	9
p_i	0.9701	$1.50 \cdot 10^{-2}$	$5.03 \cdot 10^{-3}$	$3.05 \cdot 10^{-3}$	$1.83 \cdot 10^{-3}$	$1.27 \cdot 10^{-3}$	$7.86 \cdot 10^{-4}$	$5.75 \cdot 10^{-4}$	$5.24 \cdot 10^{-4}$	$5.24 \cdot 10^{-4}$
	Number of icebergs that are at the same time inside the Block #7424 box (i)									
	10	11	12	13	14	15	16			
p_i	$5.24 \cdot 10^{-4}$	$5.75 \cdot 10^{-4}$	$3.30 \cdot 10^{-4}$	$1.35 \cdot 10^{-4}$	$6.68 \cdot 10^{-5}$	$7.61 \cdot 10^{-5}$	$1.10 \cdot 10^{-4}$			

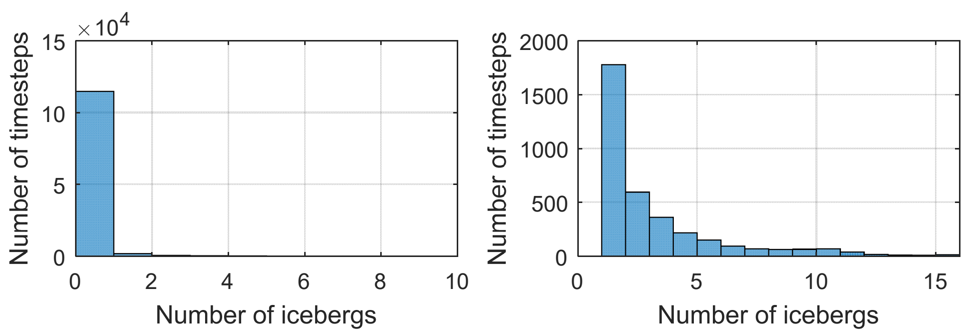

Figure 5.25. Histogram of the number of icebergs that can be at the same time (during time step of two hours) inside Block #7424 (box of 100 × 100 km). The two histograms are identical; however, the zero icebergs are excluded from the histogram to the right to improve the readability. The total number of timesteps (observations) is $1.1833 \cdot 10^5$.

Figure 5.26 shows histograms of the characteristic dimensions (length, width, height) and mass of the icebergs as they enter Block #7424. The mass here is approximated as ($M_i = L_i \cdot W_i \cdot H_i \cdot \rho_i$).

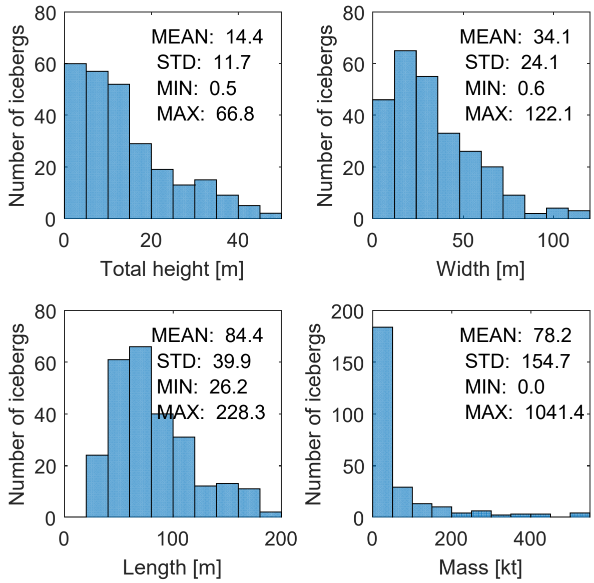

Figure 5.26. Histogram of dimensions and mass of icebergs as they enter the 100 × 100 km box at Block #7424.

The results shown so far include all icebergs irrespective of their sizes, i.e., they include bergy bits and even growlers. If the small-size floating glacial ice features like growlers are to be disregarded, the probability of iceberg intrusions into Block #7424 will be reduced. Figure 5.27 shows the number icebergs entering Block #7424 as a function of iceberg total height (sail + keel).

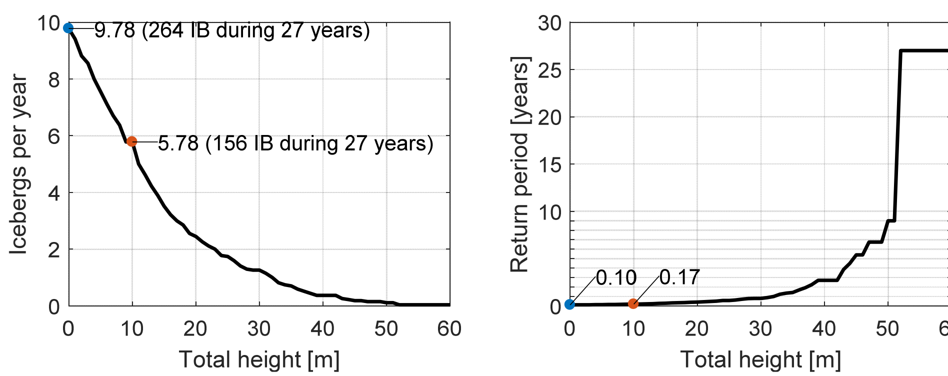

Figure 5.27. Effect of imposing a threshold for minimal total height of icebergs. Left: Number of icebergs entering Block #7424. Right: Return period (Expected average number of years for an iceberg of given height to enter Block #7424).

If we impose a threshold on the total height of 10 m (considering Archimedes' principle, we are effectively eliminating growlers from our calculation, which are defined as icebergs with freeboard smaller than 1 m), we see from Figure 5.27 that the average number of icebergs entering Block #7424 reduces from 9.78 to 5.78 per year.

In the following we update all the previous results with the criterion that icebergs of total height less than 10 m (freeboard smaller than 1 m) are neglected. Figure 5.28 shows the updated number of icebergs entering a 100 × 100 km box during the 27-years simulation period. Figure 5.29 shows the updated histograms of the characteristic dimensions (length, width, height) and mass of the icebergs as they entered Block #7424. Figure 5.30 presents the updated expected number of icebergs per year in a 100 ×

100 km box. Figure 5.31 shows the updated yearly probability of iceberg occurrence in a 100 ×100 km box (i.e., at least one iceberg entering the box). Figure 5.32 presents the updated histogram of the number of icebergs that can be at the same time (during time step of two hours) inside Block #7424. The maximum number now reduces to 10. Table 5.12 shows the updated probabilities of having multiple icebergs at the same time in Block #7424.

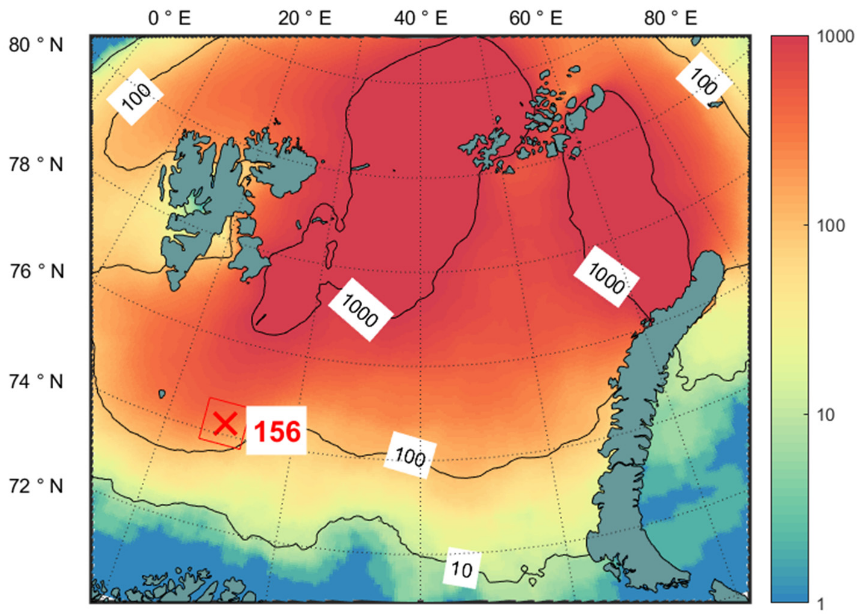

Figure 5.28. Updated total number of icebergs in a 100 × 100 km box during the simulated 27 years. Icebergs with total height less than 10 m are neglected.

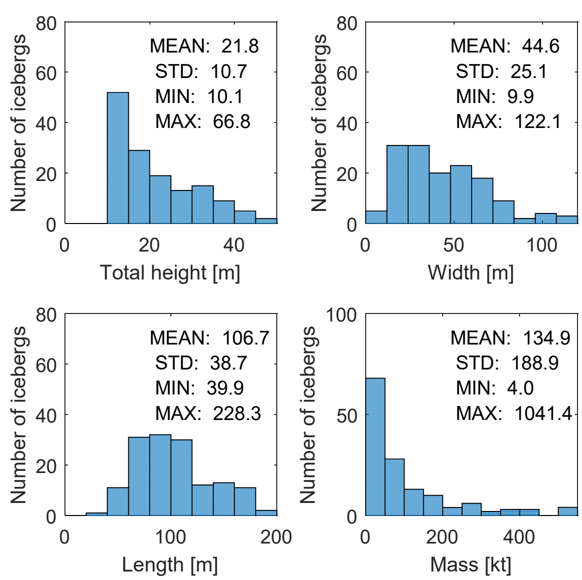

Figure 5.29 Updated histograms of dimensions and mass of icebergs as they enter the 100 x 100 km box at Block #7424. Icebergs with total height less than 10 m are neglected.

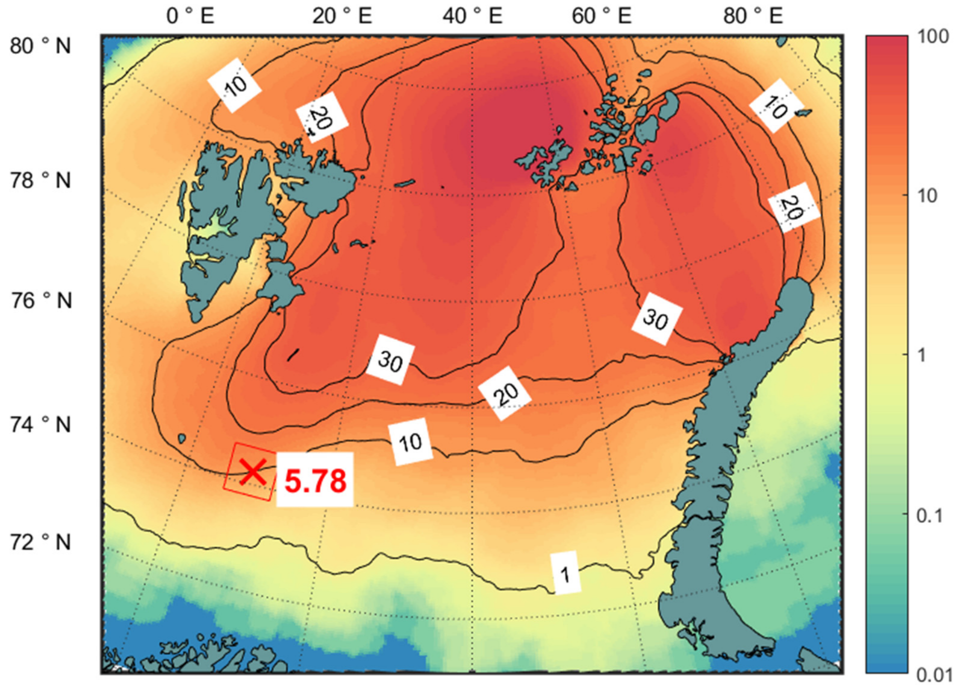

Figure 5.30. Updated expected number of icebergs per year in a 100 × 100 km box. Icebergs with total height less than 10 m are neglected.

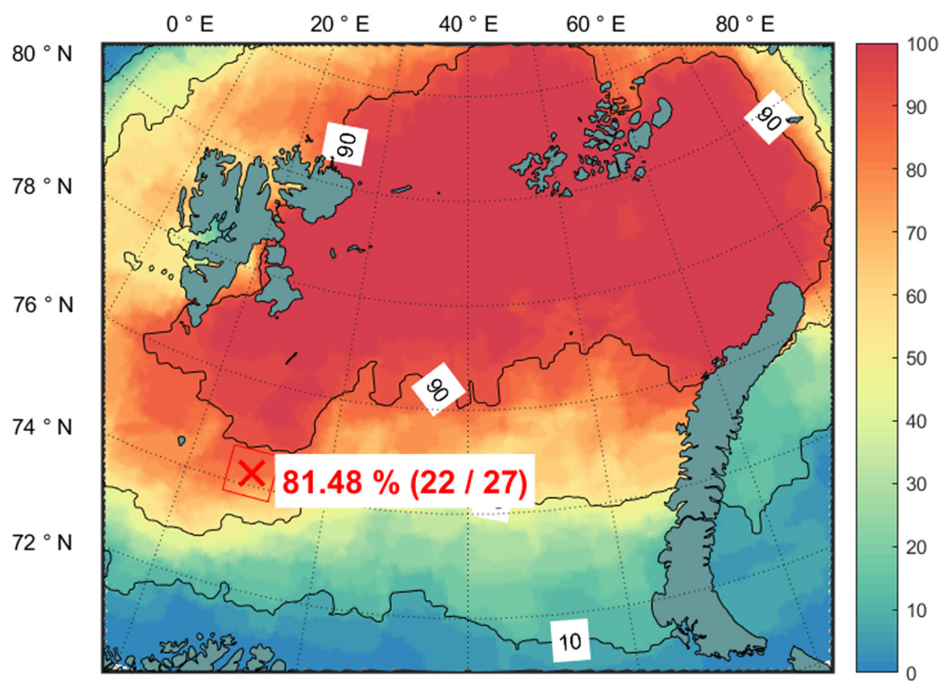

Figure 5.31. Updated yearly probability of iceberg occurrence in a 100 × 100 km box (i.e., at least one iceberg entering). Icebergs with total height less than 10 m are neglected.

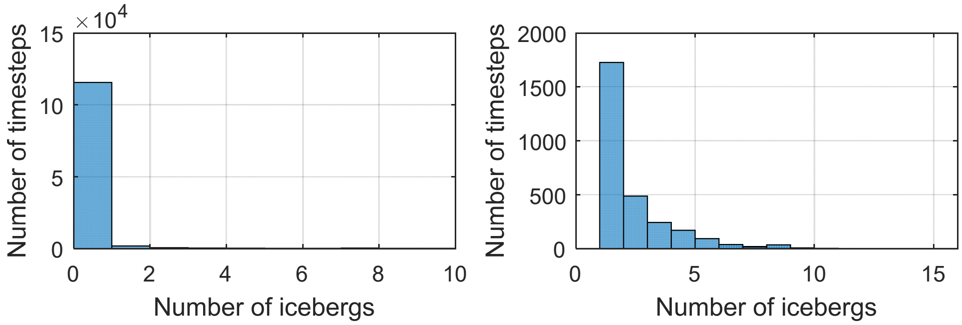

Figure 5.32. Histogram of the number of icebergs that can be at the same time (during time step of two hours) inside Block #7424 (box of 100 × 100 km). The two histograms are identical, however, the zero icebergs are excluded from the histogram to the right to improve the readability. Icebergs with total height less than 10 m are neglected. The total number of timesteps (observations) is $1.1833 \cdot 10^5$.

Table 5.12. Probability of having *i* icebergs at the same time inside Block #7424. Icebergs with total height less than 10 m are neglected.

	Number of icebergs that are at the same time inside the Block #7424 box (i)										
	0	1	2	3	4	5	6	7	8	9	10
p_i	0.976	$1.46 \cdot 10^{-2}$	$4.11 \cdot 10^{-3}$	$2.05 \cdot 10^{-3}$	$1.42 \cdot 10^{-3}$	$7.69 \cdot 10^{-4}$	$3.13 \cdot 10^{-4}$	$1.18 \cdot 10^{-4}$	$2.87 \cdot 10^{-4}$	$4.23 \cdot 10^{-5}$	$8.46 \cdot 10^{-6}$

As a summary of the results from the conservative scenario shown above, 264 icebergs entered Block #7424 during the 27-years of simulations where only 156 of them had total height larger than 10 m. Figure 5.33 below illustrates the trajectories of these 156 icebergs from their origin until they deteriorated to total height smaller than 10 m. In addition, in Table 5.13 the number of icebergs coming from each origin is presented.

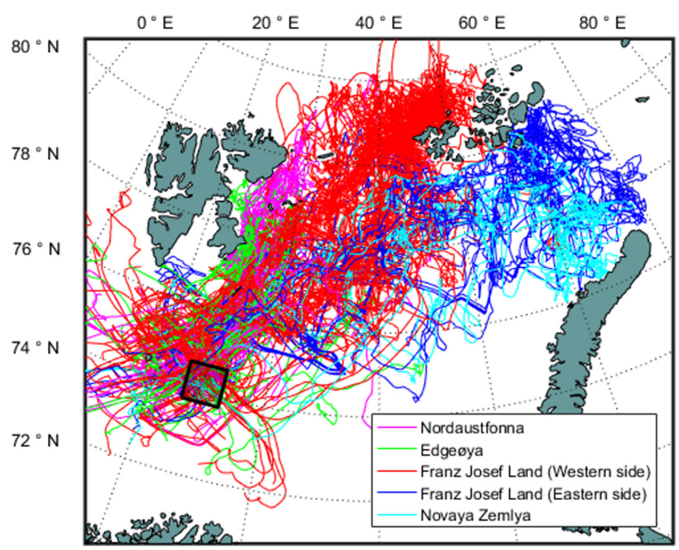

Figure 5.33. Trajectories of 156 icebergs that have entered the 100 × 100 km box at Block #7424. Trajectories are plotted from the origin of icebergs until the icebergs deteriorated to total thickness smaller than 10 m.

Table 5.13. Origin of the 39 tracks that entered the 100 × 100 km box at Block #7424.

Origin icebergs	Number of icebergs	Percentage [%]
Nordaustfonna	21	13.46
Edgeøya	23	14.74
Franz Josef Land (Western side)	80	51.28
Franz Josef Land (Eastern side)	21	13.46
Novaya Zemlya	11	7.05

5.2.3 Comparison with the Atlas of Arctic Icebergs

Figure 5.31 presents the annual probability of occurrence of icebergs and thus can be directly compared with Chart 3.37 in the Atlas of Arctic Icebergs (Abramov and Tunik, 1996), see also Figure 5.18. Such comparison is shown in Figure 5.34 where our results are presented side by side with results from the Abramov Atlas. Our results for the conservative scenario yield 85.19% annual probability of occurrence of icebergs at Block #7424, whereas Abramov Atlas reads about 7.5%. This appears as a considerable difference. However, the difference can be explained by:

- Since we assume a maximum iceberg production rate from the 5 sources simultaneously, the simulation results of the conservative scenario are expected to overestimate the annual probability of occurrence of icebergs at Block #7424.
- On the other hand, we believe that the Abramov Atlas underestimates the annual probability of occurrence of icebergs at the part of the Barents Sea that contains Block #7424. The Abramov Atlas does not give any indication about the frequency of scouting missions in the area of Block #7424 and it can be only concluded that they were not very frequent. This reasoning is also supported by Dezecot and Eik (2015), where the reading from Abramov Atlas was multiplied by a factor of 3 to account for the uncertainties in the Atlas. To determine the annual probability of occurrence of icebergs at block "A" indicated in the right panel of Figure 5.34, Dezecot and Eik (2015) read the value of 10% from the Abramov Atlas and then multiplied by 3 ending up with a probability of 30%. Our simulation results indicate 44.44% annual probability of occurrence of icebergs at block "A", which is in reasonable agreement with Dezecot and Eik (2015), for more details about block "A" results, see Appendix F.

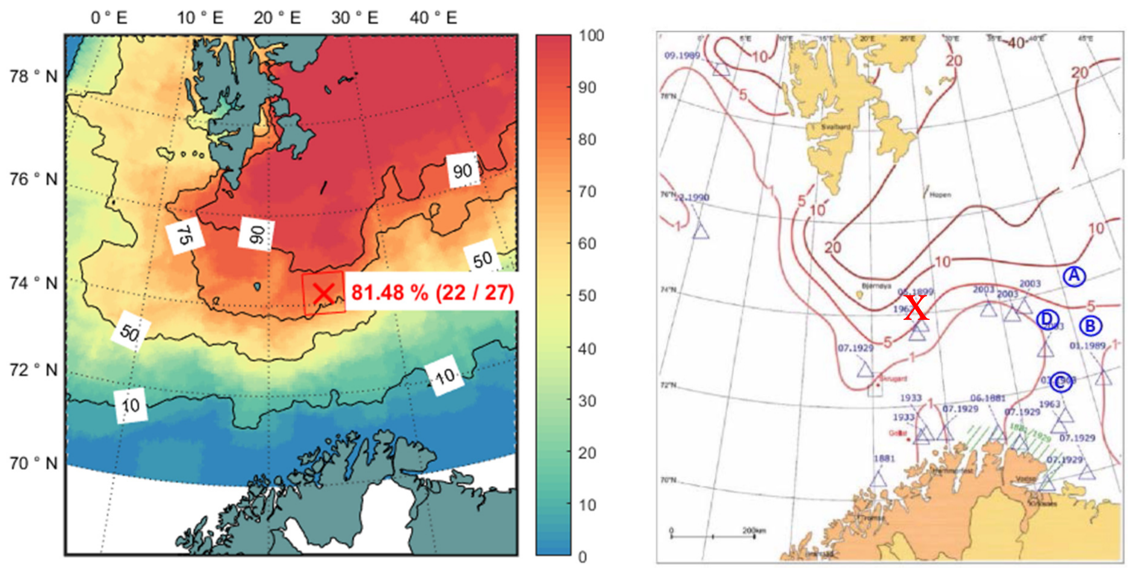

Figure 5.34. Yearly probability of iceberg occurrence in a 100 × 100 km box. Left: results from our simulation. Right: results from the Atlas of Arctic Icebergs as presented in Dezecot and Eik (2015).

5.3 Annual iceberg encounter frequency at Block #7424

In the previous section, we presented our estimates for the number of icebergs entering Block #7424 per year for the conservative scenario (Note that Block #7424 is defined herein by a box of 100 × 100 km centred at 74° 14' 31.05" N 24° 30' 18.62" E). We showed histograms of dimensions and mass of icebergs as they enter Block #7424. We have also derived the annual probability of occurrence of icebergs at Block #7424. The task in this section is to estimate the number of icebergs that may hit a structure at Block #7424 per year. For this purpose, we developed a numerical model for simulating icebergs' drift and deterioration within Block #7424. This model is called herein the "local model". It shares similar properties to the global model used to simulate the drift of icebergs in the Barents Sea, but it utilizes sea current data of higher temporal resolution (i.e. includes tidal currents) and it accounts for drift forces due to ocean surface tilt. The statistical distributions of dimensions and mass of icebergs entering Block #7424, which were derived from the global model, are used to initiate the local model. A sufficiently large number of icebergs are generated from these statistical distributions. The initial position of all these icebergs in the local model is 74° 14' 31.05" N 24° 30' 18.62" E. The initial (start) time for each of the icebergs is random following a uniform distribution over the past 27 years. The local model calculates the local probability of collision between icebergs and a structure at Block #7424 following the approach of Mathiesen et al. (1992). We vary the size of the structure in this study as 100 × 100 m, 500 × 500 m and 1000 × 1000 m.

In the remaining of this section we describe the local model and the approach to estimate the annual iceberg encounter frequency at Block #7424. We present our results and compare them to results from other calculation methods like the ones suggested by ISO 19906 (2019).

5.3.1 Local Model Description

5.3.1.1 Drift equations

The basic equation in the local model is given by:

$$m \cdot (1 + C_m) \frac{d}{dt}(V_i - V_g - V_t) = F_a + F_w + F_c + F_{wd} + F_{si} \tag{5.25}$$

where m is the iceberg mass, C_m is the added mass coefficient, V_i is the iceberg velocity, V_g is the geostrophic current, V_t is the tidal current, F_a and F_w are the air and current form drag, respectively, F_c is the Coriolis force, F_{wd} is the mean wave drift force and F_{si} is the sea ice drag. Assuming that the Coriolis force acting on the sea water will be balanced by the sea surface tilt (in the absence of wind), it can be shown that Eq. (5.25) considers the effects of sea surface tilt on the iceberg drift (see Appendix D). The formulae to calculate drag forces are the same used in the global model and will not be repeated.

5.3.1.2 Deterioration equations

The deterioration equations of the local model are identical to the ones used for the global analysis. The equations are given in Eqs. (5.17) to (5.23).

5.3.1.3 Sources and size distribution icebergs

As stated above, sufficiently large number of icebergs (100 icebergs) are generated from statistical distributions derived from the global model. Using more icebergs resulted in nearly identical results (see Appendix E). The initial position of all these icebergs in the local model is 74° 14' 31.05" N 24° 30' 18.62" E. The initial (start) time for each of the icebergs is random following a uniform distribution over the past 27 years.

When growlers are included in the analysis, the dimensions of the generated icebergs are randomly drawn from the histograms showed in Figure 5.26. On the other hand, when growlers are excluded from the analysis, the dimensions of the generated icebergs are randomly drawn from the histograms shown in Figure 5.29.

5.3.1.4 Meteorological data

The meteorological input data are identical to the one used for the global analysis (see Table 5.9), except for the current data. For the local model, the currents are defined as the sum of the geostrophic current (V_g), the wind driven current (V_{wind}) and the tidal current (V_t):

$$V_w = V_g + V_{wind} + V_t \tag{5.26}$$

The geostrophic data are based on Slagstad et al. (1990). The wind induced surface current is defined as:

$$V_{wind} = \frac{2}{100} \cdot ws \cdot [sin(wdir)\ \ cos(wdir)] \tag{5.27}$$

in which *ws* is the wind speed and *wdir* the wind direction. The tidal current is generated from the 4 major tidal constituents (M2, S2, N2 and K1) using the method of Gjevik et al. (1994).

5.3.1.5 Collision risk – analysis approach

We follow the approach presented by Mathiesen et al. (1992) to estimate the risk collision between an iceberg and a 100 × 100 m, 500 × 500 m or 1000 × 1000 m structure at Block #7424. The annual iceberg encounter frequency reads:

$$E_N = P_l \cdot N \tag{5.28}$$

where E_N is the number of icebergs colliding with the structure per year, P_l is the local probability of collision (derived from the local model), and N is the expected number of icebergs entering Block #7424 per year (derived from the global model).

The local probability of collision is calculated from the local model as follows:

For each iceberg,

1. The spatial domain of 100 × 100 km is subdivided into smaller boxes or windows of size l x l.
2. The number of boxes that contain part of the iceberg track is counted.
3. The above two steps are repeated for decreasing box sizes. For this study, the maximum box size was 25 km and the minimum box size was 3 km.
4. The number of boxes that contain part of the iceberg track, *N(l),* are plotted versus the window size, l, on a log-log scale.

For all icebergs,

5. Combine the log (*N(l)*) versus log *(l)* curves for all icebergs in one plot and find the curve that represents weighted average of all curves.
6. Fit the curve resulted from step 5 to estimate the fractal dimension (*D*), the constant (*C*) and the scaling factor (l_0) in Equation (5.29)**.**

$$N(l) = C\left(\frac{l}{l_0}\right)^{-D} \tag{5.29}$$

7. Finally, the local probability P_l, is computed as:

$$P_l = \frac{C}{k} \cdot \left(\frac{l}{l_0}\right)^{2-D} \tag{5.30}$$

   where k equals $\frac{(100 \cdot 100)}{{l_0}^2} = 10000$.

5.3.2 Results and discussions

To assure the statistical validity of the results, the local simulations are repeated 5 times. We find that the results from the 5 runs are very similar and henceforth, we present and analyse the results of only one run.

5.3.2.1 Results excluding growlers

The trajectories of the 100 simulated icebergs are presented in Figure 5.35. An iceberg is taken out of the simulation when it leaves the 100 × 100 km box, indicated by the red dotted square, or when an iceberg has melted.

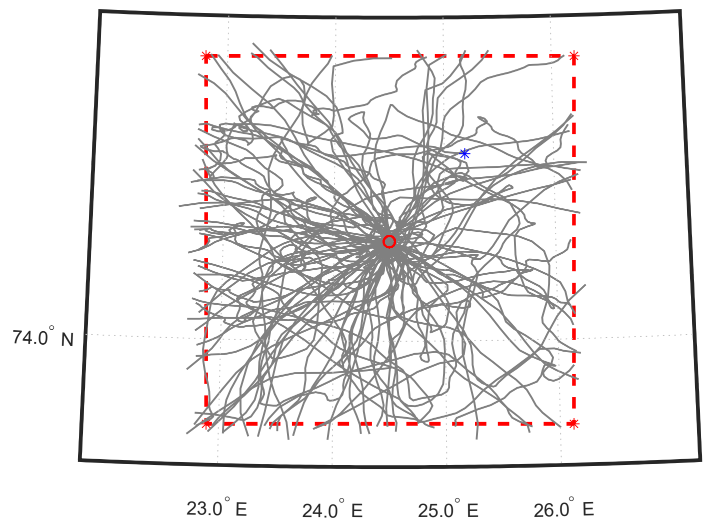

Figure 5.35. Simulated iceberg tracks for the computation of the local probability of collision. The red circle indicates where the icebergs are generated, and the blue stars show the locations where icebergs are melted.

In Figure 5.36, the number of boxes that include part of the iceberg track are plotted against the box size *l*.

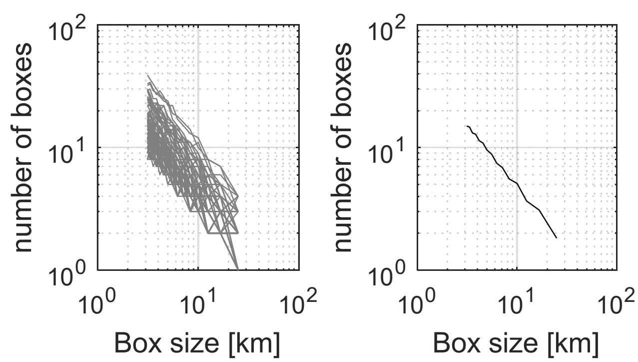

Figure 5.36. The number of boxes that contain part of the iceberg track versus the box size. In the left figure, all the iceberg tracks are plotted separately. The right figure is the weighted average of the 100 simulated icebergs. Note that the slope of this line is the fractal dimension *D*.

The calculated local probabilities, from Eq. (5.30), are shown in Table 5.14.

Table 5.14. The local iceberg collision probability with structures of varying sizes.

	Structure size (*l*)		
	100 × 100 m	500 × 500 m	1000 × 1000 m
Local Probability (P_l)	$4.78 \cdot 10^{-4}$	$2.41 \cdot 10^{-3}$	$4.85 \cdot 10^{-3}$

From the global model, the expected number of icebergs (excluding growlers) entering Block #7424 per year for the conservative scenario (*N*) is 5.78. Using Equation (5.28) with $N = 5.78$ and P_l as in Table 5.14, the annual iceberg encounter frequency (E_N) is calculated and the results are shown in Table 5.15

Table 5.15. The annual iceberg encounter frequency at Block #7424.

	Structure size (*l*)		
	100 × 100 m	500 × 500 m	1000 × 1000 m
Annual iceberg encounter frequency (E_N)	$2.76 \cdot 10^{-3}$	$1.39 \cdot 10^{-2}$	$2.80 \cdot 10^{-2}$

5.3.2.2 Comparison to ISO 19906 (2019)

In this section we use the "swept area approach" presented by Fuglem et al. (1996) and suggested by ISO 19906 (2019), to calculate the annual iceberg encounter frequency at Block #7424. According to Fuglem et al. (1996), the annual expected number of iceberg encounters (η_e) can be expressed as:

$$\eta_e = \rho_a \cdot (l + \bar{l}_i) \cdot \bar{V}_l \cdot T \qquad (5.31)$$

where ρ_a is the areal density of icebergs per square metre, l is the structure size, $\bar{l}_i$ is the mean iceberg effective width (taken here as the iceberg's mean length), $\bar{V}_l$ is the mean iceberg drift speed, and T is the number of seconds per year.

Using Equation (5.24) and utilising results from the global model (see Figure 5.32 and Table 5.12), the areal density of icebergs per square metre (ρ_a) is estimated as:

$$\rho_a = \frac{(1\cdot 1.46\cdot 10^{-2})+(2\cdot 4.11\cdot 10^{-3})+(3\cdot 2.05\cdot 10^{-3})+(4\cdot 1.42\cdot 10^{-3})+(5\cdot 7.69\cdot 10^{-4})+(6\cdot 3.13\cdot 10^{-4})+(7\cdot 1.18\cdot 10^{-4})+(8\cdot 2.87\cdot 10^{-4})+(9\cdot 4.23\cdot 10^{-5})+(10\cdot 8.46\cdot 10^{-6})}{100\cdot 100\cdot 10^{6}} =$$

$4.39 \cdot 10^{-12}$ Icebergs per square metre.

The results from the local model show that the drift speed of the 100 icebergs simulated are distributed as shown in Figure 5.37. Thus, the mean iceberg drift speed ($\bar{V}_l$) is 0.3 m/s.

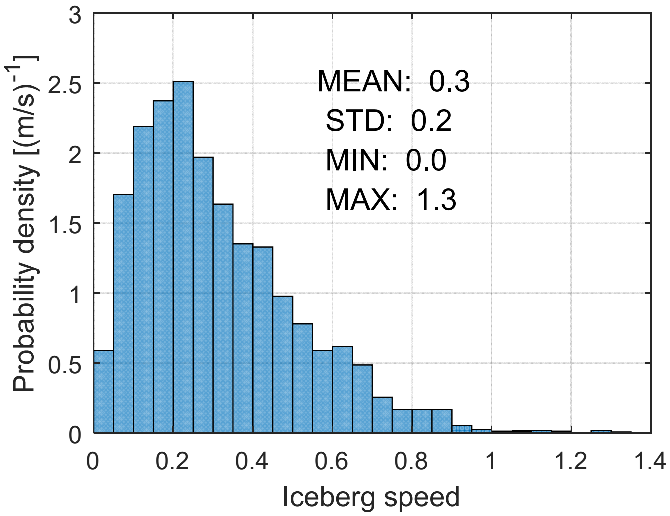

Figure 5.37. Histogram of the iceberg speed.

The mean iceberg effective width ($\bar{l}_i$) can be read from Figure 5.29 as $\bar{l}_i = 106.7$ m. One can calculate the annual iceberg encounter frequency using Equation (5.31). Table 5.16 shows the results for 3 different sizes of the structure.

Table 5.16. The annual iceberg encounter frequency at Block #7424 using the Fuglem et al. (1996) method.

	Structure size (*l*)		
	100 × 100 m	500 × 500 m	1000 × 1000 m
Annual iceberg encounter frequency (E_N)	$8.60 \cdot 10^{-3}$	$2.52 \cdot 10^{-2}$	$4.60 \cdot 10^{-2}$

Dezecot and Eik (2015) used a different approach (Equation (5.32)) to approximate iceberg areal density.

$$\rho_a = \rho \cdot R \cdot P \tag{5.32}$$

where ρ is the crude areal density (suggested as 2 per 100 × 100 km box), R is the iceberg residence time within the box and P is the annual probability of occurrence, which is estimated from the global model as P = 81.48% at Block #7424 (see Figure 5.31).

The results from the local model show that the residence time of the 100 simulated icebergs are distributed as shown in Figure 5.38. Thus, the mean iceberg residence time (R) is 67.3 hours.

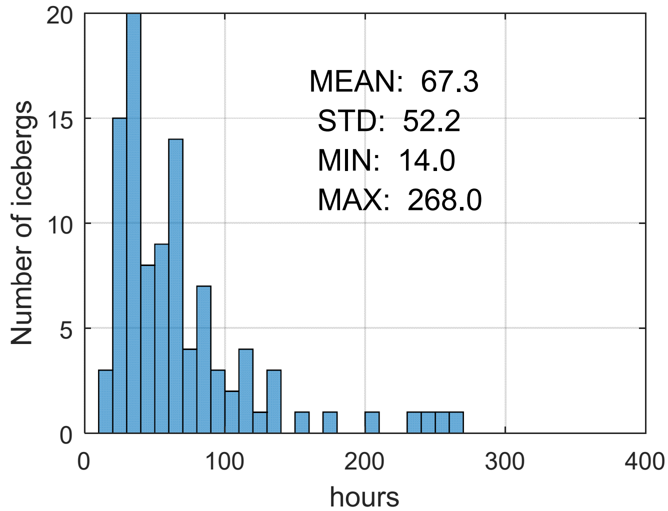

Figure 5.38. Histogram of the iceberg residence time within the 100 × 100 km box at Block #7424.

The iceberg areal density according to Equation (5.32) reads:

$\rho_a = \frac{2}{100 \cdot 100 \cdot 10^6} \cdot \frac{67.3}{365 \cdot 24} \cdot \frac{81.48}{100} = 1.25 \cdot 10^{-12}$ Icebergs per square metre

Using Equation (5.31) again with the above estimate of the areal density, Table 5.17 shows the results for 3 different sizes of the structure.

Table 5.17. The annual iceberg encounter frequency at Block #7424 using estimate of ρ_a based on Dezecot and Eik (2015).

	Structure size (*l*)		
	100 × 100 m	500 × 500 m	1000 × 1000 m
Annual iceberg encounter frequency (E_N)	$2.40 \cdot 10^{-3}$	$7.20 \cdot 10^{-3}$	$1.31 \cdot 10^{-2}$

Table 5.18. The annual iceberg encounter frequency at Block #7424 Field for the conservative scenario, i.e.

Annual iceberg encounter frequency (E_N) *using the method of:*	Structure size (*l*)		
	100 × 100 m	500 × 500 m	1000 × 1000 m
Mathiesen et al. (1992)	$2.76 \cdot 10^{-3}$	$1.39 \cdot 10^{-2}$	$2.80 \cdot 10^{-2}$
Fuglem et al. (1996)	$8.60 \cdot 10^{-3}$	$2.52 \cdot 10^{-2}$	$4.60 \cdot 10^{-2}$
Fuglem et al. (1996) with ρ_a estimated according to Dezecot and Eik (2015)	$2.40 \cdot 10^{-3}$	$7.20 \cdot 10^{-3}$	$1.31 \cdot 10^{-2}$

5.3.2.3 Results including growlers

The dimensions of the 100 generated icebergs are randomly drawn from the histograms showed in Figure 5.26. The results from the local model are shown in Table 5.19.

Table 5.19. The local iceberg collision probability with structures of varying sizes.

	Structure size (l)		
	100 × 100 m	500 × 500 m	1000 × 1000 m
Local Probability (P_l)	$4.77 \cdot 10^{-4}$	$2.40 \cdot 10^{-3}$	$4.81 \cdot 10^{-3}$

Considering that the expected number of icebergs (including growlers) per year at Block #7424 is 9.78, the annual iceberg encounter frequency at Block #7424 is shown in Table 5.20.

Table 5.20. The annual iceberg encounter frequency at Block #7424.

	Structure size (l)		
	100 × 100 m	500 × 500 m	1000 × 1000 m
Annual iceberg encounter frequency (E_N)	$4.67 \cdot 10^{-3}$	$2.35 \cdot 10^{-2}$	$4.70 \cdot 10^{-2}$

5.3.2.4 Summary of the results

Floating glacial ice features of various sizes may pose a threat to the structural integrity of man-made structures in parts of the Barents Sea. This report presents data relevant for such studies at Block #7424 (N73°28'10.028'', E 24° 17'36.713''):

- Statistics and numerical modelling of glacial ice (analyses of data on origin, drift patterns and velocities, deterioration rate, probability of occurrence), and encounter probability.
- Estimates of the properties of these ice features if they occur in the vicinity of Block #7424.

Analyses of the glacial ice encounter frequency are done by performing simulations of iceberg drift from their origin. The simulations are performed in two stages:

- The first stage simulates the drift of icebergs from their origin and across the Barents Sea. The essence here is to count the number of icebergs that enters a box of 100 × 100 km centred at Block #7424.
- The number of icebergs annually released from Franz Josef Land, Svalbard and Novaya Zemlya are estimated based on the available data.
- The number of icebergs released annually can have a major impact on the final estimate of the glacial ice encounter frequency. Thus, a sensitivity analysis is done by running four different scenarios with different inputs for this parameter.

- The second stage focuses on the 100 × 100 km box at Block #7424 and simulates the drift of many icebergs in order to calculate the probability of glacial ice hitting a structure of a certain size (given that the iceberg has entered the box at Block #7424). Combining the information about the mean number of icebergs that enters the box annually and probability of an iceberg hitting a structure given that it has entered the 100 × 100 km box, the result is derived as an annual encounter frequency.

In order to establish a conservative approach, we have estimated the extreme number of icebergs created annually at the 5 sources considered. The Atlas of Arctic Icebergs (Abramov and Tunik, 1996) provides extreme numbers of icebergs observed in vicinities of calving locations observed for one year. We take these numbers and assume that the 5 sources will simultaneously yield their maximum number of icebergs each year during the 27-years of simulation (in total 325 icebergs are released annually). For a structure with dimensions of 100 × 100 m, the resulting annual encounter frequency based on this conservative scenario is $4.67 \cdot 10^{-3}$ ($2.76 \cdot 10^{-3}$ without growlers). Besides the conservative scenario, we present (based on our experience in the region) our best guesstimate scenario where a total of 200 icebergs is released annually. The resulting annual encounter frequency based on our guesstimate scenario for a 100 × 100 m structure is $2.8 \cdot 10^{-3}$ ($1.75 \cdot 10^{-3}$ without growlers).

In addition to the estimated annual iceberg encounter frequency, the simulations give a resulting geometry of icebergs as they enter the 100 × 100 km box at Block #7424 (length, width, total height), as well as the probability distribution of iceberg drift speeds during the simulations. Table 5.21 presents a summary of the calculation results for the different scenarios. The annual iceberg encounter frequency presented in the table are calculated with the method of Mathiesen et al. (1992).

Table 5.21. Summary of the calculation results for the different scenarios.

	Best Guesstimate Scenario	Less Conservative Estimate Scenario	Conservative Estimate Scenario	Overly Conservative Estimate Scenario
Results including growlers				
Total number of icebergs entering Block #7424 in 27 years	170	120	264	513
Number of icebergs per year entering Block #7424	6.3	4.44	9.78	19
Yearly probability of iceberg occurrence at Block #7424	74.07 %	70.37 %	85.19 %	85.19 %
Results excluding growlers				
Total number of icebergs entering Block #7424 in 27 years	99	66	156	326
Number of icebergs per year entering Block #7424	3.67	2.44	5.78	12.07
Yearly probability of iceberg occurrence at Block #7424	70.37 %	59.26 %	81.48 %	81.48 %
Origin of the icebergs entered Block #7424 (excluding growlers) [% of the total number]				
Nordaustfonna	8.08	4.55	13.46	7.67
Edgeøya	6.06	12.12	14.74	14.42

Franz Josef Land (Western side)	56.57	65.15	51.28	60.12
Franz Josef Land (Eastern side)	26.26	10.61	13.46	12.27
Novaya Zemlya	3.03	7.58	7.05	5.52
Annual iceberg encounter frequency at Block #7424 (including growlers)				
Annual iceberg encounter frequency for structure of 100 × 100 m	$2.8 \cdot 10^{-3}$	$2.11 \cdot 10^{-3}$	$4.67 \cdot 10^{-3}$	$9.06 \cdot 10^{-3}$
Annual iceberg encounter frequency for structure of 200 × 200 m	$1.42 \cdot 10^{-2}$	$1.07 \cdot 10^{-2}$	$2.35 \cdot 10^{-2}$	$4.56 \cdot 10^{-2}$
Annual iceberg encounter frequency for structure of 1000 × 1000 m	$2.91 \cdot 10^{-2}$	$2.14 \cdot 10^{-2}$	$4.70 \cdot 10^{-2}$	$9.20 \cdot 10^{-2}$
Annual iceberg encounter frequency at Block #7424 (excluding growlers)				
Annual iceberg encounter frequency for structure of 100 × 100 m	$1.75 \cdot 10^{-3}$	$1.64 \cdot 10^{-3}$	$2.76 \cdot 10^{-3}$	$5.77 \cdot 10^{-3}$
Annual iceberg encounter frequency for structure of 200 × 200 m	$8.86 \cdot 10^{-3}$	$5.88 \cdot 10^{-3}$	$1.39 \cdot 10^{-2}$	$2.91 \cdot 10^{-2}$
Annual iceberg encounter frequency for structure of 1000 × 1000 m	$1.78 \cdot 10^{-2}$	$1.18 \cdot 10^{-2}$	$2.80 \cdot 10^{-2}$	$5.85 \cdot 10^{-2}$

5.4 Iceberg observations from remote sensing data

Because of global warming and the resulting changes in the cryosphere, the number of icebergs in the Barents Sea is expected to increase in the years to come. These icebergs pose a threat to navigation and offshore installations through direct collision or by scouring the ocean floor by grounding. As per Abramov (1996), most icebergs in Barents Sea are small; below 50 m in length. However, a minority of icebergs on a scale of 100 m or more are also found in the region. These icebergs calve from the glaciers at Franz Josef Land, Svalbard, and Novaya Zemlya (Spring, 1994). Figure 5.5 shows the major iceberg sources in Barents Sea. An accurate estimate of the number and size of the icebergs produced is important for operations in the Barents Sea.

Oceanographic field campaigns and ice reconnaissance flights have been used previously for the detection of icebergs. However, with the advancement of remote sensing techniques it is becoming more common and convenient to detect icebergs using satellite imagery. One of the most widely used remote sensing techniques is synthetic aperture radar (SAR), which is being utilized for European ENVISAT and Canadian RADARSAT, and it is capable of providing high resolution data during day or night without weather constraints. SAR data with a pixel size of 20m is capable of capturing most larger bergs. Multispectral Imagery sensors are also frequently used for the iceberg detection. The sensors measure reflected energy from the icebergs within several bands of the electromagnetic spectrum. Sentinel-2, Landsat and Spot are examples of satellites using MSI. Another commonly used remote sensing technique is satellite radar altimetry. It provides information such as sea surface and marine gravity anomalies. ERS-1, Sentinel-3 and Saral are based on altimetry principles.

A lot of work has been done on remote sensing of ice using radio frequency waves. In areas such as the Barents Sea it is challenging to detect icebergs in harsh environments using radio frequency waves, as the majority of the icebergs is small, and these are not clearly visible on marine radars. In addition, high waves cause signal distortion. Heavy sea states appear as bright spots on the radar image which makes it difficult to distinguish the iceberg from the waves. A viable option is to use sensors utilizing shorter wavelength waves (micrometre region of electromagnetic spectrum) (Kim et al., 2015). Near infrared

(NIR), shortwave infrared (SWIR) and thermal infrared can be used for the smaller icebergs' detection. A downside of these shorter wavelengths is a limited ability to penetrate cloud cover. Sentinel-2 is an example of a satellite assembly in which an incoming light beam is split into visible, NIR and SWIR bands with the help of stripe filters in the detector assembly. Sentinel-2 comprises of twin polar-orbiting satellites which produce data containing 13 spectral bands; four bands at 10 m, six at 20 m and three at 60 m resolution. The coverage of Sentinel 2 is between latitudes 56° south and 84° north. Therefore sentinel-2 covers the areas of interest for this study.

Sentinel-2 data of clear days with daylight is selected and downloaded for the assessment of iceberg production rates and size distributions. Data is assessed for the year 2018 and the locations indicated in Figure 5.5. The downloaded data is processed in SNAP to extract the imagery with 10m resolution and only for the regions close to glaciers. The processed *.tiff* files are further utilized in QGIS for the identification of icebergs larger than 50m (5pixels) and information regarding iceberg area, length and width are obtained as output. For all the locations, sentinel-2 data is downloaded for a period from May to November. In order to avoid the recounting of a same iceberg, images that are at least one week apart are used for further processing. In addition, it was manually checked if the same iceberg could be identified twice and if so, it was taken out of the data, so it only occurs ones. The results obtained are discussed below for each location.

5.4.1 Franz Josef Land West

Figure 5.39 and Figure 5.40 show the dates in 2018 for which data is collected and used for the image processing. In total 8 images where available, out of which only 3 could be processed for the analysis. From the images, a total of 258 icebergs are observed in 2018. The largest iceberg length observed was 954 m, recorded on the 14th of September 2018. Its corresponding width is roughly 250 m. A distribution of length, width and area of the icebergs is shown in the Figure 5.41 in the form of a histogram. Mean length and width of the icebergs at this location are 101.5m and 62.5m respectively.

Figure 5.39 Dates of the collected Sentinel-2 images for Franz Josef Land West.

Figure 5.40 Dates of the Sentinel-2 images that were used to produce the results for Franz Josef Land West.

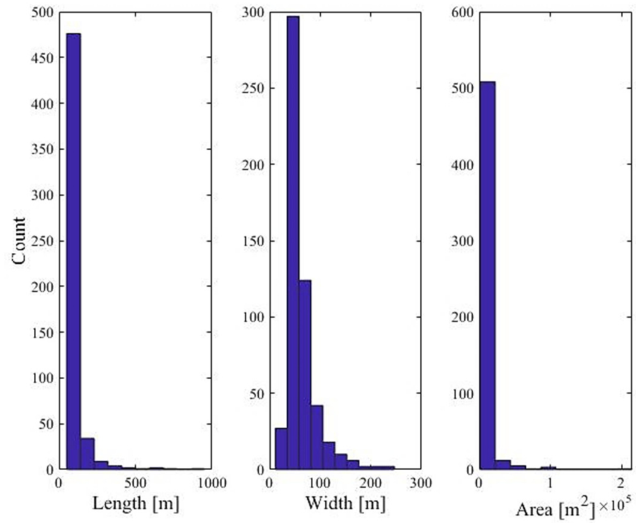

Figure 5.41 Histograms of the iceberg length, width and area for Franz Josef Land West.

5.4.2 Franz Josef Land East

In year 2018, total 10 images were downloaded for Franz Josef Land East and out of these images 5 were used for iceberg counting. The capture dates of the used images is shown in Figure 5.42 and Figure 5.43. The total number of icebergs observed are 1088. The icebergs have a mean length and width of 109 m and 73 m, respectively. The largest iceberg is observed on 19-07-2018, with a length of 972 m and width of 45.3 m. A distribution for length, width and area of icebergs is presented in Figure 5.44.

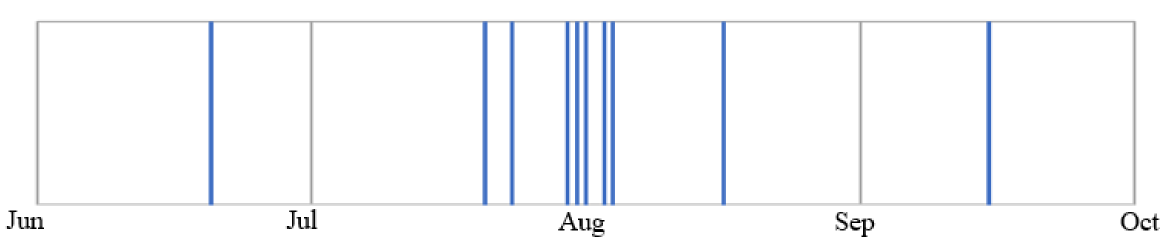

Figure 5.42 Dates of the collected Sentinel-2 images for Franz Josef Land East.

Figure 5.43 Dates of the Sentinel-2 images that were used to produce the results for Franz Josef Land East.

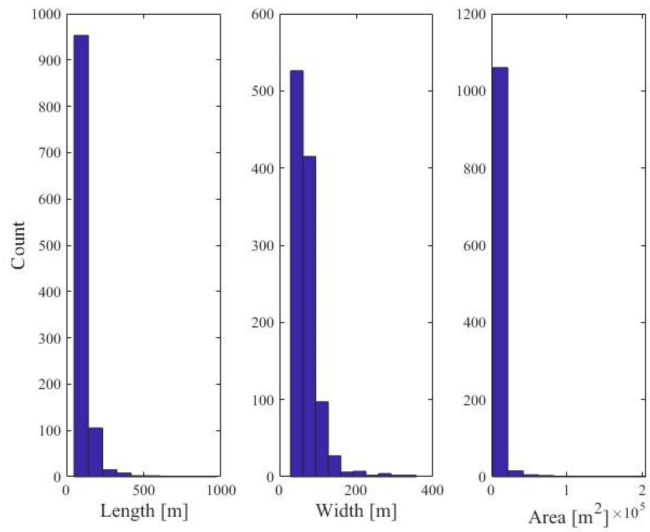

Figure 5.44 Histograms of the iceberg length, width and area for Franz Josef Land East.

5.4.3 Nordaustfonna

For Nordaustonna, Sentinel-2 images of 14 days are downloaded and 8 images are further analysed. In total, 615 icebergs of length larger than 50m are observed in the area. The average length of icebergs is around 58m and the average width is 38m. The distribution of length, width and area is shown in Figure 5.47. The largest iceberg with a length of 150.5m is observed in the mid-September.

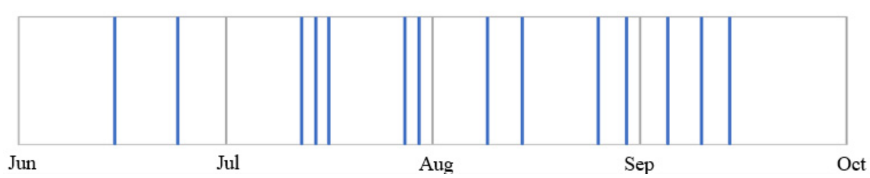

Figure 5.45 Dates of the collected Sentinel-2 images for Nordaustfonna.

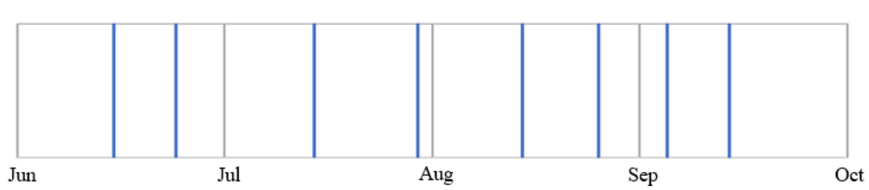

Figure 5.46 Dates of the Sentinel-2 images that were used to produce the results for Nordaustfonna.

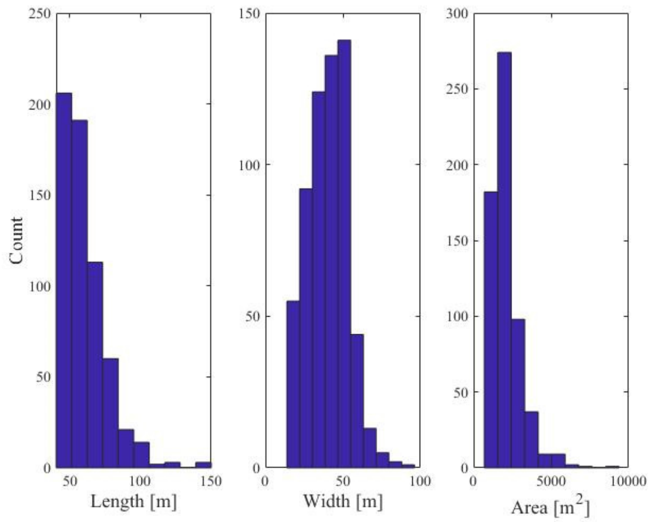

Figure 5.47 Histograms of the iceberg length, width and area for Nordaustfonna.

5.4.4 Novaya Zemlaya

There are three main locations at Novaya Zemlaya which are associated with the production of icebergs. These locations are indicated as Loc-1, Loc-2 and Loc-3 in the Figure 5.48. For all the locations, Sentinel data of 9 dates was downloaded, and after investigation images of 6 dates are used to obtain information about the number of icebergs at Novaya Zemlaya. The dates on which the selected images were captured are shown in Figure 5.49 and Figure 5.50.

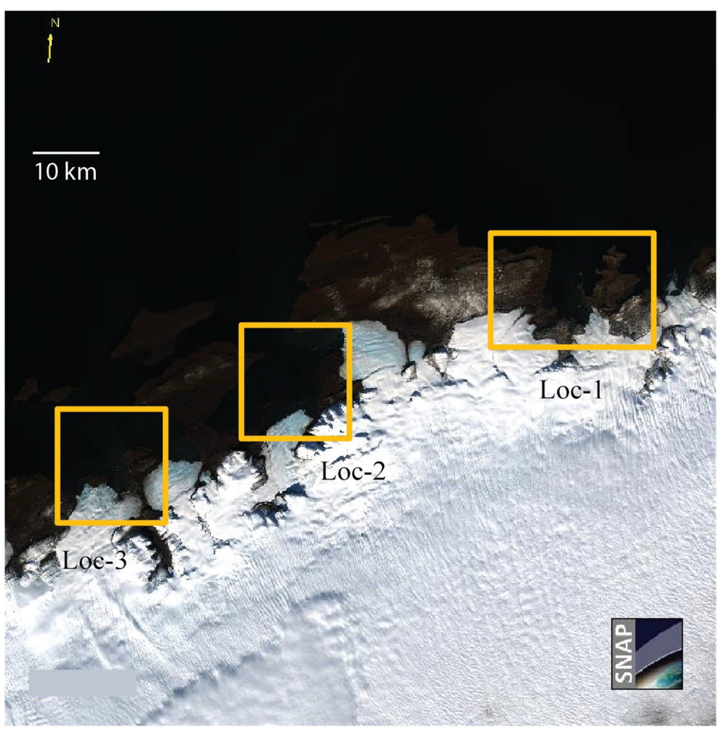

Figure 5.48 Sources of Icebergs in Novaya Zemlaya.

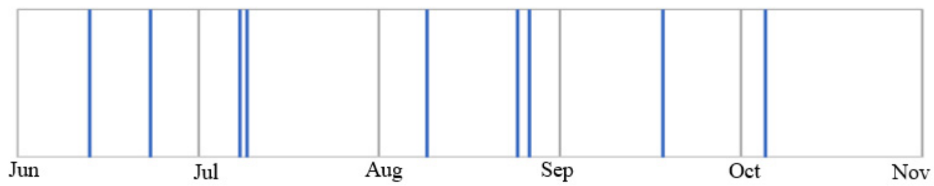

Figure 5.49 Dates of the collected Sentinel-2 images for Novaya Zemlaya.

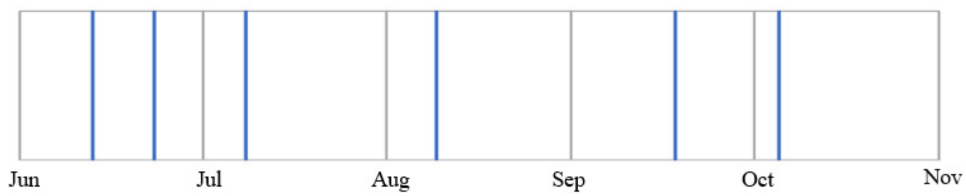

Figure 5.50 Dates of the Sentinel-2 images that were used to produce the results for Novaya Zemlaya.

Distributions for length, width and area of iceberg for the three locations are presented in Figure 5.51, Figure 5.52 and Figure 5.53. The mean length of icebergs produced at Loc-1, Loc-2 and Loc-3 is 62 m, 57.5 m and 58 m, respectively. The mean width of icebergs is around 40 m for all three locations. The largest iceberg is observed at Loc-1 on 04-10-2018 and it has a length of 210m. A total of 574 icebergs were observed in Novaya Zemlaya out of which 201 are found at Loc-1, 239 at Loc-2 and 134 at Loc-3. The mean value of iceberg area is around 2000m^2 for all locations.

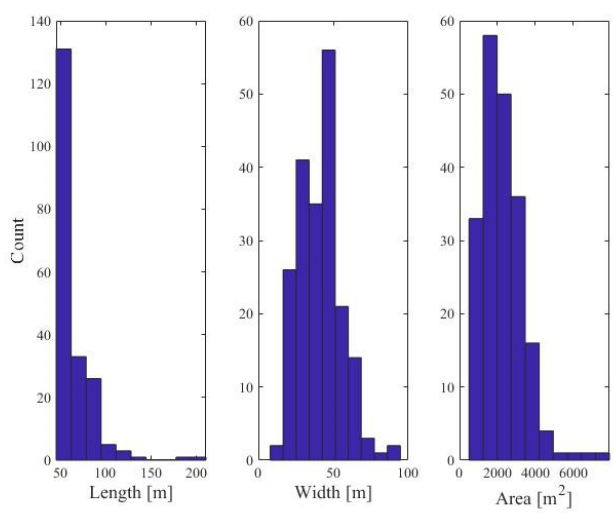

Figure 5.51 Histograms of the iceberg length, width and area for Novaya Zemalya (Loc-1).

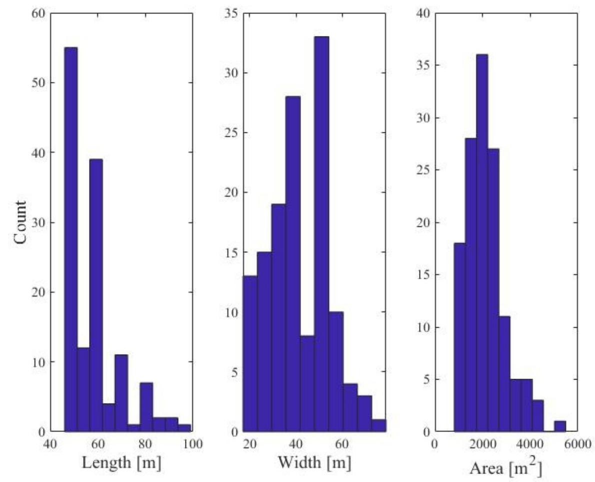

Figure 5.52 Histograms of the iceberg length, width and area for Novaya Zemalya (Loc-2).

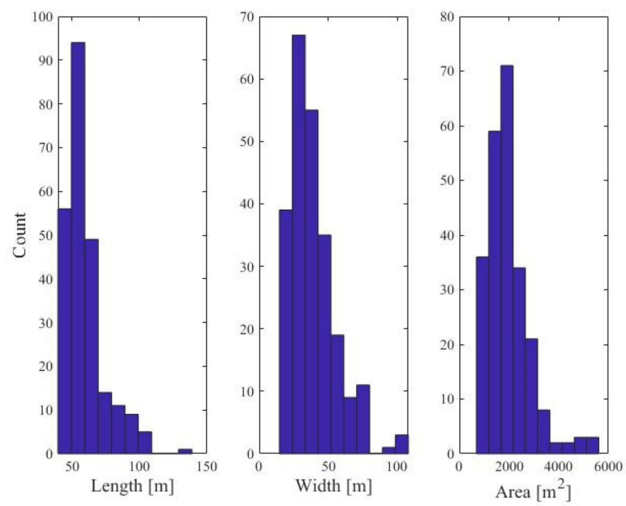

Figure 5.53 Histograms of the iceberg length, width and area for Novaya Zemalya (Loc-3).

5.4.5 Edgeøya (Stonebreen)

The most satellite images available for Edgeøya;15 images. Out of these images, 8 are used based on visibility and recounting criteria for further processing. Figure 5.54 and Figure 5.55 show the distribution of dates. A total 165 icebergs are observed with mean length and mean width of 66 m and 41 m, respectively. Histograms showing the distribution of length, width and areas of observed icebergs is presented in Figure 5.56. The largest iceberg, with a length of 416 m, is observed on 07-06-2018.

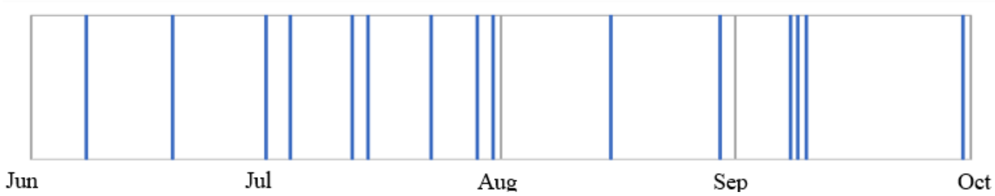

Figure 5.54 Dates of the collected Sentinel-2 images for Edgeøya.

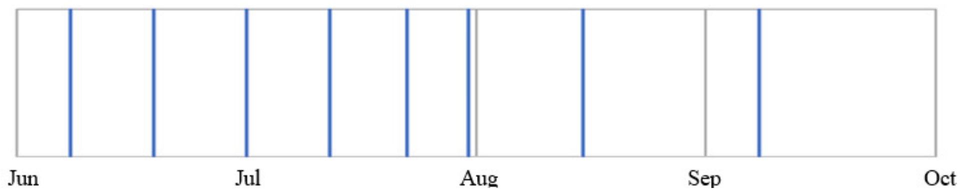

Figure 5.55 Dates of the Sentinel-2 images that were used to produce the results for Edgeøya.

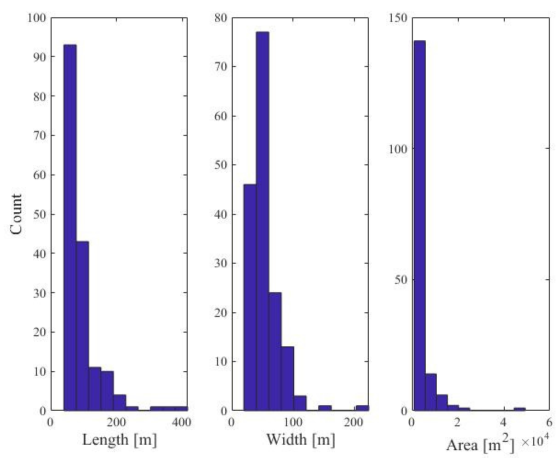

Figure 5.56 Histograms of the iceberg length, width and area for Edgeøya.

5.4.6 Comparison with existing data

From all the sources of icebergs in Barents Sea, a total 3396 icebergs are observed and more than 60% of these are calved from the glaciers in Franz Josef Land. The maximum length and width of the observed icebergs are 990 m and 356 m, respectively, with the area being as high as 0.22 km^2. A representative distribution of length, width and areas of all icebergs is presented in Figure 5.57. The mean value of length and width are 86 m and 56 m, respectively, with a mean of area of around 4800 m^2.

The produced data is further analysed to develop a relation between iceberg length and width, see Figure 5.58. A trendline of the data is plotted which gives the following relation;

$$W_i = 1.6103.L_i^{\,0.7946}$$

where,

Wi = width of Iceberg in [m]

Li = length of Iceberg in [m]

The relation is compared with the empirical relationship for the calculation of iceberg width from Dezecot and Eik (2015);

$$W_i = 0.7 \cdot L_i \cdot exp(-0.00062 \cdot L_i)$$

The formula generated from the data gives the results which are within 5% difference of empirical formula and this difference reduces with increasing iceberg length.

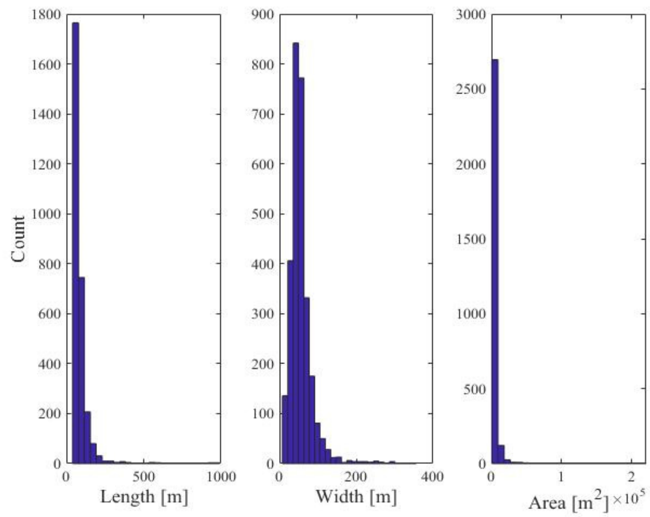

Figure 5.57 Histograms of the iceberg length, width and area for Barents Sea for year 2018.

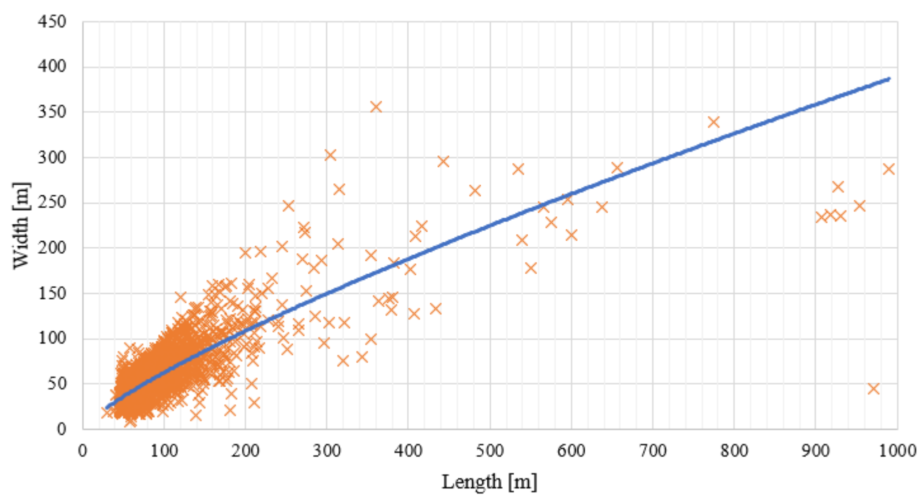

Figure 5.58 Graph showing relationship of iceberg length and width for Barents Sea for year 2018.

Figure 5.59 shows the power spectral density (PDF) of the iceberg length obtained from the satellite images in comparison to the PDF of the Weibull distribution fitted to the IDAP data. The PDF obtained by image processing is more skewed to the left, indicating a lower mean iceberg length.

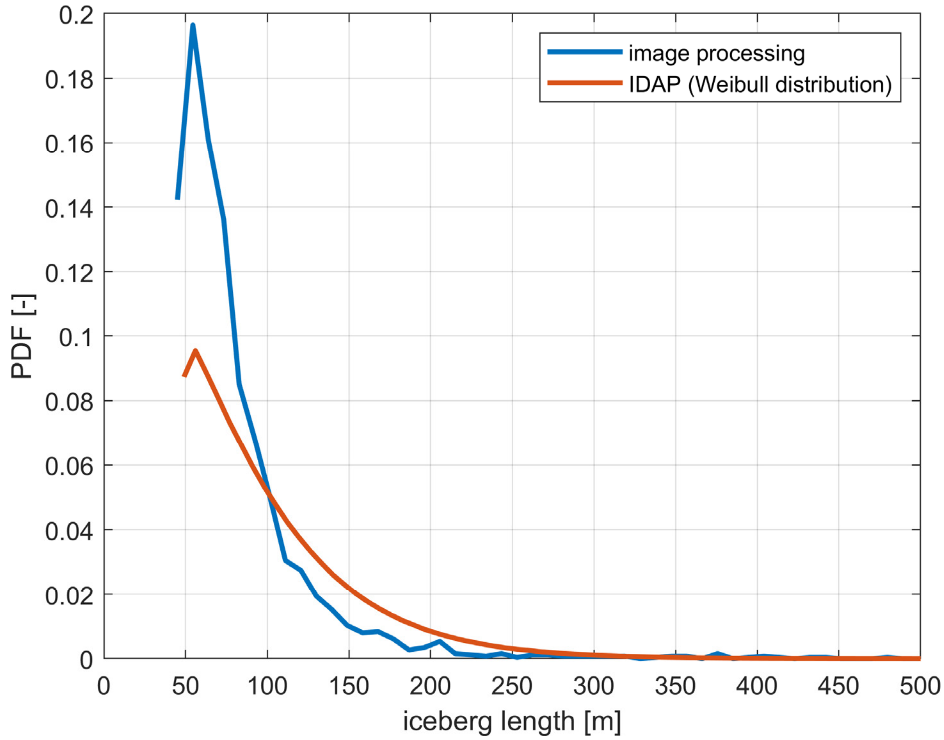

Figure 5.59 Power spectral density of the iceberg lengths obtained from satellite imagery and the iceberg lengths given by the Weibull distribution fitted to the IDAP data.

A possible reason for the difference in distributions is that the iceberg lengths analysed in this study were measured at the iceberg sources, while the IDAP data includes a broader measurement area. The smaller bergs observed at the sources may melt before drifting far into the open sea, thereby changing the iceberg length distribution.

5.4.7 Summary

Remote sensing can provide a valuable additional data source for more detailed estimates of iceberg production rates, shapes and size distribution. In this section, optical images from the Sentinel 2 satellite assembly were used to obtain an estimate of iceberg sizes, shapes and numbers at the potential iceberg sources for the Barents Sea. The data obtained on iceberg size and iceberg length-to-width ratio is in good agreement with the empirical relations used for the global simulation model input in Section 5.2.1.3. The number of images analysed is not enough to obtain a reliable estimate of the total number of icebergs produced by each glacier. The number of images analysed is limited because the image analysis procedure used mainly relies on manual image processing. If the iceberg detection and classification procedure can be automated, then a larger number of satellite images could be analysed, and the remote sensing data could be used in conjunction with existing data sources to get a more reliable estimate of the iceberg production rates of the iceberg sources for the Barents Sea.

5.5 Discussion on the impact of climate change

The Arctic environment is changing dramatically due to climate change and it is important to consider the effects of climate change on the predicted annual probabilities of iceberg encounters in the Barents Sea. In this section, we will present future predictions of the meteorological conditions used as input to our iceberg drift model. Due to time constraints, we were not able to run new simulations that include climate change effects. Therefore, this section provides only a discussion on the possible impact of climate change on our results.

The global assessment of climate change is well documented by the *International Panel on Climate Change* (IPCC, 2013). Global warming due to climate change is not homogeneous over the Earth. The Arctic region is warming approximately two to three times faster than the global average due to polar amplification. This amplification is expected to continue in a future warmer climate. The changing Arctic climate is for instance shown by increased temperatures, loss of summer sea ice, impacts on local ecosystems and earlier snow melt. To predict future changes, *the Coupled Model Intercomparison Project Phase 5* (CMIP5) aims to improve knowledge about climate change by running Earth System Models. This project consists of approximately 20 climate modelling groups from around the world. The models are all forced by the same four emission scenarios, which are defined as *Representative Concentration Pathway* (RCP) trajectories. The four different scenarios, namely RCP2.6, RCP4.5, RCP6.0 and RCP8.5, are labelled after their radiative forcings (i.e., 2.6, 4.5, 6.0, and 8.5 W/m^2, respectively). A short description of these scenarios is presented in Table 5.22.

Table 5.22. Short description of the four different forcing scenarios

Scenario	Short description
RCP2.6	The peak emissions occur between 2010 and 2020, which will then decline substantially.
RCP4.5	The peak emissions occur at 2040, then decline
RCP6.0	The peak emissions occur at 2080, then decline
RCP8.5	Emissions continue to rise through the 21st century

To investigate the effect of future climate change on the annual encounter frequency of icebergs in the Barents Sea, we require future predictions of the meteorological conditions. In Table 5.23 we present all the meteorological input parameters used in our global model together with the proposed new implementations. We propose to alter multiple input parameters while keeping the currents, wind speed and sea ice drift the same. The main reason for this is because is it not known how these parameters will change in the future.

Table 5.23. The input parameters to the iceberg drift model together with the suggested implementation for future climate change impact.

Input parameter:	Source	Implementation
Ocean surface temperature	CMIP5	New values from CMIP5 model
Sea ice concentration	CMIP5	New values from CMIP5 model
Sea ice thickness	CMIP5	New values from CMIP5 model
Waves	Paper	Increase significant wave height +10%
Currents	-	Not changed
Sea ice drift	-	Not changed
10 m wind speed and direction	-	Not changed

Most of the data are taken from CMIP5 data, which can freely be downloaded from:

https://cds.climate.copernicus.eu/cdsapp#!/dataset/projections-cmip5-monthly-single levels?tab=overview.

In the remainder of this section, we will present and discuss the predicted change of the proposed updated input parameters, for the RCP4.5 climate scenario. In addition, we discuss what impacts this most likely will have on our results from the global model.

5.5.1.1 Ocean surface temperature

The projected ocean surface temperature is taken from the NorESM1-M model, which is part of CMIP5, and is presented in Figure 5.60 for the entire Barents Sea. The map shows the difference between the average values between the years 2073 to 2100 and the mean of the years 1991 to 2017. In addition, Figure 5.61 presents timeseries from one point in the Barents Sea up to the year 2100. It is evident that the ocean surface temperature is expected to increase. For the shown RCP4.5 scenario, the increase can be up to 5 °C. An increase in ocean surface temperature will increase the melting rate of the icebergs, causing them to deteriorate faster, leading to less icebergs drifting south of the Barents Sea.

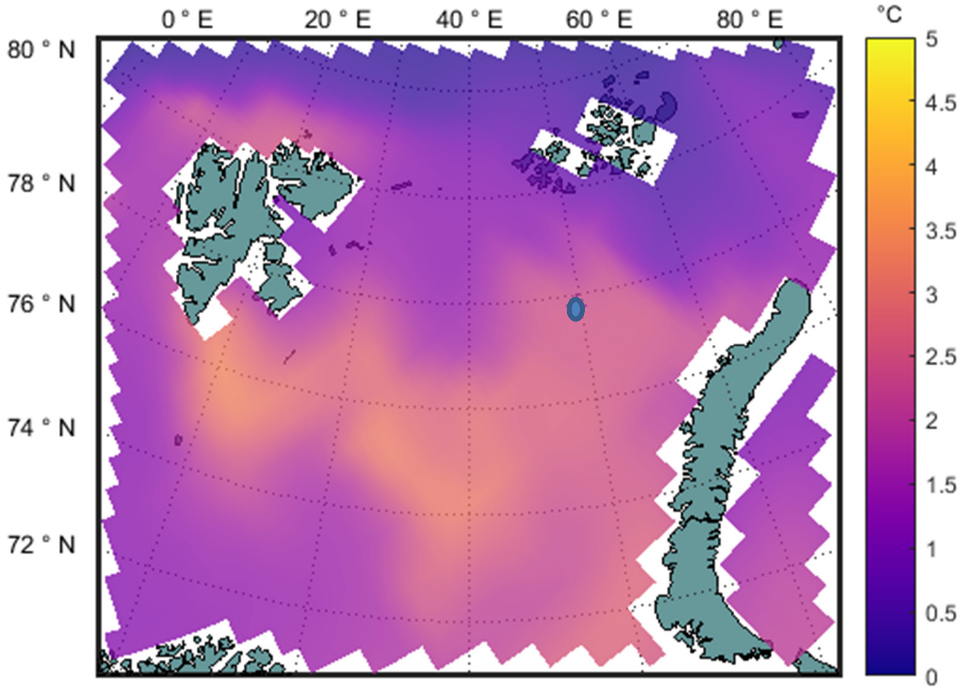

Figure 5.60. The difference in ocean surface temperature computed as the average of the years 2073 to 2100 minus the average of the years 1991 to 2017 (for RCP4.5).

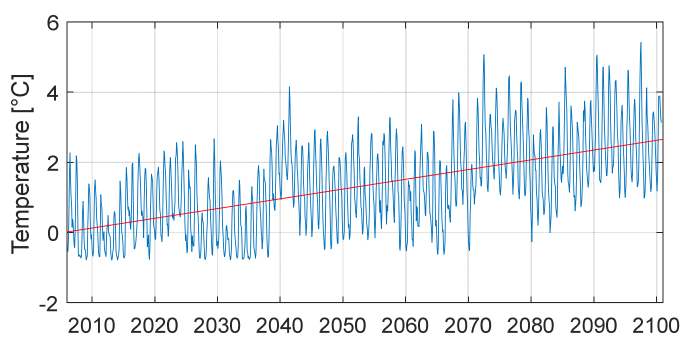

Figure 5.61. For RCP4.5: Ocean surface temperature up to the year 2100 (in blue line). The red line shows a linear fit to the data. The location where this data is extracted can be seen in Figure 5.60 (blue circle).

5.5.1.2 Sea ice thickness and concentration

Sea ice in the Barents Sea has decreased dramatically during the last few decades. This trend is expected to continue as Arctic temperature will continue to rise. In Figure 5.62 we present the predicted sea ice edge (defined as the 15% ice concentration contour line) from the NorESM1-M model from 2006 until 2100. From this figure a clear retreat of the sea ice cover is observed. The study of Onarheim and Årthun (2017) predicted an ice-free Barents Sea within the time period 2061-2088. The receding ice cover will most likely cause icebergs to come less far south. When icebergs are locked in within the sea ice, they experience hardly any deterioration. With less sea ice, icebergs will drift more in open water, causing it to deteriorate faster. Moreover, the receding ice cover leads to a longer fetch, causing a more severe wave climate; see the paragraph below regarding the wave climate.

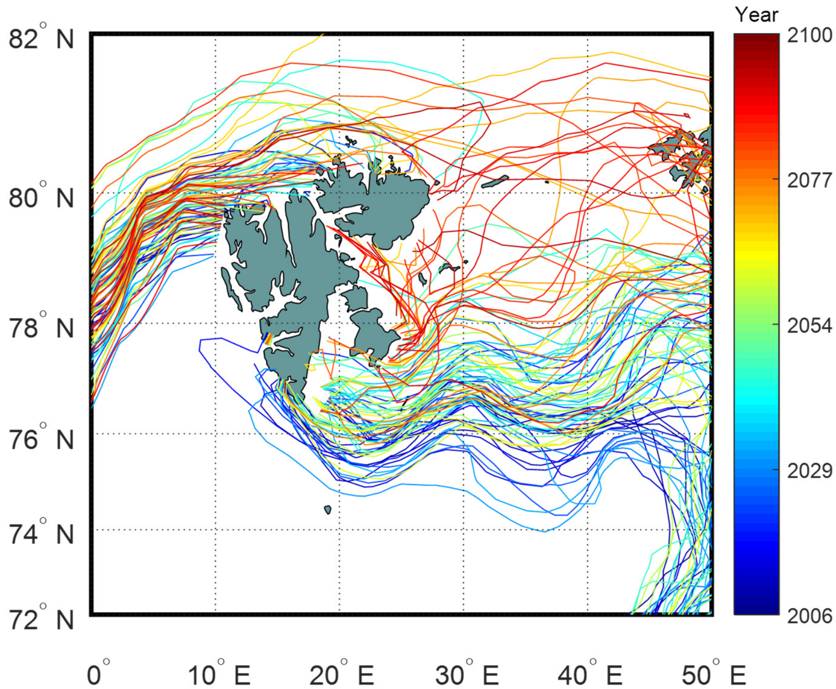

Figure 5.62 For RCP4.5: Predicted yearly maximum sea ice edge from 2006 till 2100 from the NorESM1-M model, which is part of CMIP5. The contour line is defined as the 15% ice concentration. The colour code of the contour lines presents the year of the prediction.

5.5.1.3 Waves

The projected wave climate in the Northeast Atlantic for the 21st century was studied by Aarnes et al. (2017). They fed the wave model WAM with the future projections from the CMIP5 models considering the RCP4.5 and RCP8.5 emission scenarios. Their main results are presented in Figure 5.63. The general trend is that a decreasing significant wave height is expected by the end of the 21st century. However, the exception to this is the Barents Sea. The receding ice cover will give rise to a longer fetch and hence, higher waves. The significant wave height is expected to increase by approximately 10% in the Barents Sea. A more severe wave climate will have two effects on our iceberg drift model. First, the iceberg may drift further as the mean wave drift force is increased. On the other hand, higher waves will increase the amount of wave erosion, resulting in a faster deterioration of the icebergs.

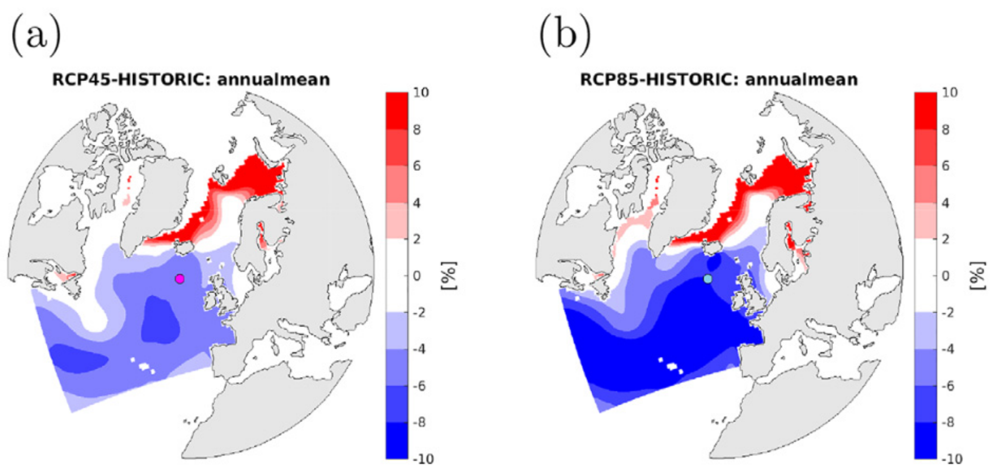

Figure 5.63 The change in significant wave height between the periods 2071-2100 and 1971-2000 given as a percentage relative to the historical period, taken from Aarnes et al. (2017).

5.6 Summary of Task #2

Task #2 of this projects presents an estimation method and an estimate of the probability of iceberg encounters in the Barents Sea. First, the available data sources are discussed. The main sources of iceberg data in the Barents Sea are The Atlas of Arctic Icebergs (Abramov and Tunik, 1996) and the ICEBASE and IDAP iceberg mapping programs. The location and release rate of the main iceberg sources for the Barents Sea are identified as Frans Josef Land West, Frans Josef Land East, Nordaustfonna (Svalbard), Edgeøya (Svalbard) and Novaya Zemlaya. Data on iceberg release rates, shape and size distributions are used as input to a global iceberg drift model covering the entire Barents Sea. The drift model is used to simulate iceberg drift over a 27-year period. The results from the drift model are presented in the form of contour maps showing the iceberg probability and the average number of icebergs in 100x100 km blocks. In agreement with the Petroleum Safety Authority, Block #7424 is chosen as the location of a more detailed analysis of iceberg encounter frequency. The global iceberg drift model predicts that there are on average 9.8 icebergs entering a 100 x 100 km box around the center of Block #7424, located at 74° 14' 31.05" N 24° 30' 18.62" E. The model predicts that icebergs will be present in the box around Block #7424 in 85% of the years. A local model is used to estimate the annual iceberg encounter probability in regions ranging from 100x100 m to 1000x1000 m in size. Three different analysis methods were used. The annual encounter frequency depends on the region size and the analysis method used and ranges from $1.75 \cdot 10^{-3}$ to $9.2 \cdot 10^{-2}$. Finally, the possibility of using remote sensing data as an additional data source of iceberg shape, size and release rate is discussed. The use of satellite images in the analysis of iceberg size and shape distributions is demonstrated. In addition, the possible impact of climate change on the quantity of icebergs in the Barents Sea is discussed.

6 Task #3: Impact Analysis

The purpose of Task 3 is to understand the nature of glacial ice and structure interactions at Accidental Limit State (ALS) and to evaluate the structural response of a column and a pontoon of a semi-submersible platform under glacial ice impacts. In particular, we are interested in the influence of local geometries of the glacial ice features. To address this issue, three different methods were developed/utilised to analyse the shared-energy dissipation between a glacial ice feature and the structure. These methods are:

- Method #1: Integrated analysis
- Method #2: Weakly-coupled analysis
- Method #3: Fully-coupled analysis

The methods are based on different simplifications of the problem. The integrated and weakly-coupled analyses' (Methods #1 and #2) primary application regimes are for ice features that are relatively blunt; and they are very computationally effective. The fully-coupled analysis (Method #3) is capable of simulating ice features of arbitrary geometry. The method updates the ice feature's geometric changes during its crushing process and calculates the ice crushing influences on structural deformation in a fully-coupled manner. In this chapter, we first use Methods #1 and #2 to test a range of local geometry that might be of interest for more detailed simulations. Later, we adopt the fully-coupled analysis and simulated 6 relevant local geometries to identify the critical geometry that leads to the maximum deformation/damage in the structure. Given the identified critical geometry, we selected two blunt geometries (including the critical geometry) and applied both the integrated and weakly-coupled analysis extensively in simulating around 1800 impact locations for each glacial ice geometry. Based on these simulations, the weakly-coupled analysis produces the 'deformation/damage map' around the structure illustrating sensitive areas. In addition, with the identified critical ice geometry, the fully couple method was utilised to produce the Force – Deformation (F-D) curves on 7 representative locations on the column and 4 representative locations on the pontoon. Thus, a comprehensive damage assessment, i.e., the overall structural deformation/damage around the structure produced from 1800 impacts; and 11 detailed representative F-D curves, is presented in this chapter.

6.1 Methods overview

It is believed that the shared energy methodology shall be less conservative compared to other design methodologies (e.g., rigid ice impacting a deformable structure in ST5). In the 'shared energy regime', different methods may be used/developed depending on the required accuracy of the results and desired efficiency of the model. In this report and as stated above, we are investigating three of such methods. The major differences of these methods can be visualised by the sketch in Figure 6.1.

In the integrated analysis method, the force-deformation/crushing curves for the ice and structure are not interacting with each other. Each of the curves is obtained by assuming the other body to be rigid and it represents a limiting scenario as shown in Figure 6.1a. Next, the two force-deformation curves are integrated to determine in which direction the energy dissipation flows. For example, given the same contact force level, i.e., (same F value), the area beneath the force – ice crushing curve ($F-\delta$ curve) represents the energy dissipation by crushing the glacial ice feature, whereas the area below the force – displacement curve ($F-d$ curve[5]) represents the energy dissipated in the structure. The steepness of these two curves represents how strong each body is at a given force level. The steeper (or stronger) body dissipates less energy and vice versa. This method is computationally most efficient as the two limiting calculations do not interfere with each other, but mutual interaction is disregarded.

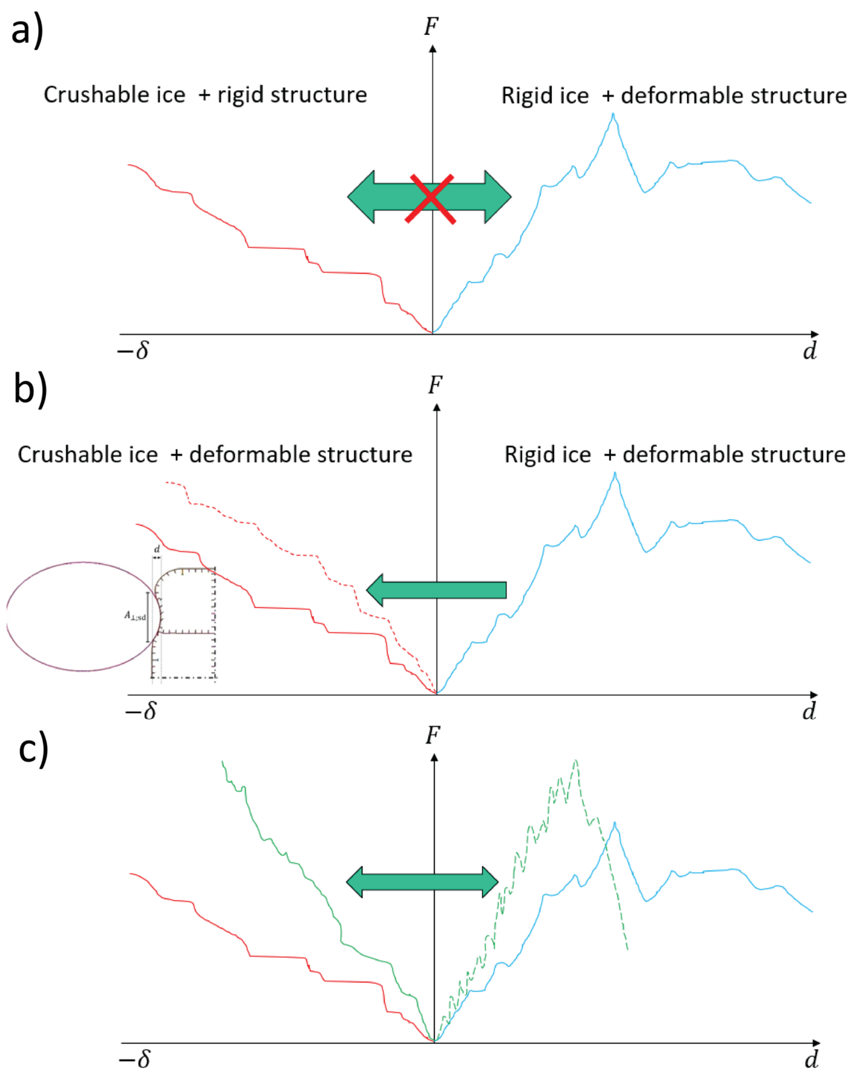

Figure 6.1 A general illustration of differences among the three different methods.

Figure 6.1b is the so-called weakly-coupled method. In contrast to the integrated approach, the development of the ice force - crushing curve ($F-\delta$ curve) is in accordance with the structural deformation. i.e. it is influenced by the structure deformation ($F-d$) curve. As depicted in the deformation plot in Figure 6.1b, when the structure deforms, a larger contact area is formed, and the force needed to crush the ice increases. The consequence of this is that the true $F-\delta$ curve (red dashed line) is lifted (becomes stronger) compared to the integrated approach (red solid curve). This method represents an improvement compared to the integrated approach and has a wider range of applicability

[5] In later description, the symbol ' $F-d$ ' curve means the same as F-D curve in the sentence.

as long as the local geometry of the ice feature is not changing significantly in the course of crushing. The method is only slightly more computationally expensive compared to the integrated analysis as the coupling is only one-directional.

Figure 6.1c demonstrates the fully-coupled approach, in which, the ice crushing and structural deformation processes are mutually influencing each other. This method can, in principle, handle all types of complicated scenarios irrespective of the local ice geometry, crushing depth, impact duration etc., as long as the ice material model and structural material models calibrated satisfactorily. It is however, computationally the most expensive method among the three.

6.2 Model preparation

The target structural elements studied herein are the column and the pontoon of a semi-submersible platform. In this section, finite element models of the column and the pontoon are described including modelling of the steel material. Force-displacement (F-D) curves of the structures subjected to rigid ice impacts on different locations are generated.

6.2.1 Finite Element Modelling of platform's column

The column leg (C10, S10) of the Midgard structure was modelled by Tavakoli and Amdahl (2010) for the assessment of structural strength against supply vessel collisions. Structural drawings of the column are shown in Figure 6.2, Figure 6.3 and Figure 6.4. The column was modelled from EL8125 through EL39000 according to Figure 6.4. Only the front part of one column was modelled. The overall dimensions of the Finite-Element model are 17200 mm × 30875 mm × 6100 mm (w × h × d).

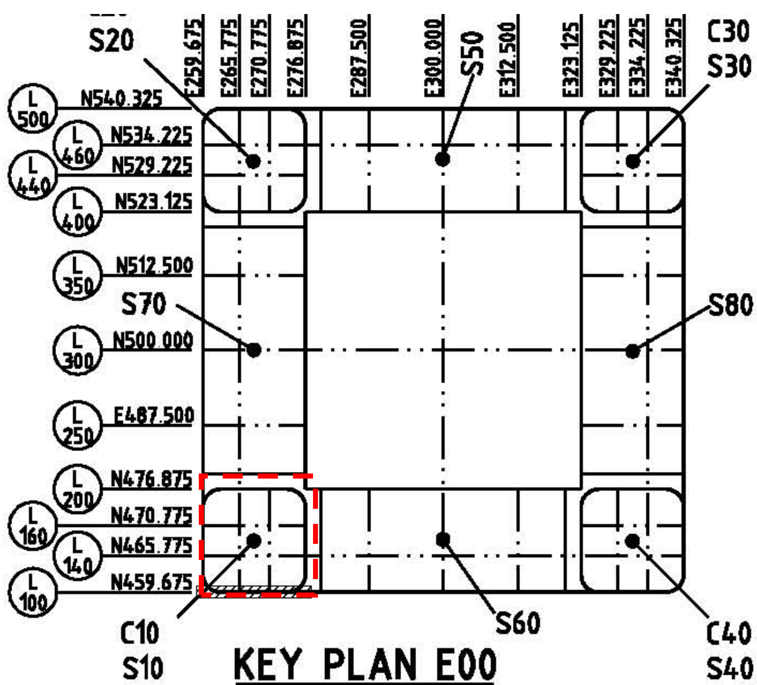

Figure 6.2 The Midgard structure.

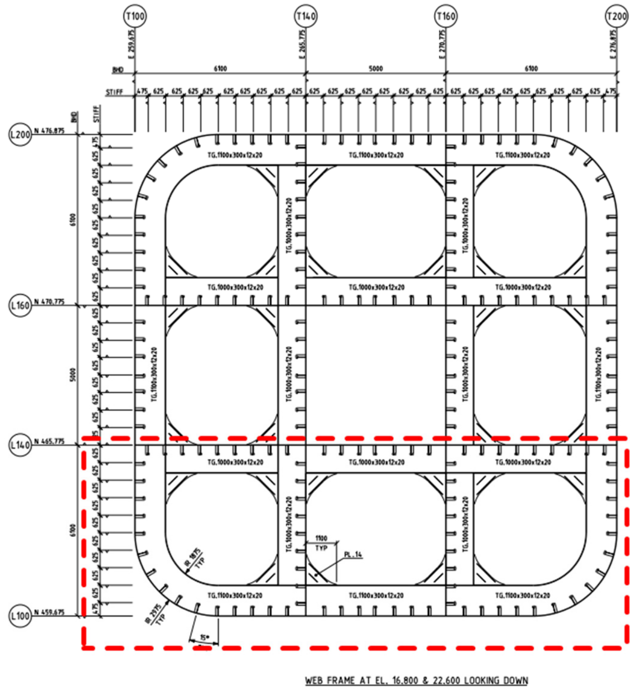

Figure 6.3 The section of the column.

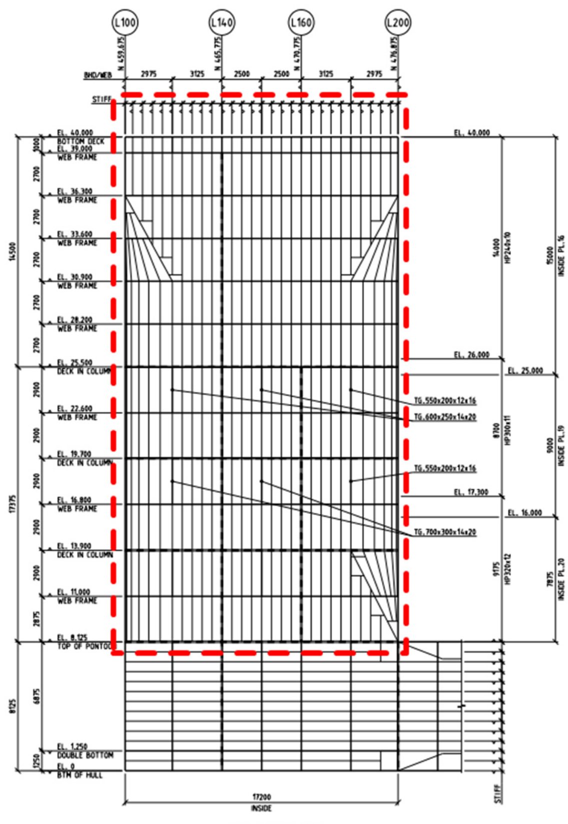

Figure 6.4 The structure column.

The finite element model of the column is shown in Figure 6.5. The column outer shell is in the range of 16-18 mm. The vertical stiffeners used in the column are HP320×12, HP300×11 and HP240×10. These stiffeners were modelled as L-bars with dimensions 320×50×40×12 (mm), 300×50×50×11 (mm) and 240×40×30×10 (mm). This gives nearly the same height, width and the cross-sectional area as the HPs. The column model was meshed using approximately 245,000 4-noded shell elements. The general element size is 120 mm.

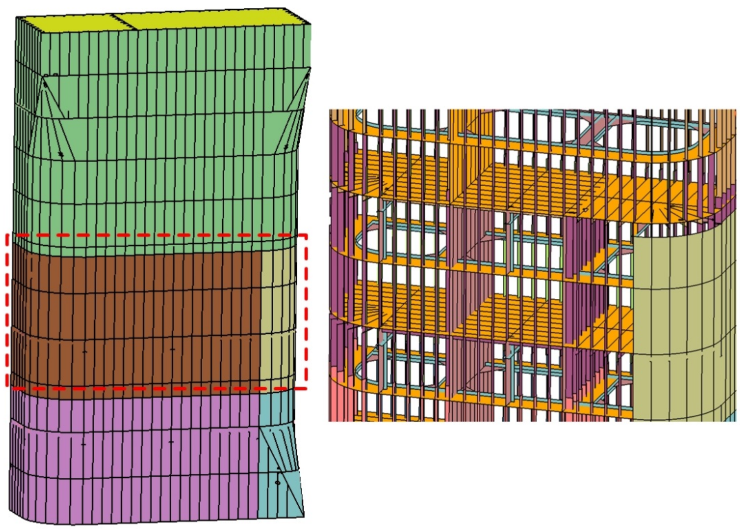

Figure 6.5 The finite element model of the structure column.

6.2.2 Finite Element Modelling of platform's pontoon

The platform's pontoon was modelled according to available drawings. Key dimensions of the pontoon model are given in Table 6.1, and the pontoon finite element model is shown in Figure 6.5. Six frames were modelled along the length direction with a frame spacing of 2.285 m. These frames are strengthened further with brackets. The outer shell is equipped with stiffeners with dimensions of L275×100×11.5×15. The stiffener spacing is 0.66 m.

Table 6.1 Pontoon dimensions for the studied semi-submersible platform.

Pontoon	Dimension
Breadth (m)	10.98
Frame distance (mm)	2285
Fame web height (mm)	1220
Frame web thickness (mm)	17
Frame flange width (mm)	200
Frame flange thickness (mm)	15
Stiffener distance (mm)	660
Stiffener type	L275×100×11.5×15
Shell plating (mm)	17

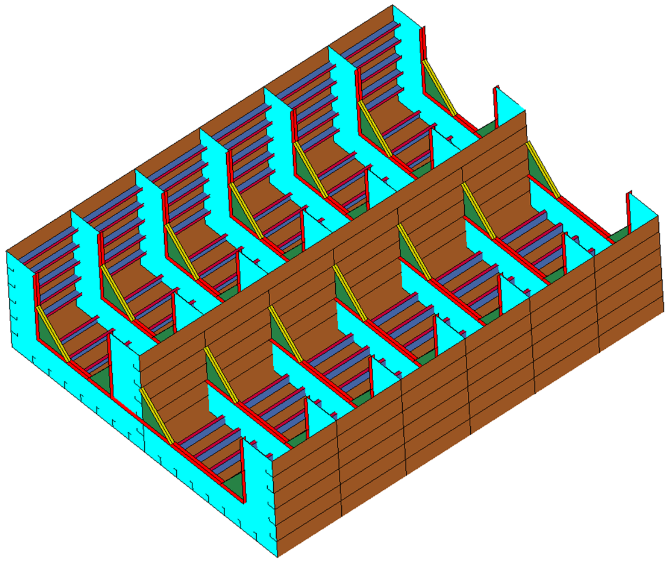

Figure 6.6. Finite element model of the platform pontoon.

6.2.3 Structural material and fracture modelling

Material and fracture modelling are crucial to determine the structural strength in the ice collision analysis. Material fracture will degrade the structural strength to and beyond the point of collapse. Another effect of fracture is leakage and flooding of compartments that may lead to stability problems. It is very challenging to accurately simulate fracture initiation and propagation with large shell elements. The complexity lies in the fact that fracture is a localized phenomenon in the length scale of plate thickness. This is difficult to capture with shell elements with length several times the plate thickness. In addition, fracture depends highly on the stress state, material deformation history and it is sensitive to the mesh size adopted. It is essential to calibrate the material properties correctly in order to capture strain localisations and subsequent fracture.

The probabilistic nature of material properties makes fracture modelling even more complicated (Yu and Amdahl, 2018). Due to the significance of material and fracture modelling and its physical complexity, a proper model is necessary to achieve realistic results.

The power law hardening with a yield plateau is used to model the material. The hardening is described by the yield criterion

$$f=\sigma_{eq}-\sigma_f\left(\varepsilon_{eq}\right)=0 \tag{6-1}$$

where σ_{eq} is the von-Mises equivalent stress. The current flow stress σ_f is a function of the equivalent plastic strain ε_{eq} via the Hollomon-type power law hardening rule:

$$\sigma_f\left(\varepsilon_{eq}\right)=\begin{cases}\sigma_0 & if\ \varepsilon_{eq}\le\varepsilon_{plateau}\\ K\left(\varepsilon_{0,eff}+\varepsilon_{eq}\right)^n & if\ \varepsilon_{eq}>\varepsilon_{plateau}\end{cases} \tag{6-2}$$

where K and n are the hardening parameters and σ_0 is the initial yield stress. To account for the existence of a strain plateau, hardening is delayed until the plastic strain reaches the plateau strain $\varepsilon_{plateau}$. Thus, $\varepsilon_{0,eff}$ is defined by the relation

$$\varepsilon_{0,eff} = \varepsilon_0 - \varepsilon_{plateau} = \left(\frac{\sigma_y}{K}\right)^{1/n} - \varepsilon_{plateau} \tag{6-3}$$

where ε_0 is the strain at initial yield. Any strain rate effect is not taken into account.

The BWH (Bressan-Williams-Hill) instability criterion is used to model fracture in the ice collision simulation. The BWH instability criterion was proposed by Alsos et al. (2008) and combines Hill's local necking model (Hill, 1952) and the Bressan-Williams shear stress criterion (Bressan and Williams, 1983). The BWH criterion considers that fracture occurs at the onset of local necking instability neglecting the post-necking regime, which is conservative. The BWH criterion has been validated to be of good accuracy by comparison with various collision experiments (Storheim et al., 2015, Marinatos and Samuelides, 2013). The BWH criterion can be expressed in the principle stress space as follows:

$$\sigma_1 = \begin{cases} \dfrac{2K}{\sqrt{3}} \dfrac{1+\frac{1}{2}\beta}{\sqrt{\beta^2+\beta+1}} \left(\dfrac{2}{\sqrt{3}} \dfrac{\hat{\varepsilon}_1}{1+\beta} \sqrt{\beta^2+\beta+1} \right)^n & if \ -1 < \beta \le 0 \\ \dfrac{2K}{\sqrt{3}} \dfrac{\left(\frac{2}{\sqrt{3}} \hat{\varepsilon}_1 \right)^n}{\sqrt{1-\left(\frac{\beta}{2+\beta} \right)^2}} & if \quad 0 < \beta \le 1 \end{cases} \tag{6-4}$$

where β is the ratio of the minor and the major principal strain rates, $\beta = \dot{\varepsilon}_2 / \dot{\varepsilon}_1$. The critical strain $\hat{\varepsilon}_1$ can be assumed to be equal to the power law coefficient n in accordance with Hill's criterion.

Fracture is simulated by eroding the failed elements when the fracture criterion is fulfilled. A through-thickness integration point is failed by setting the stresses to zero once the failure criterion is satisfied. Element erosion occurs once the middle integration point fails. This approach is preferred over requiring all integration points to fail prior to erosion because nodal fibre rotations in elements undergoing large strains may limit the strains in the remaining integration points, thus resulting in no erosion of the element.

Two kinds of steel material grades are used for the structures, and the material properties are shown in Table 6.2. The column plate is equipped with a yield stress of 420 MPa, while the column stiffeners and the pontoon are fabricated with a steel yield stress of 355 MPa.

Table 6.2: Properties of the steel material.

Steel	Young's Modulus (MPa)	Yield Strength (MPa)	Poisson Ratio	Power law K (MPa)	Power law n
column plates	2.07×10^5	420	0.3	860	0.16
column HPs and pontoon	2.07×10^5	355	0.3	780	0.22

6.2.4 Resistance of the column and the pontoon to rigid ice impacts

Rigid ice impacts on the pontoon model and the column model are carried out by means of the explicit Nonlinear Finite Element Analysis (NLFEA) software LS-DYNA 971. The four-node Belytschko-Lin-Tsay shell element with reduced integration is used with 5 integration points through the thickness. Hourglass stiffness is added using the stiffness-based form (option 4 in LS-DYNA). This is very efficient and gives a low dissipation of spurious hourglass energy (less than 2-3%). The rear side, the top and the bottom of the column are constrained in all degrees of freedom (translation in direction of x-, y- and z-axis and rotation around x-, y- and z-axis). Both ends of the pontoon model along the length direction are fixed against all degrees of freedom as well as the nodes at the pontoon top. The rigid ice model is given a prescribed velocity of 3 m/s. Two kinds of contacts are defined in this analysis, i.e. self-contact and master-slave contact. For the rigid ice-structure collision, the master-slave contact is used with the structure being the slave part. Self-contacts are defined for the structure to detect possible internal contacts of structural members due to deformation. A static friction coefficient of 0.3 is used for all contacts.

With the numerical settings and material model implemented, the F-D curves at different locations of the structure can be simulated by impacting these locations with a rigid glacial ice feature. 6 and 4 locations were analysed for the structure's column and the pontoon, respectively, thus giving 10 F-D curves for the structural responses. The collision locations for which the F-D curves are determined are shown in Figure 6.7. The F-D curves established for these locations are considered to be representative for most of the credible impact scenarios. Figure 6.8 shows the various F-D curves for impacts with an ellipsoidal rigid ice with long dimeter (2a = 15m).

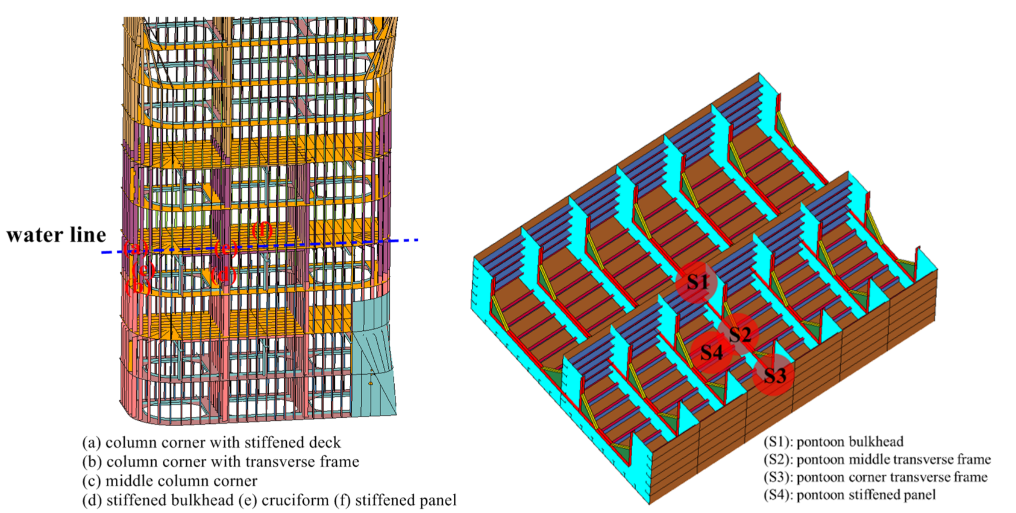

Figure 6.7 Impact locations for which the structure force-deformation curves have been determined using FEM simulations. On the column (left) and on the pontoon (right). By "cruciform" (location e) is meant intersection between deck and bulkhead.

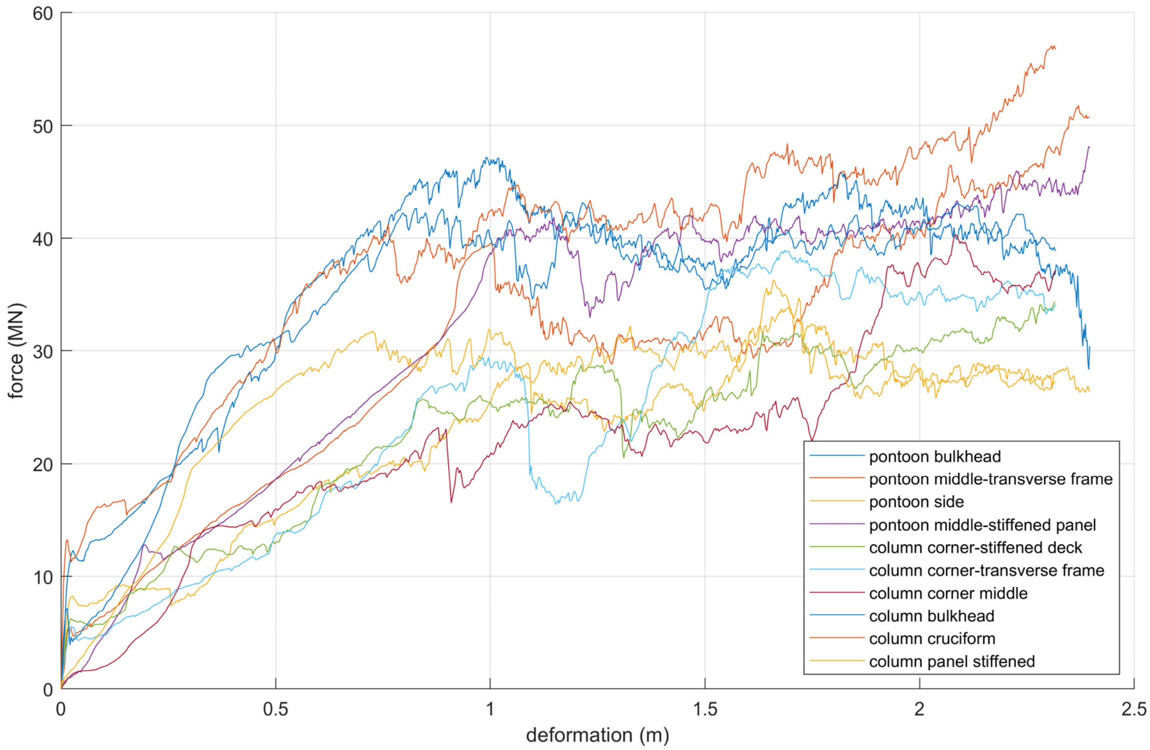

Figure 6.8 F-D curves of the structure at the 10 simulated impact locations (6 at the column and 4 at the pontoon). The rigid ice is ellipsoidal with $2a$ = 15 m, and $2b$ = $2c$ =10.4 m.

These simulated F-D curves are used as inputs to the integrated analysis and weakly-coupled analysis, both of which are described in detail in the following sections.

6.3 Integrated Analysis (Method #1)

The integrated approach (see Figure 6.1a) was previously adopted in the project ST19 to assess damage. More details of this approach can be found in the previous ST19 report. It essentially integrates the simulation results of two limiting scenarios, i.e., a rigid ice feature impacting a deformable structure plus a crushable ice feature impacting a rigid structure; and from this the share of the energy distribution is determined.

This procedure follows the same principles as those used for ship impacts according to NORSOK N-004 Appendix A (NORSOK, 2017). The principle is sketched in Figure 6.9. The ship may represent the ice feature in the present context. The force-deformation curve for the installation is established assuming the ship to be rigid. Likewise, the force-deformation curve for the ship is established assuming the installation to be rigid. The resulting damage is determined when the energy dissipation (equal to the area under force deformation curves) reaches the *demand* for energy dissipation, as determined by the external mechanics analysis.

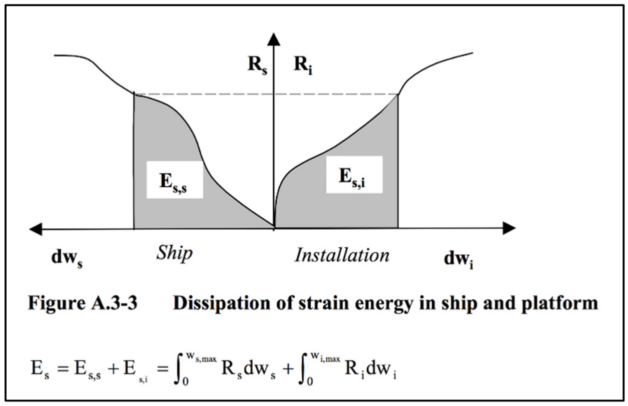

Figure 6.9 Estimation of force and damage (deformation) for ship impact against an installation according to Norsok N-004.

It is noted that this approach does not take the interaction effects into account, such as deformation of the ship bow increases the contact area and may hence increase the resistance of the installation. Simplified methods to account for this interaction in ship impacts are proposed in a revision of DNV GL RP-C204. Similarly, interaction effects exist for ice-structure impacts, but those will not be taken into account by this method, i.e. Method #1.

In summary, the following procedure will be used to determine the damage and energy dissipation in Method #1:

- Analysis principles for ship-installation impacts in NORSOK N-004/DNV GL RPC204 will be adopted.
- Extreme local pressures over limited areas will not be considered; it is the resistance to the total force that is essential in the ALS.
- Coupled analysis of the interaction between structural deformation and ice crushing is disregarded.
- Only the two limiting scenarios will be analysed and integrated for assessment of structural damage. The analysis procedure illustrated in Figure 6.10 and are summarized below:
  - *Contact force – penetration depth* relationships for the ice will be established using SAMS, i.e., by analysing ice impacts against a rigid structure.
  - Force-deformation relationship for the structure will be established using NLFEM analysis in LS-DYNA, i.e., by analysing rigid ice impacts against the structure.
  - The crushing of the ice and the structure damage is determined such that the total energy dissipation is equal to the demand for energy dissipation.
- The procedure is sufficiently accurate as long as the impact period is small compared to the eigenperiods for the relevant rigid-body motions of the ice or the structure, i.e., the impact force and inertia forces predominate the response.

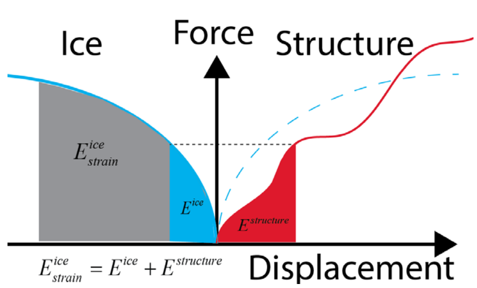

Figure 6.10 Determination of resulting damage in ice and structure.

6.4 Weakly-coupled Approach (Method #2)

In the weakly-coupled simulations, the force-deformation behaviour of the structure is first determined by modelling the interaction between a rigid glacial ice feature and a deformable structure, using FEM analyses (see Section 6.2). The resulting force-deformation (F-D) curves in Figure 6.8 are subsequently used by SAMS when modelling the interaction forces considering both the external and internal mechanics simultaneously.

6.4.1 Structure force-deformation mapping based on FEM simulation results

The 11 force-deformation (F-D) curves of the structure shown in Figure 6.8 are used to create F-D curves at any location at the semi-submersible's columns and the pontoons. This is done by linear interpolation as illustrated in Figure 6.11. The interpolated F-D curve is determined by four coefficients, which represent weighing factors for the four surrounding F-D curves.

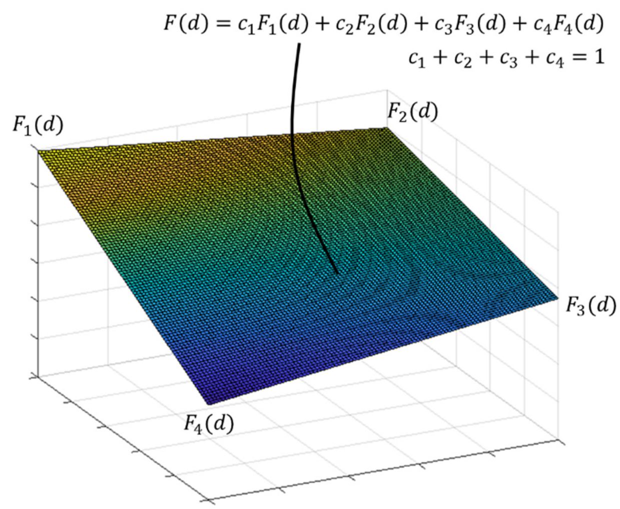

Figure 6.11 The F-D behaviour of impact locations is determined by linear interpolation between the points for which the F-D curves are known.

An example of an interpolated F-D curve for a location at the column is shown in Figure 6.12 and Figure 6.13. In this example, the ice impacts a location on column (see the greed dot in Figure 6.12) without direct F-D information. However, there are four neighbouring locations (see the red dots in Figure 6.12) with F-D information available. The F-D curve resulting from interpolation of the known F-D curves is shown in the right figure of Figure 6.13.

If we perform such F-D curves' interpolations for all potential impact locations around the structure, a structural resistance data based can be constructed. Observing the right-hand plot of Figure 6.13, we can extract the 'initial stiffness' of each F-D curve through dividing the plateaued force level by the corresponding displacement when the plateaued force level was firstly reached. This 'initial stiffness' is a measure of how stiff the structure is at different locations. We can visualise this 'initial stiffness' information in Figure 6.14 illustrating the structural strength distribution around the structure in the form of a 'strength map'. The colour in the map is a measure of the structural resistance to impacts form the chosen ice feature. The locations of stronger bulkheads and stiffeners are clearly visible in brighter colours. For the black parts, the F-D behaviour is not known.

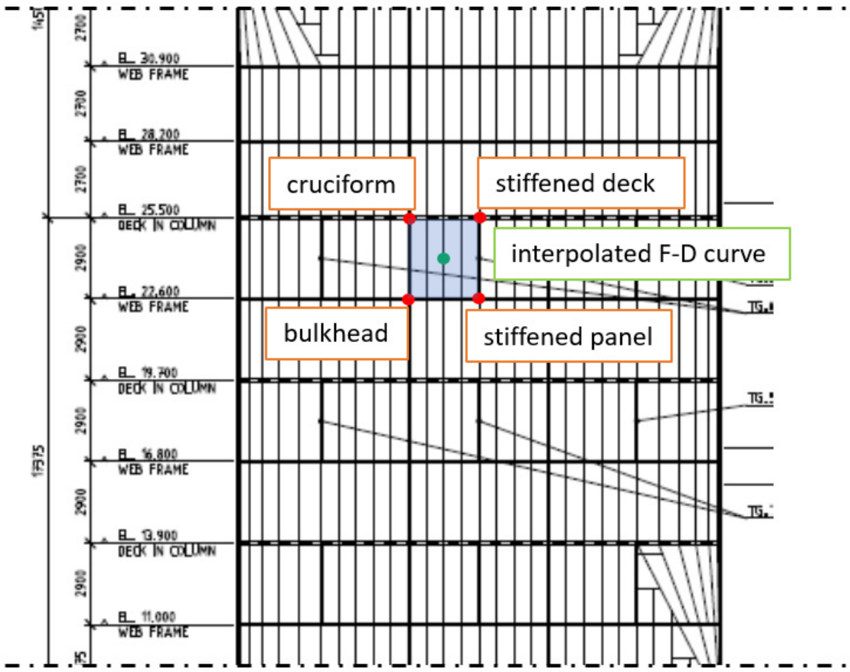

Figure 6.12 Impact location (greed dot)'s F-D curve reconstruction with four neighbouring locations (red dots) whose F-D curves are available.

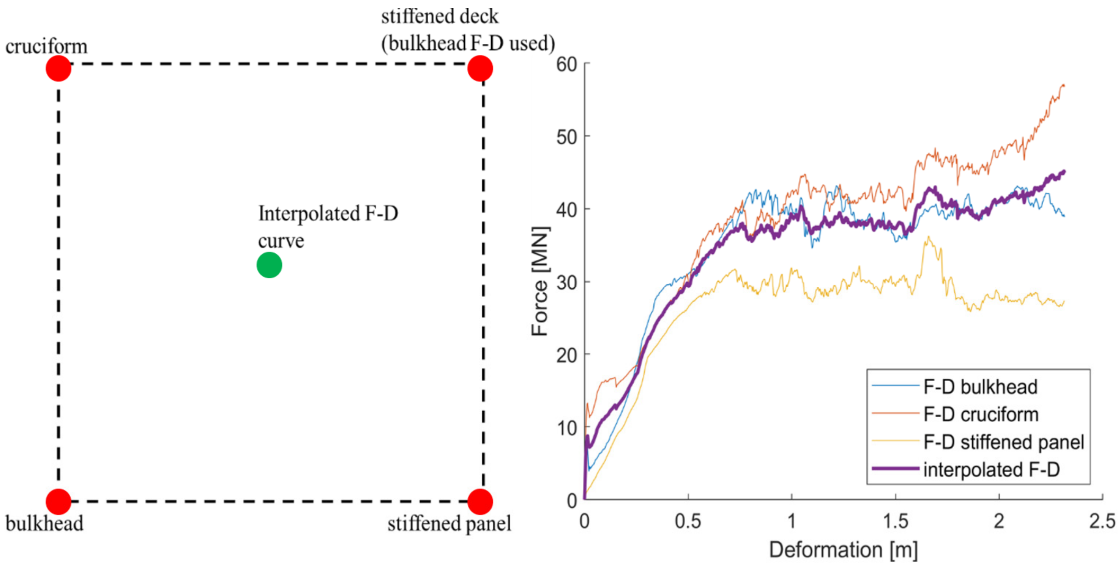

Figure 6.13 Example of an F-D curve determined by linear interpolation.

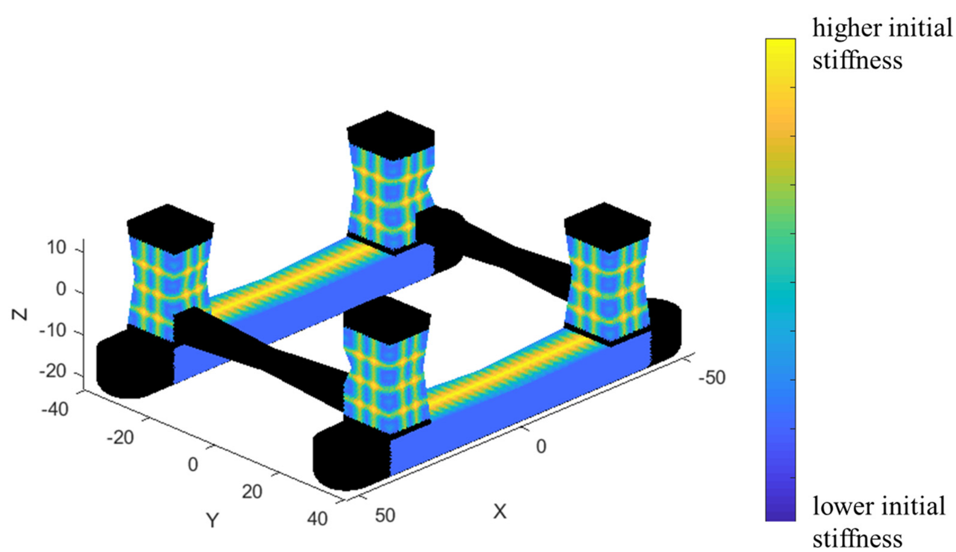

Figure 6.14 Strength map of the columns and pontoons of the semi-submersible.

6.4.2 Weakly-coupled simulations using SAMS

The strength map of the structure, as shown in Figure 6.14, is used in combination with the glacial ice material model in SAMS to simulate interactions between crushable ice and a deformable structure. The simulation output includes the contact geometry, the contact force, and the dissipated energy in ice crushing and structure deformation as a function of time. The procedure and results of a single simulation are described in detail in this section.

6.4.3 Contact algorithm

The contact algorithm is summarized in the flowchart in Figure 6.15. First, the contact between the semi-submersible and the glacial ice feature must be detected. Then, the contact point is determined. The F-D curve of the structure at the impact location is determined using the contact point and the structure's strength map. The force needed to crush the ice is determined based on the projected contact area. The force needed to deform the structure is also determined based on the structure deformation that has occurred already (initially 0) and the F-D curve. If the force needed to deform the structure is lower than the force needed to crush the ice, the structure will deform, and the maximum contact force is governed by the structural resistance. Consequently, the structural deformation increases in the next step. Otherwise, the ice crushing force is governing the maximum contact force, and the structure deformation will remain the same. The comparison of the force-deformation curves is made in each time step; and the structure deformation is updated if structure deformation occurs, and the projected contact area needed to calculate the ice crushing force is also updated.

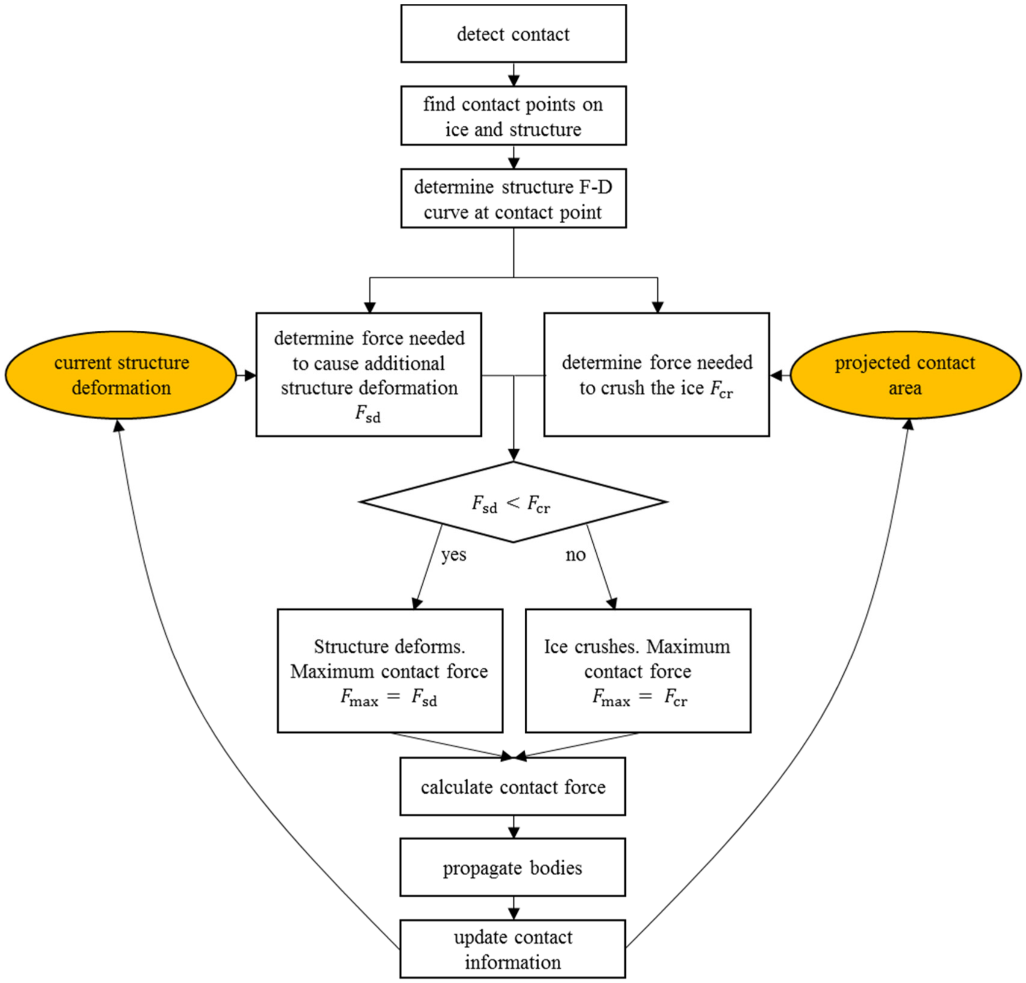

Figure 6.15 Summary of contact algorithm.

The force needed to crush the ice is based on the projected contact area of the undeformed structure and the intact ice feature. There is a notable difference between this approach and the integrated-analysis approach (Method #1). In Method #1, the force needed to cause ice crushing is only dependent on the amount of ice that is to be crushed. In the Method #2, the force needed to crush the ice also increases as a result of the structure deformation. The ice-structure contact area is dependent on the ice crushing deformation as well as the structure deformation. FEM simulations with rigid ice and a deformable structure show that the increase of the projected contact area due to structure deformation is roughly proportional to the increase of contact area due to ice crushing. This is illustrated in Figure 6.16.

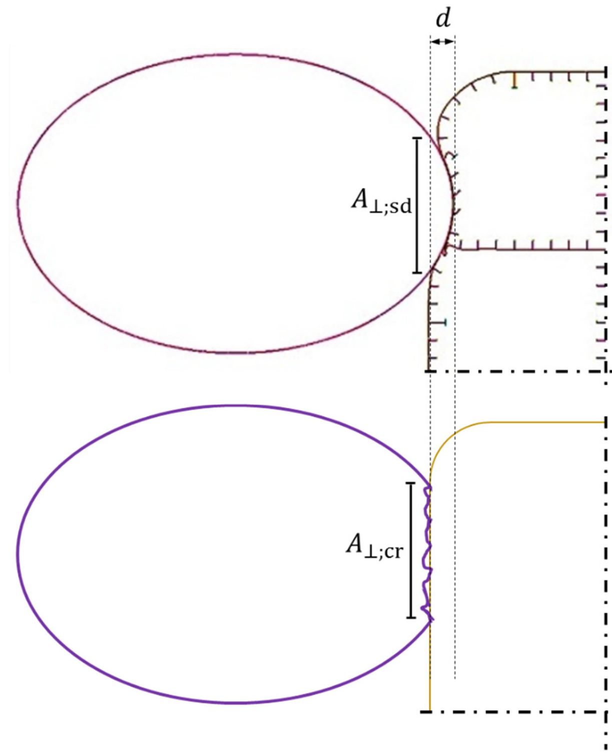

Figure 6.16 The projected contact area as a function of structure deformation (top) is similar to the projected contact area as a function of ice crushing (bottom).

The force needed to crush the ice is determined based on the projected contact area $A_\perp$ and the crushing specific energy as in Eq. (6-5):

$$F_{cr} = A_\perp \cdot \text{CSE} \tag{6-5}$$

The projected contact area $A_\perp$ is calculated using the position and orientation of the undeformed structure with respect to the undeformed ice. This is equivalent to the two extreme cases shown in Figure 6.16 due to the fact that the structural deformation and ice crushing depth are equivalent and additive to attain the total deformation '*d*'. Therefore, this is also equivalent to when both ice and structure are deforming/crushing as the summation of the two scenarios in Figure 6.16. Either way will yield the same contact area $A_\perp$ as long as the total deformation '*d*' is calculated.

The force needed to deform the structure, F_{sd} is, is determined from the structure F-D curve at the impact location, $F_s(d)$, at a given deformation d_s:

$$F_{sd} = F_s(d)\,|_{d=d_s} \tag{6-6}$$

6.4.4 Example simulation

The results produced by SAMS from the weakly-coupled simulations are shown for an example case. The simulation parameters are as follows:

Initial position:	[-83.0, -32.0] m (origin at COG of semi-submersible)
Drift direction:	0^o, see Figure 6.17
Drift velocity:	4.0 m/s
Vertical offset:	0 m (both glacial ice feature and structure are in hydrostatic buoyancy position in no-wave conditions)
Ice-structure friction coefficient:	0.15
Structure mass:	39 200 tons
Structure Radius of gyration (x,y,z):	[36, 34, 42] m
Bergy bit density:	900 kg/m^3
Crushing Specific Energy (CSE) bergy bit:	3.0 MN/m^3
Initial bergy bit velocity:	4.0 m/s
Added mass bergy bit (70% of mass):	535.5 tons

The initial conditions are visualized in Figure 6.17.

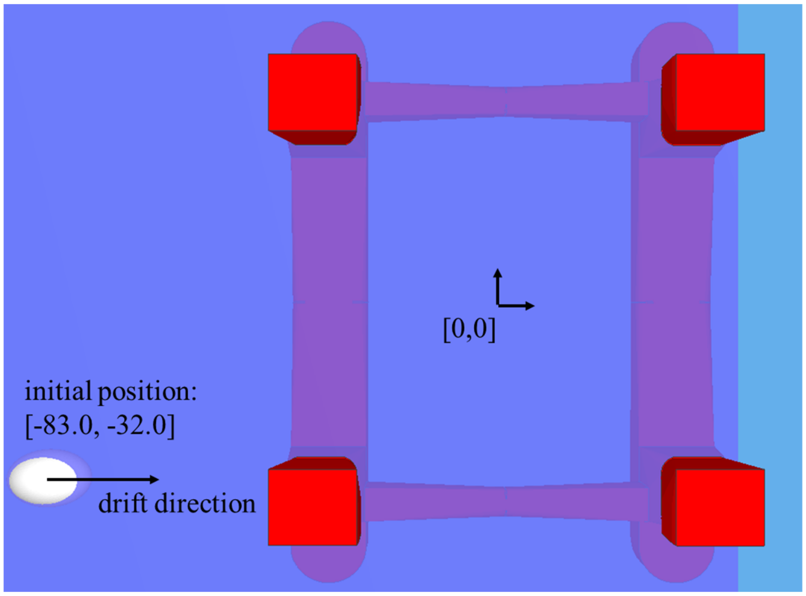

Figure 6.17 Initial conditions of weakly-coupled simulation example, top view.

The geometry at the moment of impact is visualized in Figure 6.18 and Figure 6.19.

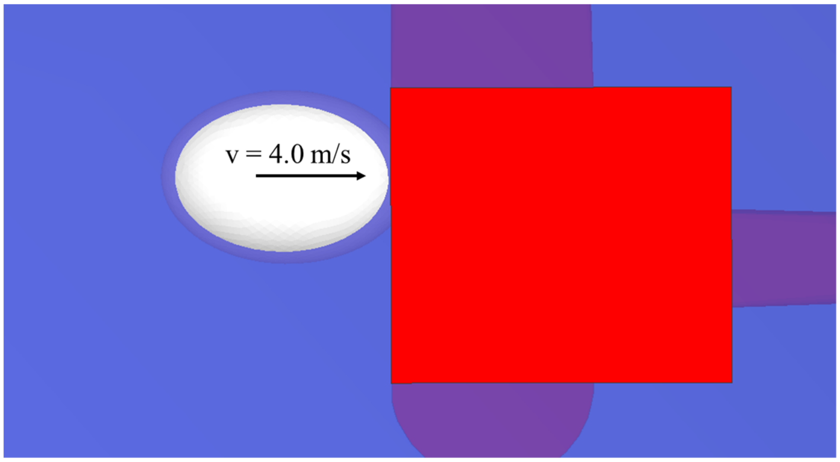

Figure 6.18 Impact location and velocity in the weakly-coupled simulation example, top view.

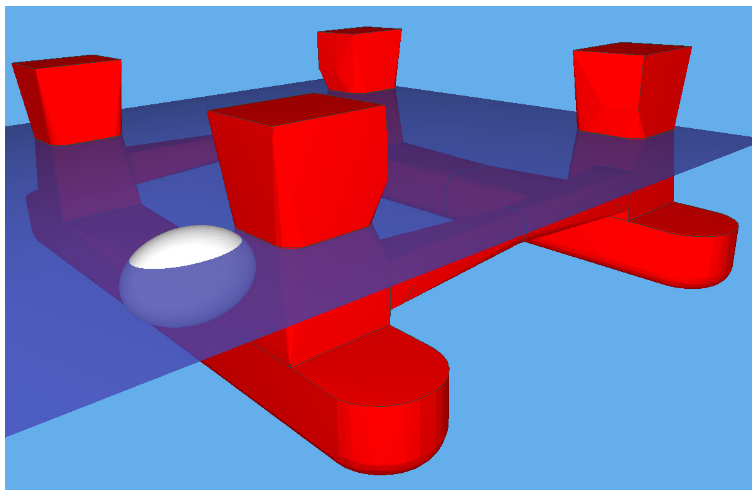

Figure 6.19 Impact location in the weakly-coupled simulation example from a different perspective.

The F-D curve of the structure at the impact location is determined based on the point of first contact and the structure's strength map. The construction of the structure's strength map is explained in Section 6.4.1. Figure 6.20 shows the impact location in the structure's strength map. The impact point is on a column bulkhead and relatively close to a cruciform (bulkhead/deck intersection). The contact area between the structure and the ice at the moment of maximum contact force is shown in grey.

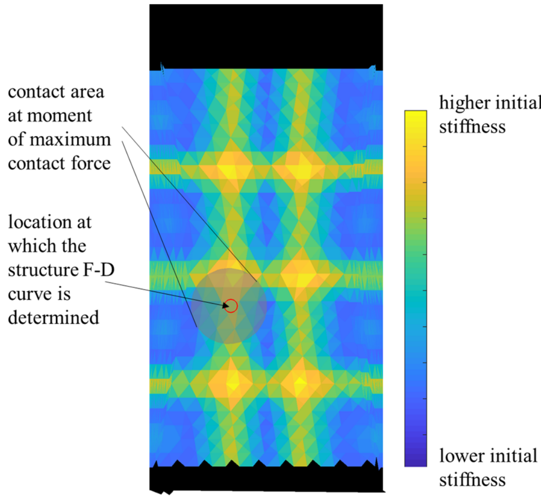

Figure 6.20 Side-view of the impacted column. The impact location is shown in relation to the strength map of the column.

As shown in Figure 6.15, at each time step the force needed to deform the structure and the force needed to crush the ice are compared. The lower of the two is governing the contact force. The force needed to crush the ice is dependent on the total contact deformation, whereas the force needed to deform the structure is dependent on only the structure deformation and the structure F-D curve. The F-D curves of the total deformation, the ice deformation and the structure deformation for the impact location of this example case are shown in Figure 6.21. Initially, there is little structure deformation and the glacial ice feature crushes. After an ice crushing of ~0.11 m, the contact force is so large that the structure starts to deform significantly. This leads in turn to an increase in the contact area, and the force needed to crush the ice becomes larger. The force needed to crush the ice increases therefore faster than the force needed to cause additional structure deformation. Therefore, there is no more ice crushing after the initial contact phase, and the impact energy is dissipated predominantly by plastic structural deformation.

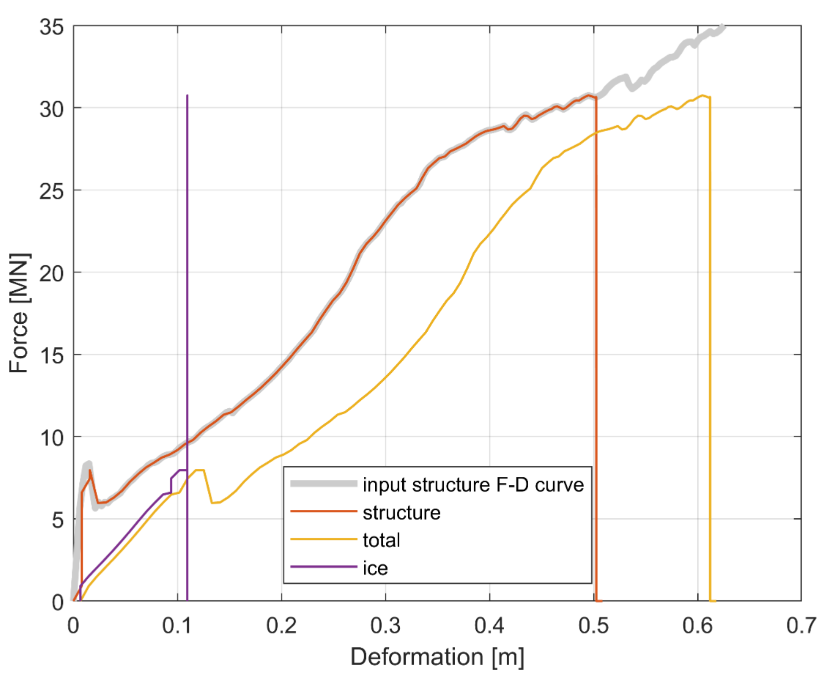

Figure 6.21. The total contact deformation, the structure deformation and the ice deformation as a function of the contact force.

Figure 6.22 shows the energy dissipation as a function of time. In the initial contact phase, there is little structure deformation: energy dissipation is primarily governed by ice crushing. After ~0.03 s, the ice stops crushing, and the structure starts to deform significantly. For the rest of the contact period, the energy dissipation is governed by structure deformation.

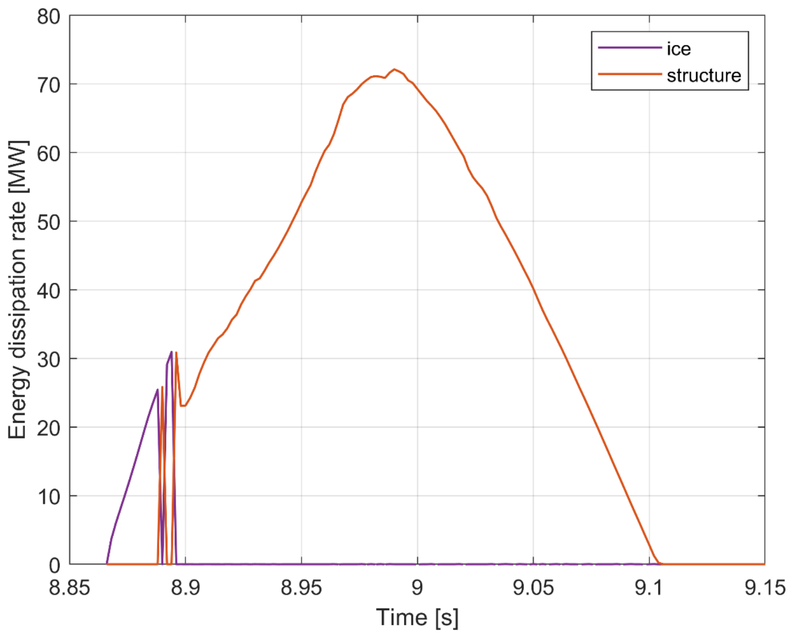

Figure 6.22 Energy dissipation as a function of time. Initially, energy is dissipated by ice crushing. Later, the energy dissipation is governed by the plastic deformation of the structure.

For this impact case, the demand for strain energy dissipation is 9.7 MJ. 9.3 MJ (or 95.4%) of the energy is dissipated by structure deformation. Only 0.4 MJ (or 4.6%) of the energy is dissipated by ice crushing.

6.5 Fully-Coupled Analysis by NLFEM (Method #3)

The fully-coupled approach is based on a hydrostatic pressure-dependent elastic-plastic model for the ice material. The ice model is implemented in the NLFEM software LS-DYNA with user subroutines together with the BWH fracture criterion for steel such that the impact response of the ice and the structures and mutual interactions can be calculated simultaneously. This method is, however, computationally the most expensive method and can only be applied for impacts at selected locations. In this section, the ice material model and its calibration are described.

6.5.1 Ice Material Model

Ice as a material has complicated mechanical properties, which vary with location, temperature, grain size and orientation as well as loading conditions (strain rate, confinement). Existing material models are still not sufficiently mature to reproduce ice behaviour comprehensively. In order to facilitate practical design of structures against abnormal ice loading, Liu et al. (2011) developed an elastic-plastic isotropic material model for ice, where the yield stress is dependent on the hydrostatic pressure so as to represent ice confinement. The model captures major ice deformation characteristics and can be readily implemented in NLFEM codes intended for structural analysis. The model is adopted in this work to analyse the structural response of the platform subjected to ice impacts including ice-structure interactions.

In the model by Liu et al. (2011), the behaviour of ice is modelled using the 'Tsai-Wu' elliptic yield criterion and a strain based failure criterion dependent on the hydrostatic pressure. The yield surface as a function of both the second invariant of the deviatoric stress J_2 and the hydrostatic pressure p is defined as follows:

$$J_2 = \frac{1}{2} S_{ij} : S_{ij} \tag{6-7}$$

$$f\left(p, J_2\right) = J_2 - \left(a_0 + a_1 p + a_2 p^2\right) = 0 \tag{6-8}$$

where, a_1, a_2 and a_3 are material coefficients to be specified by users, and S_{ij} is the deviatoric stress tensor.

To simulate the mechanical effects of ice crushing, an empirical failure criterion is adopted based on the effective plastic strain ε_{eq}^{p} and hydrostatic pressure $p = -\frac{\sigma_{kk}}{3}$ (pressure positive in compression):

$$\varepsilon_f = \varepsilon_0 + \left(\frac{p}{p_2} - \gamma\right)^2 \tag{6-9}$$

where, p_2 is the larger root of the yield function, ε_0 and γ are the parameters to be calibrated to experiments.

The ice material properties used in the simulation are given in the Table 6.3. Material coefficients a_0, a_1 and a_2 correspond to unset of inelastic behaviour at 9.0 MPa for uniaxial compressive loading and at 0.82 MPa for uniaxial tensile loading.

Table 6.3 Input parameters for the numerical simulations.

Parameters	Value	References
Ice density (Kg/m^3)	900	ISO 19906 (2019)
Poisson Ratio	0.3	Timco and Weeks (2010)
Ice friction	0.15	Liu et al. (2011)
Material coefficient a_0 (MPa^2)	2.588	Kierkegaard (1993)
Material coefficient a_1 (MPa)	8.63	Kierkegaard (1993)
Material coefficient a_2 (-)	-0.163	Kierkegaard (1993)

6.5.2 Calibration and comparison with Pond Inlet Experiments

A series of medium-scale indentation tests of ice in the Pond Inlet (Canada), 1984 were used for the calibration of the ice material model. The tests (Kennedy, 1990) were conducted with the use of a spherical indenter with a radius of 2.3 m driven by 4 hydraulic actuators, each with a 4 MN capacity. The indented ice face was in a lateral tunnel excavated into the side of a grounded iceberg, near the settlement of Pond Inlet on the northern coast of Baffin Island, NWT(Daley, 1994). Figure 6.23 shows a sketch of the test arrangement.

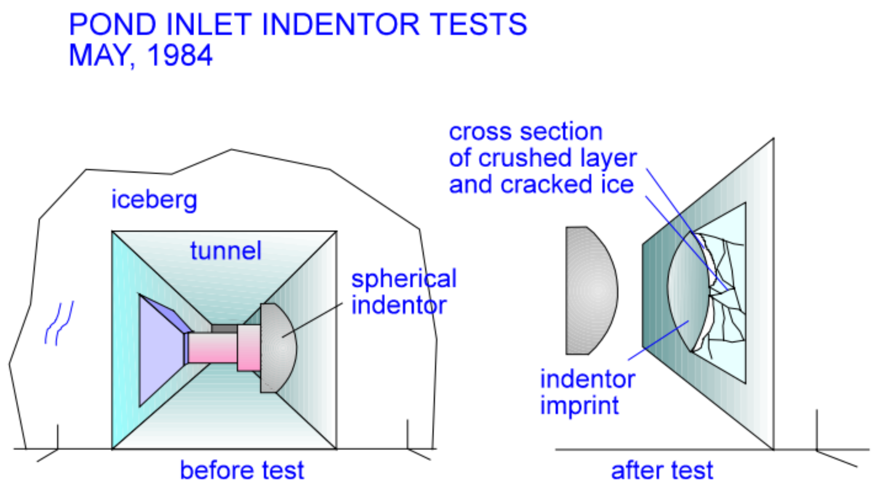

Figure 6.23 Arrangement of the Pond Inlet indentation test (Daley, 1994).

Figure 6.24(a) plots the force-displacement curves of 4 different cases from the Pond Inlet tests with an indenter radius of 2.3 m. The ice force-indentation curves exhibit significant scatter, demonstrating the inherent uncertainties of ice mechanical properties.

The ISO 19906 (2019) standard recommends an ice pressure area relationship of $\begin{matrix} p = 7.4A^{-0.7}\,(\text{MPa}) & when\ A \le 10\,m^2 \\ p = 1.48\quad(\text{MPa}) & when\ A > 10\,m^2 \end{matrix}$ for designing structures against local ice loading, mostly in the ULS. The ISO curve was derived from a series of indentation tests in the Beaufort Sea including the Pond Inlet tests, and the values were determined by the mean value plus three times the standard deviation. The ISO curve gives very large pressures for small contact areas but decreases rapidly when the contact area increases. In ALS conditions, large deformations are expected either in the ice or in the structures or both, which yield large contact areas. Instead of calibrating against the ISO design curves, the process pressure-area relationship underlying the local ice-load calculations for PC 3 vessels in IACS PC code $p = 3.2A^{-0.1}\,(\text{MPa})$ was found to better represent the physical value of the energy absorption of iceberg ice during crushing and spalling failure. Hence, when the force curve $F = 3.2A^{0.9}$ is used in ALS design, the local pressures and forces will be smaller than the ISO 19906 (2019) pressure-area curves for $A < 4\,m^2$, and larger for $A > 4\,m^2$ as shown in Figure 6.24 (b).

The force curve $F = 3.2A^{0.9}$ is compared with the Pond Inlet test curves in Figure 6.24(a). It is observed that selected curve gives quite accurately the same energy dissipation, i.e. the area under the force-displacement curve is on average the same as the test curves.

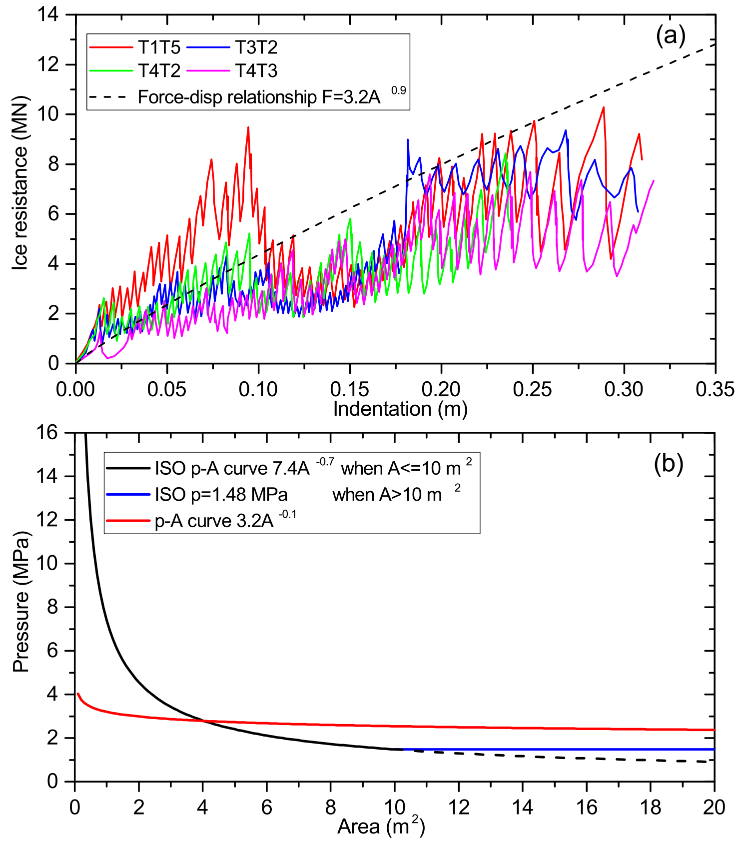

Figure 6.24 (a) Force-displacement curves of the Pond Inlet tests (Kennedy, 1990) (b) Pressure area relationships for the design ice.

There are two ways to calibrate to the fitted force-displacement relationship;

a) to push the rigid indenter into an ice block as done in the Pond Inlet tests
b) to use a rigid plate to crush a spherical ice as shown in Figure 6.25.

One might believe that the two calibrations will not make any difference and can be used interchangeably. This is however, not the case according to the simulations carried out. Figure 6.26 shows the calibrated curves and ice failure criteria to the same design ice resistance curve using the two different ways of calibration. A mesh size of 50 mm is adopted for the ice block in calibration type (a). For calibration type (b), the spherical ice is difficult to mesh with a uniform mesh size, but the mesh size is in general kept in the range of 35-75 mm. The results indicate that the two calibrations yield quite different ice failure criteria. In addition, from Figure 6.26, if the ice failure criterion based on calibration type (a) is used to simulate the (b) case, we obtain a much lower force level, which is less than half of the desired ice resistance. The significant differences are mainly due to the ice confinement.

The calibration (a) with a rigid spherical indenter crushing an ice block yields a much more compact ice due to confinement from neighbouring ice, whereas the ice in calibration (b) is less confined and therefore the force level is much lower. This phenomenon is observed based on simulation results using the adopted pressure-dependent ice material model. Currently, no direct evidence from tests or experiments are available to confirm the large difference between the two calibrations. If calibration method (a) is used, it is likely that the force level during ice indentation in a structure will fall *between* the two curves, depending on the confinement. When calibration method (b) is used, the force level for various degrees of confinement will lie *above* the calibrated curve. Initial analyses showed that the use of calibration method (a) would only cause crushing of ice and virtually no deformation of the structure. With the lack of experimental evidence for this behaviour of the ice, it was decided to adopt calibration method (b), which gives a stronger ice. This is considered to be conservative.

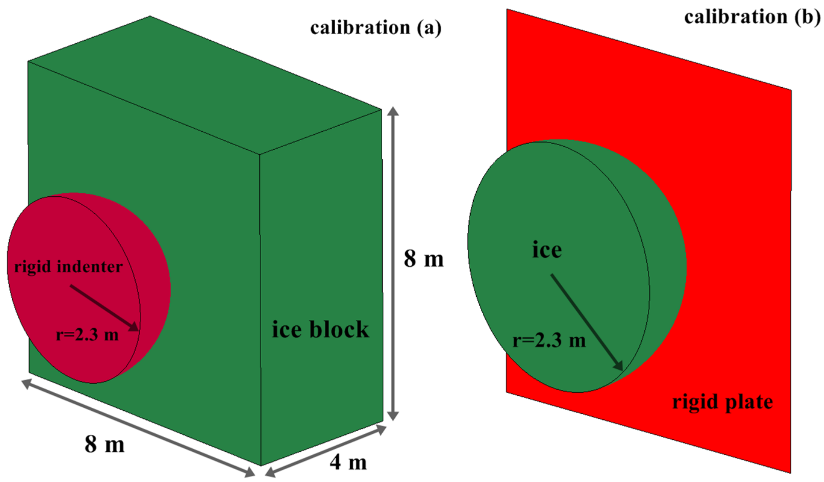

Figure 6.25 Two methods for the calibration of the ice material; (a) rigid spherical indenter versus a more confined ice block leading to a weak ice material model (b) rigid plate versus less confined spherical ice leading to a strong ice material model.

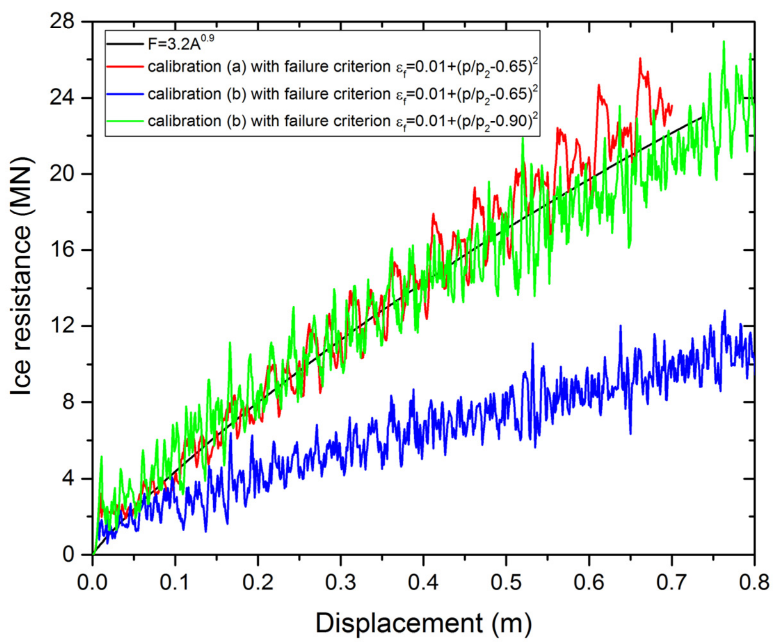

Figure 6.26 Two different calibrations of the ice failure criteria to the design ice curve.

A study of the mesh size sensitivity of the ice model was conducted using calibration case (a), where the mesh size of the ice block could be well controlled. Figure 6.18 shows simulation results with five different mesh sizes of 100 mm, 75 mm, 50 mm, 35 mm and 25 mm for the ice block and a common ice failure strain of $\varepsilon_f = 0.01 + \left(p / p_2 - 0.65 \right)^2$. The results indicate that the ice material model with a strain-based fracture criterion is very sensitive to the adopted mesh sizes. This can be expected because models with finer meshes are more likely to capture highly concentrated local strains while coarser meshes will blur local strain details by averaging the stress and strain within the element. Therefore, for the same failure strain criterion, models with a fine mesh will be eroded more easily compared to those with a coarse mesh, and thus give a lower force level. This is in fact, analogous to the mesh size sensitivity of fracture prediction of steel plates modelled with large shell elements

One solution to this sensitivity is to use the same mesh size as the one used in the calibration. It is however difficult to mesh the target ellipsoidal or spherical ice shape with uniform sizes. A viable approach for the calibration of the ice model, accounting for the mesh size sensitivity, is to not rely on one calibration and use the calibrated one fracture criterion for all shapes, but to calibrate to the design ice curve case by case. This means that one calibration of the fracture strain is needed for each ice shape and actual meshing. This strategy is adopted in the report, and the corresponding calibration parameters are given for each ice shapes.

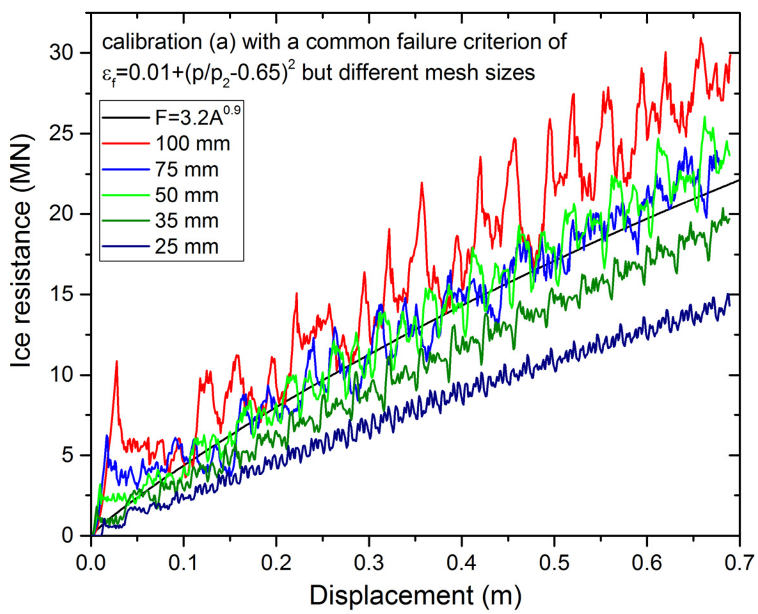

Figure 6.27 Mesh size sensitivity of the ice model for a given ice shape.

6.6 Application: searching for the critical local sharpness using the fully-coupled approach

During glacial ice impacts, ice-structure interactions are challenging yet crucial for structural safety considerations. From the structural side assuming a rigid ice feature, the sharper the local ice geometry becomes, the more easily the structures can be ruptured. Examples of this are illustrated in Figure 6.28 and Figure 6.29, where a rigid elliptical ice with a common short axis of 2*b* = 5.2 m but different long axis (2*a*) collides with stiffened panels of the platform column front. The case with 2*a* = 15m corresponds to the ice geometry used in ST19. The resulting force displacement curves that are shown in Figure 6.29, indicate that a sharper ice local geometry will trigger more localised structural deformations and thereby cause early fracture.

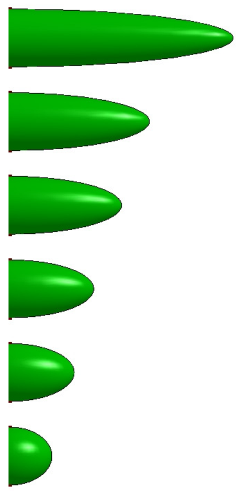

	radius of curvature (m)	radius of curvature/stiffened panel length
2a=80 m	0.68	0.23
2a=50 m	1.08	0.37
2a=40 m	1.35	0.47
2a=30 m	1.80	0.62
2a=23 m	2.35	0.81
2a=15 m	3.61	1.24

Figure 6.28 Ellipsoidal ice models with different sharpness.

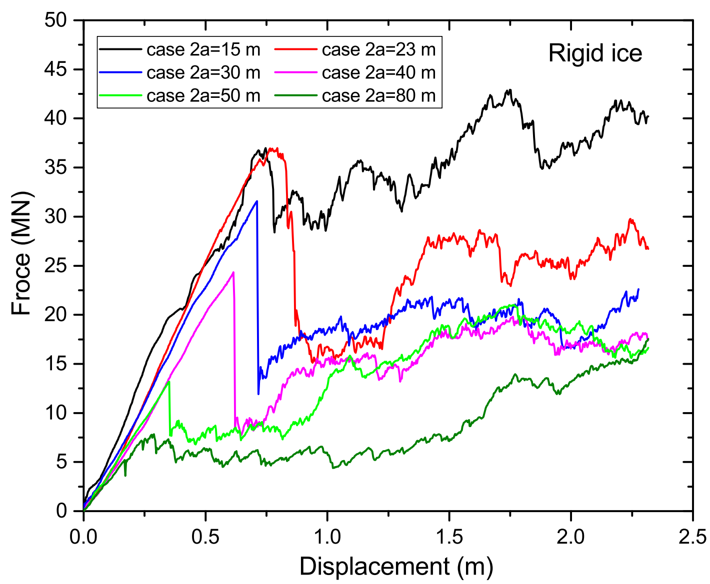

Figure 6.29 Force displacement curves of stiffened panels in the platform column subjected to impacts from rigid ice with a common short axis of 5.2 m and different long axis.

However, when realistic ice properties are accounted for, a sharp ice geometry will get crushed more easily compared to a blunt one. The crushing makes the glacial ice feature less sharp and increases the contact area. By considering both realistic ice properties and a deformable structure, it may be possible to identify an ice geometry with certain critical sharpness such that the ice shape is sufficiently sharp to induce early steel fracture compared to the blunt ice; i.e. the ice is also sufficiently strong to withstand structural loading before fracture of the steel material. In order to find the critical local ice sharpness, the fully-coupled approach was adopted, where the user code for the ice material and the code of BWH criterion for steel fracture were combined. Before these analyses can be undertaken, case by case calibration of the ice model will be needed.

6.6.1 Case by case calibration of the ice model

The ice model uses a strain-based fracture criterion for ice failure, and this makes the model sensitive to the adopted mesh size; see Section 6.5.2. Furthermore, as the target ellipsoidal shapes of ice is difficult to model with the same mesh size, calibration were done on a case-by-case basis. The six ellipsoidal ice geometries with different sharpness are shown in Figure 6.30. The size of the mesh (i.e., solid elements) is generally in the range of 35-75 mm.

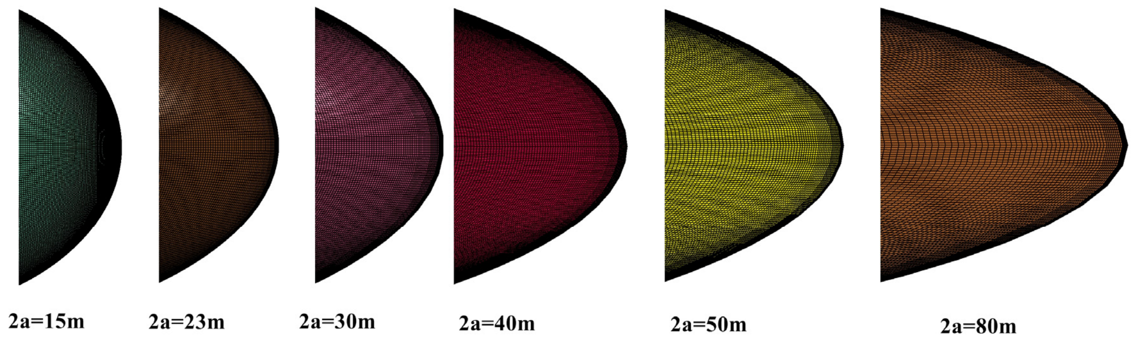

Figure 6.30 Modelling of ellipsoidal ice with different local sharpness using solid elements.

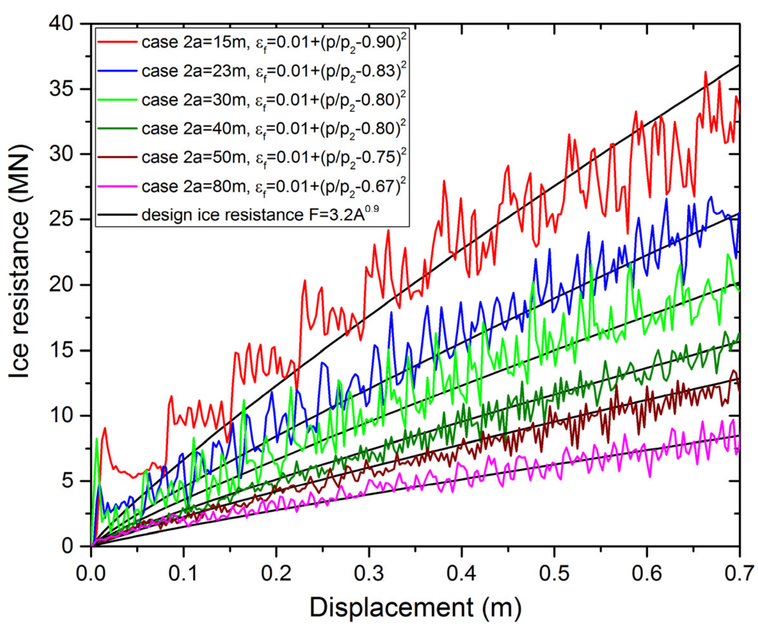

Figure 6.31 Case by case calibration of ellipsoidal ice with different sharpness.

The 6 ellipsoidal ice models are calibrated to the target ice design curve of $F = 3.2A^{0.9}$ (MN) in Figure 6.31 by crushing the ice model with rigid plates (i.e., Calibration b) in Figure 6.25). The largest force-deformation curve is obtained with the bluntest ice, but the force versus area relationship is the same for all shapes. The calibrated force curves follow well the design ice resistance curve with small oscillations. The calibrated ice failure strain tends to decrease as the ice geometry gets sharper. The ice models and the associated calibrated ice failure criteria were used in subsequent simulations of ice-platform column impacts.

6.6.2 Identification of critical ice sharpness

For the purpose of identifying the critical ice sharpness, the calibrated 6 ellipsoidal ice models are used to impact the stiffened panels of the platform front. The resulting resistance versus total displacement, i.e., the deformation of both ice and the structure, is plotted in Figure 6.32. It is observed that ice resistance dominates for ellipsoidal ice with $2a$ = 40 m, 50 m and 80 m, whereas structural resistance dominates for ellipsoidal ice with $2a$ = 15 m and 23 m. The resulting force versus deformation relationships of the ice and the structure, and the corresponding energy dissipation are plotted in Figure 6.33 and Figure 6.34. For a relatively blunt ice with $2a$ = 15 m and 23 m, the ice undergoes little deformation, and most energy is dissipated by the structure. This represents *ductile design* of the structure. When the long axis is increased to $2a$ = 30 m, the ice starts to be crushed significantly, and at the same time large structural deformations occur also in the structure. In this case, almost half of the energy is absorbed by the ice while the other half is absorbed by the structure. By further increase of the long axis to $2a$ = 40 m, 50 m and 80 m, ice gets crushed continuously and an increased proportion of the total energy is absorbed by the ice, but the structure still dissipates considerable energy. This may be classified as *shared energy design*.

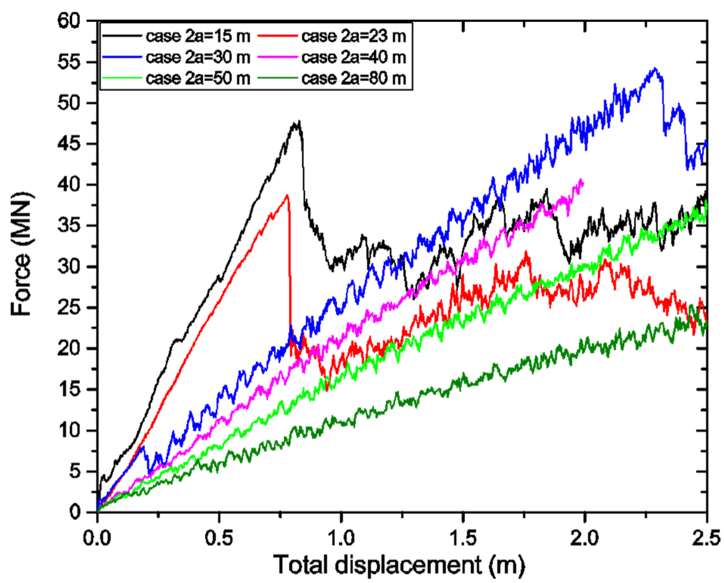

Figure 6.32 Force versus total displacement curves for platform stiffened panels under impacts from different ellipsoidal ice geometries.

The comparison of the resistance curves of the integrated approach and the fully-coupled approach in Figure 6.33 and Figure 6.34 indicates significant ice structure interaction. When the long axis is $2a$ = 15 m and 23 m, the ice is rather strong, and the structural resistance generally agrees with that from integrated analysis with rigid ice. The force-displacement curves from fully-coupled analysis does, however, not follow the design ice resistance of $F = 3.2A^{0.9}\,(\mathrm{MN})$, but is significantly larger. The likely reason is that the deformed structure wraps around the ellipsoidal ice and thereby increases the contact area as well as making the ice more confined. When the long axis is $2a$ = 30 m, 40 m, 50 m and 80 m, both the ice and the structure deform and absorb energy. The force-deformation curves for both the ice and the structure from fully-coupled simulations are larger than those of the integrated approach. For the fully-coupled method, fracture does not occur at the displacement where the outer shell ruptures using the rigid ice. This is due to the increased contact area caused by the deformation of both the ice and the structure which eases local stress and strain concentrations. Hence, the integrated approach may yield overly conservative predictions of shell rupture for relatively sharp ice.

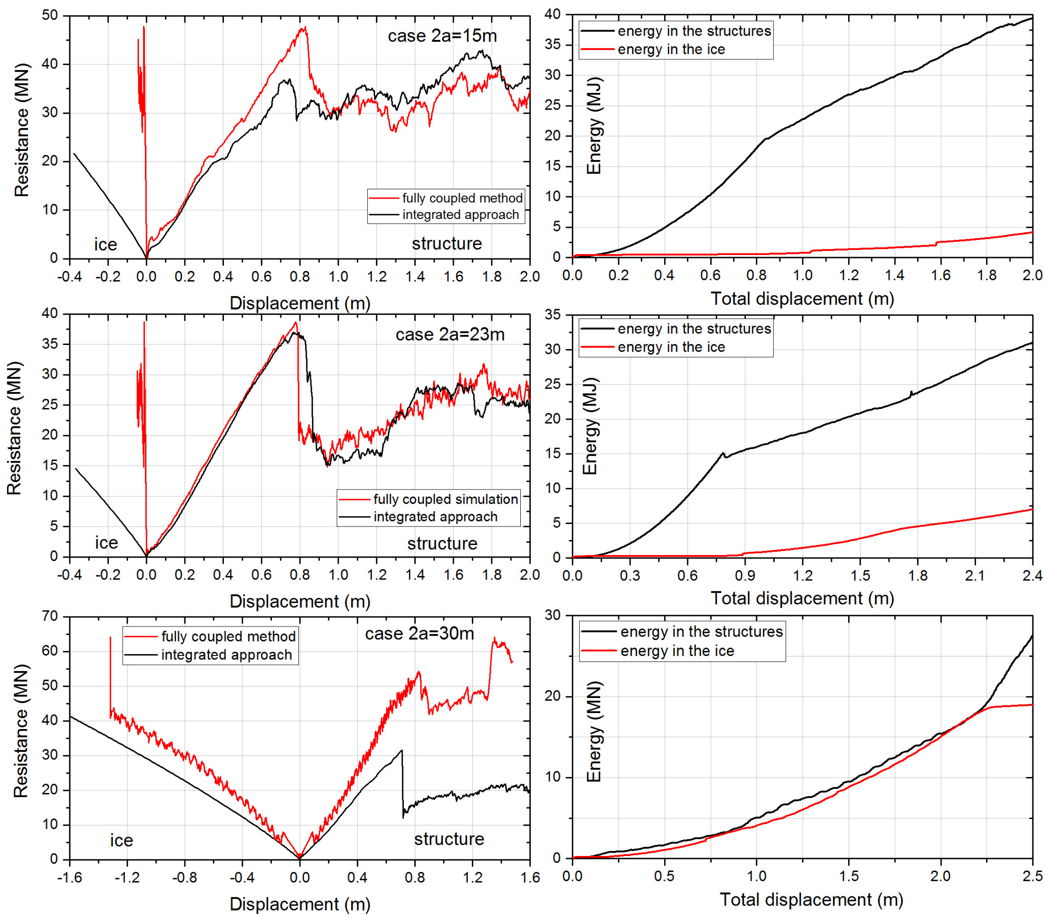

Figure 6.33 Force-displacement and energy absorption curves of ice and the structures using fully-coupled simulations for the case of 2*a*=15 m, 23 m, and 30 m.

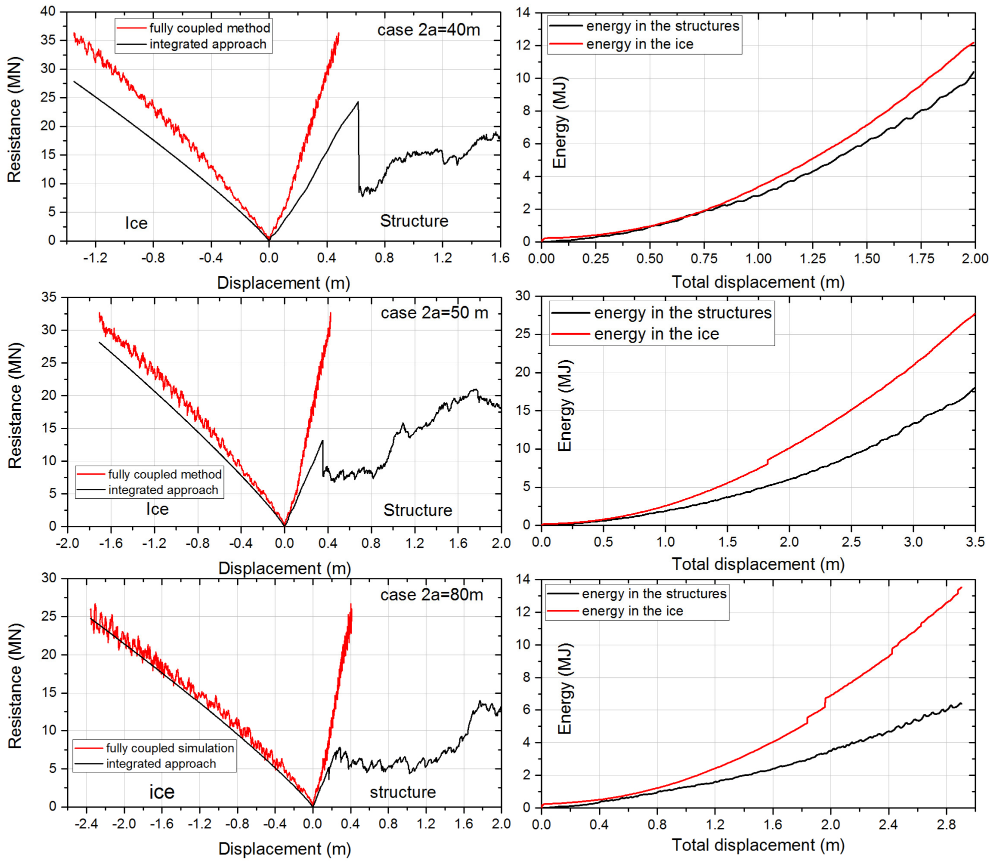

Figure 6.34 Force-displacement and energy absorption curves of ice and the structures using fully-coupled simulations for the case of $2a$=40 m, 50 m, and 80 m.

Structural damage and ice crushing at different characteristic displacements are given in Figure 6.35 and Figure 6.36 for blunt ice with $2a$ = 15 m and 23 m, and Figure 6.37 and Figure 6.38 for sharp ice with a long axis of $2a$ = 30 m and 80 m. From Figure 6.35 with $2a$ = 15 m, the ice penetrates the stiffened panel of the platform front with minor ice damage. As the displacement increases, extensive damage also occurs on the platform deck and the bulkhead, whereas the intersection of the deck and the bulkhead or a frame represents "hard spots" of the structure, which is capable of crushing the ice significantly. In the case of $2a$ = 23 m, refer Figure 6.36, the ice is capable of penetrating the outer shell with minor ice crushing. The total energy dissipation accumulates to 15 MJ at the onset of initial rupture in the shell plating. When the contact increases to the transverse frame or deck, the ice undergoes significant crushing.

When the long axis varies from $2a$ = 23 m to $2a$ = 30 m in Figure 6.37, there is a drastic transition from *ductile behaviour* with minor ice damage to *shared energy behaviour* with significant ice crushing. During this process, the structure is also deformed severely, and fracture occurs along the bulkhead at a very late stage for a total displacement of 3.0 m. The fracture pattern is different from the rupture of stiffened panels in the case $2a$ = 15 and 23. Similar ice crushing and structural deformations are observed for increasing long axis, but rupture of the structure does not occur for the considered impact energy.

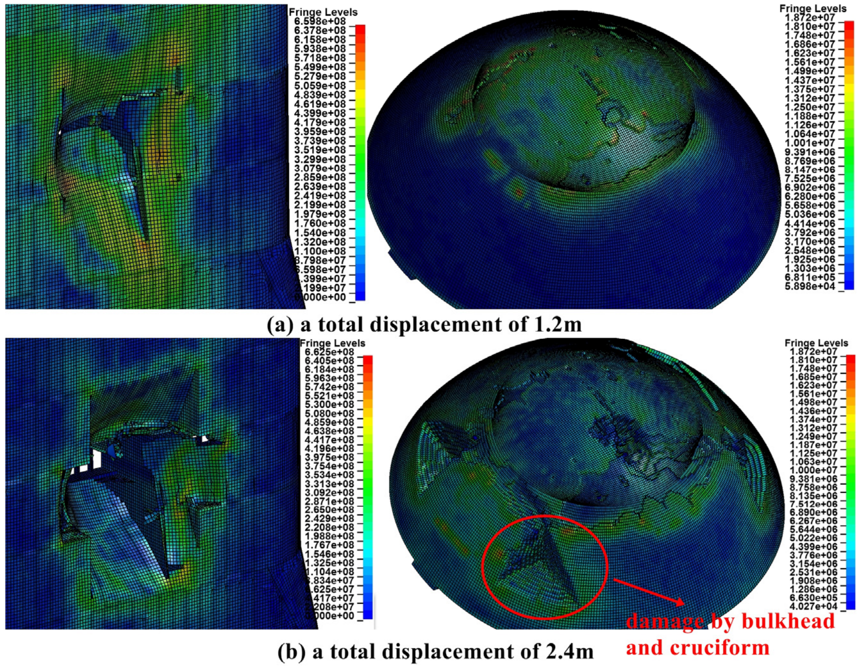

Figure 6.35. Structural damage and ice crushing for the case of 2*a* = 15 m.

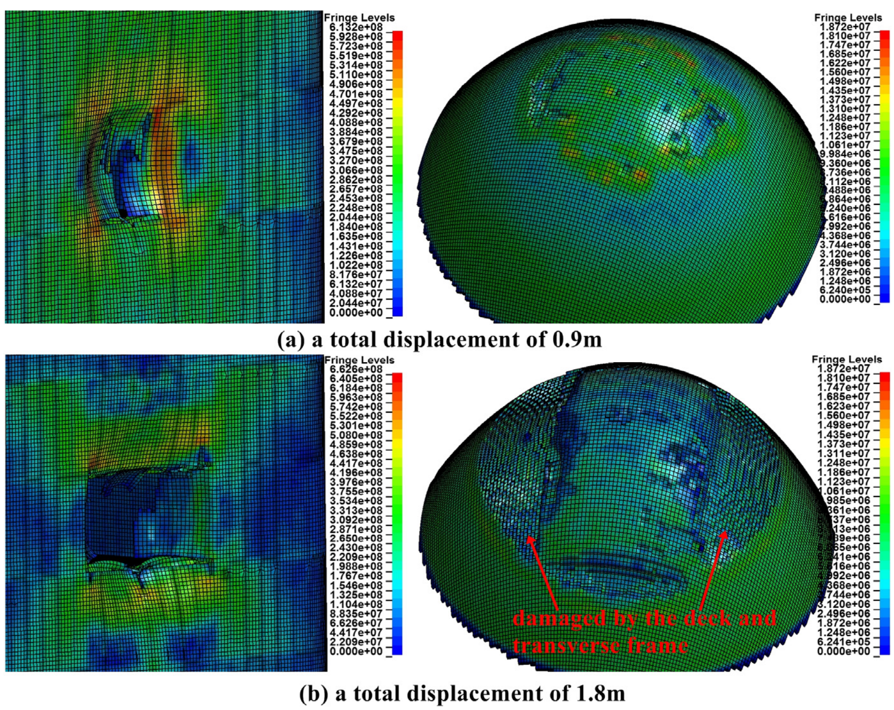

Figure 6.36. Structural damage and ice crushing for the case of 2*a* = 23 m.

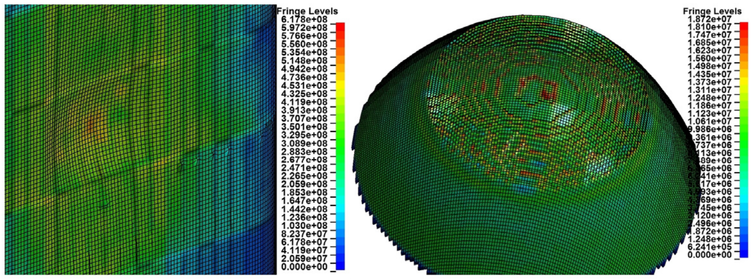

(a) a total displacement of 1.2m

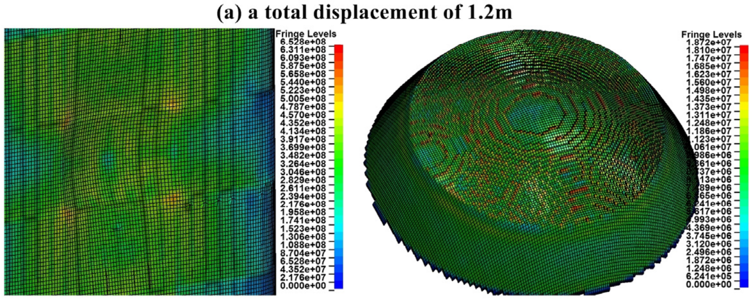

(b) a total displacement of 1.8m

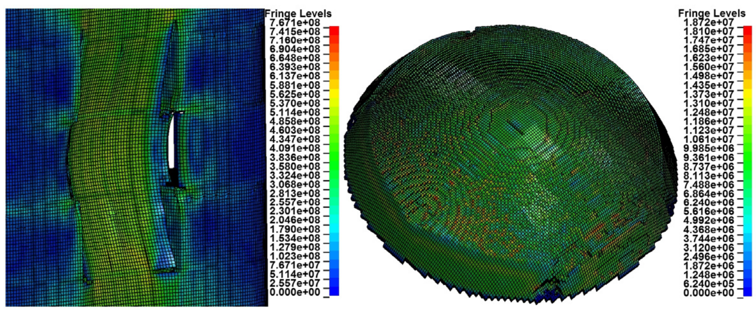

(c) a total displacement of 3.0 m

Figure 6.37. Structural damage and ice crushing for the case of $2a$ = 30 m.

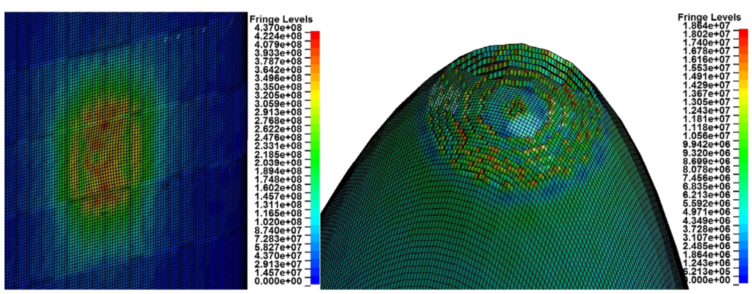

(a) a total displacement of 0.9 m

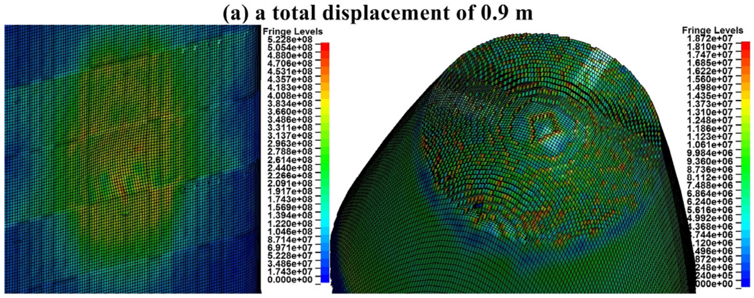

(b) a total displacement of 2.4 m

Figure 6.38. Structural damage and ice crushing for the case of $2a$ = 80 m.

Intuitively, when the glacial ice feature becomes blunter, more energy shall be dissipated by the structure. On the other hand, when the glacial ice gets sharper, it is more easily crushed and thus dissipates more energy. This intuitive trend is quantitatively shown in Figure 6.39. Assume that the total impact energy that should be dissipated by the ice and the structure is 7.5 MJ or 15 MJ (more about reasons behind these numbers will come later), Figure 6.39 shows the portion of the impact energy that will respectively be dissipated by crushing the ice and by deforming the structure for various ice local sharpness. The results show clearly that Method #3 captures quite well the above-mentioned trend. Between the cases of $2a$ = 20 m and $2a$ = 30 m, a sudden transition from 'ductile behaviour' to more 'strength behaviour' is taking place, which is the case with $2a$ = 23 m.

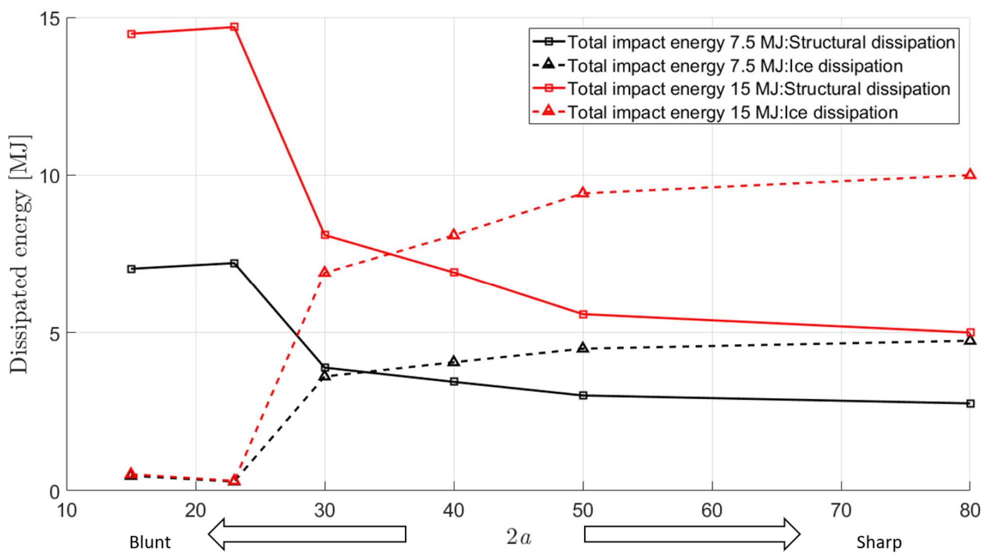

Figure 6.39 Energy dissipation between structure and ice with varying sharpness levels, simulated by the fully-coupled NLFEM (Method #3).

However, dissipating more energy does not necessarily mean that the structure will sustain more damage. When impacted by a blunt ice feature, the structure will be activated over a large contact area, which, with slight deformation/damage will lead to significant energy dissipation. Therefore, in order to find the critical local sharpness, which leads to significant structural energy dissipation but at the same time the contact area is small to create large deformation/damage, we convert the energy plot in Figure 6.39 into deformation/damage plot in Figure 6.40.

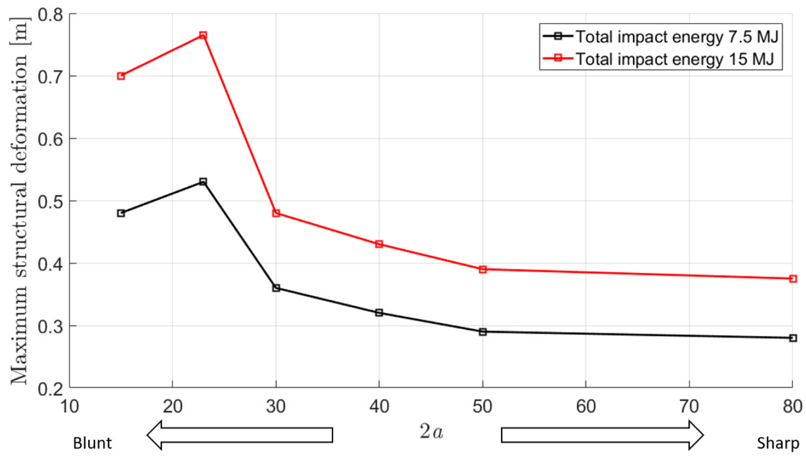

Figure 6.40 Structural deformation/damage under the impact of glacial ice features with different sharpness.

Figure 6.40 shows that maximum structural deformation takes place at around $2a$ = 23 m.

In summary, all the six ellipsoidal ice shapes with different sharpness are capable of causing large structural deformations depending on the available impact energy. The ellipsoidal ice with a long axis of 23 m is considered to be the critical geometry. It is observed from Figure 6.33 that for the case with $2a$ = 23 m, the total energy dissipated at the onset of fracture of the shell plating attains a minimum of 15 MJ. It is also interesting to observe that the radius of curvature of the identified critical ice geometry over the stiffened panel length is about 0.81 (see Figure 6.28). This indicates that the critical shape is influenced by the local structural design. Most likely when the radius of curvature of local geometry of the glacial ice feature is close to the spacing between stiffened panels, it becomes unfavourable to the structure; and accordingly, this glacial ice feature becomes a critical geometry.

6.7 Structural response analysis for ice impacts with $2a$ = 23m

The ellipsoidal ice with the critical geometry identified in Section 6.6.2 with a long axis of $2a$ = 23 m and a short axis of $2b = 2c$ = 10.4 m is assumed to impact different locations on the platform column and pontoon (the same locations defined in Figure 6.7). The structural responses are analysed with three different approaches, and the results are compared and discussed.

6.7.1 Fully-Coupled-Simulations

- ***Ice impacts on the column***

Figure 6.41 displays the force versus the total displacement at different impact locations of the platform column. The curves show significant effects of ice-structure interaction. In general, they do not follow rigid ice only or rigid structure only curve but are mixed. Figure 6.42 and Figure 6.43 show the corresponding force displacement curves of the structure and the ice separately and corresponding energy absorption. For the impacts on stiffened panels of the column front and column corner, the ice is very stiff and impacts the structures with minor ice damage; this is termed *ductile behaviour*. Outer shell fracture occurs at a total energy dissipation of 15 MJ for the column front and 11 MJ for the column corner. The structural damage and ice crushing for the case of ice impact on the column corner are given in Figure 6.44. The ice is virtually rigid most of the time but is crushed to some extent when it is in contact with the stiffened deck.

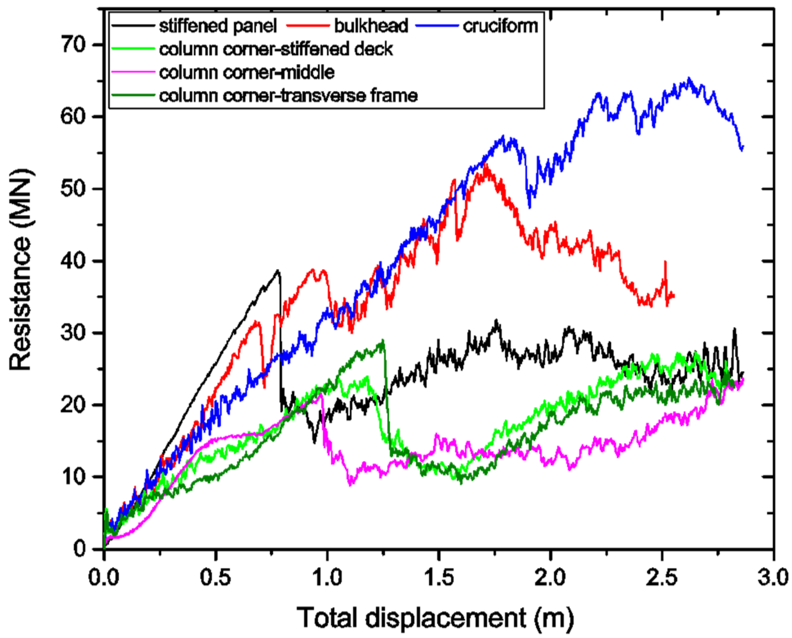

Figure 6.41. Force versus total displacement curves for ice impacts on different locations of the platform column.

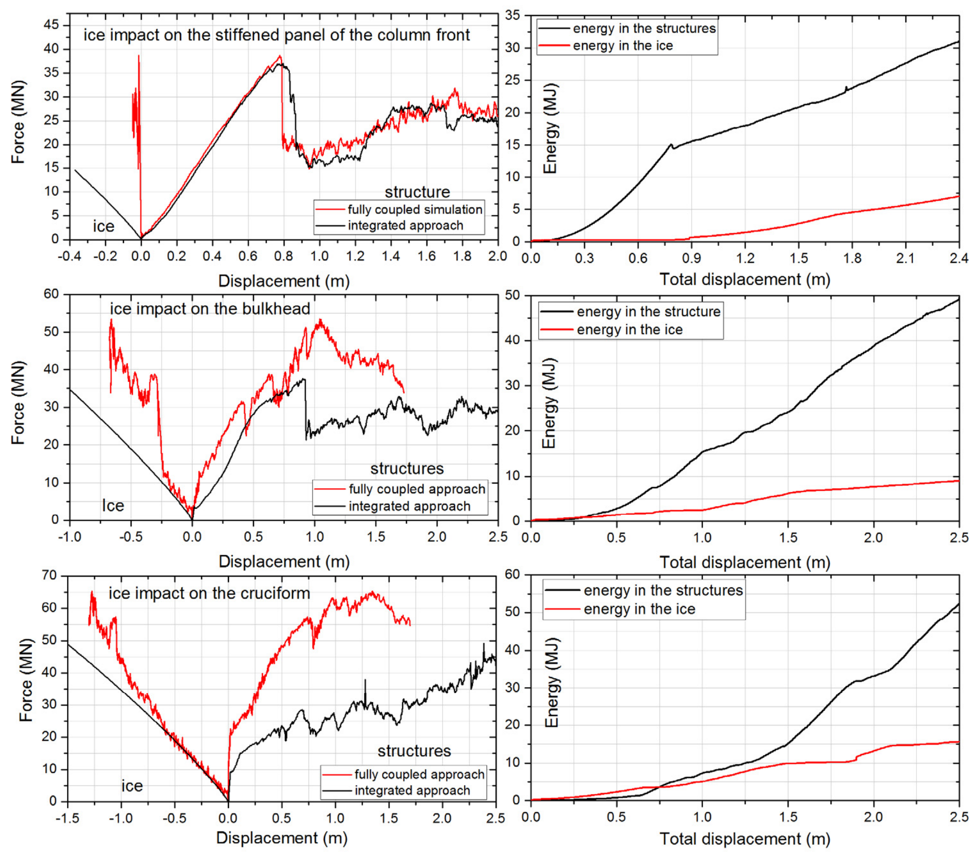

Figure 6.42 Left: Structural damage and ice crushing for ellipsoidal ice with *2a*=23 m impacting the stiffened panel, the bulkhead and the intersection between a deck and bulkhead of the platform column. Integrated approach means either ice or structure is rigid. Right: Energy dissipation in structure and ice from fully-coupled analysis.

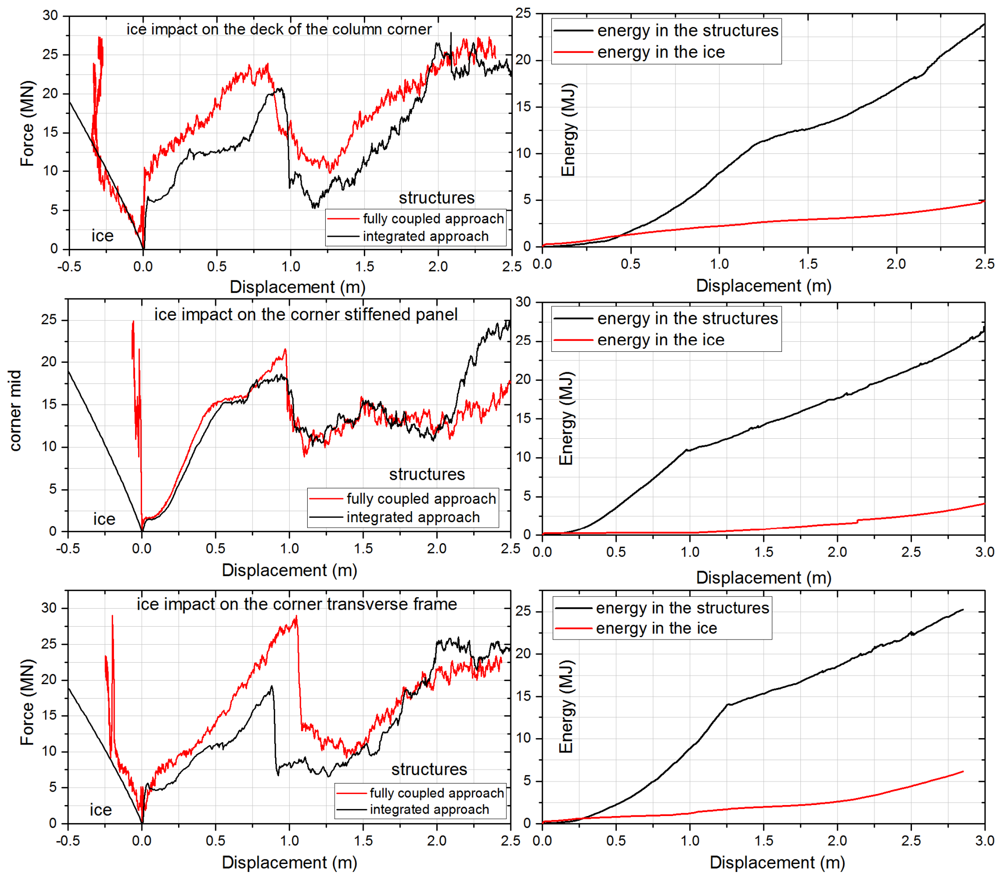

Figure 6.43 Left: Force displacement curves of the structure and ice for the ellipsoidal ice with *2a*=23 m impacting the deck, the transverse frame and middle of the column corner. Integrated approach means either ice or structure is rigid. Right: Energy dissipation in structure and ice from fully-coupled analysis.

For ice impacts on the bulkhead, the intersection between the bulkhead and the deck, the corner deck and the corner transverse frame, both the ice and the structure are damaged, and significant ice structure interaction takes place. Consider the case of ice impacts on the intersection between the bulkhead and the deck. From the resistance curves in Figure 6.42 and the plots of structural damage and ice crushing in Figure 6.45, it appears that the intersection between the bulkhead and the deck is very stiff initially and crushes the ice significantly. The ice crushing force curve follows perfectly the design ice curve up to a deformation of 0.6 m, from which the intersection structure starts to collapse and deflect. After an ice crushing of 0.6 m, both ice and the structure deform and absorb energy. The structural deformation increases the contact area and therefore the ice resistance starts to deviate from the design ice curve. At the same time, the load carrying capacity of the structure increases with the increased contact area. A similar behaviour is also observed for ice impacts on the bulkhead, the corner deck and the corner transverse frame.

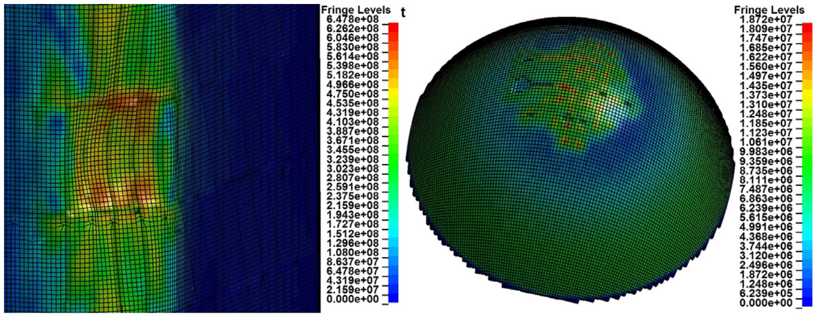

(a) a total displacement of 0.9 m

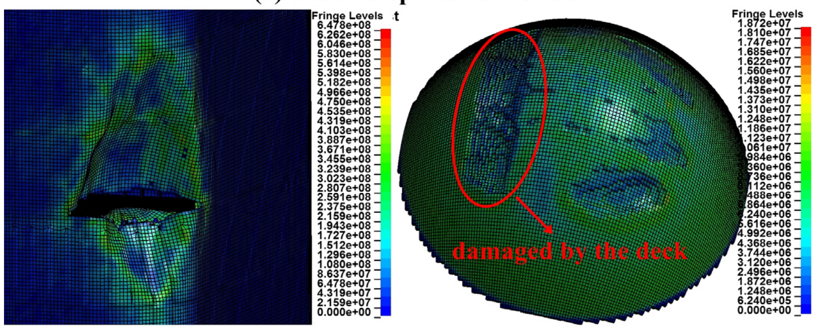

(b) a total displacement of 2.1 m

Figure 6.44 Structural damage and ice crushing for ice impact on the corner stiffened panel.

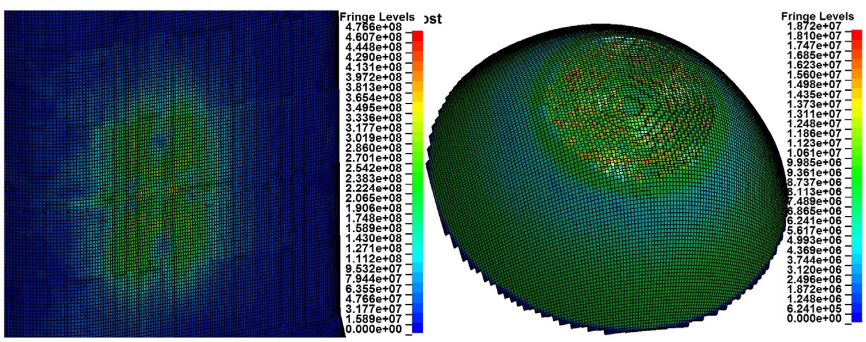

(a) a total displacement of 0.6 m

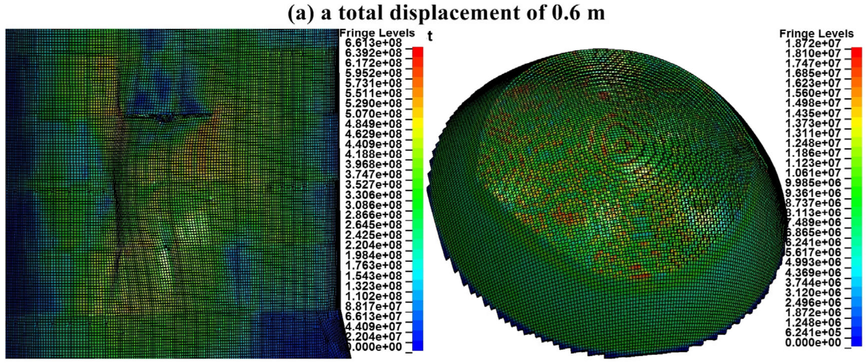

(b) a total displacement of 2.4 m

Figure 6.45 Structural damage and ice crushing for ice impact on the cruciform of the column front.

- ***Ice impacts on the pontoon***

Figure 6.46 shows the force versus total displacement curves for the ellipsoidal ice with $2a$ = 23 m impacting different locations of the platform pontoon. The collision scenarios are defined in Figure 6.7, where Scenario 1 represents ice impact on the intersection of the bulkhead and the transverse frame, Scenario 2 on the middle of the transverse frame, Scenario 3 on the side of transverse frame and Scenario 4 on the pontoon stiffened panels. The curves indicate significant interaction between the ice and the structure, i.e. the weak side governs the resistance curves, and often it shifts several times during the deformation. The corresponding force displacement curves of the ice and the structures separately and the energy absorption are plotted in Figure 6.47 and Figure 6.48. The intersection of the bulkhead and the transverse frame represent hard spots of the pontoon. The behaviour is very similar to that of impacts with the column intersection. The structural damage and ice crushing condition for Scenario 1 is given in Figure 6.49. Up to a total distance of 0.6 m, the cruciform gets little damage while ice is crushed significantly. Upon further crushing, both the ice and the structure obtain significant damage.

For impact scenarios #2 on the middle of transverse frame and Scenario #3 on the side of the transverse frame, the ice and the structure deform simultaneously and interact. An illustration of the structural damage and ice crushing is given in Figure 6.50 for Scenario #2. For impact Scenario #4 on the pontoon stiffened panel, the ice is quite stiff and almost all energy is dissipated by the deformation of the structure. The corresponding ice and structural damage are shown in Figure 6.51.

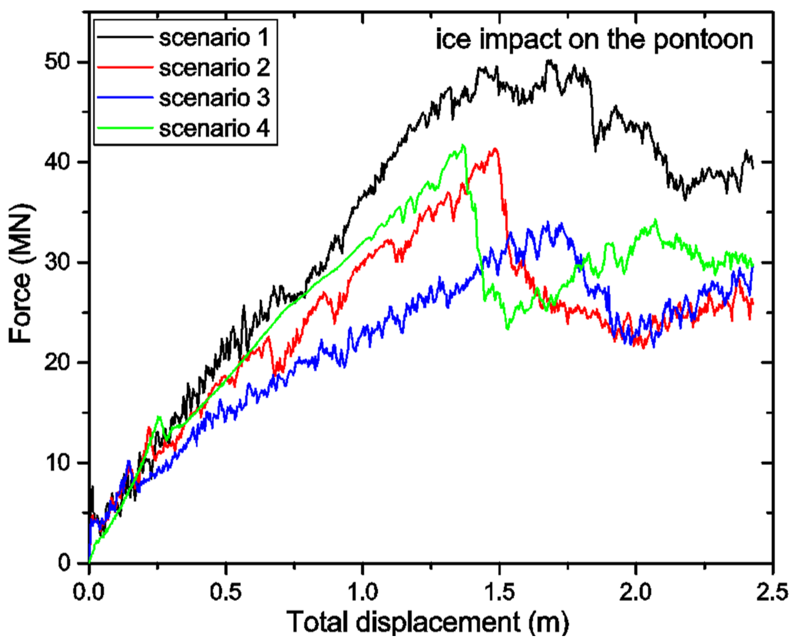

Figure 6.46 Force versus total displacement curves for ice impacts on different locations of the pontoon (different scenarios correspond to different impact locations in Figure 6.7).

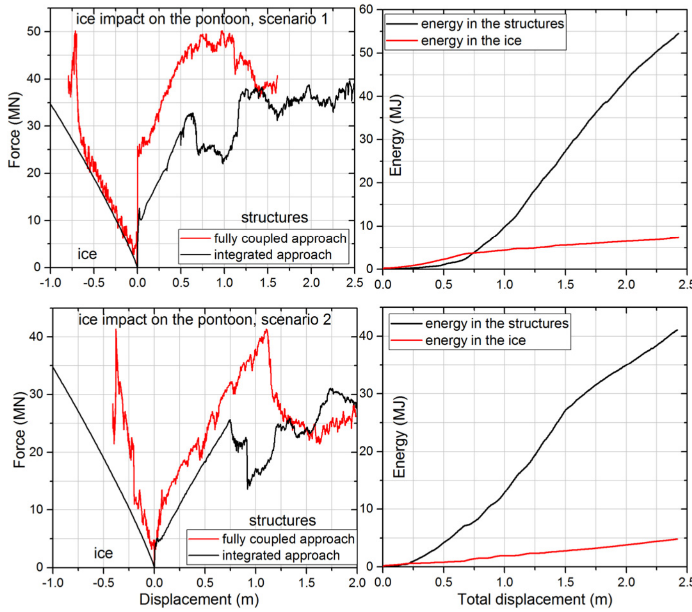

Figure 6.47 Left: Force displacement curves of the structure and ice for the ellipsoidal ice with 2a=23 m impacting the pontoon, Scenario 1 on the intersection of the bulkhead and the transverse frame and Scenario 2 on the middle of the transverse frame. Integrated approach means either ice or structure is rigid. Right: Energy dissipation in structure and ice from fully-coupled analysis.

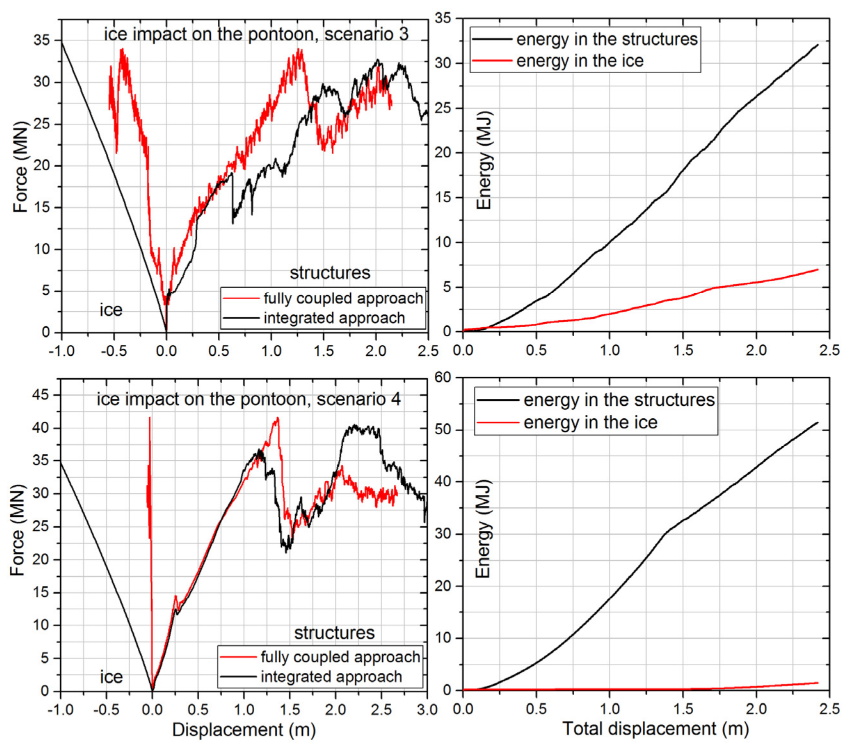

Figure 6.48 Left: Force displacement curves of the structure and ice for the ellipsoidal ice with 2a=23 m impacting the pontoon, Scenario 3 on the frame end and Scenario 4 on the stiffened panel. Integrated approach means either ice or structure is rigid. Right: Energy dissipation in structure and ice from fully-coupled analysis.

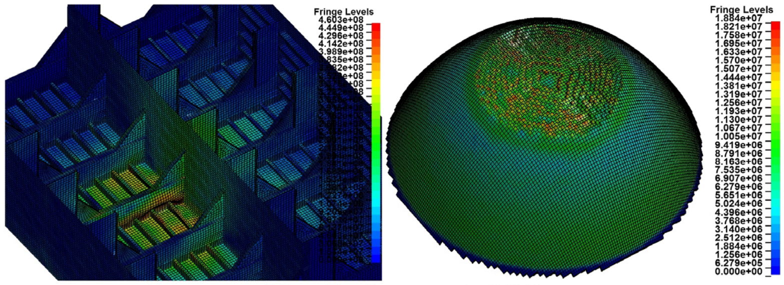

(a) a displacement of 0.6 m

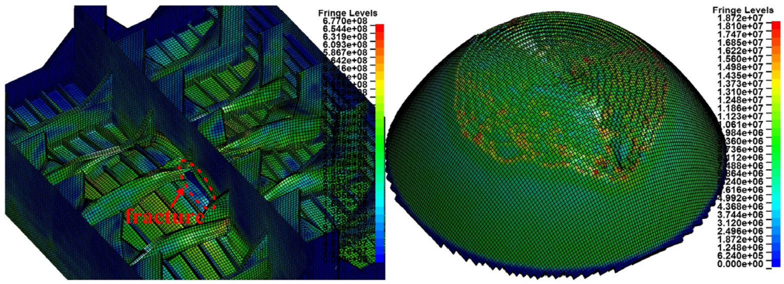

(b) a displacement of 2.1 m

Figure 6.49 Structural damage and ice crushing for ice impact on the intersection of the bulkhead and the transverse frame, Scenario #1.

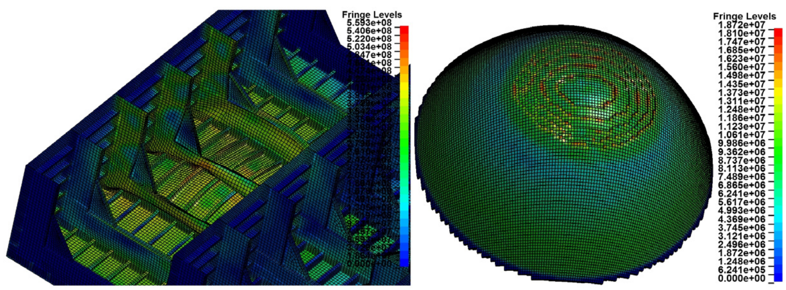

(a) a displacement of 0.9 m

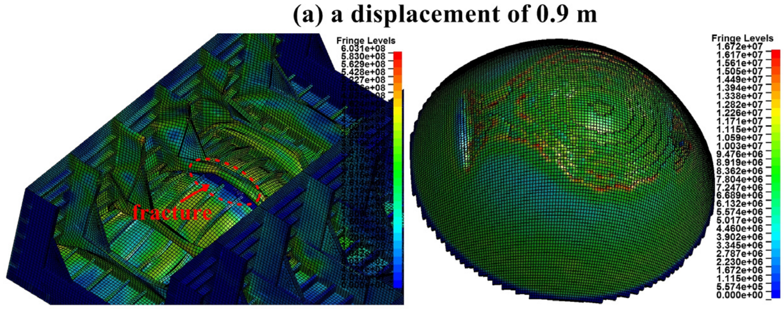

(b) a displacement of 1.8 m

Figure 6.50 Structural damage and ice crushing for ice impact on the pontoon transverse frame, Scenario #2.

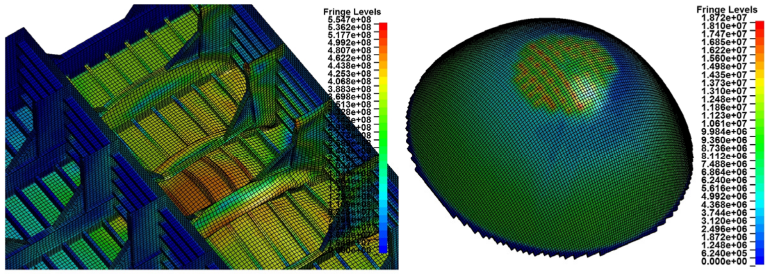

(a) a displacement of 0.9 m

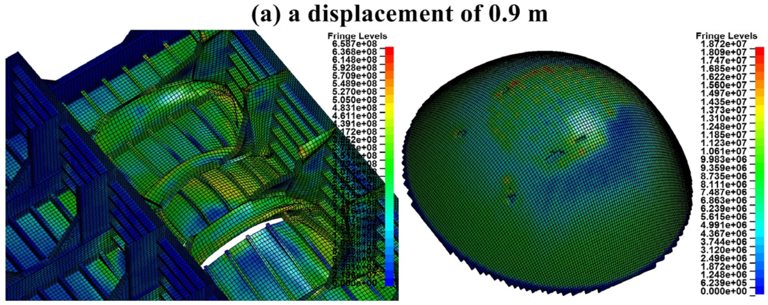

(b) a displacement of 1.5 m

Figure 6.51 Structural damage and ice crushing for ice impact on the pontoon stiffened panel, Scenario #4.

In this section, the fully-coupled method (Method #3) was utilised to analyse the coupled behaviour of ice crushing and structural deformation for the critical shape of 2*a* = 23 m. The analyses were conducted for both the platform column and pontoon at 10 selected locations (see Figure 6.7). The fully-coupled analysis comprises essentially an internal mechanic analysis and it was conducted in such a way that the glacial ice impacted the structure with a constant velocity of 3 m/s. The simulation continued until considerable total energy had been dissipated. This also means that the results obtained in Figure 6.33 (case 2*a* = 23 m), Figure 6.42, Figure 6.43, Figure 6.47, and Figure 6.48 are generic and valid for all type of energy levels. As long as one knows the impact energy that needs to be dissipated, these graphs provide the information required to determine the ice crushing depth, structural deformation/damage, and the share of energy dissipation. In addition to illustrating the outcome of the fully-coupled method, the results from integrated analysis (Method #1) results were presented for the purpose of comparison.

Next, analysis with the weakly-coupled approach (Method #2) will be presented.

6.7.2 Weakly-coupled Simulations

The fully-coupled approach (Method #3) focuses on internal mechanics while the weakly-coupled approach (Method #2) includes both the external mechanics and internal mechanics. For a given glacial ice feature and wave conditions, the external mechanics and internal mechanics are calculated simultaneously and efficiently by SAMS in just one run. The energy dissipation and structural deformations are calculated directly. This section presents the simulation results of an extensive list of impact scenarios.

6.7.2.1 Simulation set-up

The weakly-coupled approach has been described in Section 6.4 together with its implementation and testing. In this section, two geometries of the glacial ice feature (Figure 6.52) shall be adopted to simulate impacts at various locations of the platform using the weakly-coupled analysis. These geometries are the ellipsoid with 2*a* = 15 m (Figure 6.52a), which is the same geometry analysed in ST19, and the critical geometry of 2*a* = 23 m (Figure 6.52b) that was identified in the previous sections.

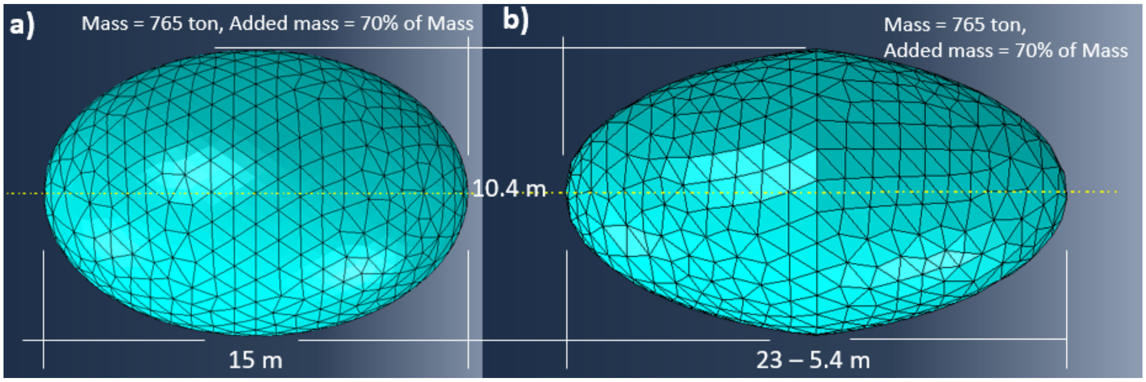

Figure 6.52 The geometry of the glacial ice feature utilised in the weakly-coupled analysis within SAMS (left: $2a$ = 15m; right: $2a$ = 23m with 5.4 m middle section truncated to maintain the same mass).

Because the implemented weakly-coupled approach within SAMS is computationally efficient, a large number of impact scenarios can be simulated. In the simulations, the glacial ice features are positioned at various locations, orientations and heights with reference to the structure (see Figure 6.53 and Figure 6.54) and then they impact the structure with various initial velocities. The different impact scenarios are summarised in Table 6.4. 1800 different impact scenarios are simulated for each of the two glacial ice features shown in Figure 6.52 (i.e., a total of 3600 simulations). The vertical offset, horizontal offset and drift direction are systematically varied in order to obtain the impact energy and loading values for a wide range of impact scenarios. This is done following the same set-up as in the previous project ST19. Recall that ST19 adopts a wave condition of a 100-year return period with a significant wave height of 13.8 m and wave period of 18 s.

Table 6.4: Test matrix of spheroidal ice feature in open water.

Ice feature	Range	Number of values
Vertical offset	-10.8 to 10.8[1]	9
Horizontal offset	-67.5 to 67.5	20
Drift direction	0º to 90º	10

[1] Variation from the hydrostatic buoyancy position of the ice feature and the semi-submersible structure in no-wave conditions (i.e., at SWL).

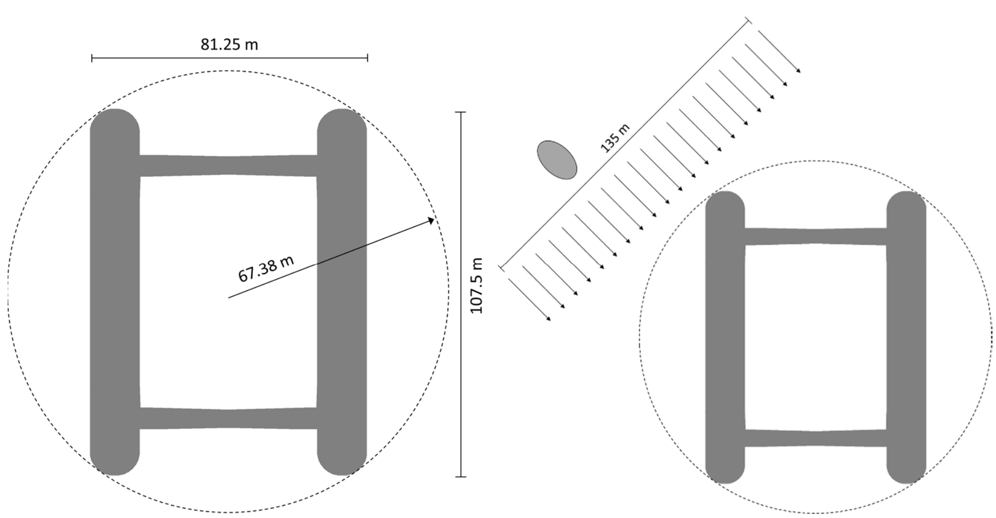

Figure 6.53: Top view of the semi-submersible structure, showing main structure dimensions and the radius of the minimum bounding circle (left). Ice feature horizontal offset as applied for each impact direction and impact height (right).

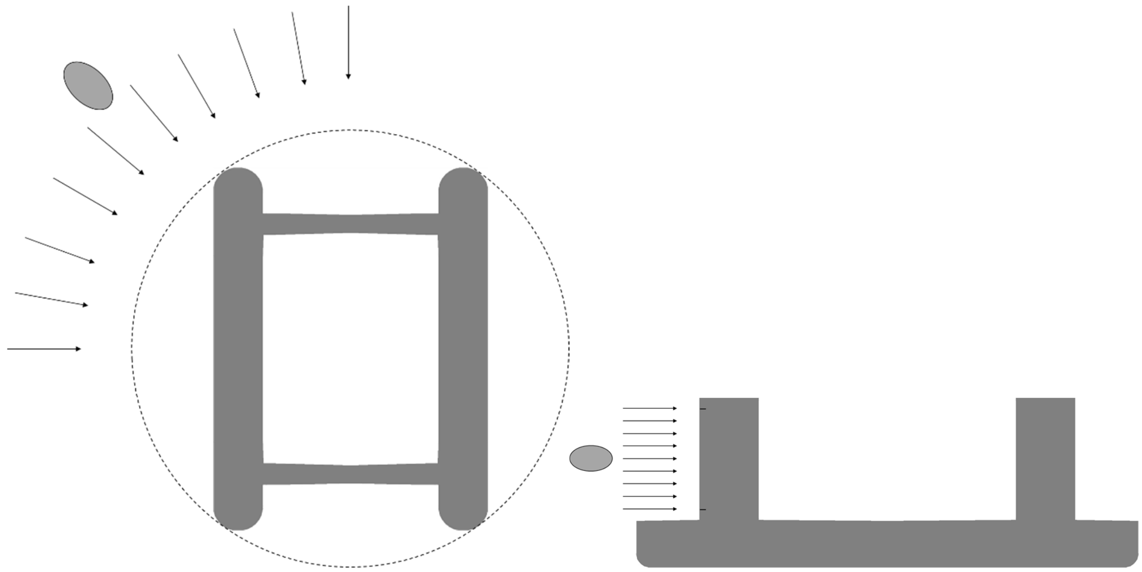

Figure 6.54: Simulated drift directions (left) and vertical offsets (right).

When it comes to the impact probability at different heights and impact velocities (relative motion), the results from ST19 are directly utilised and are re-presented in Figure 6.55 and Figure 6.56. Although new results of relative motion (compared to the ST19 results) were presented in Section 4.5.1, , we decided to utilise the old results from ST19 as shown in Figure 6.55 and Figure 6.56. The reason for this is that only the cuboidal glacial ice feature's impact velocities and height ranges were calculated in Section 4.5.1 and not the ellipsoidal ice. Additionally, we do not expect the results to be too much different as shown in earlier Table 4.5 and Table 4.6.

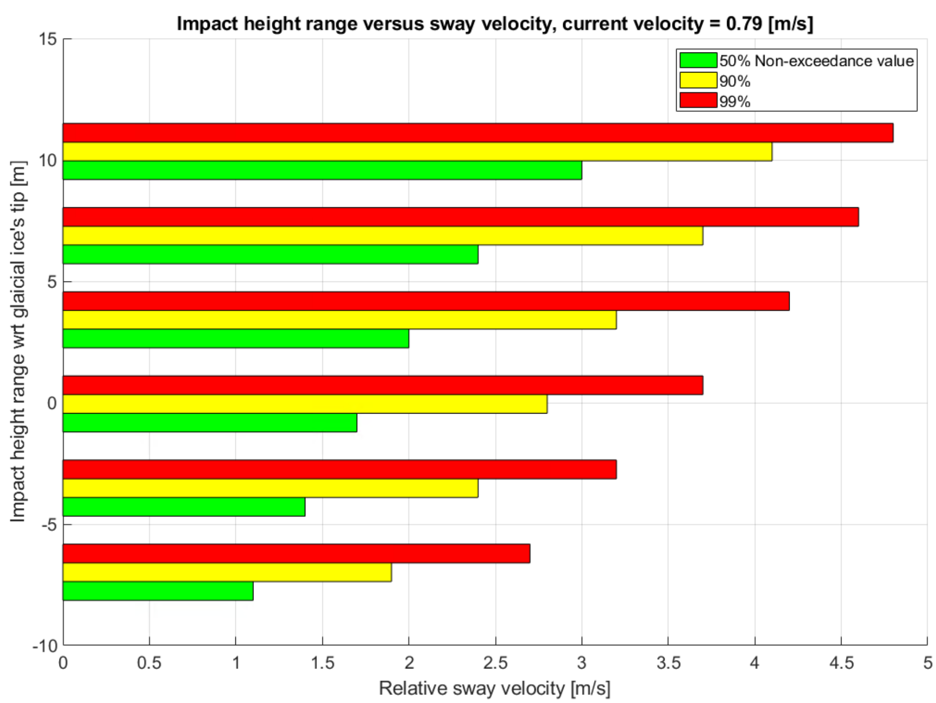

Figure 6.55: Impact velocities in sway direction at different heights with different non-exceedance levels (originally from Figure 3.13 of ST19 report).

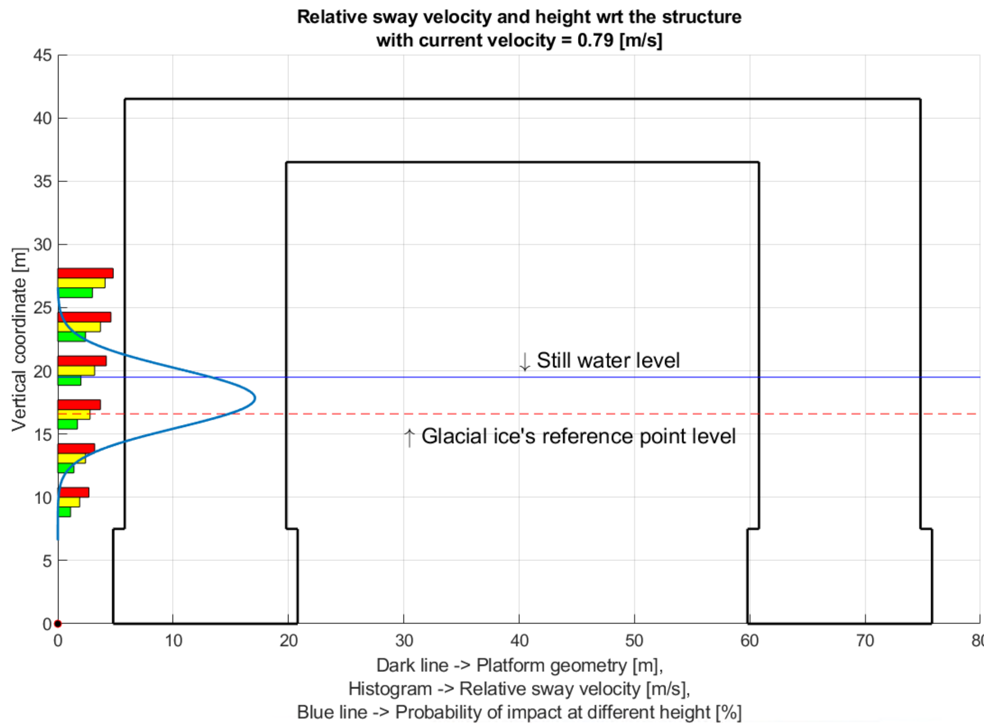

Figure 6.56: Impact velocities in sway direction and the associated impact probability at different heights with reference to the structure (originally from Figure 3.14 of ST19 report).

6.7.2.2 Simulation results by the weakly-coupled approach

With hundreds of impact simulations, the weakly-coupled analysis provides a 'deformation map', which is projected directly on the structure (see Figure 6.57 and Figure 6.58 for the two glacial ice geometries). These two figures identify the locations that are most sensitive to suffer structural damage/deformation for the given glacial ice geometry, indicated by pro-red zone colours. Apart from the spatial distribution of the structural deformation, the figures show that the maximum structural deformation is less than 0.6 m in most locations.

Within the around 1800 impact scenarios (3600 in total for both ice feature), the exact structural deformation statistics (i.e., cumulative distribution) is illustrated in Figure 6.59. The figure shows that the structural deformation for these two geometries are rather close to each other with a maximum deformation of 0.56 m and 0.58 m, respectively for the $2a$ = 15 m and $2a$ = 23 m scenarios. Moreover, more than 90% of the impact cases in both scenarios lead to structural deformation that is smaller than 0.36 m.

A similar trend is also observed for the 'total impact energy', 'the energy that needs to be dissipated by the structure or the ice'. These results are presented in Figure 6.60, Figure 6.61, and Figure 6.62. Given the predefined sizes of the glacial ice features' (see Figure 6.52) and wave conditions, the maximum total impact energy in both cases are less than 7.5 MJ. Moreover, more than 90% of the impact energies are less than 3.5 MJ.

The observed similarities in results for the $2a$ = 15 m and $2a$ = 23 m scenarios are expected. It was also shown in the fully-coupled analysis in Figure 6.33 that at low energy levels, the results for these two cases are quite close to each other.

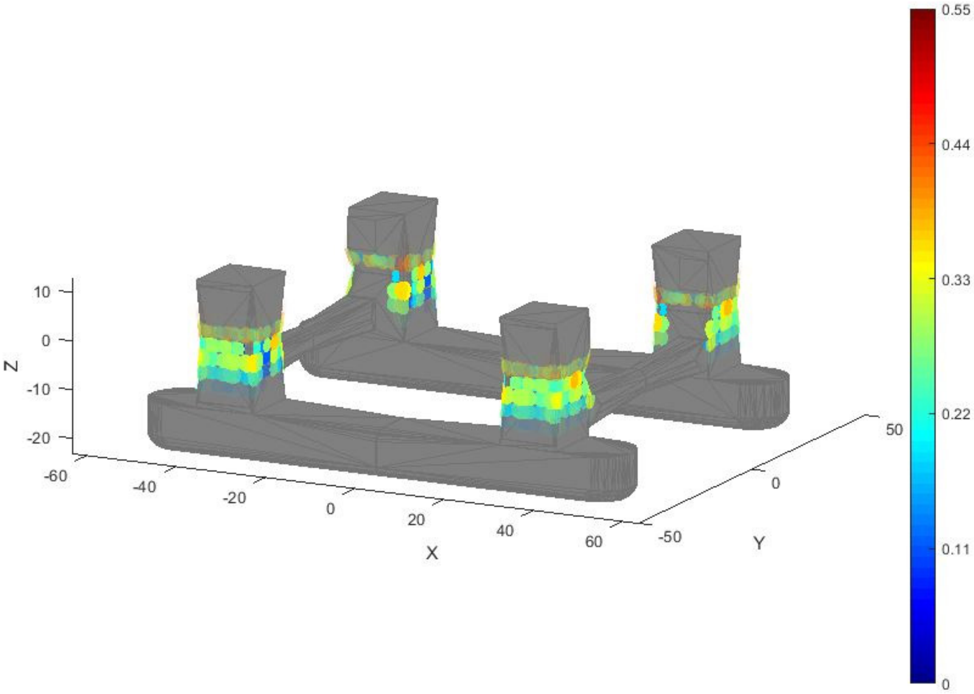

Figure 6.57 Deformation map on the structure for impacts with the glacial ice feature with 2a = 15 m (Figure 6.52a), unit: [m].

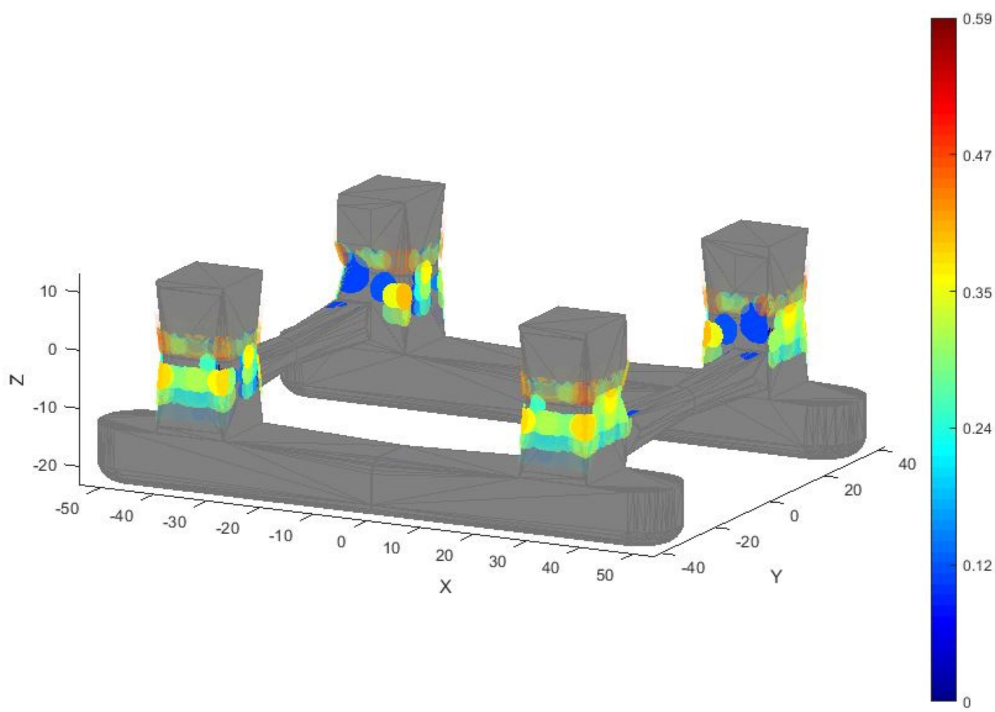

Figure 6.58 Deformation map on the structure for impacts with the glacial ice feature with 2a = 23 m (Figure 6.52b), unit: [m].

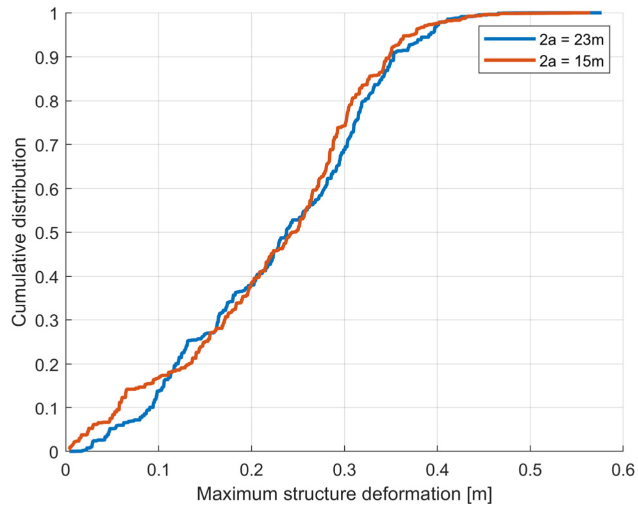

Figure 6.59 Cumulative distribution of the maximum structural deformation at various locations among from around 1800 impact scenarios.

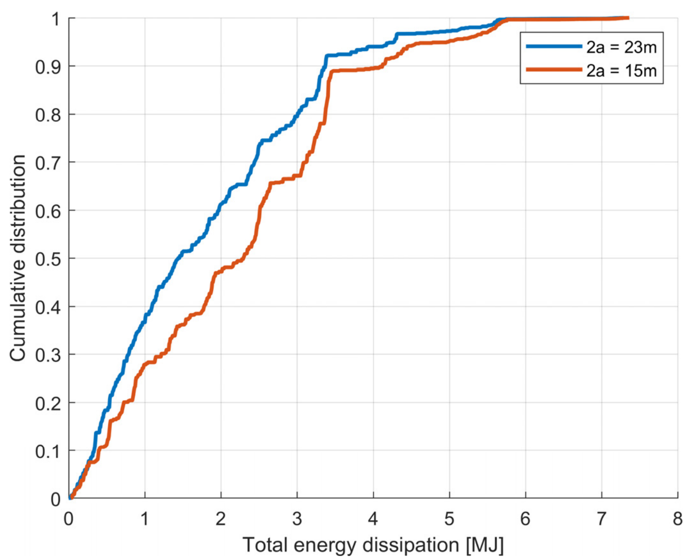

Figure 6.60 Cumulative distribution of the total impact energy (that needs to be dissipated) from around 1800 impact scenarios.

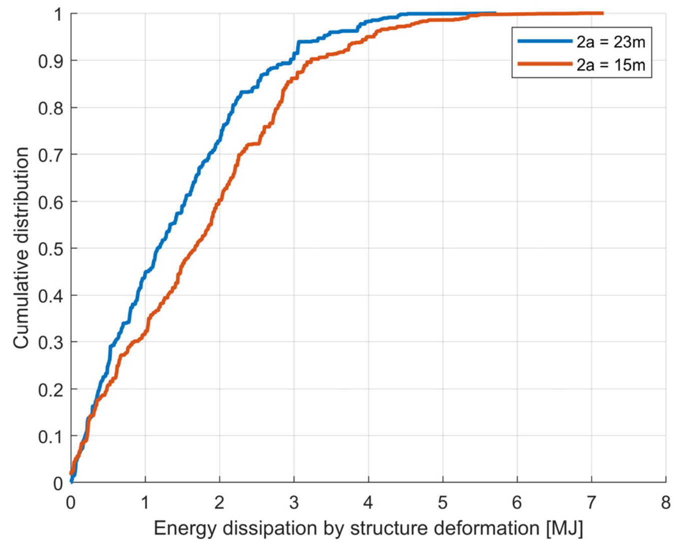

Figure 6.61 Cumulative distribution of the impact energy that is dissipated by the structure from around 1800 impact scenarios.

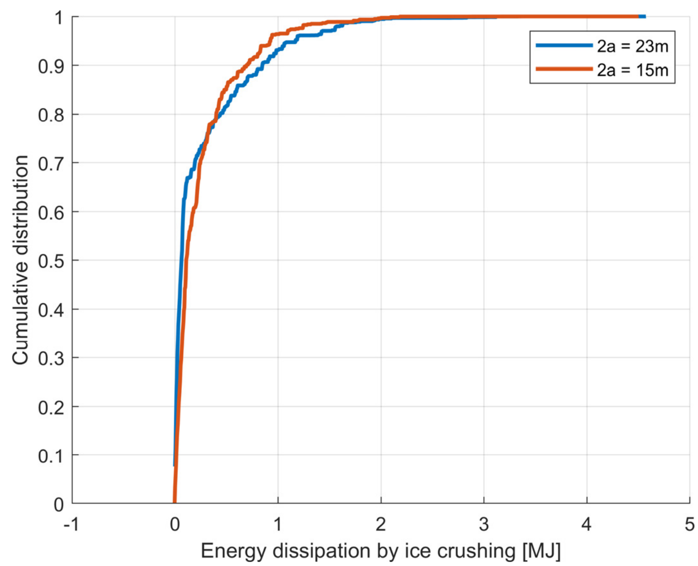

Figure 6.62 Cumulative distribution of the impact energy that is dissipated by the glacial ice feature from around 1800 impact scenarios.

It is emphasized that the above results are specific for the chosen glacial ice geometries. If a different sized ice feature is chosen, the total impact energy will be different, which in turn leads to different maximum structural deformations. It is particularly noticed, according to the study performed in Chapter 6 (Task #4), that the lower limit of the detectability of glacial ice should be 30 m instead of 15 m. The figures presented in this section are mainly valid for a glacial ice features with a characteristic length in the range of 15 m (see Figure 6.52). If the size increases from 15 m to 30 m, the maximum impact energy will be significantly increased; and the energy dissipation ratio shall also be different from that in Figure 6.61 and Figure 6.62.

6.8 Damage Assessment Comparison

In this chapter (Chapter 6), three different methods to perform damage assessment and evaluate the dissipation of impact energy in a shared manner were presented. Each of the three methods has their own advantages and application ranges. Implicitly, the 'integrated approach' and 'weakly-coupled approach' (i.e., Method #1 and #2) assume that the ice geometry does not change significantly during ice crushing such that the resulting F-D curve of the structure does not deviates much from the F-D curve of the structure that could be derived based on the rigid ice assumption. Once extensive ice crushing starts to occur, it will influence the structural deformation; this effect can only the tackled by the fully-coupled approach. As the glacial ice feature gets sharper, it is expected that deep ice crushing shall take place and, in this scenario, only the fully-coupled approach shall yield credible results. On the other hand, when the ice is rather blunt in the contact area, all three methods are expected to yield similar results.

A comparison of the damage assessment based on the three methods is presented in Figure 6.63 and Figure 6.64 for ellipsoidal ice with different sharpness impacting the stiffened panel of the column front. Favourable agreement between the weakly-coupled analysis (green curves) and the fully-coupled analysis (red curve) is observed for the blunt ice scenario (i.e., when ice radius of curvature divided by the stiffened panel length is larger than the critical value of 0.81). When the ice feature gets sharper, both the weakly-coupled and the integrated analysis start to deviate from the fully-coupled analysis.

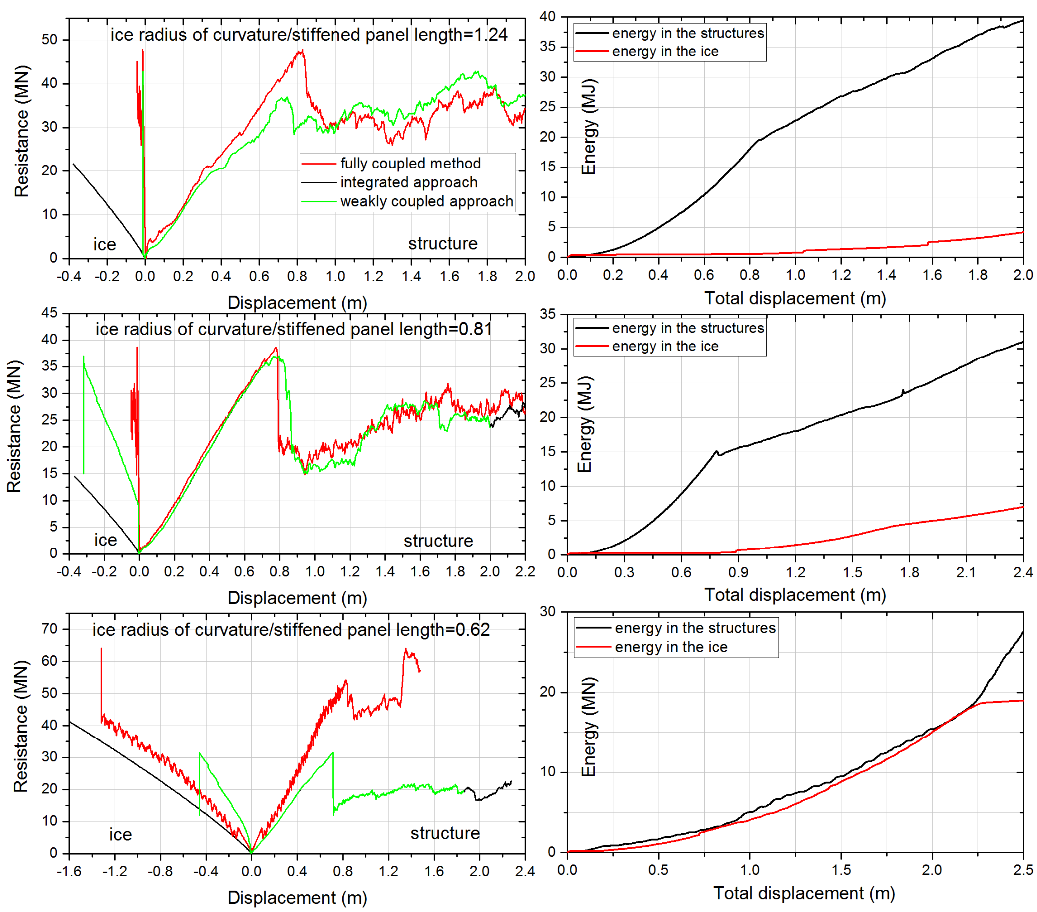

Figure 6.63 Damage prediction for the three methods for various glacial ice feature sharpness (from top to down are: $2a$ = 15, 23, 30 m).

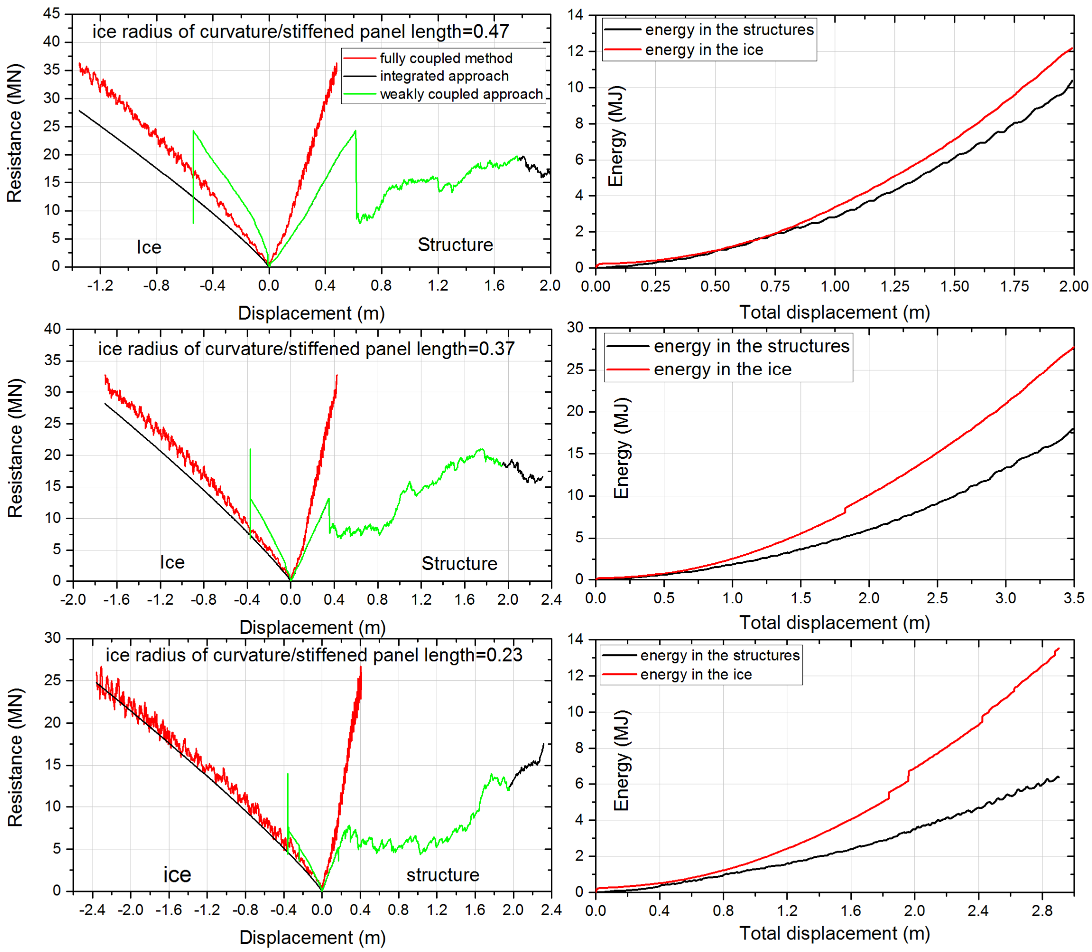

Figure 6.64 Damage prediction for the three methods for various glacial ice feature sharpness (from top to down are: $2a$ = 40, 50, 80 m).

By selecting the maximum structural deformation as an indicator of structural damage, we can plot the predictions of the three methods for various ice sharpness for a total energy dissipation of 7.5 MJ as shown in Figure 6.65. Two separate regions can be identified from Figure 6.65. In the blunt region, it is observed that the weakly-coupled analysis yields result rather close to the fully-coupled analysis; whereas the integrated analysis seems to be less conservative (or too “risky”). It is expected, however, that as the ice gets even blunter, these three methods shall yield identical results.

In the sharp ice region, where the ice crushes significantly and thus influence the structural deformation, only the fully-coupled analysis performs well. Compared to the fully-coupled analysis, both the weakly-coupled and integrated analysis appear to be far too conservative as they both overpredict significantly the structural deformation.

In between these two extreme regions, there is a transition zone (between ice’s radius of curvature / stiffened panel length ≈ 0.47 ~ 0.81) that the three methods are still producing close enough results. Within this transition zone, we observe a turning point (at the grey dashed line) when the ice’s radius of curvature over the stiffened panel length is around 0.47. When ice gets sharper than this turning point, Methods #1 and #2 start to deviate significantly from the prediction of Method #3. This turning point signifies the rising importance of ice crushing and its influence on structural deformation, as can be predicted by Method #3. Geometrically, this turning point also represents the situation when the ice feature's local area can nicely fit between the stiffened panel (i.e., the diameter of the ice feature's local area and the stiffened panel length become almost equal).

In summary, Figure 6.65 shows that when the ice feature gets blunter than the critical geometry (yellow dashed line), both the weakly-coupled and fully-coupled analysis yield satisfactory results; when the ice feature gets sharper than the turning point (grey dashed line), the results predicted by the fully-coupled analysis appears to be more trustworthy. In between the transition zone, the results predicted by the weakly-coupled approach seems to be reasonably close to those predicted by the fully-coupled analysis with a certain degree of conservatism. It is also believed that both the turning point and critical geometry of the ice feature are largely influenced by the structural dimension.

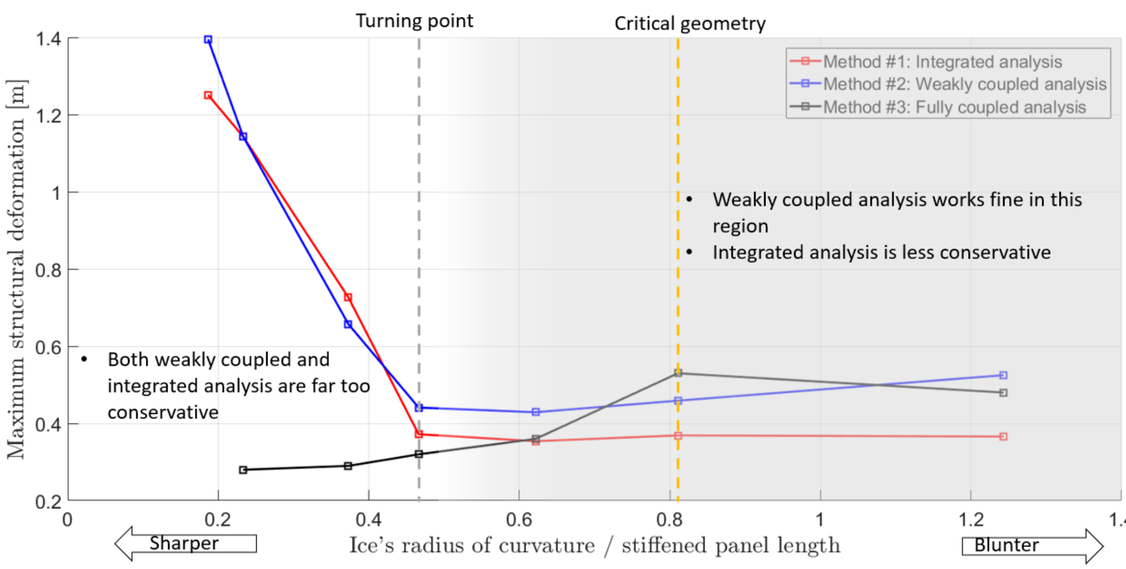

Figure 6.65 Maximum structural deformation with a total energy dissipation of 7.5 MJ for all three different methods for various glacial ice features' sharpness (from left to right, each marker of the same colour represents glacial ice feature with its long axis: 2*a* = 80, 50, 40, 30, 23, 15 m).

6.9 Summary of Task #3

The objective of Task #3's is to assess the influence of the local geometry (sharpness) on the damage prediction. The challenge lies in the fact that there are two consequences that vary with the local sharpness in a contradictory manner: the sharper the ice feature becomes, the easier it is to penetrate the structure; while on the other hand the easier it is to crush the ice. Given the same impact energy, the structure will be relatively safe for the extremely sharp and extremely blunt ice features. In between these two 'limiting cases', a critical scenario exists with a critical local sharpness that impose the maximum damage to the structure.

Three different methods were developed and utilised to evaluate different local sharpness's influence and to identify this critical geometry. These three methods are:

- Method #1: Integrated analysis
- Method #2: Weakly-coupled analysis

- Method #3: Fully-coupled analysis

The fully-coupled analysis is the most trustworthy method when it comes to analyse glacial ice feature with various local sharpness because the method includes a more realistic material model for ice and at the same time, includes an advanced fracture criterion for steel in the structural response analysis. However, this method requires extensive calibrations and can only be used in a few cases in practise. In Task #3, the Pond Inlet 'test data' derived process- based P-A curve was adopted to perform a case-by-case calibrations to the ice material model. In total, 6 calibrations were performed for each sharpness level. The calibrations were performed carefully including mesh sensitivity analyses. Upon successful calibrations, 6 sets of Nonlinear Finite Element (NLFEM) fully-coupled simulations were performed. Results from the fully-coupled simulations indicate that the relative strength of the structure and the ice is significantly influenced by the ice feature's local sharpness and the structural dimensions; the sharpness is meaningful only when it is measured relative to certain structural dimensions. For the tested cases, the critical sharpness is obtained when the ice feature's local radius of curvature is about 0.8 times the stiffened panel length. When the glacial ice feature gets blunter or sharper, less structural deformation/damage is expected. It should be noted that the critical ice sharpness is determined for the stiffened panels of the column front, where the ice is most likely to impact.

Weakly-coupled and integrated analysis were also adopted to perform damage assessment for these 6 local geometries. It is found that:

- The weakly-coupled and integrated analysis perform satisfactorily when the local sharpness is blunter than the critical geometry. In addition, the weakly-coupled analysis appears to be superior to the integrated analysis in this application range.
- When glacial ice feature gets sharper than the 'turning point', which represents the situation when the ice feature fits nicely in between the stiffened panels, both the weakly-coupled and integrated analysis appear to be conservative. This turning point signifies the growing importance of the ice crushing's influences on structural deformation as the ice gets sharper.
- In many ways, these three methods are complimentary to each other. For example, the 6 sharpness levels simulated by Method #3 were initially estimated by the Methods #1 and #2. In addition, Methods #1 and #2 were also utilised to give reference values supporting the calibration process of the ice material model used in Method #3.

With the identification of the critical local sharpness and the applicability range of the various methods, extensive damage assessments were performed with the weakly-coupled method. Unlike the fully-coupled method, the weakly-coupled analysis is computationally efficient and is capable of executing hundreds of impact simulations with little cost. With this method, we simulated two ice geometries (i.e., the critical ice geometry and a relatively blunt one) for approximately 3600 total impact scenarios. A deformation/damage map is directly produced by this method. From the map, one can easily identify the critical locations were the largest structural deformation/damage is expected. Given the impact energy of 7.5 MJ, the maximum structural deformation in both cases is found to be less than 0.6 m and 90% of the locations gets a deformation that is less than 0.36 m.

7 Task #4: Detectability of Small Glacial Ice Features

Glacial ice can pose a significant impact hazard to ships and offshore structures. In many areas with offshore structures and glacial ice, ice management is necessary to operate safely (McClintock et al., 2002, McClintock et al., 2007). For the ice management system to be able to respond to glacial ice on an encounter path, the first step is to detect them (Eik, 2008). The earlier glacial ice can be detected, the longer time is available to respond, underlining the importance of good detection ability. Similarly, ships require the ability to detect glacial ice to avoid impacts during navigation.

However, difficulties regarding the detection of small glacial ice features have been reported in literature (Rossiter et al., 1995, O'Connell, 2008). Small glacial ice features are defined as pieces of glacial ice with characteristic waterline lengths of less than 15 meters (McClintock et al., 2007). They can be further divided into two categories: bergy bits, with lengths of 5 to less than 15 meters, and growlers, with lengths of less than 5 meters. Other sources define glacial ice in terms of height above the sea surface as well (Rossiter et al., 1995). Here, bergy bits are defined to have heights of 1 meter to less than 5 meters, while growlers have heights of less than 1 meter.

In the previous report "Ptil – Konstruksjonssikkerhet i arktiske områder (ST5)" (Ekeberg et al., 2018), the authors assessed impacts between between floating structures and glacial ice features smaller than 15 meters. Later, in the report "ST19" (Lu et al., 2018), the limit of 15 meters was maintained for the impact analysis.

The rationale behind restricting the previous studies to glacial ice features smaller than 15 meters was explained in ST5. Here, the authors write that ice management systems have limited capability to detect and avoid a collision with glacial ice smaller than 15 meters, with a reference to (Rossiter et al., 1995). Rossiter et al. (1995) write that the radar technology at the time was only able to reliably detect smaller ice pieces in low to moderate sea states.

Interestingly, the authors do not state that glacial ice features smaller than specifically 15 meters are difficult to detect, only that the detection difficulties apply to small ice features. In addition, Rossiter et al. (1995) defines the size of small ice features differently than ST5. Growlers are defined to have a waterline length below 6 meters, while bergy bits have a waterline length from 6 meters to below 20 meters.

In the same report, Rossiter et al. (1995) write that enhanced signal processing through advances in computing has the potential to improve detection capabilities. It may be interesting to revisit the fundamental assumption that small glacial ice pieces cannot reliably be detected from the perspective of modern radar signal processing.

To assess how reasonable the 15-meter limit is, it is first necessary to review the capabilities to detect small glacial ice features. Secondly, instrumental factors will be discussed, as well as their ability to detect glacial ice. In the third and fourth subtask, radar images of icebergs and corresponding optical images will be examined.

7.1 Detection through marine radar

To discuss the detection of glacial ice features, we will restrict our focus to detection by marine radar. From our experience with icebreaker surveys in the Arctic, optical observations of glacial ice may be limited during winter season due to darkness, fog, snowfall, optical lens' water condensation etc. In the same way, optical sensors are restricted by the same problems as manual observations. Satellite images and radar are used for iceberg detection, but their value for tactical decisions is hampered by low resolution, infrequent sensing, and time delay in transferring data. On the other hand, marine radar provides immediate tactical information about the vicinity, and although radar performance declines in high waves and heavy rain, it provides more information than visual observations in such conditions.

Our experiences are shared with other authors in literature. For example, (McClintock et al., 2007) state the following based on experiences from iceberg management at the Grand Banks:

"*Visual iceberg detection, whether from offshore facilities, supply vessels or aircraft, is always best but is severely limited by fog. Consequently, there is a heavy reliance on radar systems for iceberg detection regardless of the platform. Locally at Grand Banks facilities, detection is either visual or by marine radar. Regionally, it is done by aircraft, supply vessels and satellites, and further afield using aircraft or satellite.*" (McClintock et al., 2007)

Another actor with a similar experience was Equinor. McClintock et al. (2002) performed drilling trials in the Fylla Bank area west of Greenland for ten weeks during the summer of 2000. The Fylla area resembles the Grand Banks area in several aspects, including the numerous icebergs, frequently strong winds and currents, and poor visibility. They found that marine radar was the most important detection tool for tactical purposes. In their case, the combination of visual and radar sightings from their support vessels provided the basis for their ice management decisions. They had access to RADARSAT data, which they found useful as a source of information from a strategic perspective, but not tactical. For other operations with similar ice management needs, they recommended using radar with detection range of 24 miles and 360-degree coverage, in addition to enhanced capability to detect small glacier ice features.

7.2 Marine Radar

7.2.1 Basic principles

Radar (formerly the acronym RADAR, meaning Radio Detection And Ranging) is an instrument which transmits radio or microwave frequency electromagnetic waves into its surroundings and detects when objects in the vicinity reflects them (Richards et al., 2010). The reflected signal is captured by a receiver antenna, amplified and converted into an electronic signal. The signal is processed and finally displayed on a screen. Different objects will reflect radio waves differently, which results in different signals. That makes it possible to identify different objects on a radar screen, as an object will likely reflect radio waves differently than its surroundings.

The amount of radio waves received from an object is expressed in terms of signal power P_r, measured in watts. The received signal power is dependent on several different parameters, summarized in the so-called radar range equation:

$$P_r = \frac{P_t G_t G_r \lambda^2 \sigma}{(4\pi)^3 R^4} \tag{7.1}$$

Here, P_t is the peak transmitted power in watts, G_t and G_r are the gains of the transmitter and receiver antenna respectively, λ is the wavelength of the electromagnetic waves, R is the distance from the radar to the target, and σ is the mean radar cross-section of the object, measured in square meters (Richards et al., 2010).

The radar cross-section of an object is a measure of the amount of incoming radio energy on the object that is reflected towards the source. Essentially, it is the reflective strength of an object, and it is the “size” of the object as seen by radar. For glacial ice, it will be proportional to the exposed area above water. However, the radar cross-section is not only the inherent property of an object. It is also affected by environmental parameters, such as wind, rain and snow. The effect that environmental disturbances have on received signal power can be included in the radar cross-section, which is why it is usually defined as the mean reflectivity over time.

There are several important things to note about the radar range equation and its variables, which affect our understanding of the detection of glacial ice features. Firstly, note that only the radar cross-section factor and distance are dependent upon the radar target, the other factors are related to the radar system and will stay constant when the same radar with the same settings are used.

Secondly, it should be noted that there is a large relative difference in how each parameter scales with the received signal power. The received signal power scales linearly with the radar cross-section σ. However, it also scales inversely with the fourth root of the distance R, i.e. $P_r \sim 1/R^4$. A small change in distance will have a much greater effect on the received power than a similar change in the radar cross-section.

7.2.2 Marine radar parameters

The most common marine radars in use on vessels today are classified as either X-band or S-band radars, depending on their frequency and wavelength (Canadian Coast Guard, 2012). X-band operates between 8-12 GHz, typically at 10 GHz (3 cm wavelength). S-band operates between 2-4 GHz, typically at 3 GHz (10 cm wavelength). The difference in wavelength results in a difference in radar return, and they therefore suit different purposes.

Generally, X-band provides more detail with a higher resolution (McClintock et al., 2007, Canadian Coast Guard, 2012). According to Rossiter et al. (1995), X-band also has longer iceberg detection ranges. However, S-band has better performance in heavy sea clutter and in poor weather conditions, such as dense fog, rain and snow. Radar performance in such conditions will be discussed further under section 7.7.

Another important difference in the performance of X-band and S-band marine radar comes from the fact that the reflectivity and radar cross-section of glacial ice is highly frequency dependent (C-CORE, 2007). The radar cross-section for glacial ice generally increases with frequency, meaning that reflectivity will be higher for X-band radar compared to S-band.

There are several other technical parameters involved in detection by marine radar, which will be discussed further in section 7.8.

7.3 Challenges of detecting glacial ice with radar

One of the factors which make the radar detection of icebergs challenging is their relatively poor radio wave reflectivity compared to their size, caused by the low electrical conductivity of glacial ice. Objects of the same size but with better conductivity, such as metal ships, will present a much larger radar signal. The fact that sea water is conductive makes the iceberg radio reflectivity even smaller relative to its surroundings. The poor reflectivity of glacial ice results in a similarly low radar cross-section compared to other objects with the same projected area. This is shown in Table 7.1.

Table 7.1: An overview of the radar cross-section of glacial ice compared to other materials. Adapted from (Rossiter et al., 1995).

Target	Radar Cross-section (m^2)	Projected Area (m^2)
Growler	0.01 - 0.10	2
Bergy bit	0.5 - 1.0	60
Small iceberg	5 - 10	400
Supply vessel	150	400
Liferaft (4 person)	0.25 - 0.50	3
Steel sphere (1.13 m diameter)	1	1

As was shown in Eq. (7.1), the received radar power scales linearly with radar cross-section. Thus, Table 7.1 shows that the reflected signal from a supply vessel is 10-15 times stronger than a small iceberg of the same size at the same distance.

In Task #4, we are mainly focusing on small glacial ice features, e.g., bergy bits and growlers. As shown in Table 7.1, their respective radar cross-section area is even one or two magnitudes lower than small icebergs. This further increases the detection difficulties. In the forthcoming sections, we will describe and quantify related parameters that influences the detectability. These to-be-discussed parameters are listed as following:

- Glacial ice's size and shape
- Distance
- Environmental parameters
    a) Wave condition
    b) Glacial ice's drift speed
    c) Atmospheric conditions.

7.4 Definition of detection

To be able to discuss the detectability of glacial ice with marine radar, it is important to define what detection is, as well as the probability of detection. When should glacial ice features be considered detected?

(Rossiter et al., 1995) defines the probability of detecting an iceberg as the percentage of scans the radar echo from the iceberg appears in. I.e. if the radar echo from an iceberg appears in seven out of ten scans at a certain distance from the radar, the probability of detection is 70%. Then, the authors apply a binary detection criterion of 50%, where an iceberg is considered "detected" if the probability of detection at that range is above 50%.

In the following task, we will use the same definition of Probability Of Detection (POD) as Rossiter et al. (1995).

It is difficult to set a general minimum criterion for an acceptable POD. Different users will have different demands of their ice detection system depending on their area of application. For example, the acceptable POD will likely be different for an ice management system compared to a vessel navigating in waters with occurrences of glacial ice. Therefore, this report will not define a minimum acceptable POD, but will instead focus more on how the POD changes with several factors.

7.5 Size and shape

It has been discussed how small glacial ice features, like bergy bits and growlers, can be very difficult to detect with radar. Bergy bits have a height of 1-5 meters and will therefore have a small radar cross-section and shadow. If the bergy bit is surrounded by open water or a smooth layer of first-year ice, its radar shadow may be visible, and detection will be more likely. However, if the bergy bit is surrounded by pack ice, it can be partly obscured behind ridges and rafted ice. In broken pack ice, its radar shadow may additionally be difficult to discern from the open water between the ice floes (Canadian Coast Guard, 2012). An example of this will be presented in section 7.9.1.

Growlers have a smaller freeboard than bergy bits and are thus even harder to detect. The problems that the surroundings of the iceberg can cause on detectability of bergy bits are even worse for growlers, because of their smaller cross-section and shadow. Consequently, the detection of small icebergs can be greatly hindered or hampered by their immediate surroundings.

The shape of the glacial ice features can have a significant effect on its effective radar cross-section. Typically, rounder, dome-shaped features will have smaller radar cross-sections compared to features that have the same projected area, but with more edges and corners in the direction of the radar, such as features with cuboid geometry.

There is a certain correlation between iceberg size and shape. Especially smaller glacial ice features, such as growlers and bergy bits, tend to have more spherical geometry, as they are more quickly eroded by water after calving from an iceberg (Canadian Coast Guard, 2012). The relatively rapid shape erosion makes detecting small ice features even harder.

7.6 Distance

The radar range Eq. (7.1) shows that the theoretical power of the radar return signal scales with $1/\mathrm{R}^4$, where R is the distance to the target. Essentially, the return signal is drastically lower for distant objects compared to closer objects. This is also the case for icebergs, where a comparatively weak iceberg radar signal is further reduced at range.

However, that does not mean it is always optimal for glacial ice detection to be as close as possible. At closer ranges, the radar return signal from the sea (sea clutter) becomes large, which may partly drown out the radar signal from the glacial ice. Usually, there are some optimal radar ranges at which detection is easiest. The Canadian Coast Guard (2012) suggests that the best working distance for detection of ice in general is around 2 to 3 nautical miles (around 3.70 km to 5.56 km).

Examples of how the relative radar return signal varies with distance will be demonstrated in section 7.9. Other examples of modelling work on the subject can be found in literature, like in (Rossiter et al., 1995). Here, the authors base themselves on modelling work of the radar return from icebergs done by (Cammaert et al., 1992). The example is illustrated in Figure 7.1. In this case, they found how the probability of detection for icebergs of different lengths varied depending on distance. An overview of the radar specifications used for the modelling work can be found in Table 7.2.

Importantly, the radar modelled in Figure 7.1 was assumed to be mounted at a platform, 75 meters above sea level. The height of the radar above sea level will have consequences for both the influence of sea clutter and the maximum radar range (C-CORE, 2007). Generally, sea clutter is a larger problem at close ranges with a taller radar. Also, the maximum radar range will increase with a taller radar, because the radar range is horizon limited.

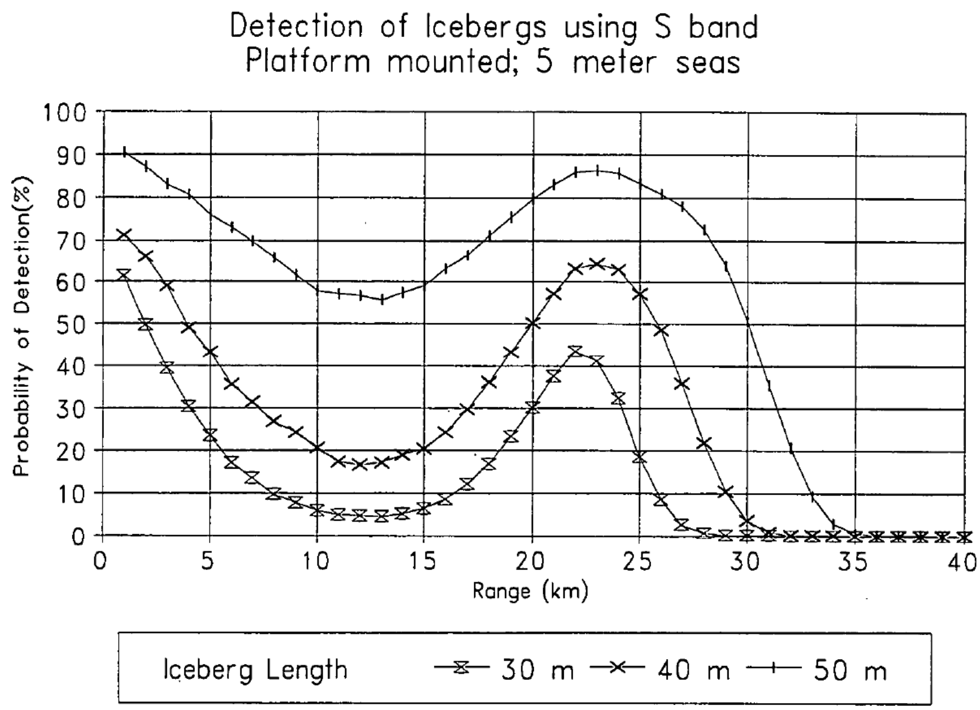

Figure 7.1 Probability of detection for icebergs in 5 meter seas by S-band radio mounted 75 meter above sea level. Adapted from Rossiter et al. (1995).

Table 7.2: Marine radar specifications used for the modelling work done by (Cammaert et al., 1992) as referenced by (Rossiter et al., 1995). Adapted from (Rossiter et al., 1995).

	X band	S band
Frequency (GHz)	9.5	3.0
Transmitter power (kW)	50	30
Receiver noise figure (dB)	5	5
Receiver bandwidth (MHz)	4	4
Pulse length (ns)	250	250
Range resolution (m)	37.5	37.5
Pulse repetition frequency (Hz)	1600	1600
Antenna gain (dB)	32	27
Horizontal beamwidth (degrees)	0.8	2.0
Antenna speed (rpm)	30	30
Antenna height (m)	75	75 and 15[1]
Signal processing :		
Pulse-to-pulse integration	Yes	Yes
Scan-to-scan integration	No	No
Typical clutter controls such as Sensitivity Time Control (STC)[2]	Yes	Yes

7.7 Environmental parameters

There are several parameters affecting the detection of glacial ice features by marine radar. The most important factors can roughly be divided into two categories: environmental and instrumental. The environmental parameters include examples like wave heights and atmospheric conditions like wind and rain. Instrumental factors include the type of marine radar in use and its capabilities, as well as the radar signal processing.

In the following sections, the most important environmental parameters will be examined and their effect on the detection of glacial ice features will be discussed.

7.7.1 Wave height

The wave height/amplitude distribution may be one of the most important parameters influencing the detection of glacial ice features. Marine radar relies on a direct line of sight towards its targets, and severe sea states with high waves can easily obscure small icebergs or glacial ice features. In addition, high waves will lead to increased radar return from the sea, known as sea clutter. Major sea clutter can severely limit the ability of radar to detect icebergs, while even growler-sized icebergs can potentially be detected in calm seas (Rossiter et al., 1995). As an example, during their drilling trials at Fylla west of Greenland, the Equinor vessels were hit by a severe storm (McClintock et al., 2002). The storm caused high enough waves and significant sea clutter to make the radars unusable for iceberg detection.

Fuglem et al. (1999) model the probability of detecting an iceberg with waterline length L as a function of the significant wave height H_S in a stationary sea state. They model the Probability Of Detection (POD) as the cumulative probability of a normal distribution with mean 6 H_S and standard deviation 1.8 H_S. Eik and Gudmestad (2010) expresses this distribution as:

$$POD(L|H_S) = F_N(L, \mu = 6H_S, \sigma = 1.8H_S) \tag{7.2}$$

Thus, when $L = 6H_S$, the Probability Of Detection for that iceberg is 0.5. The reasoning behind using the significant wave height H_S as the sole environmental parameter influencing the detection is contained in an earlier article, (Fuglem et al., 1996). Here, they write how the sea state is important in determining the drift and wave-induced motion of the icebergs. They also point out how sea state is reasonably well correlated with wind, which affects radar detection.

Eik and Gudmestad (2010) refer to the same model for the probability of detection shown in Eq. (7.2). The authors partly base their probabilistic analysis of the need for iceberg management on the same formula for POD as expressed by (Fuglem et al., 1999). Eik and Gudmestad (2010) acknowledge that other parameters influence the POD, such as distance to target, size and shape of the target, precipitation and operator skill. However, they point out that it is unfeasible to include all dependencies in a statistical model. Therefore, they focus on describing the sea state as accurately as possible, as they consider it the most important factor.

Eik and Gudmestad (2010) illustrate the POD for icebergs with different sizes as shown in Figure 7.2.

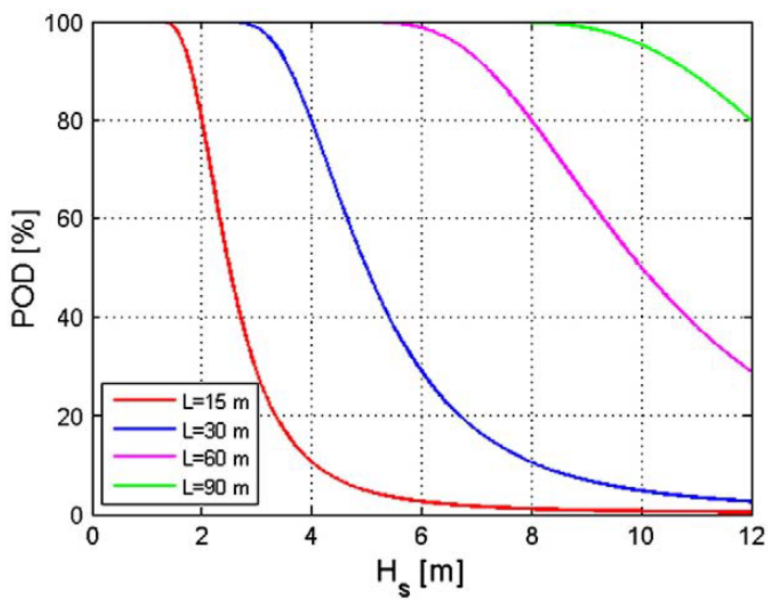

Figure 7.2 The Probability Of Detection (POD) to detect glacial ice features with different lengths L depending on sea state H_S. Adapted from Eik and Gudmestad (2010).

The figure clearly shows a major decrease in POD for small glacial ice features at certain wave heights. The POD for the small glacial ice feature's size limit that we are concerned with, e.g. with $L = 15$ m and heights of 1-5 meters, decreases significantly with only a few meters of significant wave height.

Given Eq. (7.2), we can evaluate the glacial ice features' size limit in different wave conditions. For example, the significant wave height's statistics in Block A of the Barents Sea is illustrated in Figure 7.3. For the one-year return wave condition (i.e., $q = 0.63$ curve), the minimum and maximum wave height are around 4 m in July and 9 m in Feb. According to Eq. (7.2), to attain a POD of 50%, the glacial ice feature must be larger than 24 m and 54 m respectively, both of which are larger than the 15 m stated previously.

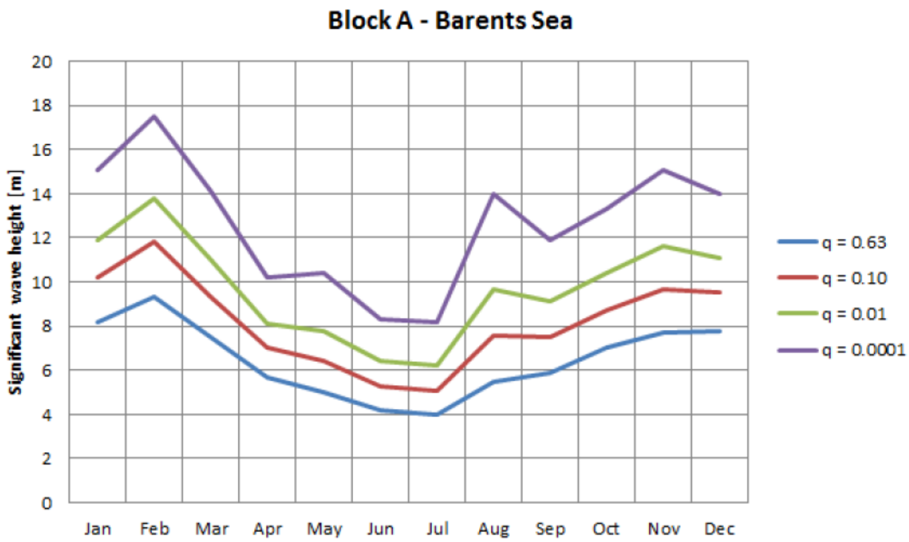

Figure 7.3 Monthly extreme values of significant wave height (H_S) of annual probability of exceedance in Block A of Barents Sea (from (Dezecot and Eik, 2015)).

However, Eik and Gudmestad (2010) raised some concerns regarding the detection distribution. They write:

"The inadequacy of the distribution for detection which has been used to demonstrate the approach has been discussed. In addition to the need for including time elapsed by the iceberg within the radar range, there are also a number of other concerns:

• The applied distribution for iceberg detection does only take into account the iceberg size and sea state. It is known that iceberg shapes which are more rounded, such as the domed shaped icebergs, are more difficult to detect thus the probability of detection should also be conditional on the iceberg shape.
• Other parameters such as distance to target and precipitation are also considered as important for the detection capabilities and should consequently be incorporated into the detection model.
• Further, it will also be beneficial to have detection models quantifying the detection capabilities by other means such as satellite images and aerial reconnaissance. »
(Eik and Gudmestad, 2010)

Clearly, a more robust analysis of the probability of detection taking these parameters into account is needed.

Other authors have also performed modelling of the detection of glacial ice with marine radar based on sea state. McClintock et al. (2002) contains a model of the expected performance of an S-band enhanced marine radar, shown in Figure 7.4. In the model, the radar signal processor is assumed to average over 20 scans. Scan averaging is a radar processing algorithm which will be explained in section 7.8.1.

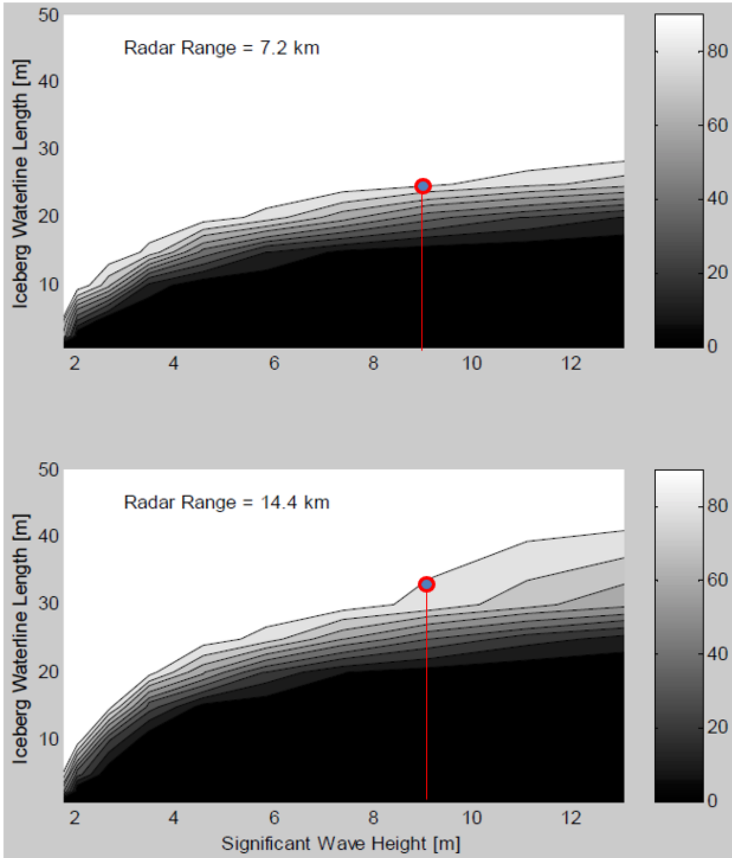

Figure 7.4 The modelled detection probability of glacial ice with different waterline lengths at two different radar ranges depending on the significant wave height. The colouration shows the detection probability, with black being 0% and white being 100% chance of detection. Adapted from (McClintock et al., 2002).

If we insert the significant wave heights of 4 m and 9 m into Figure 7.4, we see that the enhanced marine radar can lead to a large increase in the POD. A summarised comparison is shown in the following table:

Table 7.3: A comparison of the minimum sizes of glacial ice features that can be detected for conventional and enhanced marine radars. In this comparison, the POD criterion for the conventional radar is ≥ 50%, while it is 100% for the enhanced marine radar.

Wave height	Conventional radar with POD ≥ 50%	Enhanced radar with POD = 100%	
	Range = 'unknown'	Range = 7.2 km	Range = 14.4 km
4 m	≥24 m	≥18 m	≥21 m
9 m	≥54 m	≥25 m	≥32 m

Given the chosen typical wave heights, all the numbers in this table indicate that 15 m is a too small (or too optimistic) number to define a detectable glacial ice feature's lower limit.

7.7.2 Iceberg drift trajectory and speed

Eik and Gudmestad (2010) propose that the iceberg drift trajectory and speed is important for the probability of detection. Variations in iceberg drift trajectories and speed will impact the identification of the iceberg and the total time that the iceberg is visible. A slower drifting iceberg will spend more time in the ice surveillance zone and in optimal radar range. This gives the radar operators more time to react and identify the radar signal as an iceberg. Additionally, a slow iceberg will be easier to spot in cases of poor weather conditions and in cases of iceberg rotation, which will change the iceberg radar signature. Consequently, the POD for such icebergs will be larger.

Eik and Gudmestad (2010) therefore suggest that to attain an accurate POD from an ice management perspective, a third parameter in addition to iceberg length L and wave height H_S should be included in the model shown in Eq. (7.2): the time spent by the iceberg in radar range prior to detection.

It is reasonable that larger significant wave heights H_S will lead to larger iceberg drift velocities, as described in (Fuglem et al., 1996). As such, the effect of iceberg drift velocity on the probability of detection can be said to be partly accounted for in Eq. (7.2).

7.7.3 Atmospheric conditions

Atmospheric conditions such as rain, fog or snow can reduce the ability to detect glacial ice with radar (Richards et al., 2010). When radar waves travel through the atmosphere, they will experience a certain reduction in power known as attenuation. The magnitude of the attenuation depends on the environment that the electromagnetic (EM) waves must travel through and is mainly caused by two physical phenomena: absorption and scattering. When there are certain gases or particulates in the air, such as raindrops, ice crystals or even just oxygen molecules, some EM-wave energy will be absorbed and converted to heat within the particles or particulates. Further signal power is lost when the particulates are big enough to scatter EM-waves, meaning some waves are reflected into a different direction than towards the radar receiver.

The wave power reduction is the ratio of the attenuated wave to the same wave without attenuation, i.e. in vacuum. The one-way attenuation from particulates in dB can be expressed as:

$$F^2(dB) = \alpha R$$

where α is the one-way attenuation coefficient in dB/km, and R is the distance to the radar target in kilometres (Richards et al., 2010). In this case, it is assumed that detection ranges are short enough that the atmospheric conditions are homogeneous from the transmitter to the target, and α is constant.

To get an idea of the relative power loss caused by different atmospheric effects, Richards et al. (2010) lists some typical attenuation coefficients in dB/km, seen in Table 7.4.

Table 7.4: One-way attenuation coefficients for some select atmospherics for 10 GHz radar (X-band). Adapted from (Richards et al., 2010).

Description	Attenuation Coefficient (dB/km)	Water Content (g/m^3)	Remarks
Clear air	0.01	7.5	Based on sea-level elevation, 42% relative humidity, and 20°C temperature
Dust	0.004	0.1	Based on sea-level elevation, 0 relative humidity, and 20°C temperature
Radiation fog	0.0688	0.1	Based on sea-level elevation, 100% relative humidity, and 20°C temperature
Fog oil (Engine smoke)	0.43	0.0001	Based on sea-level elevation, 0 relative humidity, and 20°C temperature
Rain (4 mm/hr) (10 mm/hr)	0.05 0.17	n/a[1]	Based on sea-level elevation, 100% relative humidity, and 20°C temperature
Snow (2 mm/hr)	0.0016	n/a[1]	Based on sea-level elevation, 100% relative humidity, and 0°C temperature
Special smokes and obscurants	8.6	0.001	Based on sea-level elevation, 0 relative humidity, and 20°C temperature

[1]Attenuation coefficients for rain and snow are based primarily on fall rate in this attenuation model.

The table shows that heavy rain causes a relatively large reduction in returned signal power compared to other natural atmospheric phenomena like snow, but this depends on the rain and snow rate.

The attenuation caused by atmospheric conditions typically get more severe as the radar frequency increases. Therefore, the use of S-band (commonly 3 GHz) is preferable in poor weather conditions compared to X-band radar (commonly 10 GHz), even though X-band generally provides better ice detail (Canadian Coast Guard, 2012).

Rossiter et al. (1995) illustrates the change in probability of detection of icebergs from atmospheric conditions based on modelling work by Cammaert et al. (1992). They are repeated here, in Figure 7.5, Figure 7.6 and Figure 7.7.

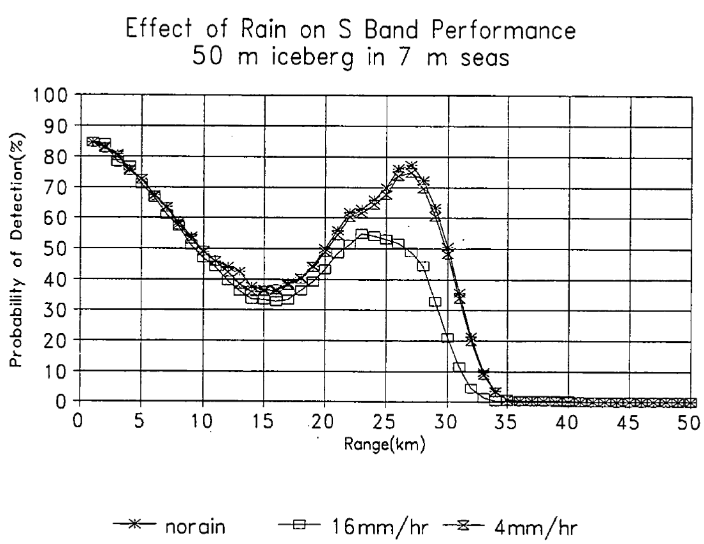

Figure 7.5 The effect of different fall rates of rain on the detection of a 50-meter iceberg in 7-meter seas by a S-band radar mounted at 75 meters height. Adapted from (Rossiter et al., 1995).

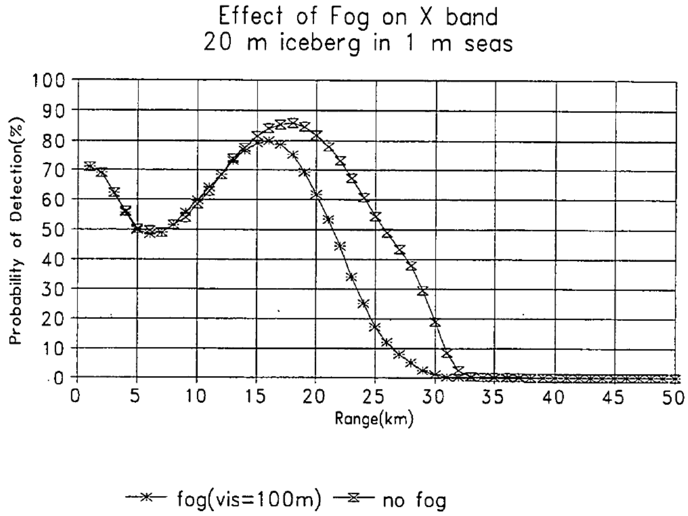

Figure 7.6 The effect of fog on the detection of a 20-meter iceberg in 1-meter seas by a X-band radar mounted at 75 meters height. Adapted from (Rossiter et al., 1995).

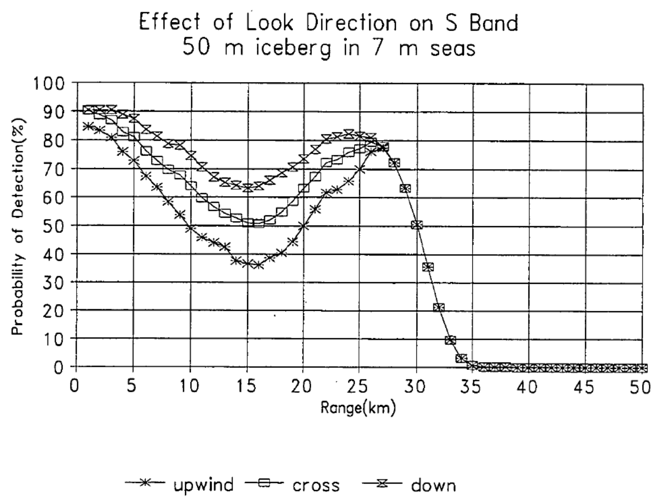

Figure 7.7 The effect of wind direction on the probability of detection of a 50-meter iceberg in 7-meter seas by a S-band radar. Adapted from (Rossiter et al., 1995).

It should be noted that Rossiter et al. (1995) do not include the details of how the modelling work was done, except for the technical parameters of the radar shown in Table 7.2. The quantitative decreases in probability of detection should therefore not be used directly without further verification. However, the figures still give a qualitative idea of how atmospheric conditions affect the probability of detection. In addition, the decrease in performance during heavy rain, fog and wind reflected in the figures is mentioned in other sources (Richards et al., 2010), and serve as a verification of the trends shown in the figures.

7.8 Screening radar systems

There are a range of different technical parameters which will affect the performance of marine radars. Some have been discussed in section 7.2.2, others will be discussed in the following sections. We concern ourselves not just with the parameters of the radar, but also the radar signal processing. Improved radar signal processing can lead to drastic improvements in glacial ice detection capabilities, and their parameters are therefore important for our purpose.

There are several parameters that can often be adjusted by the operator of the radar. Some of these are pulse length, display range, gain and threshold.

The pulse length, also called pulse width, is the time duration that the radar transmits electromagnetic waves for each pulse sent out. On many marine radars, pulse lengths are linked to the detection range, where certain pulse lengths are only available for certain detection ranges. Short pulse length is best for detection of targets in sea clutter and has better near range performance. Longer pulse lengths give better detection range. The best iceberg detection strategy is typically to change between different pulse lengths depending on the immediate tactical situation.

Display range is the range which is displayed on the radar screen. Gain is related to the sensitivity of the detection, with all signals becoming more intensive at higher gain. Setting a minimum threshold will remove signals that are below a certain strength from being displayed at all. To detect small targets in clutter, the gain must be set large enough to get an acceptable signal from the targets. The threshold must be set to a level where most of the clutter is removed while still being able to detect the targets of interest (Richards et al., 2010).

7.8.1 Enhanced marine radar

During the past 20 years, increases in computing power has led to large improvements in radar signal processing, known as enhanced marine radar (Rossiter et al., 1995, Canadian Coast Guard, 2012). The improved signal processing has made it easier to detect targets in sea clutter, as processing radar signals across several pulses and scans in real time has become more viable. For example, the radar return signals can be averaged over several scans, known as scan integration or incoherent averaging. By using this algorithm, signals from randomly distributed targets like noise or sea clutter are smoothed out while signals from slower or stationary targets are enhanced (C-CORE, 2007). This is naturally very beneficial in terms of detecting slow icebergs in high waves.

In recent years, several radar solutions have been developed specifically for detecting sea ice and glacial ice, so-called ice radars. These solutions typically have one thing in common: advanced radar signal processing which is specifically tuned to detect ice. An example of a comparison between conventional marine radar and ice radar can be seen in Figure 7.8.

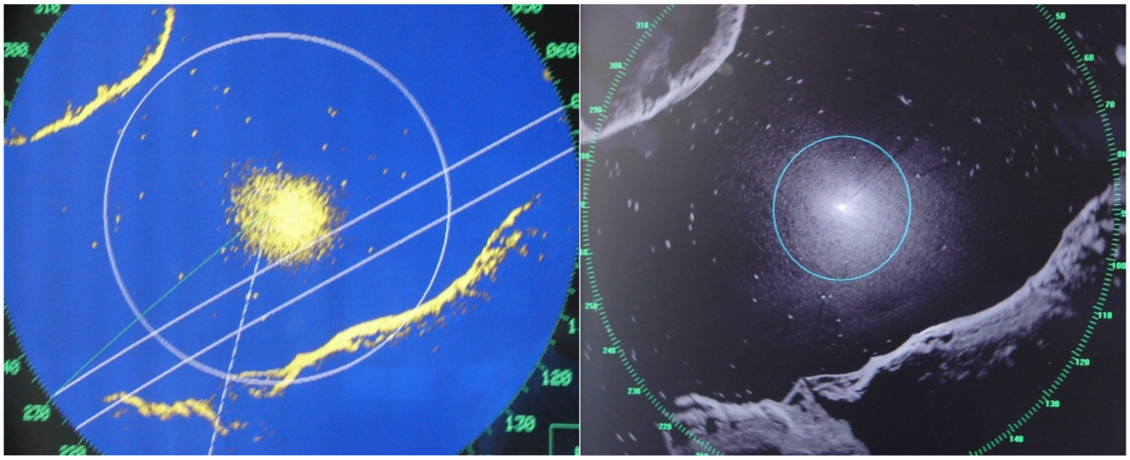

Figure 7.8 Standard (left) and enhanced (right) X-band marine radar images of the same scene. Adapted from (O'Connell, 2008).

In the following subsection, an example of an ice radar will be discussed as well as its ability to detect small glacial ice features.

7.8.2 Example of an ice radar: Rutter sigma S6 Ice Navigator™

Rutter Inc. is an example of a company that has developed a radar solution specialized for ice navigation and ice management, known as the "sigma S6 Ice Navigator™" (Rutter, 2019a, Rutter, 2019b, Rutter, 2019c). The sigma S6 Ice Navigator connects to most commercially available marine radars as a "bolt-on" solution to improve their capabilities. That is, the sigma S6 is an improvement to the radar signal processing for ice detection. They also offer to supply a dedicated radar as input for the sigma S6 system if needed.

In terms of imaging small glacial ice features, Rutter Inc. advertises that the sigma S6 system offers large improvements over conventional marine radar (Rutter, 2019c). Their claims of the capabilities of sigma S6 Ice Navigator to detect small glacial ice features are shown in Table 7.5.

Table 7.5: Overview of the sigma S6 Ice Navigator capabilities to detect small glacial ice features. Adapted from (Rutter, 2019c).

Ice Type	Size (Height Above Sea Level)	Distance Visible on X-Band Radar	Distance Visible on *sigma* S6 Ice Navigator
Bergy Bit	1 to 5 m	< 1 NM	> 4 NM
Growler	< 1 m	< 0.5 NM	> 2 NM

The numbers in the figure are based on trials performed by the Canadian Coast Guard as reported by (O'Connell, 2008). During these trials, they tested several changes to conventional marine radar and their effects on the detectability of sea ice and glacial ice. They list the following modifications made to conventional marine radar:

“• A modular radar interface (MRI) that captures high resolution radar imagery onto a computer for advanced processing and display. The radar software uses digital signal filtering techniques, including scan-to-scan averaging, to enhance and detect weak targets and improve the image display. (Sigma 2003)

• A high-speed scanner which rotates at 120 rpm, four times the rate of conventional radars, to improve the detection of small targets in heavy seas. (Rutter 2005)

• A cross-polarized system, which transmits radar pulses horizontally and receives them vertically and horizontally, will be able to discriminate between multi-year ice in first-year ice fields. (Sicom 1998)” (O’Connell, 2008)

The detection ranges listed in Table 7.5 are taken from the trials where they used a high-speed radar scanner. During these trials, they modified a conventional Bridgemaster E X-band marine radar to rotate at 30, 60 and 120 rpm. It is not given that the same detection ranges would be achieved at a slower rotation speed. Sigma S6 is sold as an addon system to conventional marine radars, but it is not mentioned if they also need to modify the rotation speed of the radar. Therefore, it is uncertain if the detection ranges given in Table 7.5 can be achieved with just the sigma S6 Ice Navigator and a conventional marine radar.

Additionally, (C-CORE, 2014) simulated the probability of detection for a sigma S6 radar system connected to a 25 kW, 8’ antenna, X-band Sperry Bridgemaster E. This radar was mounted at 14.3 meters above sea level. The simulation results are shown in Figure 7.9. The same scenario without the additional signal processing did not see a larger probability of detection than zero until the growler was closer than 2 kilometres.

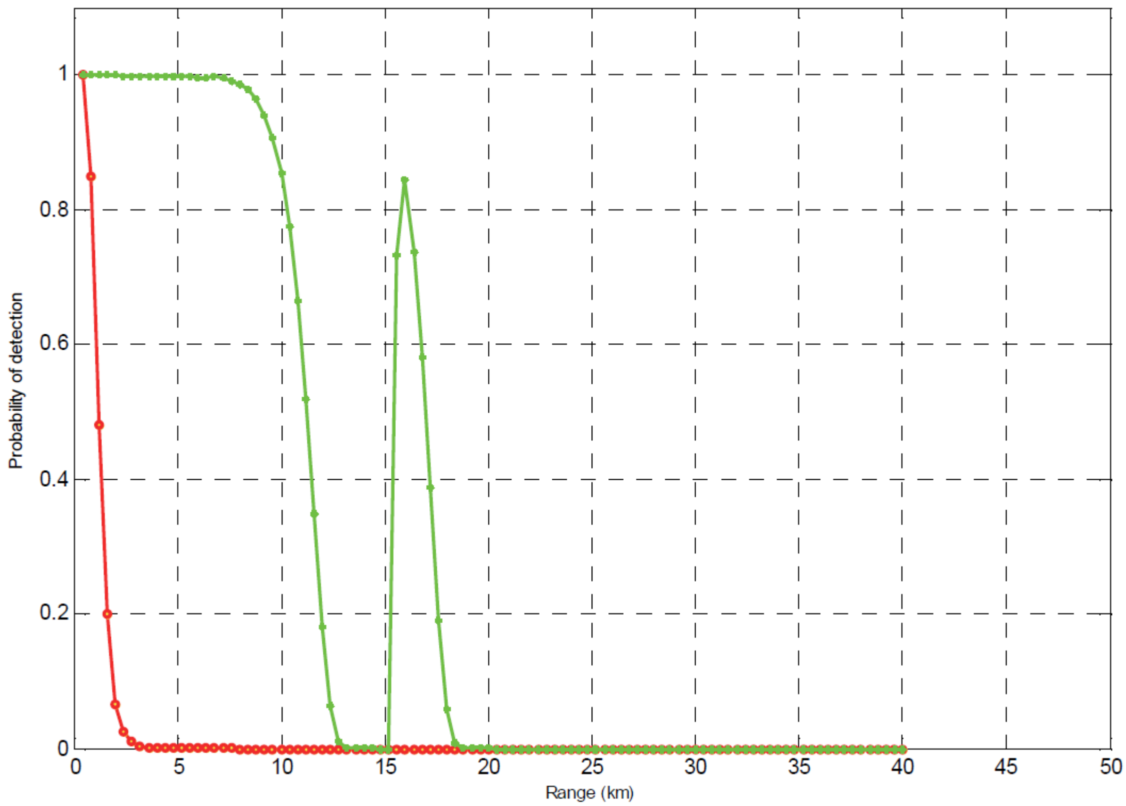

Figure 7.9 Probability of detection versus range for a 5 m growler in 4 to 6 m high waves and 20 knot winds. The green points have scan averaging included, the red points do not. Adapted from (C-CORE, 2014).

7.9 Examples of detecting glacial ice with marine radar

In this section, several cases of detecting glacial ice with marine radar will be presented. The cases are based on radar images and optical images from the Oden Arctic Technology Research Cruise (OATRC) 2013 (Lubbad et al., 2013). During the research cruise, a dual polarized sigma S6 radar system developed by Rutter Inc. was used. The radar scan rate was set to 48 rpm.

The cases feature small icebergs in areas with first-year ice, multi-year ice and ice ridges. The radar images were taken at a display range of around 1.5 NM (2.78 km), which is relatively short compared to the detection modelling like in Figure 7.1. What makes detecting small icebergs challenging in these cases is typically identifying them from surrounding sea ice features. The radar images are thus mainly for illustrative purposes, to show how the radar signal from the different objects in the environment changes with distance. In the radar images, the set display range of the radar in nautical miles (NM) is shown in the upper-right corner of the radar images, where 1 nautical mile (NM) equals 1.852 kilometres.

7.9.1 Iceberg detection case #1

Case #1 was an iceberg which was identified to have a length of 50 meters. It was passed at approximately 78° 35.785′ N, 12° 21.91′ W at around 07:25, 27. August 2013 (all times are presented in UTC time). It was described as a pinnacle-type iceberg by the observers on the cruise.

Optical images were taken of the iceberg as the Oden passed it, shown in Figure 7.10.

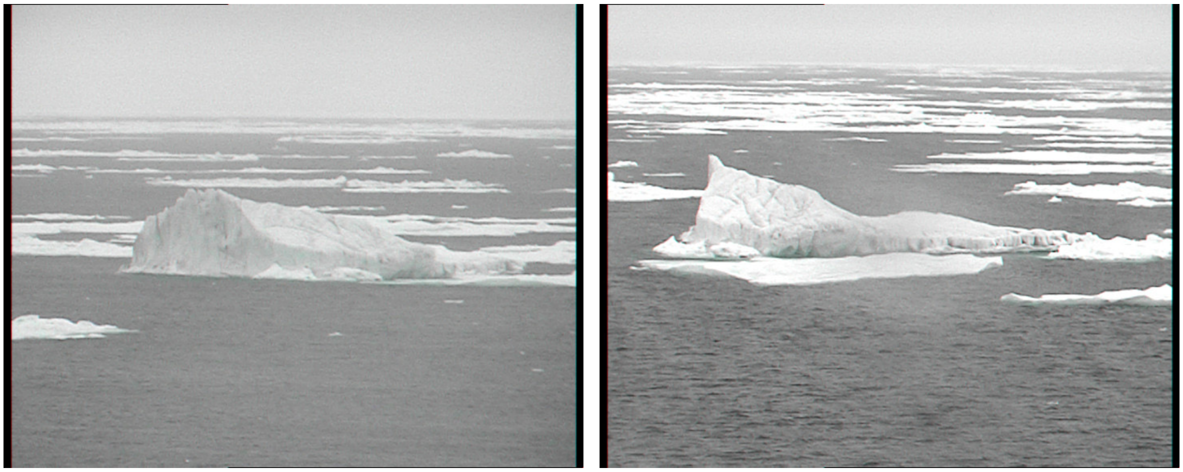

Figure 7.10 Optical images of the iceberg featured in case #1 from different perspectives. Left shows an image taken 07:17:43, right shows an image taken at 07:24:16.

Figure 7.11 to Figure 7.14 show radar images of the iceberg taken five minutes apart. The iceberg as it is first visible on radar is shown in Figure 7.11, taken at 07:05:53. At this range, the signal appears somewhat blurry. However, the intensity is larger compared to other signatures at the same range, indicating the possibility of an iceberg. As Oden moves closer to the iceberg in Figure 7.12 and Figure 7.13, the radar signal becomes more intense and the iceberg becomes easier to spot.

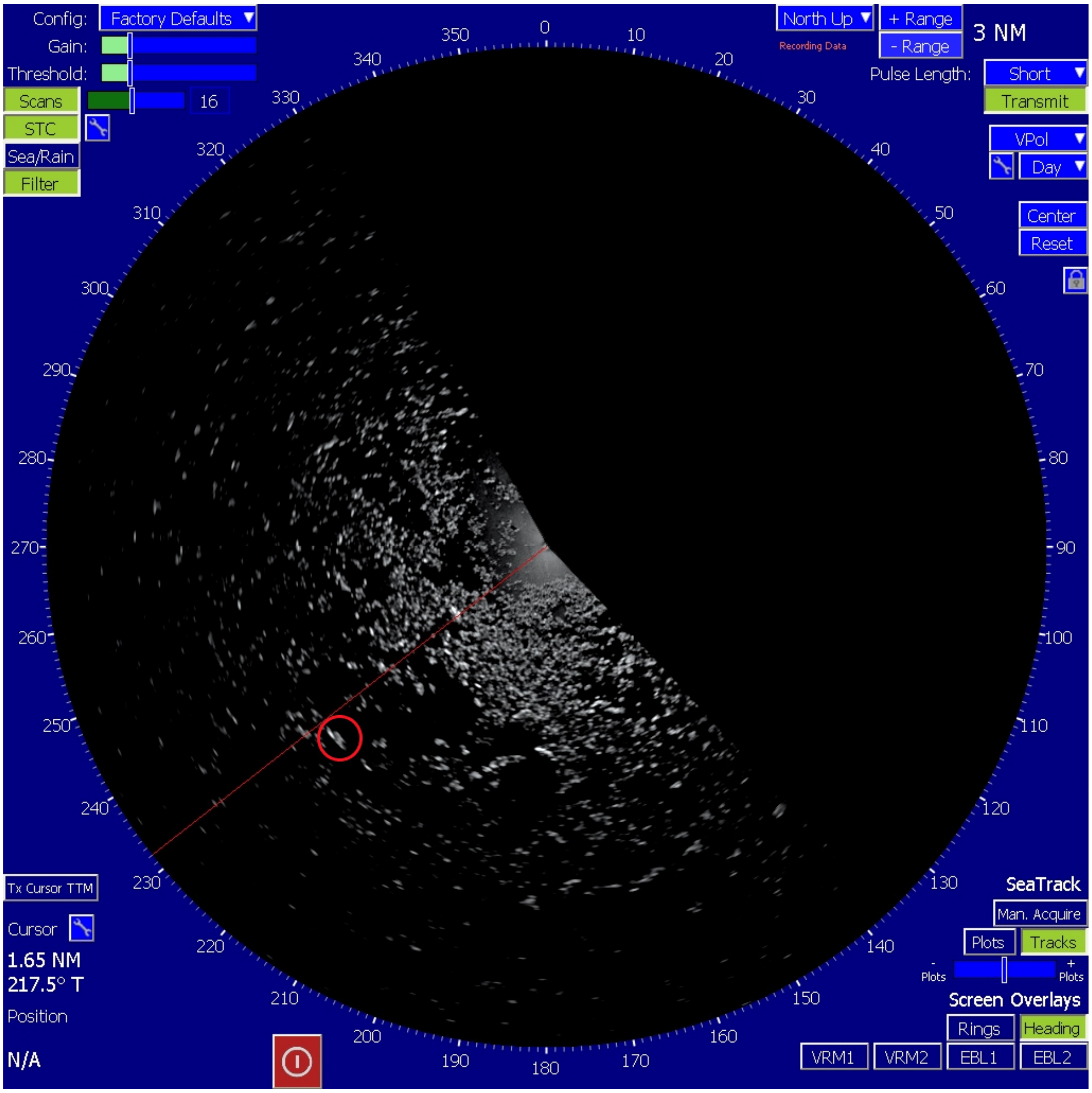

Figure 7.11 Radar image of iceberg in case #1, taken at 07:05:53. Iceberg marked in red.

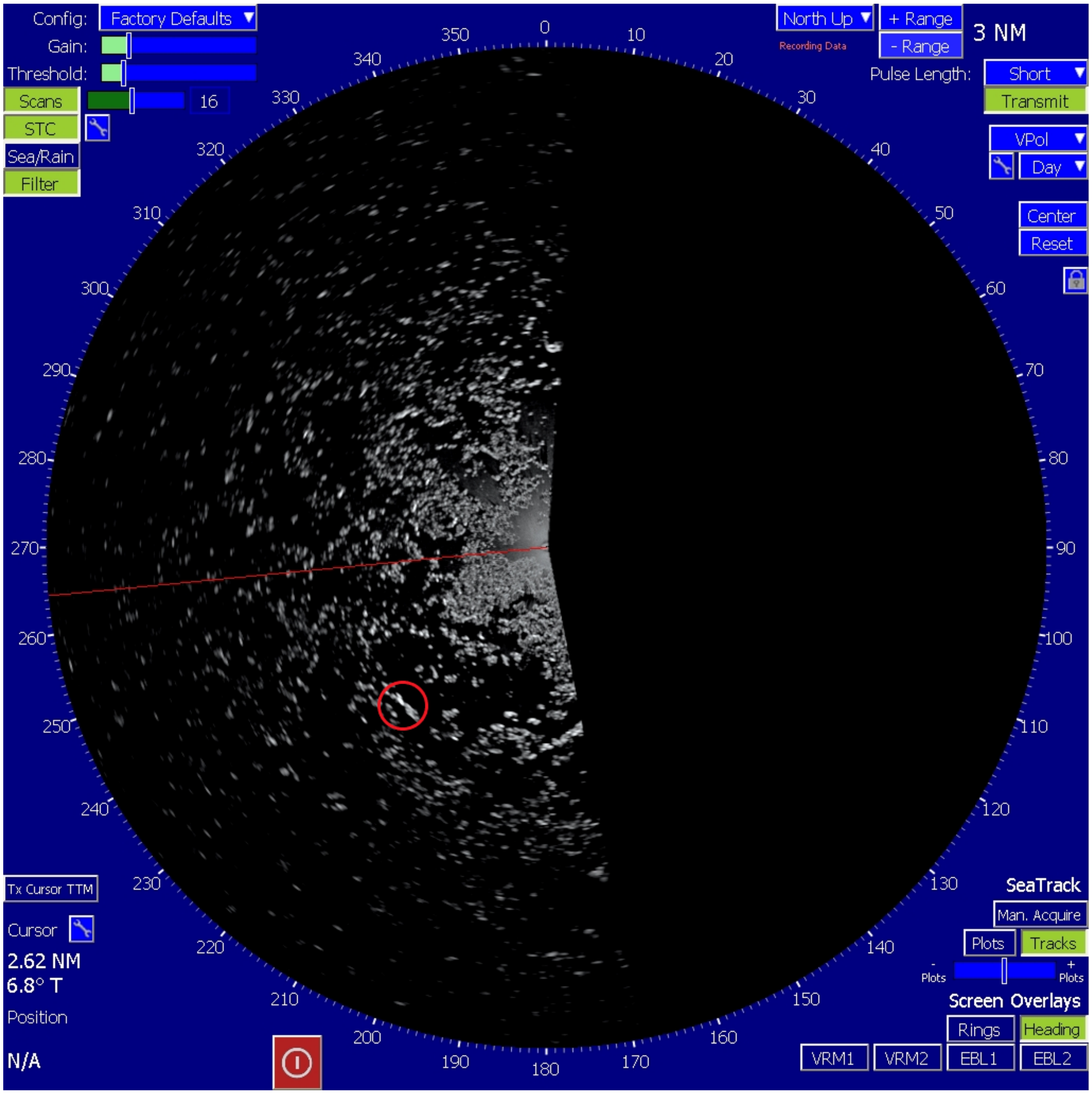

Figure 7.12 Radar image of iceberg in case #1, taken at 07:10:53. Iceberg marked in red.

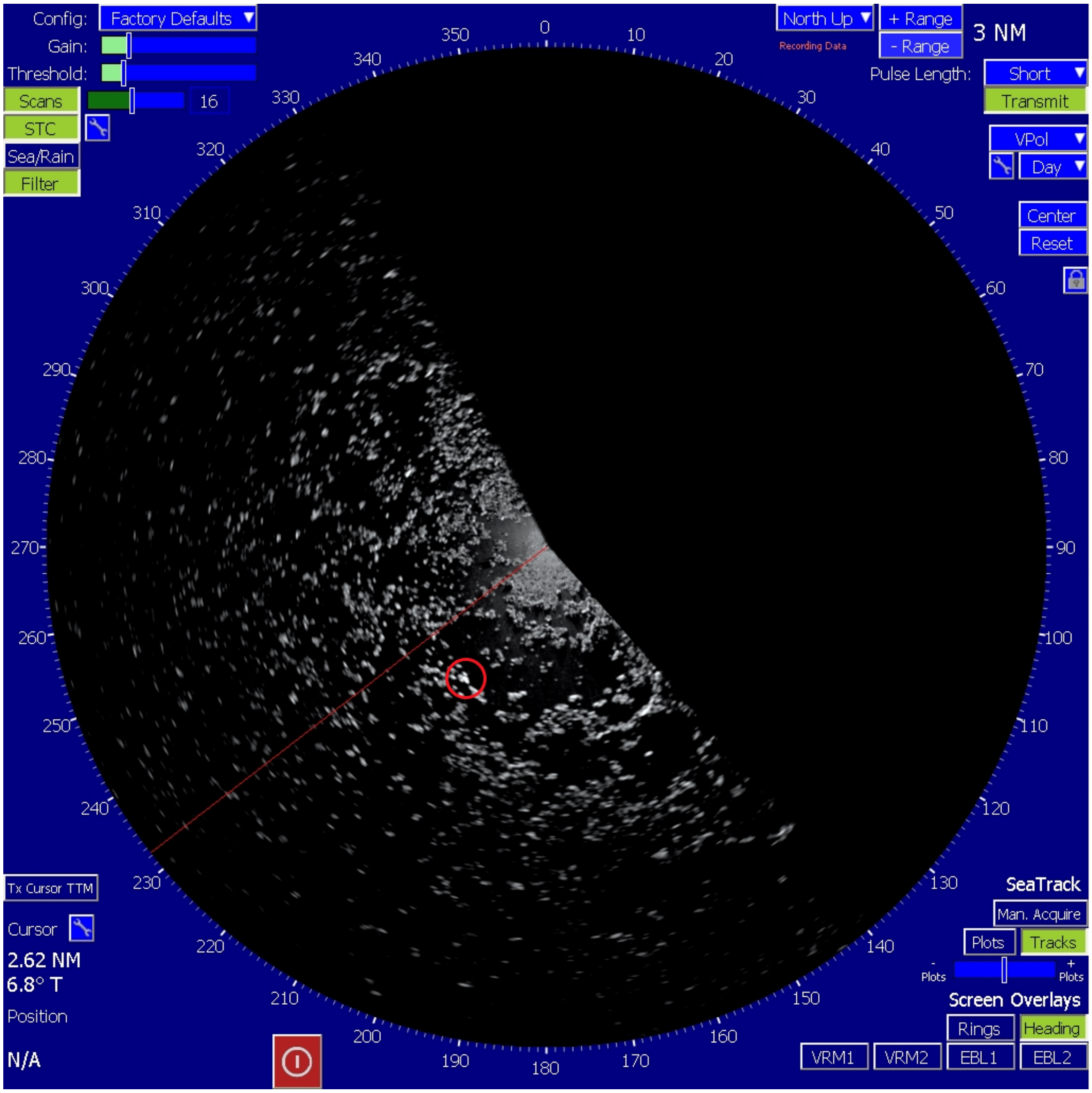

Figure 7.13 Radar image of iceberg in case #1, taken at 07:15:53. Iceberg marked in red.

From Figure 7.14, the relative radar signal from the iceberg starts decreasing compared to the sea clutter. Interestingly, the radar shadow behind the iceberg starts becoming visible at this point, as the height of the iceberg blocks out the clutter behind it. A closer look at the iceberg and the radar shadow is shown in Figure 7.15. In this case, the iceberg radar shadow can be difficult to discern from the open water between the ice features. However, the radar shadow will rotate around the iceberg as the ship moves, as it will always point in the direction away from the ship.

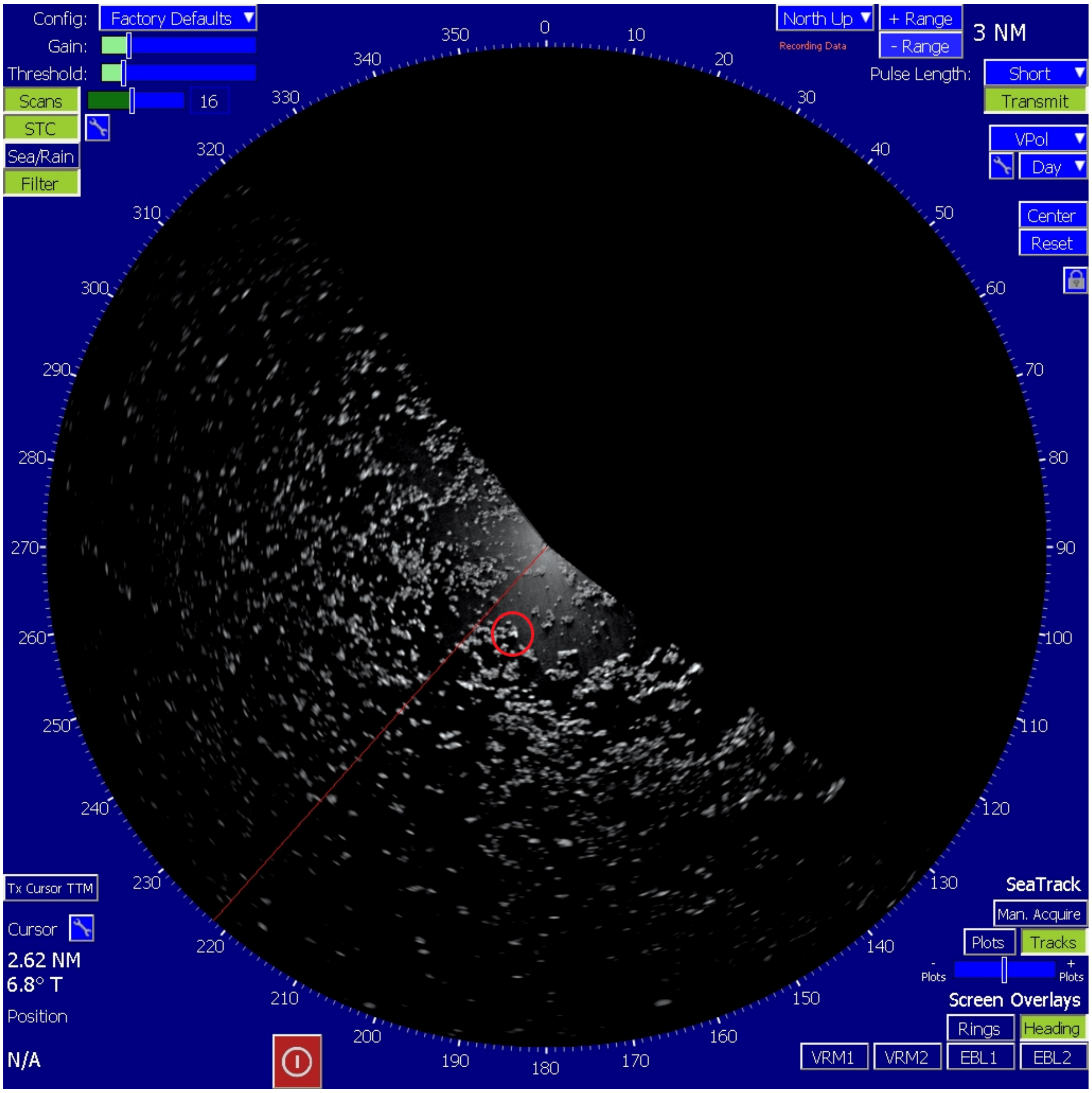

Figure 7.14 Radar image of iceberg in case #1, taken at 07:20:54. Iceberg marked in red.

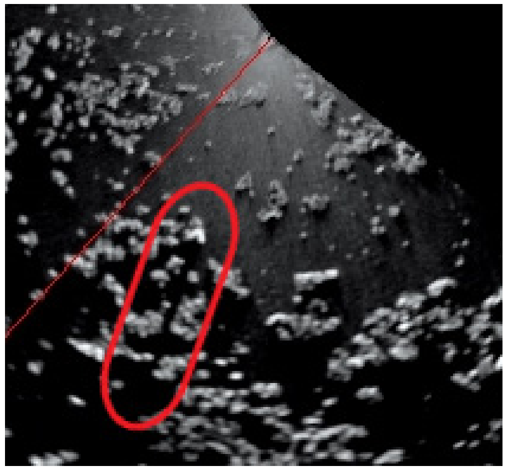

Figure 7.15 Close-up of the iceberg in Figure 7.14 and its radar shadow marked in red.

In Figure 7.16, Oden has moved much closer to the iceberg, and the display range has been reduced to 0.75 NM. The radar return signal from the iceberg relative to the sea and ice clutter has become much smaller. This is also the case for the sea ice features closest to the radar, where they have become barely visible. This trend was discussed on a theoretical basis in section 7.6. However, the sea clutter problem would likely be much more severe at close range with a conventional marine radar, as shown in Figure 7.8.

However, the large return from the sea and ice makes the iceberg radar shadow even more visible, which aids identification at this range.

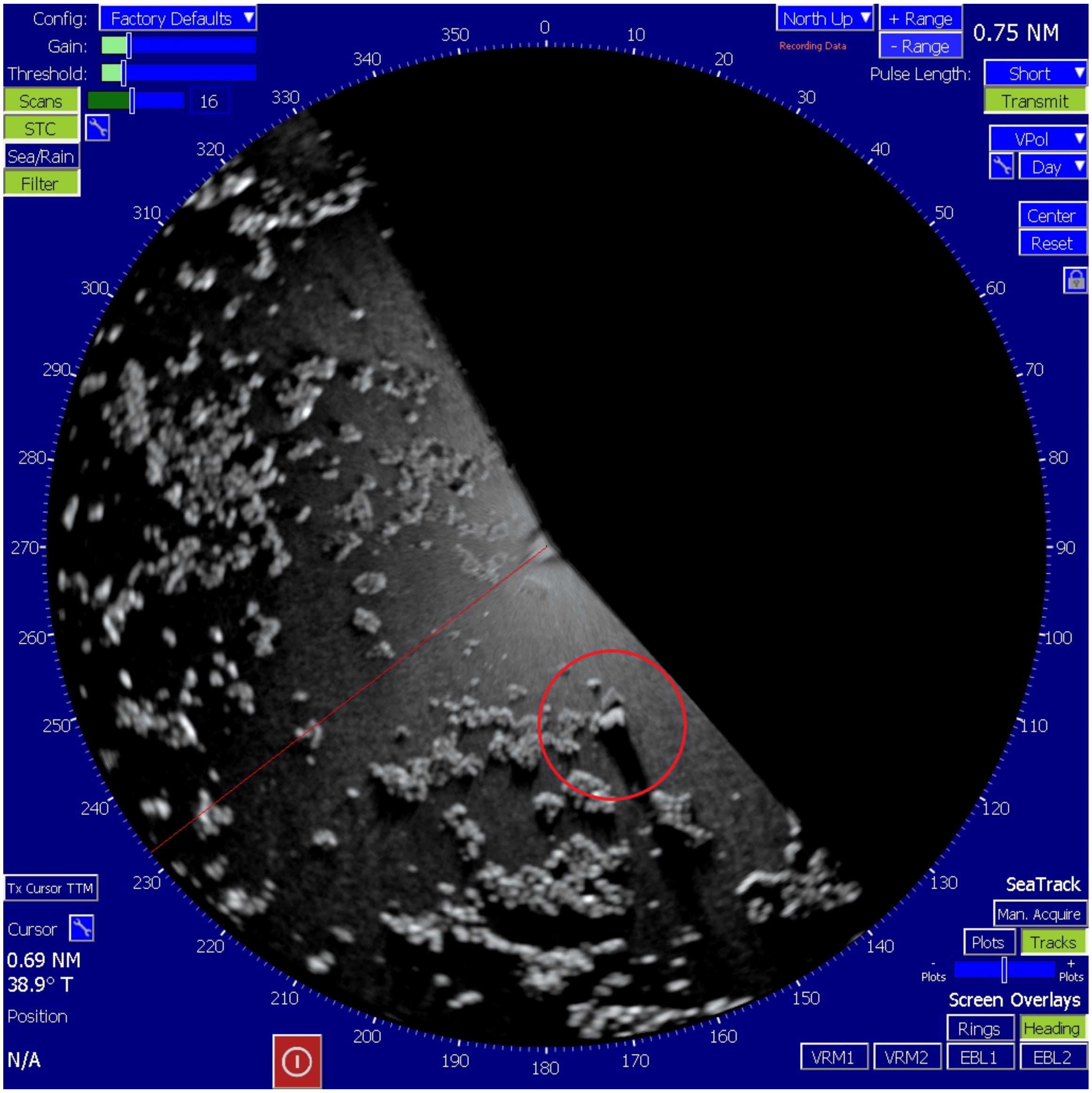

Figure 7.16 Radar image of iceberg in case #1, taken at 07:24:35. Iceberg marked in red.

7.9.2 Iceberg detection case #2

The iceberg selected for case #2 was a wedge-shaped iceberg encountered by Oden at around 78° 33.95′ N, 12° 42.88′ W at around 11:20, 28. August 2013. It was identified to have a length of approximately 30 meters. An optical image of the iceberg can be seen in Figure 7.17.

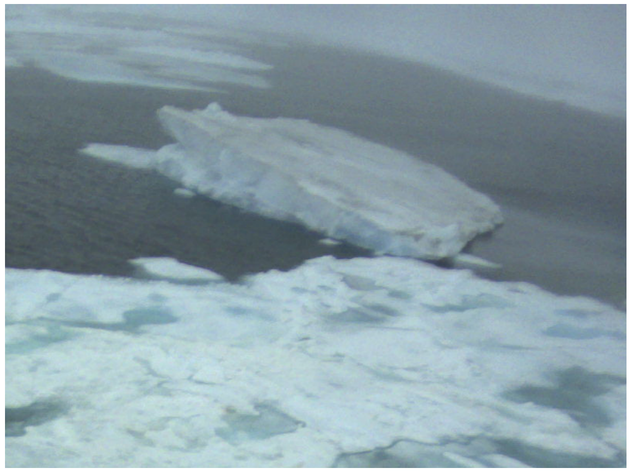

Figure 7.17 Optical image of the iceberg considered in case #2. The image was taken at approximately 11:39:10.

Figure 7.18 to Figure 7.26 show radar images taken five minutes apart as Oden approaches the iceberg pictured in Figure 7.17. This iceberg is marked in red. A second iceberg is visible on Figure 7.18 to Figure 7.22, marked in blue.

The radar signal from the primary iceberg in case #2 follows a similar trend as in case #1. At longer ranges, the iceberg marked in red is hard to distinguish from surrounding ice and from other ice features at the same range. At medium ranges, the intensity of the iceberg radar signal is much greater than other features surrounding it. And at close range, the iceberg radar signal becomes comparatively weaker in intensity compared to the sea clutter. In the same way, the large signal from the sea clutter makes the radar shadow projected by the iceberg much more visible.

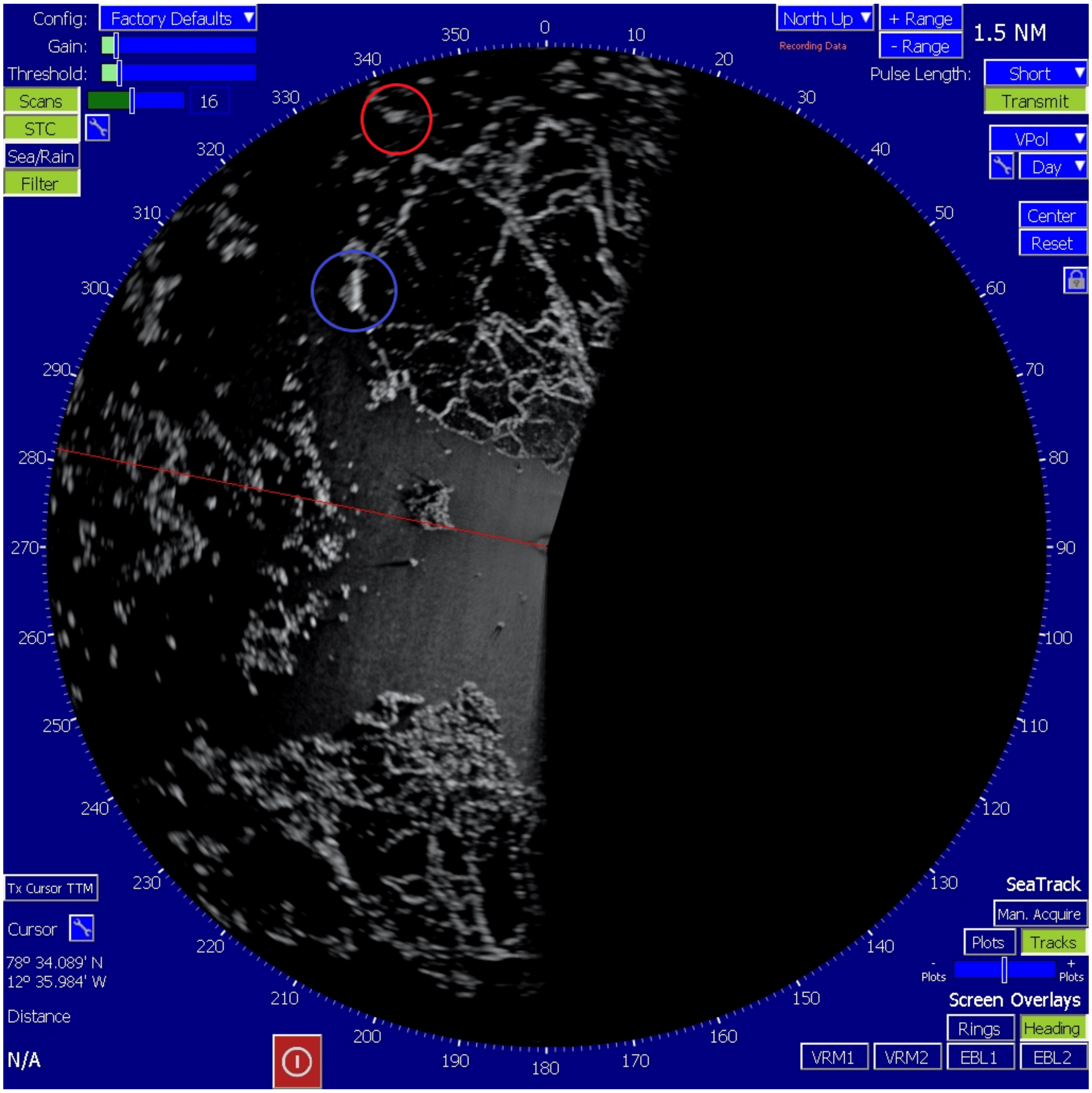

Figure 7.18 Radar image of icebergs in case #2, taken at 11:01:02. Icebergs marked in red and blue.

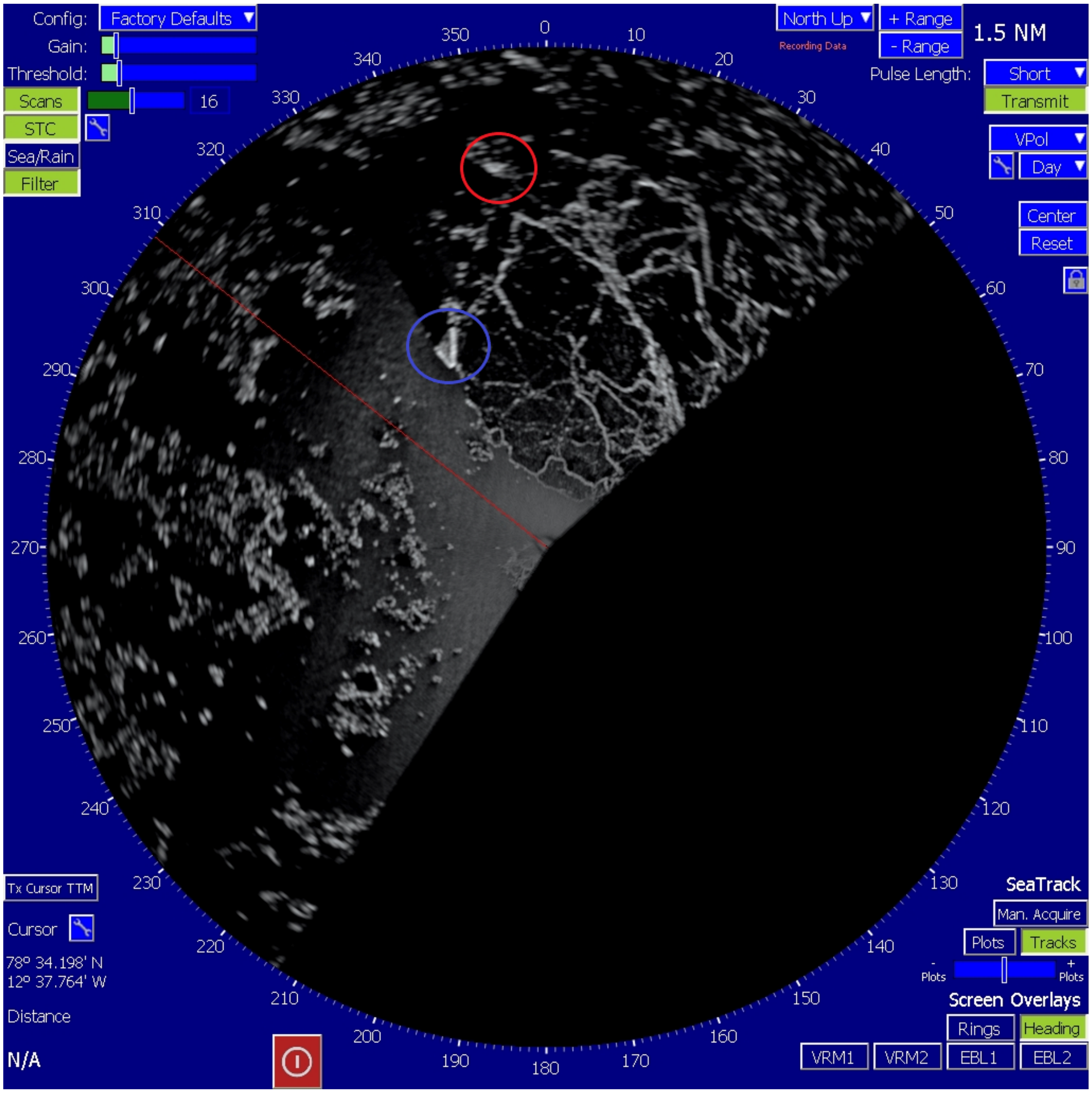

Figure 7.19 Radar image of icebergs in case #2, taken at 11:06:02. Icebergs marked in red and blue.

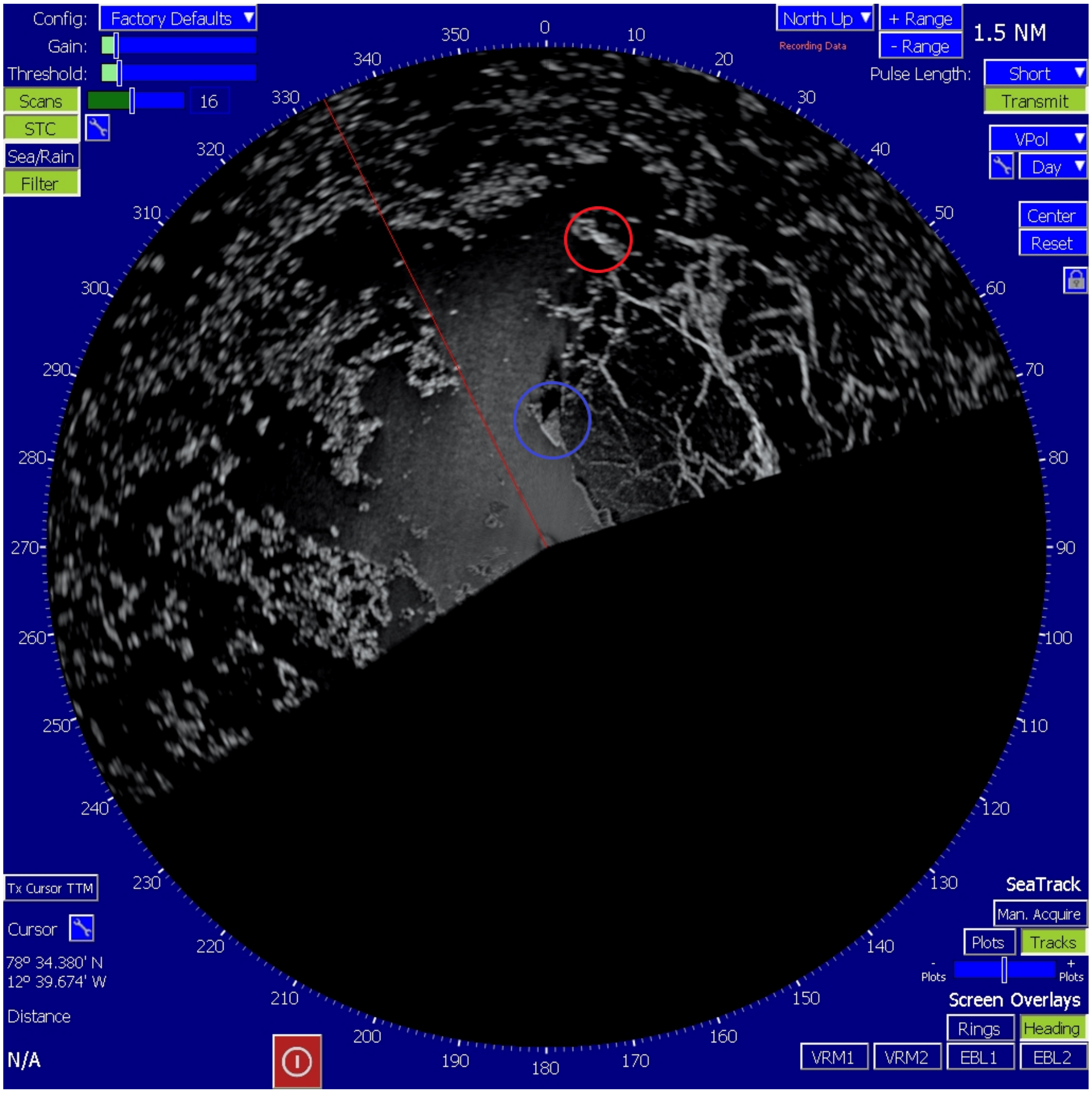

Figure 7.20 Radar image of icebergs in case #2, taken at 11:11:02. Icebergs marked in red and blue.

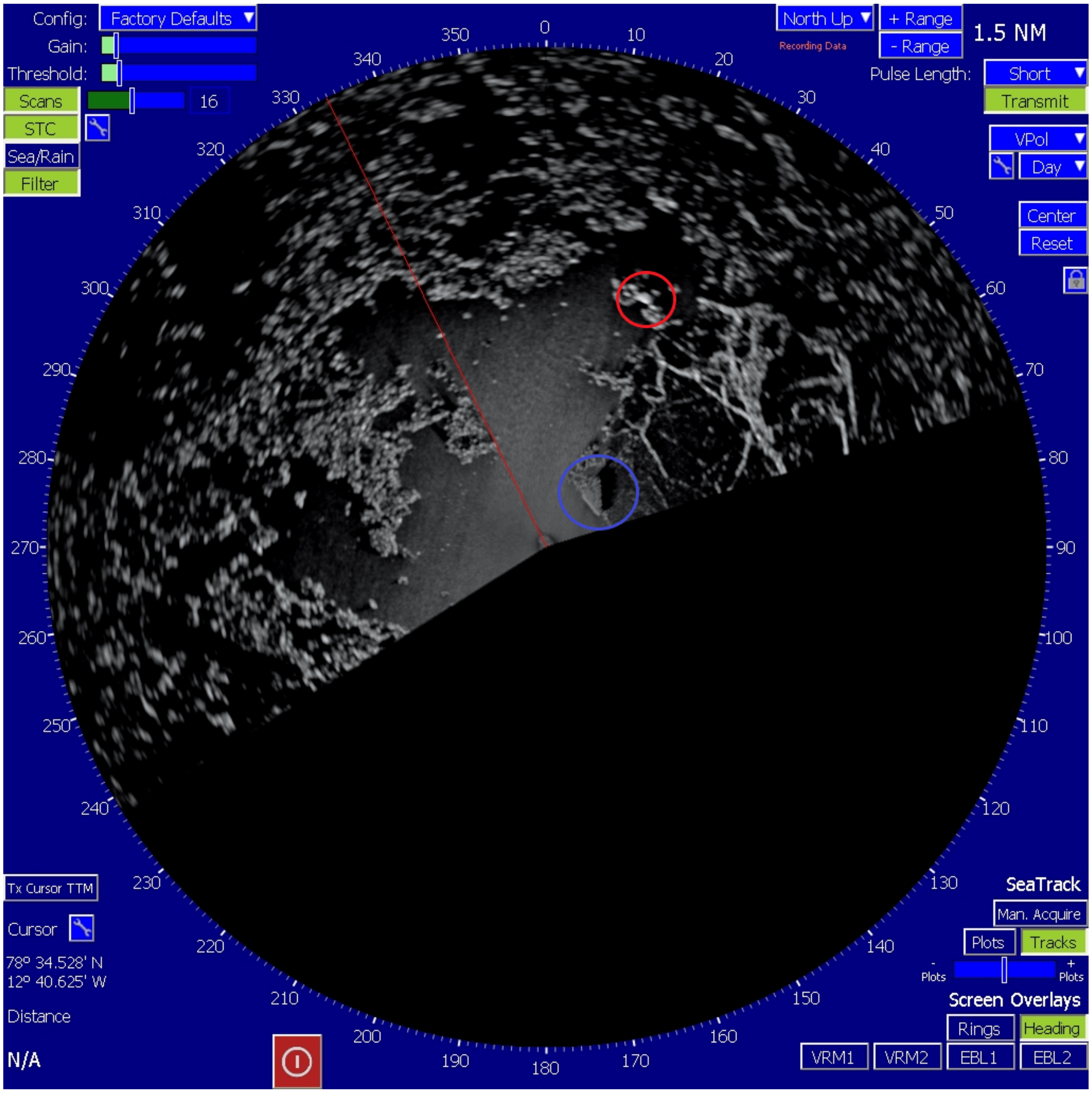

Figure 7.21 Radar image of icebergs in case #2, taken at 11:16:04. Icebergs marked in red and blue.

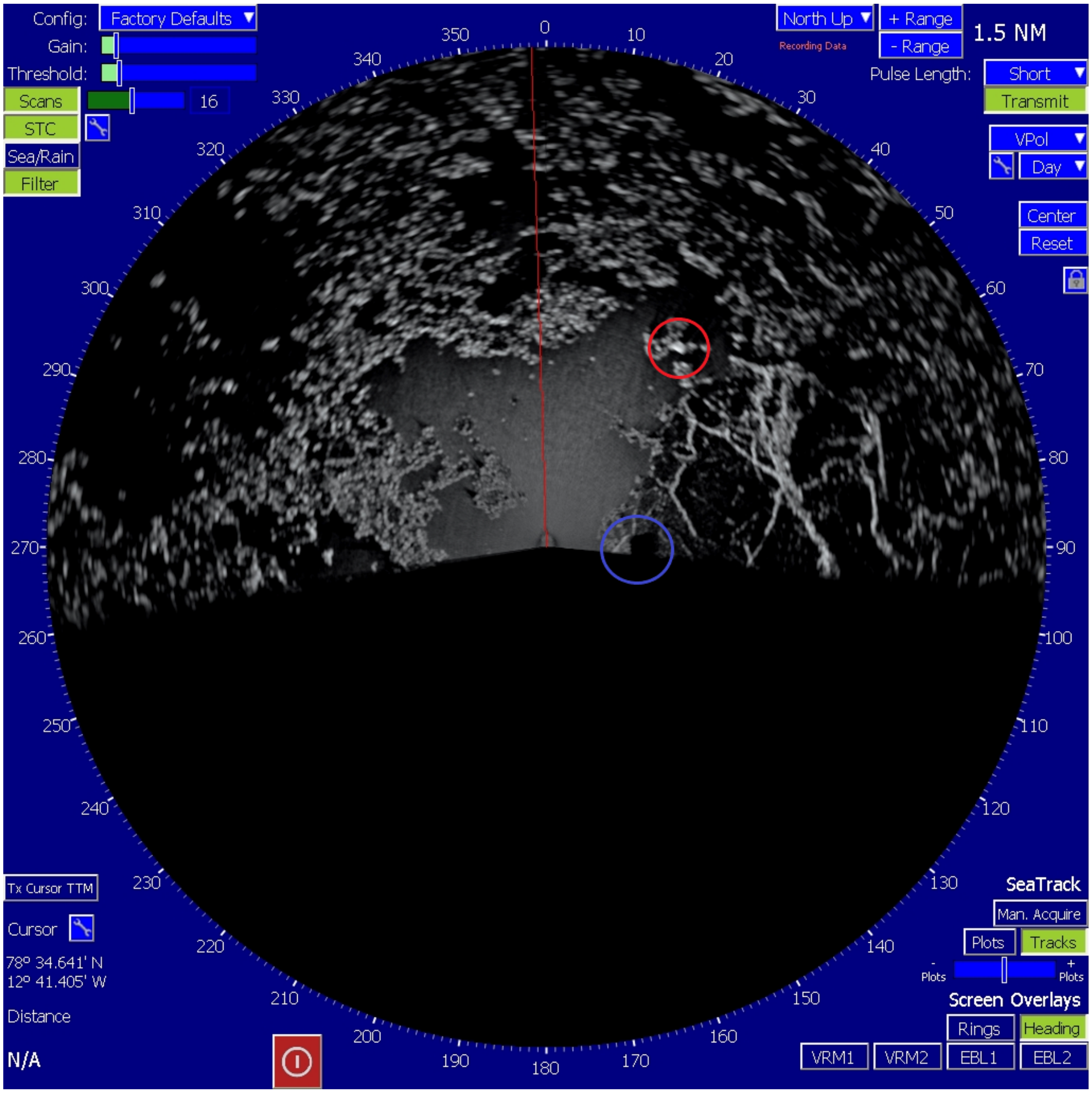

Figure 7.22 Radar image of iceberg2 in case #2, taken at 11:21:04. Icebergs marked in red and blue.

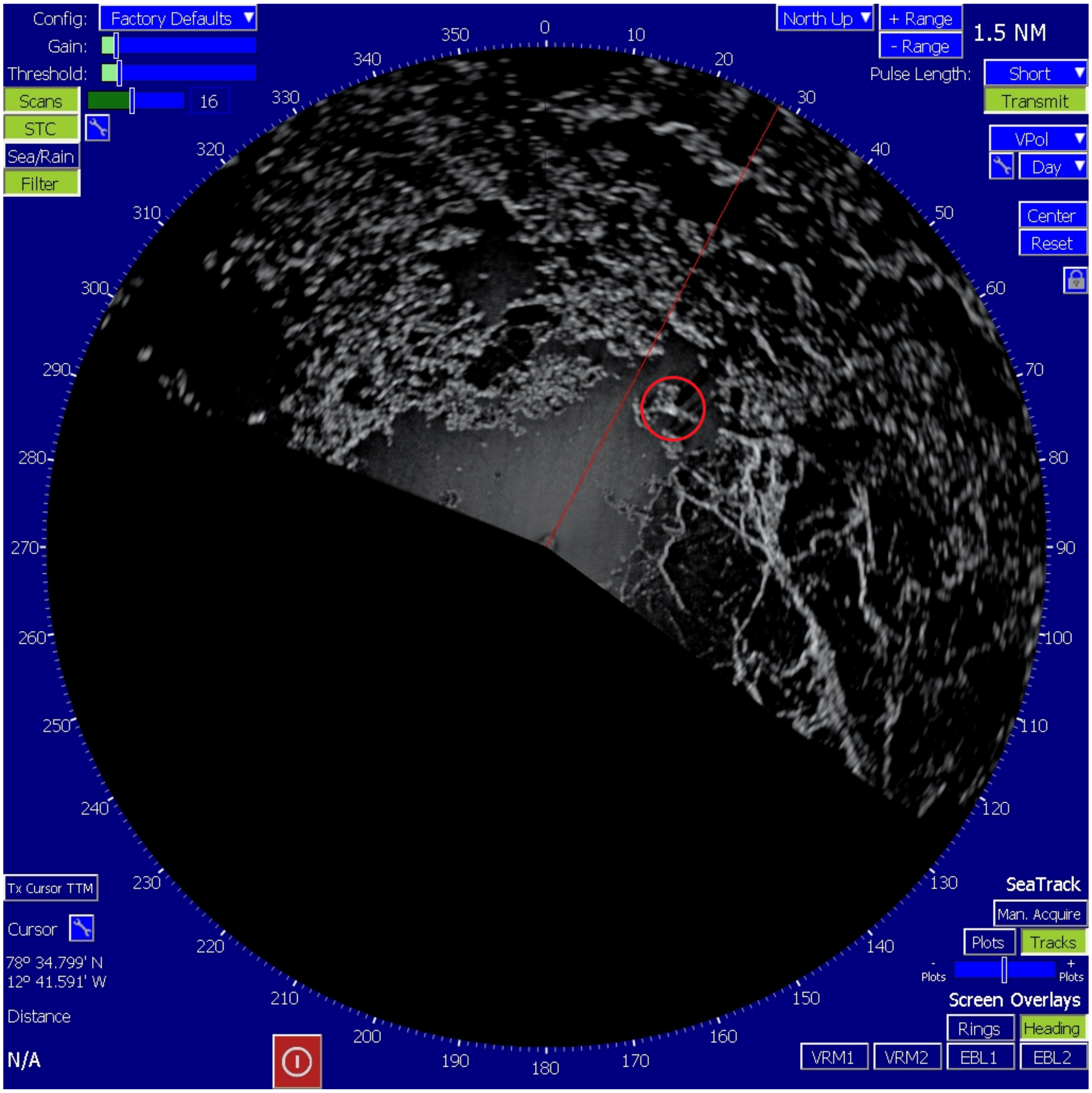

Figure 7.23 Radar image of iceberg in case #2, taken at 11:26:04. Iceberg marked in red.

A close-up of the primary iceberg and its radar shadow is shown in Figure 7.25. The radar shadow becomes less visible further away from the iceberg because the clutter signal is smaller and thus provides weaker contrast.

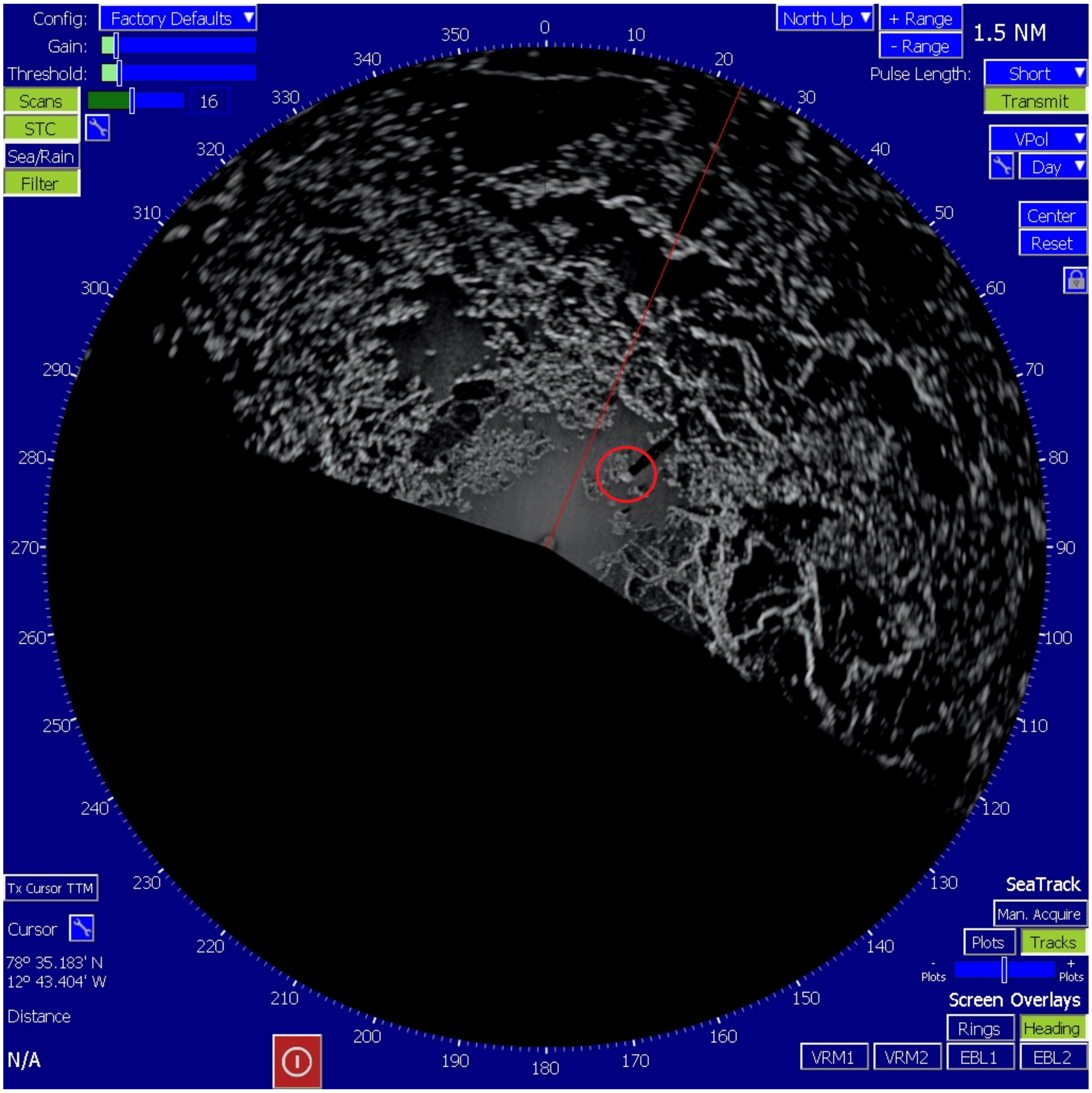

Figure 7.24 Radar image of iceberg in case #2, taken at 11:31:04. Iceberg marked in red.

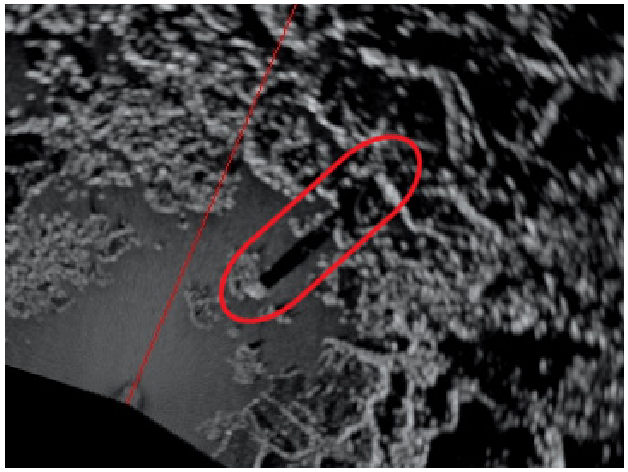

Figure 7.25 Close-up of the iceberg radar shadow as shown in Figure 7.24.

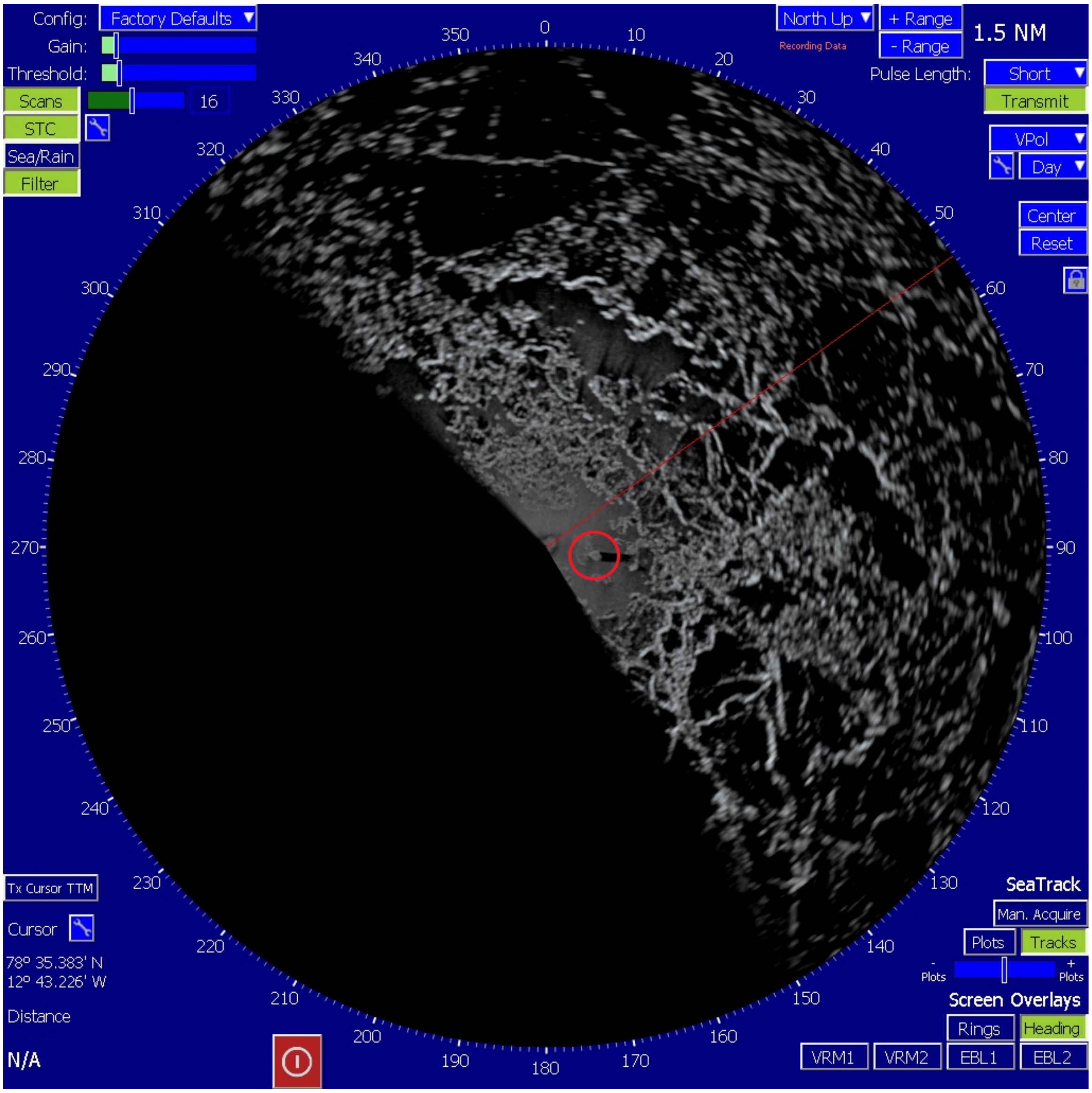

Figure 7.26: Radar image of iceberg in case #2, taken at 11:36:04. Iceberg marked in red.

7.10 Summary of Task #4

In this task, the question of the 15 meter lower limit for detectability of glacial ice has been investigated. First, a literature survey was carried out to investigate the detection of glacial ice. Marine radar was found to be the most reliable detection method for this purpose. Different parameters affecting the detection ability of marine radars were discussed, both generally and specifically for glacial ice. These parameters could roughly be divided into three different categories: glacial ice feature properties, environmental conditions and instrumental parameters.

For glacial ice feature properties, it was found that glacial ice had inherently low radar reflectivity, which may be reduced even further as the features are eroded by water to become more spherical. The radar signal was also found to decrease for smaller features and at longer ranges.

For environmental conditions, the significant wave height was found to be important for detectability. Higher waves can both obscure small glacial ice features as well as increase the relative radar return from the sea. It was found that several modelling methods of the probability of detection as a function of wave height existed. Modelling results of conventional marine radar seemed to suggest that the probability of detection for a 15-meter-long glacial ice features was less than 10% with wave heights of 5 meters. In contrast, there was a 50% probability of detection for 30-meter-long glacial ice features at the same wave height. Modelling of a marine radar with some signal processing gave around 50% probability of detection for 15-meter-long glacial ice features with 5-meter wave heights at a distance of 7.2 kilometres (Figure 7.4).

Atmospheric conditions were also found to have a significant effect on detectability, where heavy fog, rain or wind could more than halve the probability of detection at certain ranges according to modelling of conventional marine radars.

For instrumental parameters, modern radar signal processing was seen to improve detection of small glacial ice features significantly in high waves. An example of such a specialized ice radar was able to detect bergy bits at more than 4 nautical miles and growlers at more than 2 nautical miles. Additionally, the probability of detection of 5-meter glacial ice features for the same radar signal processing was modelled in literature. The glacial ice features were modelled in wave heights of between 4-6 meters and wind speeds of 20 knots. The authors found a probability of detection of above 80% at ranges of about 16 kilometres and again below 10 kilometres.

Finally, two cases of detection of small icebergs with radar in significant ice clutter was investigated. It was found that at longer ranges, it was difficult to discern the glacial ice from surrounding sea ice features. At medium ranges, the detection became much easier, as the radar signal intensity from the iceberg increased. At closer ranges, the radar signals from the sea and ice partly drowned out the iceberg signal, but the radar shadow behind the icebergs became very clear.

8 Discussions

Throughout this project, four specific tasks were carried out. The summary of each task's content and important findings can be found out in related chapters. Here, we highlight and re-present some important discussions from each of the tasks.

8.1 Discussions on Task #1

Chapter 4 documents work carried out in Task #1, which includes reviewing results from previous projects. Extensive reviews and re-calculations by a specially developed nonlinear numerical model (i.e., ST20_2019 model) were performed under this task. Answers to important questions regarding the impact velocities and impact height between a glacial ice feature and the platform were pursued.

Through re-examination of the impact velocities and impact heights by the newly developed nonlinear model (i.e., ST20_2019 model), rather encouraging and consistent results were obtained. Over the years, through different projects, the calculated impact velocities and impact heights are quite close to each other, in spite of the different methods that were utilised. The general trend shows that these results are becoming less and less conservative (see Table 4.5 and Table 4.6).

It is emphasised that the near field hydrodynamic effects of a small glacial ice feature approaching a structure/platform is not sufficiently investigated. According to the literatures, a small glacial ice feature can be re-directed away from its collision course with the platform such that no impact will happen at all. In this series of studies, i.e., ST5, ST19, ST20_2018 and ST20_2019, important hydrodynamic effects, such as repellent or attraction force, potential negative drift force, etc., were not (sufficiently) studied. The ST20_2018 report also states that more thorough near-field hydrodynamic analysis should be carried out in the future and possibly accompanied with physical experiments. It is expected that with the inclusion of near-field repellent force, the impact velocity in Table 4.5 should be even smaller or no impact at all. We therefore recommend conducting more in-depth study of the near-field hydrodynamic analyses as well as dedicated physical tests in a controlled environment.

8.2 Discussions on Task #2

Chapter 5 assesses the annual iceberg encounter frequency for structures with different sizes at Block #7424 in the Barents Sea by using a numerical model that simulates icebergs' drift and deterioration. The primary source of uncertainty in the analysis results is the number of icebergs released from the iceberg sources each year. The data used in this report is primarily obtained by aerial observations, but the frequency of scouting missions is not known. A low frequency of scouting missions would suggest that the reported iceberg sightings do not include all icebergs. On the other hand, as model input the maximum number of iceberg sightings in any given year is used, for all sources simultaneously. This may lead to an over-conservative estimate of the number of icebergs released from the sources.

Remote sensing is a promising 'new' data source that can be used to obtain accurate estimates of the iceberg release rate at sources and presence of icebergs in general. There are several publicly available data sources, among them is the Sentinel 2 imagery analysed in this study.

The use of remote-sensing data to obtain an estimate of the iceberg sizes and shapes released from the iceberg sources is demonstrated in this study. The results are in good agreement with the observations from earlier data acquisition programs, such as IDAP. The data processing performed for this study primarily consisted of the manual identification and measurement of icebergs in satellite images. This limited the number of images that could be processed. To obtain further information on iceberg statistics from remote sensing data, we recommend the following steps:

- Iceberg detection and the determination of iceberg size properties from satellite images should be (partly) automated, enabling the analysis of larger quantities of data.
- It should be further assessed to what extend cloud-penetrating electromagnetic wavelengths can be used to detect and measure icebergs.
- Procedures should be developed to track icebergs using remote sensing data, in order to prevent the double counting of icebergs.

8.3 Discussions on Task #3

Chapter 6 deals with damage assessment with three different methods. All methods follow the shared energy methodology, namely, the impact energy is dissipated both by the ice feature and the structure. These three methods are:

- Method #1: Integrated analysis
- Method #2: Weakly-coupled analysis
- Method #3: Fully-coupled analysis

Methods #1 and #2 share one similarity, i.e., they both use the Force - Displacement (F-D) curves obtained from a rigid glacial ice feature impacting a deformable structure. Therefore, these two methods can only give satisfactory results when the ice geometry does not change too much due to crushing. However, these two methods are highly efficient computationally such that hundreds of impact scenarios can be simulated in a short period of time, facilitating the construction of the impact energy map and the deformation/damage map. The weakly-coupled approach (i.e., Method #2) accounts additionally for the one-way coupling, i.e., the ice crushing process reacts to the structural deformation state and is more superior than the integrated approach (i.e., Method #1). The major application regime of Methods #1 and #2 resides in the area where the glacial ice feature is blunter than the critical glacial ice feature.

The fully-coupled simulation Method #3 is based on simultaneous calculation of the ice material response and the structural response by means of the NLFEM software LS-DYNA. The major challenge with this method is the material modelling of the ice and the structure. The ice model represents a 'design ice' calibrated form a target design Pressure-Area (P-A) relationship given in the rules. The ice material model captures major characteristics of ice crushing and significant ice structure interactions, but not the complete picture of the ice behaviour, e.g. ice spalling is not included. To what extent the adopted ice material model mimics the real ice behaviour is still not clear. Large-scale or preferably full-scale experiments with realistic structures are recommended to fill in this knowledge gap. The data can be used to gain insights into the important ice structure interactions in ALS conditions. In addition, the experimental data can be used to benchmark different ice modelling techniques. This will significantly enhance the modelling technique of ice material and improve the understanding of ice structure interactions. This benefits significantly the industrial practice and rule-making.

The results in the report are based on a calibration of the ice model to the Pressure Area (P-A) relationship of $P=3.2A^{-0.1}$ MPa, which is identical to the process pressure-area relationship adopted by IACS for Polar vessels class PC3. As ice material properties may vary significantly with target installation sites, temperature, first-year or multi-year ice, salinity, etc. There is no common consensus on which pressure-area relationship should be used in ALS design. On the other hand, the structural response is very sensitive to the ice properties adopted, and it may easily become overly conservative or unconservative depending on the choice the ice P-A curve. In the design of structures, we should be on the safe side, but not overly conservative. This calls for a very cautious selection of the P-A curve for the 'design ice'.

On the structural side, proper fracture modelling is essential to determine the structural strength under ice loading. The BWH is based on the maximum principal strain and considers fracture to occur at the onset of necking instability, thus neglecting the post-necking regime. The BWH criterion is therefore considered to be conservative. The simulations in this report mainly focus on right-angle ice impacts, and the resulting structural damage is measured by the amount of indentation/deformation. In practice, oblique impacts will induce moving ice loads along the front panel and a sliding type of structural responses. The moving loads will produce the same structural damage at a smaller force level compared to the indentation type and may cause significant degradation of the residual structural capacity. This requires more studies in the future.

8.4 Discussions on Task #4

The literature findings presented in Section 7.7.1 can be used to review the 15-meter limit of detectability. Both modelling results and literature from field trials in glacial ice detection seems to suggest that detection of small glacial ice features in high waves is difficult. Modelling results of conventional marine radar give a very low probability of detection for glacial ice with characteristic lengths of 15 meters given a wave height of 5 meters. Instead, the results seem to suggest that a size limit of about 30 meters is more accurate under such conditions.

However, several other factors influencing the Probability of Detection (POD) were not included in the models, such as atmospheric conditions, iceberg shape, and distance. As the model assumed spherical features, one would expect that a realistic glacial ice shape distribution would lead to a less conservative POD. But the presence of rain, fog and snow would decrease the POD, making the model not conservative enough. Ultimately, it is difficult to judge the relative contribution to the POD from each unaccounted factor, but from a risk assessment perspective it is prudent to lean towards a conservative estimate.

Importantly, the picture looks very different when different marine radar systems are used. Improved radar signal processing in some modern radar systems makes it much easier to spot bergy bits and growlers in high waves and will significantly improve their probability of detection. The probability of detection for such features will increase even further for certain radar systems that are specialized in ice detection. As such, depending on the application area and its demands for detection range, the 15-meter lower limit of detectability would be too optimistic for conventional marine radars for the wave conditions analysed in Task #1 of the current report, as well as in the ST5, ST19, and ST20_2018 reports.

9 Conclusions and Recommendations for Further Work

Glacial ice features of various size can pose a great threat to offshore structures in the Northern areas. According to the NORSOK N-003, presence of icebergs cannot be neglected in any part of the Barents Sea and the shelf of Jan Mayen. The probability of impact between structure and icebergs shall be estimated as a part of the design process and prior to operations in the Barents Sea. According to ISO 19906 (2019), the Barents Sea contains icebergs from the glaciers of Svalbard, Franz Josef Land and Novaya Zemlya.

These southward drift icebergs go through both thermal and wave erosions and become eventually bergy bits and growlers (i.e., small glacial ice features). Different from large icebergs, these small glacial ice features pose new challenges to the structural safety in the high North. They are more difficult to detect, to monitor and to handle by concurrent ice management techniques. In addition, due to the limited size/mass, their wave driven motions become more violent. Recognising that the impact energy depends on the velocity squared, smaller ice features may have a larger impact energy than the original iceberg. It is important to study the probabilities and consequences of such potential glacial ice impacts; and conduct corresponding damage assessment. To gain insights into the risk associated with small glacial ice features and related structural safety, the Petroleum Safety Authority Norway (PSA) initiated a series of related projects. This project (i.e., NORD ST20_2019/313) is a follow-up project of three closely related preceding projects, namely, ST5 (going through the above-mentioned entire interaction process), ST19 (with more detailed studies on impacts and damage assessments), and ST20_2018 (with more detailed studies on hydrodynamics and impacting bodies' motions in waves). As a continuation and further enrichments, in this project (ST20_2019), we have performed four main tasks:

- Task #1: Review the work performed in previous projects (i.e., ST3, ST5, ST19, and ST20_2018).
- Task #2: Study the encounter frequency and statistical distribution of glacial ice features' geometry (i.e., size and parameterised shape) at the site of interest.
- Task #3: Evaluate a glacial ice feature's local geometry's influences on structural damage assessment.
- Task #4: Examine the lower size limit of a glacial ice feature's detectability.

Extensive work has been carried out in each task. This includes developing new models, new methods, and running a large amount of simulations. In Task #1, a new nonlinear model was developed to re-examine the pre-impact motion (i.e., impact velocities and impact heights) for a glacial ice feature approaching a semi-submersible structure. In Task #2, we developed a comprehensive global numerical model that is capable of simulating the iceberg drift, thermo- and wave- erosion in the entire Barents Sea; and a local model that yields information on the iceberg encounter probability for an offshore structure of a certain size. In Task #3, in order to study the influence of the local geometry, three different simulation methods were developed. The three methods support each other, and we obtained consistent and complementary results and conclusions. In Task #4, a thorough literature review was conducted to shed light to the detectability of a glacial ice feature with marine radars in various environmental conditions. Based on the overall work, major conclusions and potential future work are summarised in the following sections.

9.1 Conclusions

Task #1 (Review of ST5, ST19, and ST20_2018):

Basically, all preceding projects tried to calculate the pre- impact motion of the glacial ice feature in different wave conditions. The relative motion between the glacial ice feature and the structure is important as it largely decides the impact energy. In these projects, different methods were developed, from relatively simple to more complex models. After reviewing these models and comparing them with the developed nonlinear model (i.e., ST20_2019 model), we found that:

- Overall, the important results regarding impact velocities and impact heights from different projects are consistent. The exact numbers are presented in Table 4.4 and Table 4.5 for the cuboidal glacial ice feature with a characteristic length of 15 m. One can easily derive the kinetic energy at the instance of impact based on the velocity and the associated glacial ice feature's mass and hydrodynamic added mass.

- The overall trend is that the impact velocities and impact heights become less conservative through the studies of these projects.
- The analyses in this project (ST20_2019) show that:
  a) The impact velocity between the glacial ice feature and the structure increases with increasing impact height.
  b) The impact velocity increases with higher sea states. However, this increase is not very pronounced partly due to the fact that in sea states with smaller significant wave heights, the increased ice mean drift speed compensates the decrease in wave driven cyclic motion.
  c) In longer/higher wave conditions, the impact height range is more spread whereas a more concentrated impact range is calculated for shorter wave conditions.
  d) In shorter wave conditions, the most probable impact height is below the CoG of the glacial ice feature in still water, indicating that submergence of the ice is taking place more frequent in shorter waves than in longer wave conditions.

Task #2 (Iceberg encounter probability):

With the simulation from both the global and local models (with a refence location of Block #7424), we found that:

- The iceberg encounter probability was modelled at Block #7424, located at 74° 14' 31.05" N 24° 30' 18.62" E. The model predicts that on average 9.8 icebergs will enter a 100 x 100 km box (perimeter) around the center of the block annually. This result is based on a conservative estimate of the number of icebergs released from the considered iceberg sources (i.e., glaciers).
- Icebergs will enter the perimeter in 85% of the years.
- An iceberg that enters the 100 x 100 km box will have a probability of $4.77 \cdot 10^{-4}$ of encountering a 100 x 100 m box within that perimeter.
- Combined with the number of icebergs entering the perimeter annually, this results in a total iceberg encounter probability of a 100 x 100 m box of $4.67 \cdot 10^{-3}$.
- Estimates of iceberg shape and size from satellite imagery matches well with iceberg shape and size distributions derived from earlier observation programs.
- Climate change will affect the iceberg encounter probability in several ways. Increased glacial discharge may increase the number of icebergs produced. Higher winds and waves may cause icebergs to drift farther South. On the other hand, warmer seas and higher waves will also cause faster iceberg erosion.

Task #3 (Impact analysis):

This task aims to study the influence of local ice geometry (local sharpness) on the structural response and the critical structural damage. Three different approaches were used with various degrees of simplifications, i.e. the integrated approach, the weakly-coupled approach and the fully-coupled approach. The critical ice geometry was identified based on the fully-coupled approach. Extensive simulations with this critical geometry were carried out with the weakly-coupled approach at different locations of the column and the pontoon. The advantages and disadvantages of each approach are compared and discussed. The following conclusions are drawn:

- The three different methods produce consistent predictions of structural damage in general, and the results complement each other. Of the three, the fully-coupled approach is the most trustworthy and is capable of simulating complex ice-structure interactions quite well. It is however, the most computationally demanding. The weakly-coupled and the integrated approaches require little computation time and can be used for a large number of simulations and subsequent probabilistic analysis. The weakly-coupled approach is superior to the integrated approach because it captures the one-way coupling of structural responses on the ice resistance.
- The integrated and weakly-coupled approaches are most suitable for scenarios with relatively little ice damage, i.e., for blunt ice shapes. The reason is that both methods do not update the structural Force – Displacement (F-D) curve when ice undergoes damage. If the ice is significantly crushed, the contact area increases. This increases the structural capacity to ice loading but is not reflected in both methods. Therefore, in scenarios with sharp ice, the fully-coupled method should be used.
- The critical ice sharpness is closely related to the structural dimensions. From the fully-coupled simulations, a critical ice sharpness is identified when the ice radius of curvatures 0.8 times the stiffened panel length. When the ratio is larger than 0.8, the ice is considered blunt, the structural capability of energy absorption increases. When the ratio is smaller than 0.8, the ice is considered sharp and becomes easier to be crushed, and less energy goes to the structure. It should be noted that the critical ratio is also sensitive to the design pressure-area (P-A) relationship used in the calibration of the ice material.
- After identifying the critical local sharpness, the fully-coupled methods was adopted to assess the structural damage for ice impacts on various location of the structure, i.e., 7 representative locations on the column and 4 locations on the pontoon. These F-D curves are presented in Figure 6.42, Figure 6.43, Figure 6.47, and Figure 6.48. These results are generic for this critical geometry irrespective of the impact energy (i.e., external mechanics calculation is not included in these simulations). For an arbitrary impact energy, one can estimate the structural damage at different representative locations based on these results.
- Different from the fully-coupled method which deals essentially with the internal mechanics, the integrated and weakly-coupled approaches contain both external mechanics and internal mechanics. Based on extensive simulations with the case of a 15-m long ellipsoidal glacial ice feature (see Figure 6.52), the maximum impact energy was identified to be less than 7.5 MJ. Moreover, more than 90% of the impact energy are less than 3.5 MJ. However, this impact energy level might be doubled based on the studies in Task #4 that the smallest detectable glacial ice feature's size might very well be 30 m instead of 15 m.
- A large number of simulations were carried out with the weakly-coupled approach. The results indicate that for a given an impact energy of 7.5 MJ, the maximum structural deformation is found to be less than 0.6 m and 90% of the location has a deformation that is less than 0.36 m. With the most unfavorable local ice geometry, the current calculations indicate that the structure can withstand a maximum impact energy level of around 15 MJ. Therefore, this 7.5 MJ impact energy scenario is considered safe. However, as mentioned in Task #4, the lower size limit of a detectable glacial ice feature can easily be doubled to 30 m and thereby a much higher impact energy can be expected. In those scenarios, the structural safety is of concern.

Task #4 (Detectability of small glacial ice features):

To assess a glacial ice feature's lower size limit concerning detection, a thorough literature review were conducted. The focus has been on studying the influences of different environmental conditions, instrumentation parameters and existing modelling results. Based on these studies, we found that:

- Among related environmental parameters, the significant wave height was found to be important for detectability. Higher waves can both obscure small glacial ice features as well as increase the relative radar return from the sea.
- Modelling results of conventional marine radar seemed to suggest that the probability of detection for a 15-meter-long glacial ice features was less than 10% with wave heights of 5 meters. In contrast, there was a 50% probability of detection for 30-meter-long glacial ice features at the same wave height.
- Enhanced radar with some signal processing can largely improve the probability of detection. For example, the probability of detection for 15-meter-long glacial ice features can be increased to 50% in wave conditions with a 5-meter significant wave height at a distance of 7.2 km (Figure 7.4).
- The detectability's lower size limit that was initially set as 15 m seems to be very unconservative depending on the specific marine operation requirements. One can refer to Figure 7.2 and Figure 7.4 to find related probability of detection information for specific applications.

9.2 Further work

Concerning the important engineering problems, i.e., impact between a small ice feature and a semi-submersible structure, based on the previous discussions and conclusions, we propose the following further work to complement the tasks that have been achieved so far.

- In-depth study of the near-field hydrodynamic analyses accompanied by physical tests.
- Further assessing the possibilities of using remote-sensing data in the detection of icebergs including possibilities for a reliable automatization to allow large-scale data processing.
- Large scale or full-scale experiments in controlled settings to validate the simulation results and to further understand the coupled ice-structure interaction process.
- To study the structural damage subjected to moving ice loads induced by oblique impacts.
- To study structural response sensitivity to the selected ice pressure area relationship.
- Results sensitivity to the simplifications of modelled ice behaviour should also be checked, e.g., viscoplastic modelling of ice can be considered.
- Probabilistic approach to structural damage assessment based on the results of this study and including statistical analysis of local ice geometries.
- For a given radar system and iceberg size (SigmaS6 (Rutter), ICE100 (Furuno), iceVision (MKIS), Delta (Ravenstvo), etc.) establishing the Probability of Detection (POD) as a function of sea state and distance.
- Coupled consideration of POD and probability of a successful ice management.
- POD for remote-sensing systems other than a marine radar should also be considered.

Reference

AARI 2005. Glaciers at Novaya Zemlya/Sources for Icebergs in the Barents Sea. Research report ordered by Statoil. .

AARNES, O. J., REISTAD, M., BREIVIK, Ø., BITNER‐GREGERSEN, E., INGOLF EIDE, L., GRAMSTAD, O., MAGNUSSON, A. K., NATVIG, B. & VANEM, E. 2017. Projected changes in significant wave height toward the end of the 21st century: Northeast A tlantic. *Journal of Geophysical Research: Oceans,* 122**,** 3394-3403.

ABRAMOV, V. A. 1996. *Atlas of Arctic Icebergs: The Greenland, Barents, Kara, Laptev, East-Siberian and Chukchi Seas and the Arctic Basin*, Backbone Publishing Company.

ALSOS, H. S., HOPPERSTAD, O. S., TÖRNQVIST, R. & AMDAHL, J. 2008. Analytical and numerical analysis of sheet metal instability using a stress based criterion. *International Journal of Solids and Structures,* 45**,** 2042-2055.

BIGG, G. R., WADLEY, M. R., STEVENS, D. P. & JOHNSON, J. A. 1997. Modelling the dynamics and thermodynamics of icebergs. *Cold Regions Science and Technology,* 26**,** 113-135.

BRESSAN, J. & WILLIAMS, J. 1983. The use of a shear instability criterion to predict local necking in sheet metal deformation. *International Journal of Mechanical Sciences,* 25**,** 155-168.

C-CORE 2007. Ice Radar Processor for Prince William Sound - Summary of Configuration and Benefits. *C-CORE Report R-07-044-546 v3.0, December 2007.*

C-CORE 2014. Iceberg Detection Performance Simulations to Support the Installation of New S6 Processor with the Reef Island Radar. *C‐CORE Report R‐14‐030‐1016, Revision 1.0.*

CAMMAERT, A., JORDAAN, I., BRUNEAU, S., CROCKER, G., FUGLEM, M., RYAN, J. & WISHAHY, M. 1992. Design criteria for ice loads on floating production systems-Final report. *C-CORE Contract Number 92-C13*.

CANADIAN COAST GUARD 2012. Ice Navigation in Canadian Waters. Ottawa, Ontario.

CARSTENS, T., COWAN, A. & OSWALD, G. 1988. Sea Ice Investigations in the Barents Sea – Summary Report.: SINTEF Report Trondheim.

COOK, R. D., MALKUS, D. S., PLESHA, M. E. & WITT, R. J. 2007. *Concepts and applications of finite element analysis*, John Wiley & Sons.

COPERNICUS, CLIMATE, CHANGE, SERVICE & (C3S). 2017. *ERA5: Fifth generation of ECMWF atmospheric reanalyses of the global climate. Copernicus Climate Change Service Climate Data Store (CDS)* [Online]. https://cds.climate.copernicus.eu/cdsapp#!/home. [Accessed].

DALEY, C. 1994. *MSI Ice Loads Data: Compilation of Medium Scale Ice Indentation Test Results and Comparison to ASPPR*, Daley R & E.

DEZECOT, C. & EIK, K. J. 2015. Barents Sea East Blocks Metocean Design Basis “Fysisk miljø i Barentshavet sørøst,”.

DNVGL 2018. Recommended practice DNV-GL-RP-C204 Design Against Accidental Loads.

DOWDESWELL, J., BENHAM, T., STROZZI, T. & HAGEN, J. 2008. Iceberg calving flux and mass balance of the Austfonna ice cap on Nordaustlandet, Svalbard. *Journal of Geophysical Research: Earth Surface,* 113.

EIK, K. 2008. Review of experiences within ice and iceberg management. *The Journal of Navigation,* 61**,** 557-572.

EIK, K. 2009. Iceberg drift modelling and validation of applied metocean hindcast data. *Cold Regions Science and Technology,* 57**,** 67-90.

EIK, K. & GUDMESTAD, O. T. 2010. Iceberg management and impact on design of offshore structures. *Cold Regions Science and Technology,* 63**,** 15-28.

EIK, K. J., KVINGEDAL, B. & NYGAARD, E. 2013. Frequency of sea ice and icebergs at Skrugard - Barents Sea. *22nd International Conference on Port and Ocean Engineering under Arctic Conditions, POAC 2013.* Espoo, Finland.

EKEBERG, O.-C., SHIPILOVA, O., BIRKNES-BERG, J. & JOHANSEN, A. 2018. Glacial Ice Impact. *In:* PETROLEUMSTILSYNET (ed.) *PTIL-Konstruksjonssikkerhet i Nordområdene.* Stavanger, Norway: DNV GL AS Oil & Gas Environmental Loading & Response.

FALTINSEN, O. M. 1993. *Sea loads on ships and offshore structures*, Cambridge Univ Pr.

FUGLEM, M., JORDAAN, I., CROCKER, G., CAMMAERT, G. & BERRY, B. 1996. Environmental factors in iceberg collision risks for floating systems. *Cold Regions Science and Technology,* 24**,** 251-261.

FUGLEM, M., MUGGERIDGE, K. & JORDAAN, I. 1999. Design load calculations for iceberg impacts. *International Journal of Offshore and Polar Engineering,* 9.

FYLLING, I. On the Statistics of Impact Velocities and Hit Positions Related to Collisions and Mating Operations for Offshore Structures (in BOSS conference). BOSS, 1994. 297-306.

GJEVIK, B., NØST, E. & STRAUME, T. 1994. Model simulations of the tides in the Barents Sea. *Journal of Geophysical Research: Oceans,* 99**,** 3337-3350.

HAGEN, J. O., KOHLER, J., MELVOLD, K. & WINTHER, J. G. 2003. Glaciers in Svalbard: mass balance, runoff and freshwater flux. *Polar Research,* 22**,** 145-159.

HILL, R. 1952. On discontinuous plastic states, with special reference to localized necking in thin sheets. *Journal of the Mechanics and Physics of Solids,* 1**,** 19-30.

IPCC 2013. Climate Change 2013: The Physical Science Basis The physical science basis. Contribution of working group I to the fourth assessment report of the intergovernmental panel on climate change Contribution of Working Group I to the Fifth Assessment Report of the Intergovernmental Panel on Climate Change [Stocker, T.F., D. Qin, G.-K. Plattner, M. Tignor, S.K. Allen, J. Boschung, A. Nauels, Y. Xia, V. Bex and P.M. Midgley (eds.)]. Cambridge University Press, Cambridge, United Kingdom and New York, NY, USA, 1535 pp.

ISAACSON, M. & MCTAGGART, K. A. 1990. Modelling of iceberg drift motions near a large offshore structure. *Cold Regions Science and Technology,* 19**,** 47-58.

ISO19906 2019. Petroleum and natural gas industries - Arctic offshore structures,International Standard, International Standardization organization, Geneva, Switzerland,.

JAKOBSSON, M., MAYER, L., COAKLEY, B., DOWDESWELL, J. A., FORBES, S., FRIDMAN, B., HODNESDAL, H., NOORMETS, R., PEDERSEN, R. & REBESCO, M. 2012. The international bathymetric chart of the Arctic Ocean (IBCAO) version 3.0. *Geophysical Research Letters,* 39.

KENNEDY, K. P. 1990. *Dynamic activity and crushed ice behavior in medium-scale ice-structure interactions.* Memorial University of Newfoundland.

KIERKEGAARD, H. 1993. *Ship collisions with icebergs*, Danmarks Tekniske Højskole, Instituttet for Skibs-og Havteknik.

KIM, A. N., SCIBILIA, F. & BOUQUET, G. Iceberg Remote Sensing in Arctic Harsh Conditions. OTC Arctic Technology Conference, 2015. Offshore Technology Conference.

KIM, E. 2014. *Experimental and Numerical Studies Related to the Coupled Behaviour of Ice Mass and Steel Structures during Accidental Collisions.* PhD, Norwegian University of Science and Technology.

KUBYSHKIN, N., BUZIN, I., SKUTIN, A. & GLAZOVSKY, A. Determination of the area of generation of big icebergs in the Barents Sea–temperature distribution analysis. The Sixteenth International Offshore and Polar Engineering Conference, 2006. International Society of Offshore and Polar Engineers.

LEVER, J. H. & SEN, D. 1987. A Method to Upgrade Iceberg Velocity Statistics to Include Wave-Induced Motion. *Journal of Offshore Mechanics and Arctic Engineering,* 109**,** 278-286.

LICHEY, C. & HELLMER, H. H. 2001. Modeling giant-iceberg drift under the influence of sea ice in the Weddell Sea, Antarctica. *Journal of Glaciology,* 47**,** 452-460.

LIU, Z., AMDAHL, J. & LØSET, S. 2011. Plasticity based material modelling of ice and its application to ship-iceberg impacts. *Cold Regions Science and Technology*.

LØSET, S. 1993. Thermal energy conservation in icebergs and tracking by temperature. *Journal of Geophysical Research: Oceans,* 98**,** 10001-10012.

LØSET, S. 2018. Lecture Notes in UNIS Course: UNIS AT-327 Arctic Offshore Engineering. Longyearbyen, Svalbard: UNIS.

LØSET, S. & CARSTENS, T. 1996. Sea ice and iceberg observations in the western Barents Sea in 1987. *Cold Regions Science and Technology,* 24**,** 323-340.

LØSET, S., SHKHINEK, K., GUDMESTAD, O. & HØYLAND, K. 2006. *Actions from Ice on Arctic Offshore and Coastal Structures,* Krasnodar, St Petersburg, Russia.

LØSET, S., VINJE, T., JENSEN, H., JOHNSEN, Å. S., LØVÅS, S. M. & ERLINGSSON, B. 1989. IDAP 88 Vessel Deployment, Volume 2: Field Observations and Analysis.

LØVÅS, S., SPRING, W. & HOLM, A. Stereo photogrammetric analysis of icebergs and sea ice from the Barents Sea Ice Data Acquisition Program (IDAP). Proceedings of 12th International Conference on Port and Ocean Engineering under Arctic Conditions, 1993. 17-20.

LU, W. & AMDAHL, J. 2019. Glacial Ice and Offshore Structure Impacts under Wave and Current Excitation. *Proceedings - International Conference on Port and Ocean Engineering under Arctic Conditions 2019* Delft, The Netherlands.

LU, W., YU, Z., VAN DEN BERG, M., LUBBAD, R., AMDAHL, J., LØSET, S. & KIM, E. 2018. Assessment of Structural Damage due to Glacial Ice Impact. *In:* PETROLEUMSTILSYNET (ed.) *PTIL-Konstruksjonssikkerhet i Nordområdene.* Stavanger: Petroleumstilsynet.

LUBBAD, R., LØSET, S. & LU, W. 2013. Oden Arctic Technology Research Cruise 2013: Field-Data report. Trondheim: Norwegian University of Science and Technology: NTNU.

MARINATOS, J. N. & SAMUELIDES, M. S. Material characterization and implementation of the RTCL, BWH and SHEAR failure criteria to finite element codes for the simulation of impacts on ship structures. 6th International Conference on Collision and Grounding of Ships and Offshore Structures, ICCGS 2013, 2013 Trondheim. 57-67.
MARTIN, T. & ADCROFT, A. 2010. Parameterizing the fresh-water flux from land ice to ocean with interactive icebergs in a coupled climate model. *Ocean Modelling,* 34**,** 111-124.
MATHIESEN, M., LØVÅS, S. M. & VEFSNMO, S. 1992. Iceberg Collision — Risk Analyses. SINTEF NHL, Report STF60 F92047. 22 p.
MCCLINTOCK, J., BULLOCK, T., MCKENNA, R., RALPH, F. & BROWN, R. 2002. Greenland iceberg management: Implications for grand banks management systems. *PERD/CHC Report***,** 20-65.
MCCLINTOCK, J., MCKENNA, R. & WOODWORTH-LYNAS, C. 2007. Grand Banks Iceberg Management. PERD/CHC Report 20-84. *Report prepared by AMEC Earth & Environmental, St. John's, NL, RF McKenna & Associates. Wakefield, QC, and PETRA International Ltd Cupids, NL*.
NORSOK 2017. Actions and action effects, N-003. *Oslo: Norwegian Technology Standards Institution*.
O'CONNELL, B. Marine radar for improved ice detection. Proceedings of the 8th International Conference and Exhibition on Performance of Ships and Structures in Ice, 20–23 July 2008, Banff, Alberta, Canada, 2008. Citeseer.
OMMANI, B., BERTHELSEN, P. A. & FIROOZKOOHI, R. 2018. Ptil – NORD ST20_2018 Loads, design and operation of floaters in the Arctic.
ONARHEIM, I. H. & ÅRTHUN, M. 2017. Toward an ice‐free Barents Sea. *Geophysical Research Letters,* 44**,** 8387-8395.
RICHARDS, M. A., SCHEER, J., HOLM, W. A. & MELVIN, W. L. 2010. *Principles of modern radar*, Citeseer.
ROSSITER, J. R., GUIGNÉ, J., HILL, C., PILKINGTON, R., REIMER, E., RYAN, J. & WRIGHT, B. 1995. *Remote Sensing Ice Detection Capabilities - East Coast*, Environmental Studies Research Funds.
RUTTER. 2019a. *Ice Navigation* [Online]. Available: https://rutter.ca/ice-navigation/ [Accessed 9. July 2019].
RUTTER. 2019b. *Ice Navigator Brochure* [Online]. Available: https://rutter.ca/wp-content/themes/RutterWebsite/pdfs/IceNavigatorBrochure.pdf [Accessed 9. July 2019].
RUTTER. 2019c. *sigma S6 Ice Navigator System Description* [Online]. Available: https://rutter.ca/wp-content/themes/RutterWebsite/pdfs/sigmaS6IceNavigatorSystemDescription.pdf [Accessed 9. July 2019].
SANDERSON, T. J. O. 1988. Ice mechanics and risks to offshore structures.
SAYEED, T., COLBOURNE, B., QUINTON, B., MOLYNEUX, D., PENG, H. & SPENCER, D. 2017. A review of iceberg and bergy bit hydrodynamic interaction with offshore structures. *Cold Regions Science and Technology,* 135**,** 34-50.
SILVA, T., BIGG, G. & NICHOLLS, K. 2006. Contribution of giant icebergs to the Southern Ocean freshwater flux. *Journal of Geophysical Research: Oceans,* 111.
SIMONSEN, M., HACKETT, B., BERTINO, L., RØED, L. P., WAAGBØ, G. A., DRIVDAL, M. & SUTHERLAND, G. 2018. PRODUCT USER MANUAL For Arctic Ocean Physical and Bio Analysis and Forecasting Products. http://cmems-resources.cls.fr/documents/PUM/CMEMS-ARC-PUM-002-ALL.pdf
SLAGSTAD, D., STØLE-HANSEN, K. & LOENG, H. 1990. Density driven currents in the Barents Sea calculated by a numerical model.
SPRING, W. 1994. Ice Data Acquisition – Summary Report. Mobil Research Dev. Corp., Dallas E&P Eng., 90 p.
SPRING, W., VINJE, T. & JENSEN, H. Iceberg and sea ice data obtained in the annual expeditions of the Barents Sea Ice Data Acquisition Program (IDAP). Proceedings of 12th International Conference on Port and Ocean Engineering under Arctic Conditions, 1993. 17-20.
STORHEIM, M., AMDAHL, J. & MARTENS, I. 2015. On the accuracy of fracture estimation in collision analysis of ship and offshore structures. *Marine Structures,* 44**,** 254-287.
TAVAKOLI, M. T. & AMDAHL, J. 2010. Analysis of collision between Midgard platform and 8000 tonnes displacement ship
TIMCO, G. W. & WEEKS, W. F. 2010. A review of the engineering properties of sea ice. *Cold Regions Science and Technology,* 60**,** 107-129.
UNIS 2009. Lance Cruise Report in the Barents Sea - May 2009, 57 p.
WAGNER, T. J., STERN, A. A., DELL, R. W. & EISENMAN, I. 2017. On the representation of capsizing in iceberg models. *Ocean Modelling,* 117**,** 88-96.
YU, Z. & AMDAHL, J. 2018. A review of structural responses and design of offshore tubular structures subjected to ship impacts. *Ocean Engineering,* 154**,** 177-203.

Appendix A

This appendix presents the results from the best guess estimate scenario. The number of icebergs released from each location is provided in

Table A. 1. The total number of icebergs released per year from the 5 sources is 200 icebergs per year. The results of the global analysis including all the icebergs are presented in Figure A. 1, Figure A. 2, Figure A. 3, Figure A. 4 and Figure A. 5. The results of the global analysis excluding growlers (icebergs with a total height less than 10 m are excluded) are presented in Figure A. 6, Figure A. 7, Figure A. 8, Figure A. 9, Figure A. 10, Figure A. 11 and Table A. 2. The local probabilities and annual encounter frequencies are shown in Table A. 3 and Table A. 4.

Table A. 1. Major iceberg calving locations and average iceberg production rates in the Barents Sea. The average number of icebergs is based on an average iceberg mass of 311000 tonnes.

Geographical area	Calving location	Number of icebergs released/year
Franz Josef Land (East)	80.5°N/62.8°E	65
Franz Josef Land (West)	81.0°N/48.7°E	111
Nordaustfonna	79.6°N/27.0°E	10
Edgeøya	77.7°N/25.0°E	5
Novaya Zemlya	76.4°N/63.0°E	9

A.1. Global analysis

A.1.1. Results including growlers

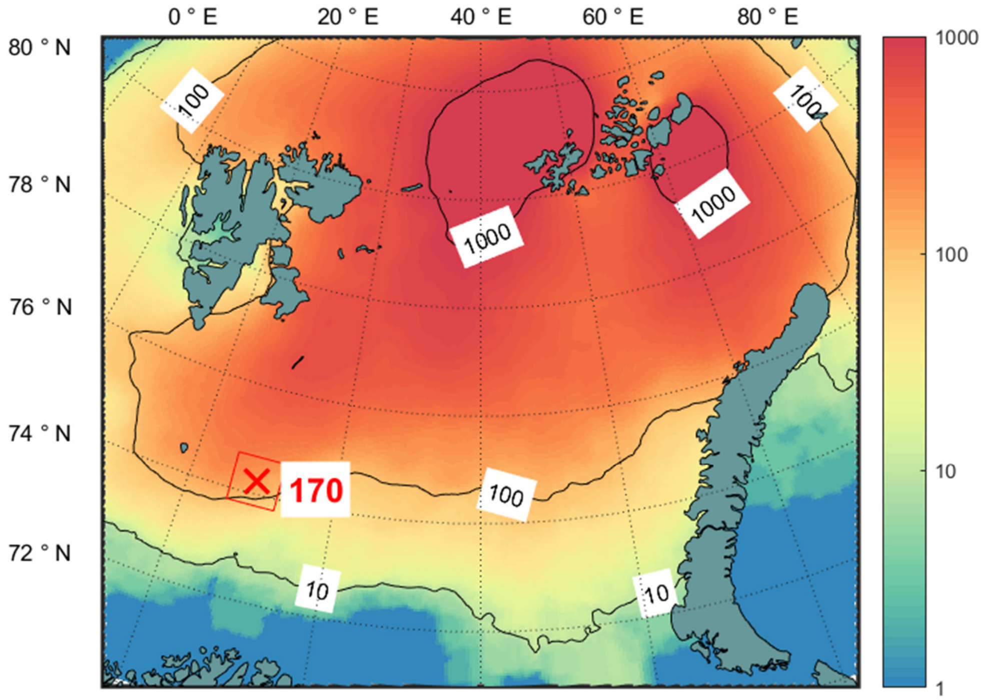

Figure A. 1. Total number of icebergs in a 100 × 100 km box during the simulated 27 years.

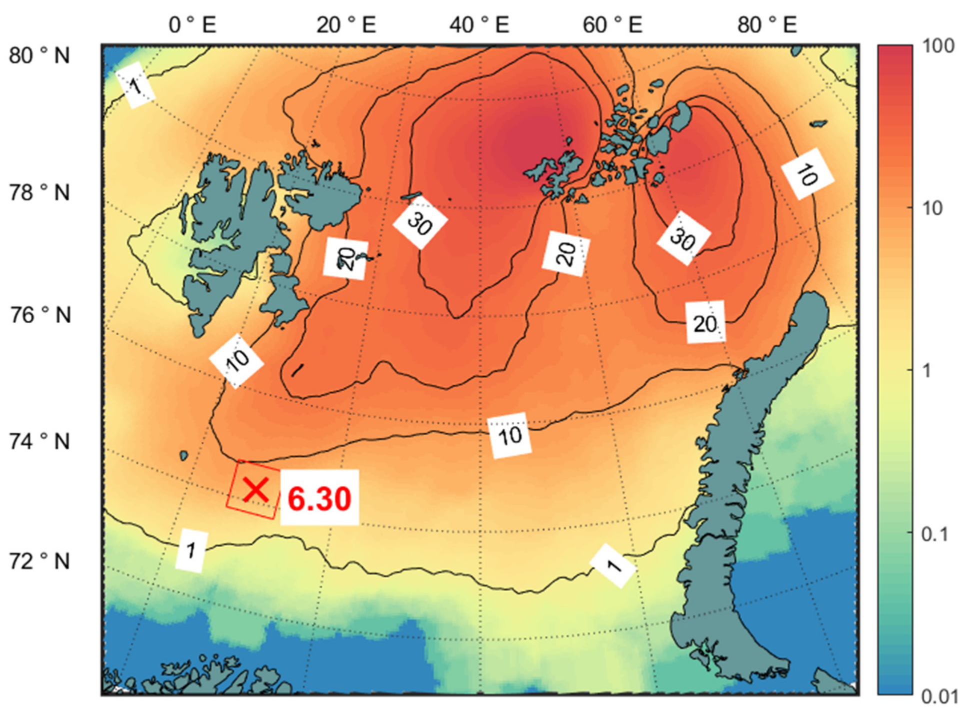

Figure A. 2. Expected number of icebergs per year in a 100 × 100 km box.

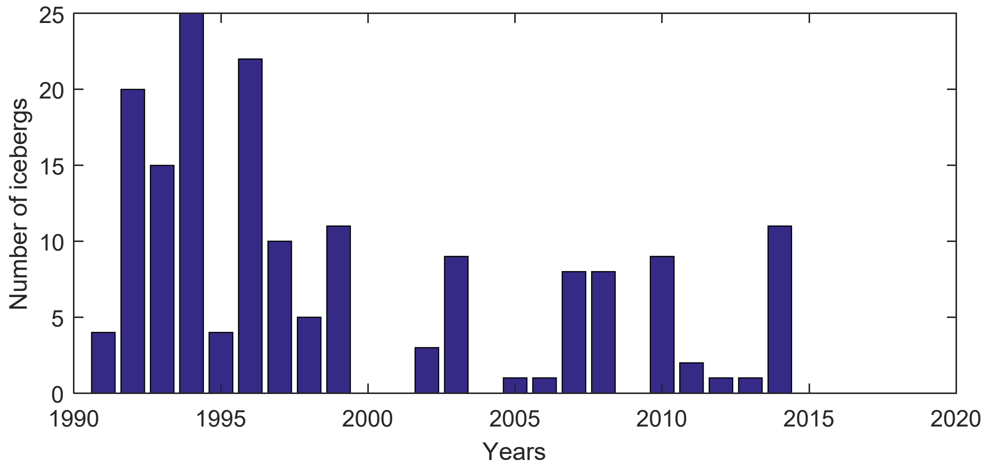

Figure A. 3. Number of icebergs entering the 100 × 100 km box at Block #7424.

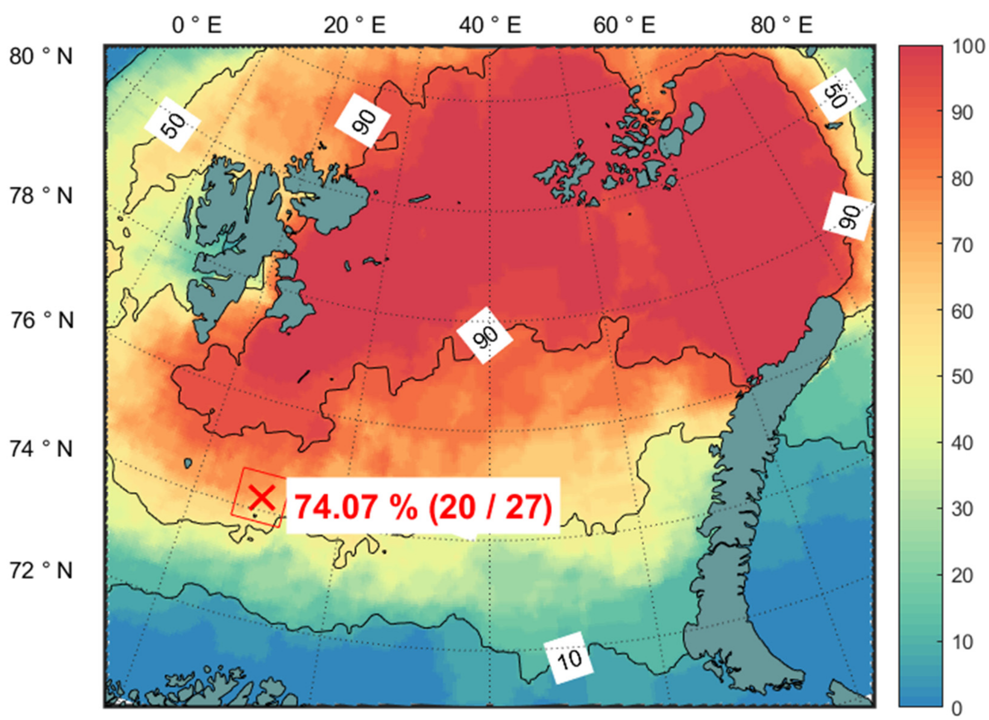

Figure A. 4. Yearly probability of iceberg occurrence in a 100 × 100 km box (i.e., at least one iceberg entering the box).

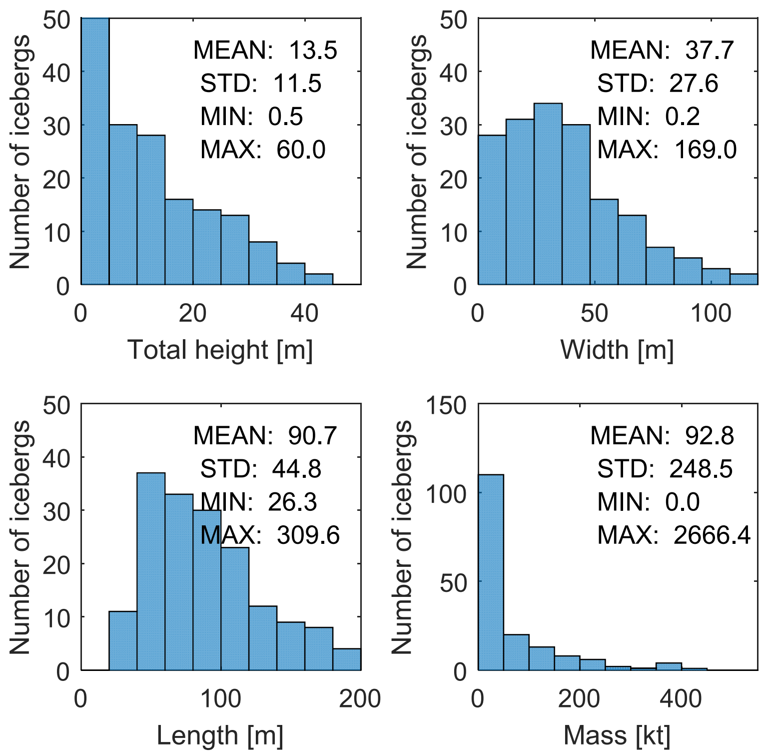

Figure A. 5. Histogram of dimensions and mass of icebergs as they enter the 100 × 100 km box at Block #7424.

A.1.2. Results excluding growlers

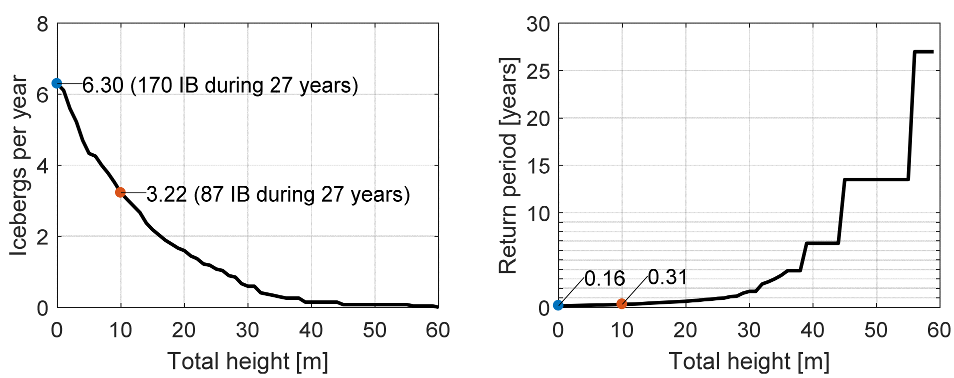

Figure A. 6. Effect of imposing a threshold for minimal total height of icebergs. Left: Number of icebergs entering Block #7424. Right: Return period (Expected average number of years for an iceberg of given height to Block #7424).

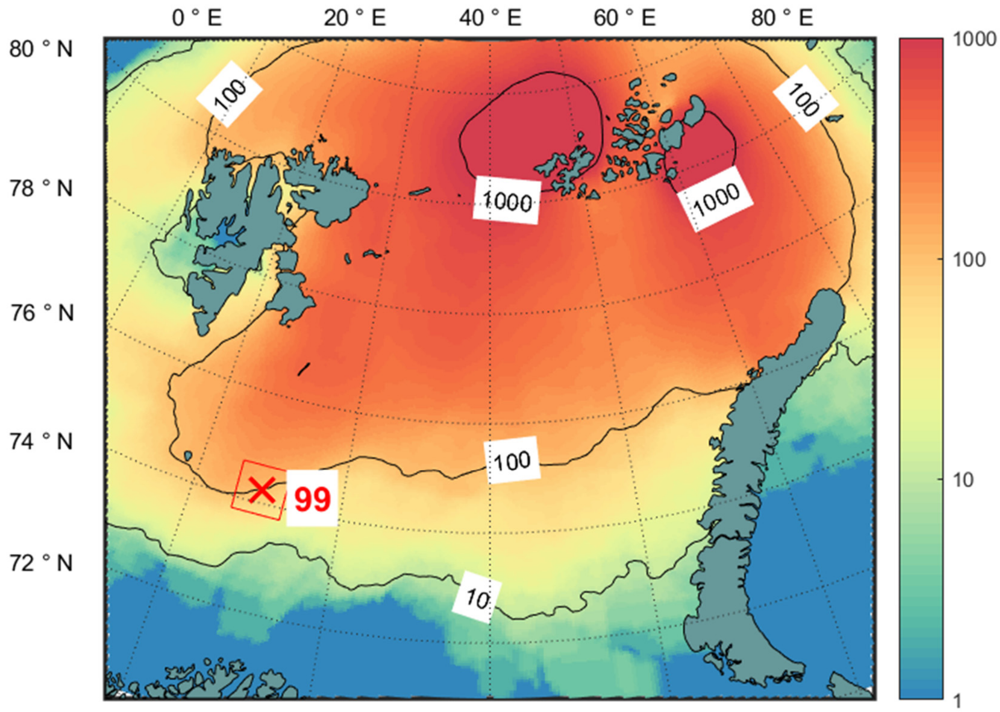

Figure A. 7. Updated total number of icebergs in a 100 × 100 km box during the simulated 27 years. Icebergs with total height less than 10 m are neglected.

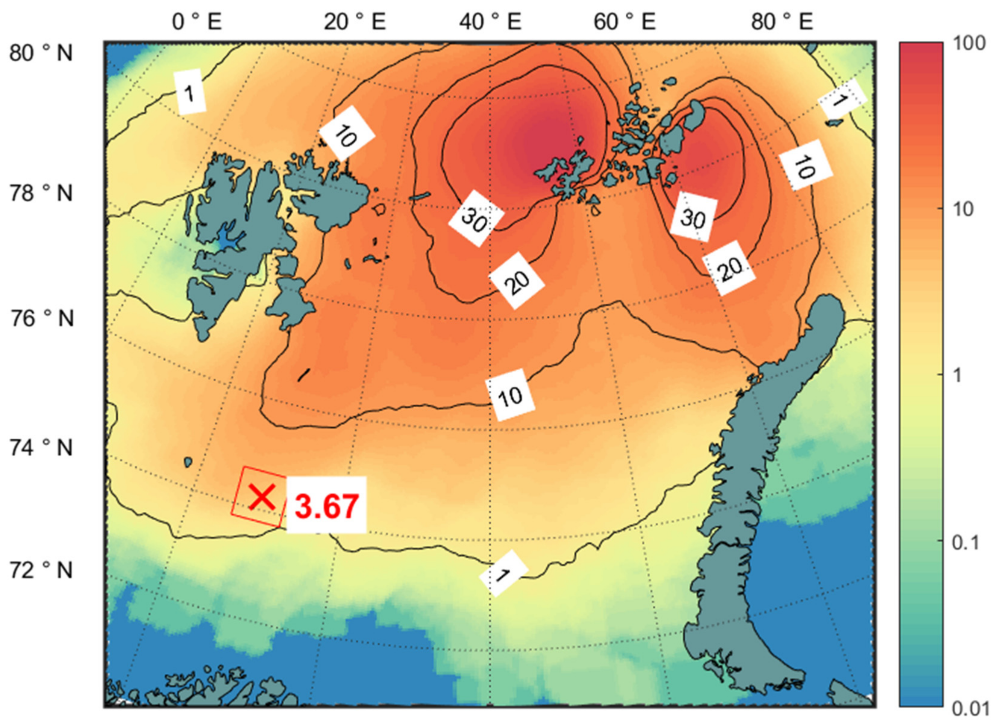

Figure A. 8. Updated expected number of icebergs per year in a 100 × 100 box. Icebergs with total height less than 10 m are neglected.

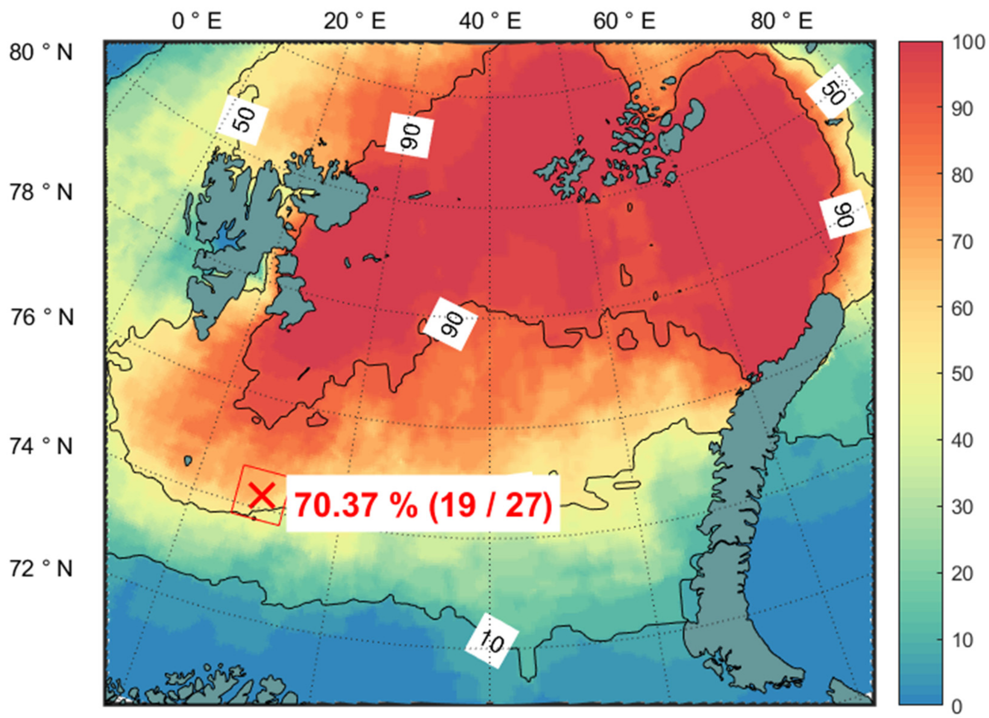

Figure A. 9. Updated yearly probability of iceberg occurrence in a 100 × 100 km box (i.e., at least one iceberg entering). Icebergs with total height less than 10 m are neglected.

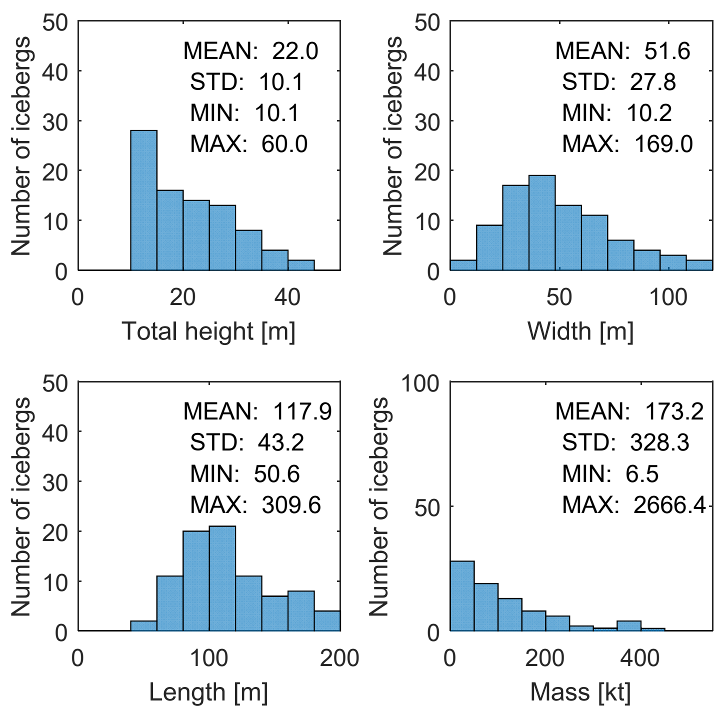

Figure A. 10. Updated histograms of dimensions and mass of icebergs as they enter the 100 × 100 km box at Block #7424. Icebergs with total height less than 10 m are neglected.

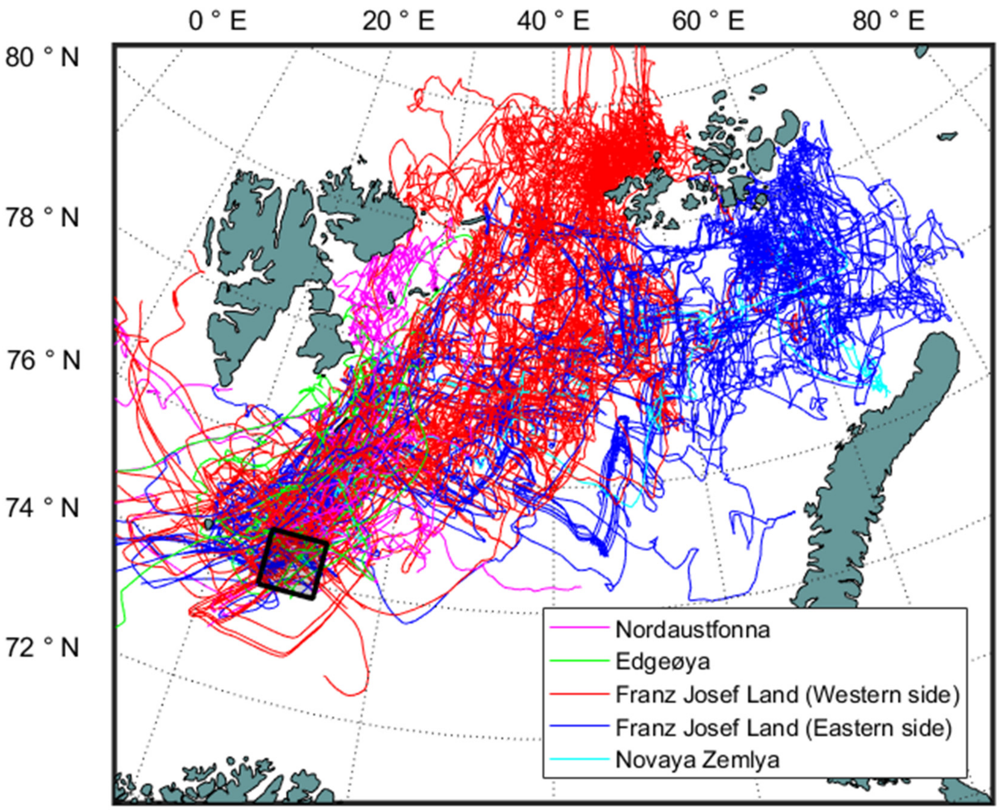

Figure A. 11. Trajectories of 99 icebergs that have entered the 100 × 100 km box at Block #7424. Trajectories are plotted from the origin of the icebergs until they deteriorated to a total thickness smaller than 10 m.

Table A. 2. Origin of the 26 tracks that entered the 100 × 100 km box at Block #7424.

Origin of icebergs	Number	Percentage [%]
Nordaustfonna	8	8.08
Edgeøya	6	6.06
Franz Josef Land (Western side)	56	56.57
Franz Josef Land (Eastern side)	26	26.26
Novaya Zemlya	3	3.03

A.2. Local analysis

A.2.1 Results excluding growlers

Table A. 3. The local iceberg collision probability with structures of varying sizes.

	Structure size (*l*)		
	100 × 100 m	500 × 500 m	1000 × 1000 m
Local Probability (P_l)	0.000478	0.00241	0.00485

Table A. 4. The annual iceberg encounter frequency at Block #7424.

	Structure size (*l*)		
	100 × 100 m	500 × 500 m	1000 × 1000 m
Annual iceberg encounter frequency (E_N)	$1.75 \cdot 10^{-3}$	$8.86 \cdot 10^{-3}$	$1.78 \cdot 10^{-2}$

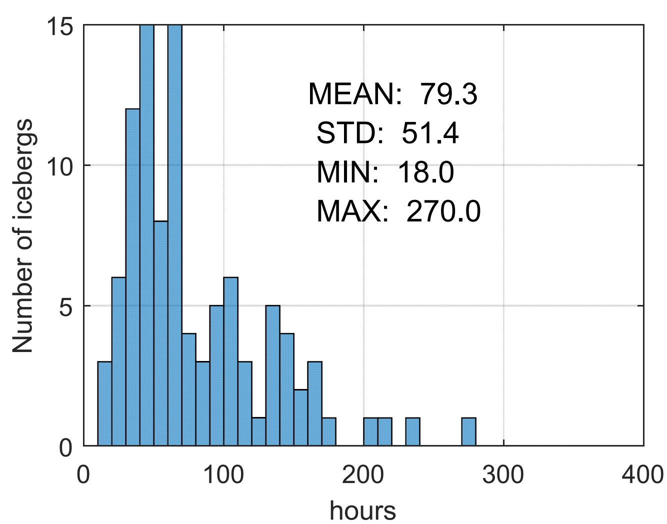

Figure A. 12. Histogram of the iceberg residence time within the 100 × 100 km box at Block #7424.

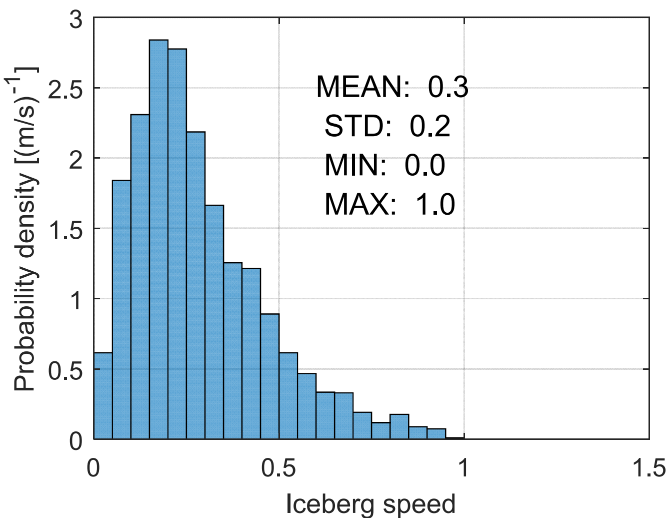

Figure A. 13. Histogram of the iceberg drift speeds (m/s).

A.2.2 Results including growlers

Table A.5. The local iceberg collision probability with structures of varying sizes.

	Structure size (l)		
	100 × 100 m	500 × 500 m	1000 × 1000 m
Local Probability (P_l)	0.000451	0.00225	0.00462

Table A. 7. The annual iceberg encounter frequency at Block #7424.

	Structure size (l)		
	100 × 100 m	500 × 500 m	1000 × 1000 m
Annual iceberg encounter frequency (E_N)	$2.8 \cdot 10^{-3}$	$1.42 \cdot 10^{-2}$	$2.91 \cdot 10^{-2}$

Appendix B

The simulations of the conservative scenario performed with the global model as described in Section 5.2 were repeated three times to ensure statistical validity. Here we present the results of Simulations #1, #2 and #3. The results of the three simulations are very similar, which gives confidence in the statistical validity of the numerical model. Note that the results of Simulation #1 are identical to the ones presented in Section 5.2.2.

B.1. Results of Simulation #1

The results of Simulation #1 are presented in Figure B. 1, Figure B. 2, Figure B. 3, Figure B. 4 and Figure B. 5 including all the icebergs, i.e., no threshold is applied on the iceberg total height. Figure B. 6 shows the effect of applying the threshold of 10 meter on the iceberg total height for the location of Block #7424.

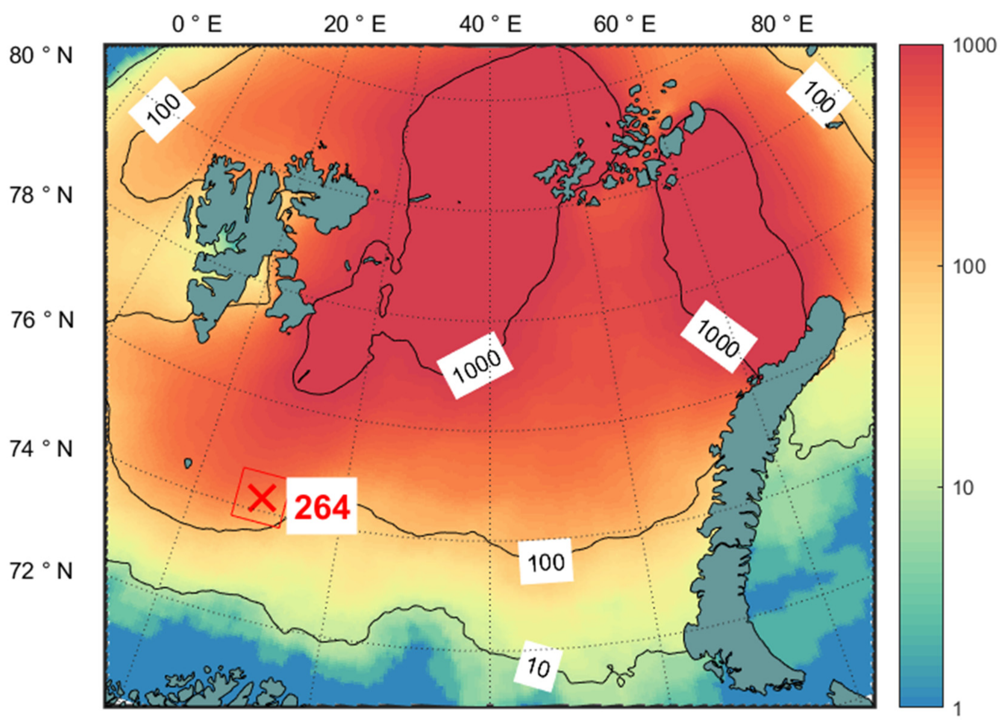

Figure B. 1. Total number of icebergs in a 100 × 100 km box during the simulated 27 years for Simulation #1.

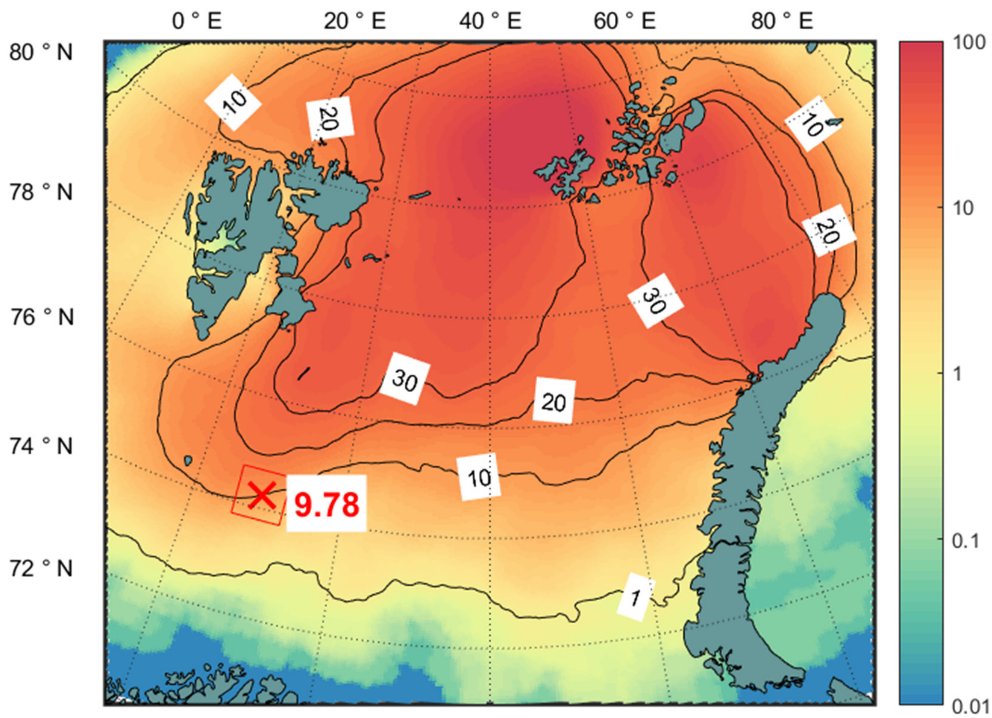

Figure B. 2. Expected number of icebergs per year in a 100 × 100 km box for Simulation #1.

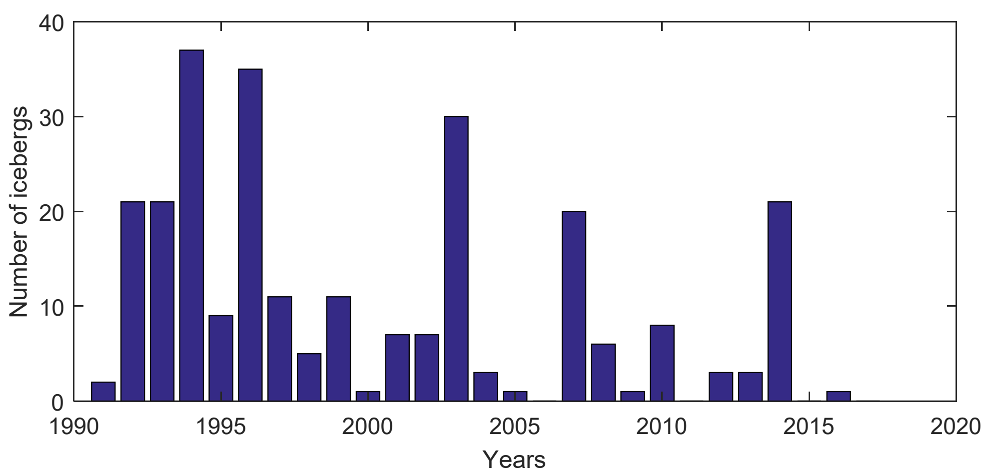

Figure B. 3. Number of icebergs entering the 100 × 100 km box at Block #7424 for Simulation #1.

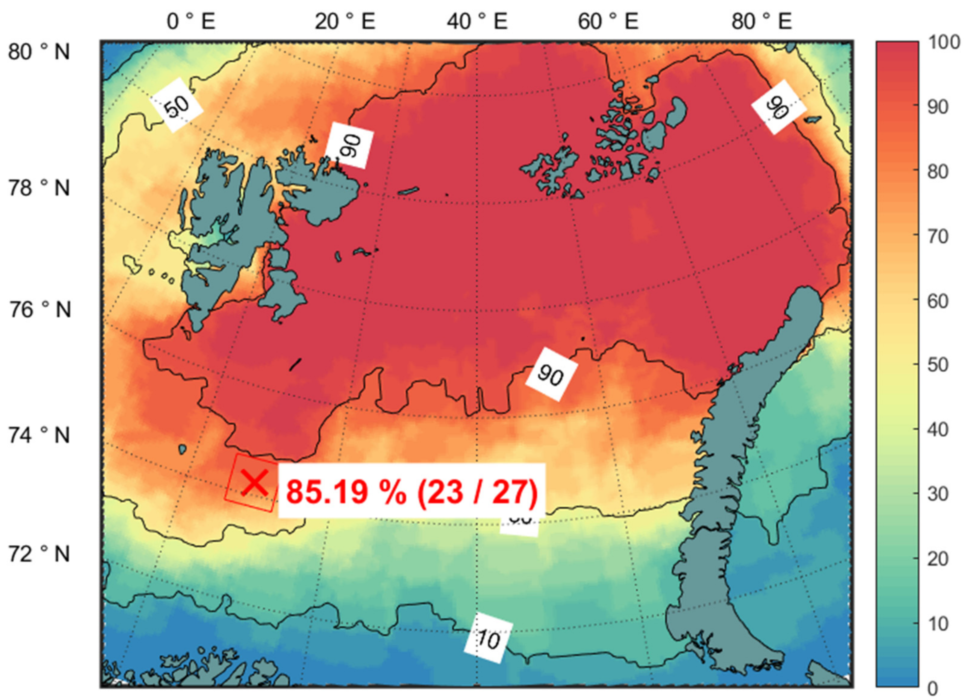

Figure B. 4. Yearly probability of iceberg occurrence in a 100 × 100 km box (i.e., at least one iceberg entering the box), for Simulation #1.

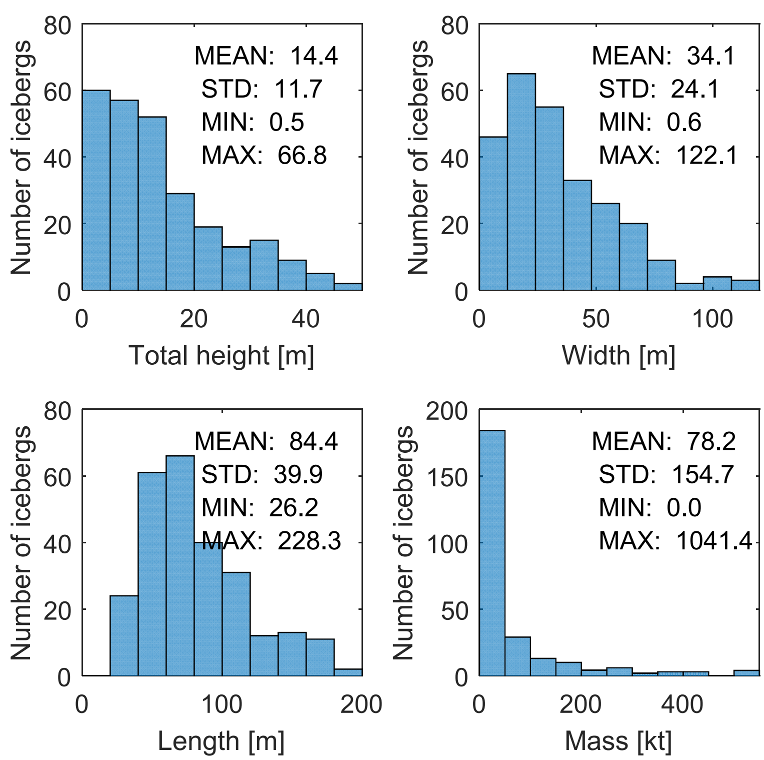

Figure B. 5. Histogram of dimensions and mass of icebergs as they enter the 100 × 100 km box at Block #7424 for Simulation #1.

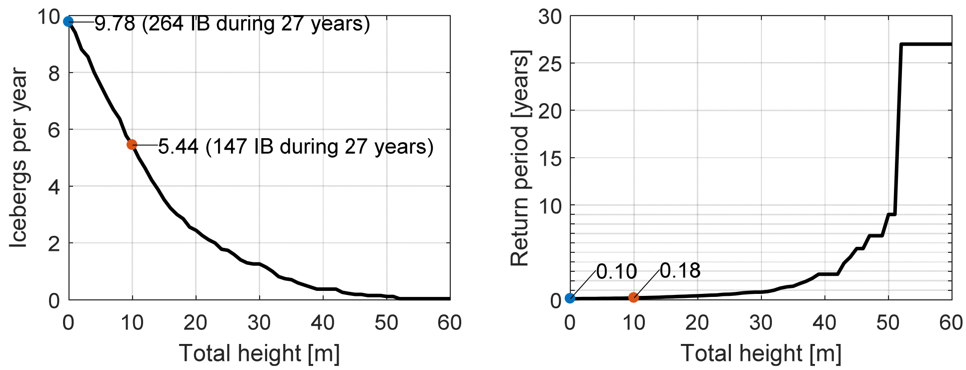

Figure B. 6. Effect of imposing a threshold for minimal total height of icebergs. Left: Number of icebergs entering Block #7424. Right: Return period (Expected average number of years for an iceberg of given height to enter Block #7424), for Simulation #1.

B.2. Results of Simulation #2

The results of Simulation #2 are presented in Figure B. 7, Figure B. 8, Figure B. 9, Figure B. 10 and Figure B. 11 including all the icebergs, i.e., no threshold is applied on the iceberg total height. Figure B. 12 shows the effect of applying the threshold of 10 meter on the iceberg total height for Block #7424.

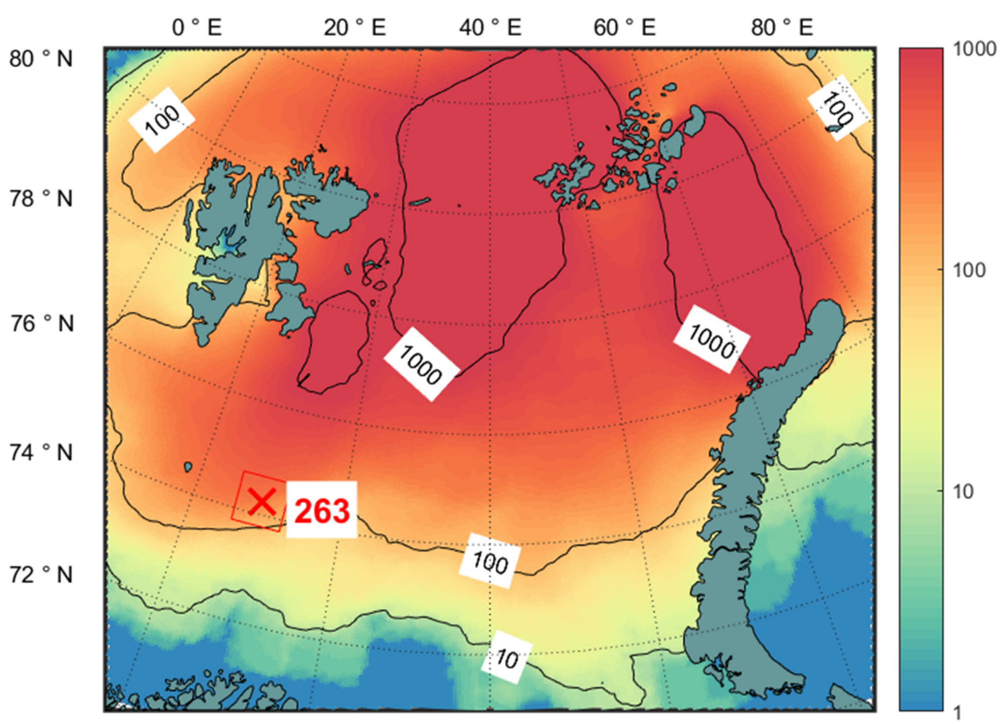

Figure B. 7. Total number of icebergs in a 100 × 100 km box during the simulated 27 years for Simulation #2.

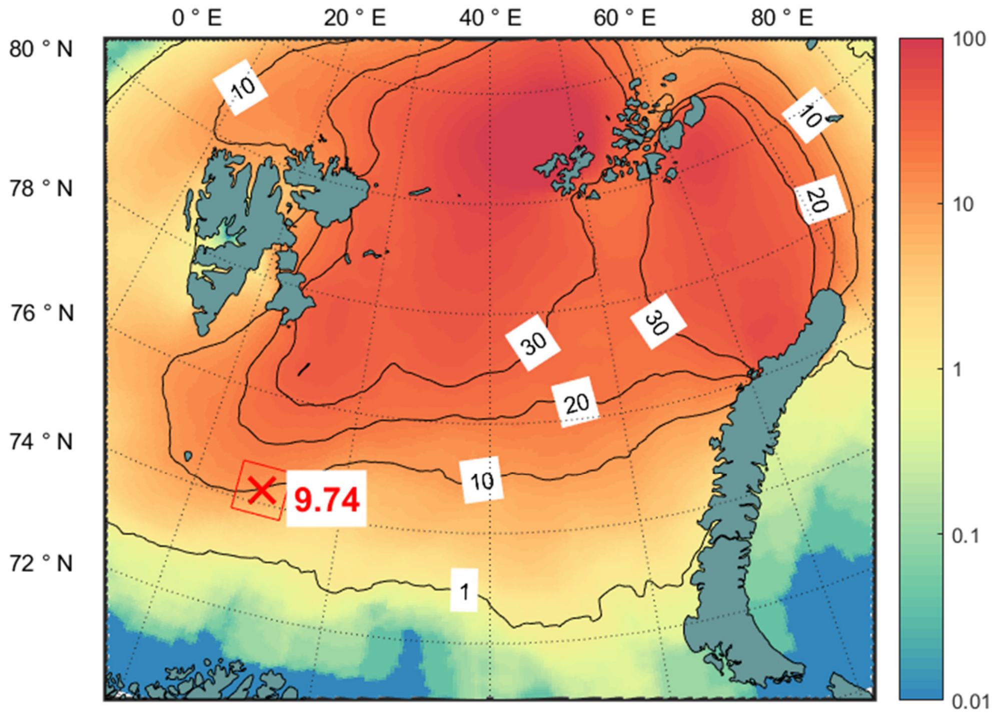

Figure B. 8. Expected number of icebergs per year in a 100 × 100 km box for Simulation #2.

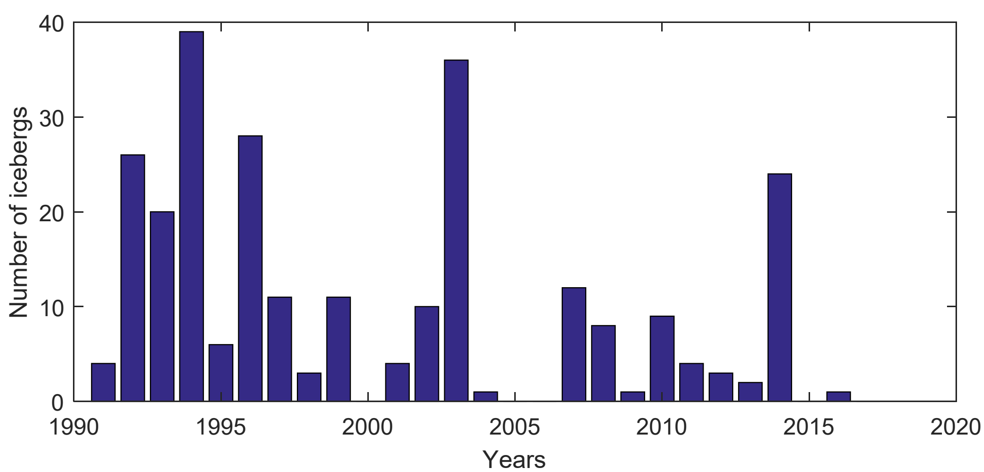

Figure B. 9. Number of icebergs entering the 100 × 100 km box at Block #7424 for Simulation #2.

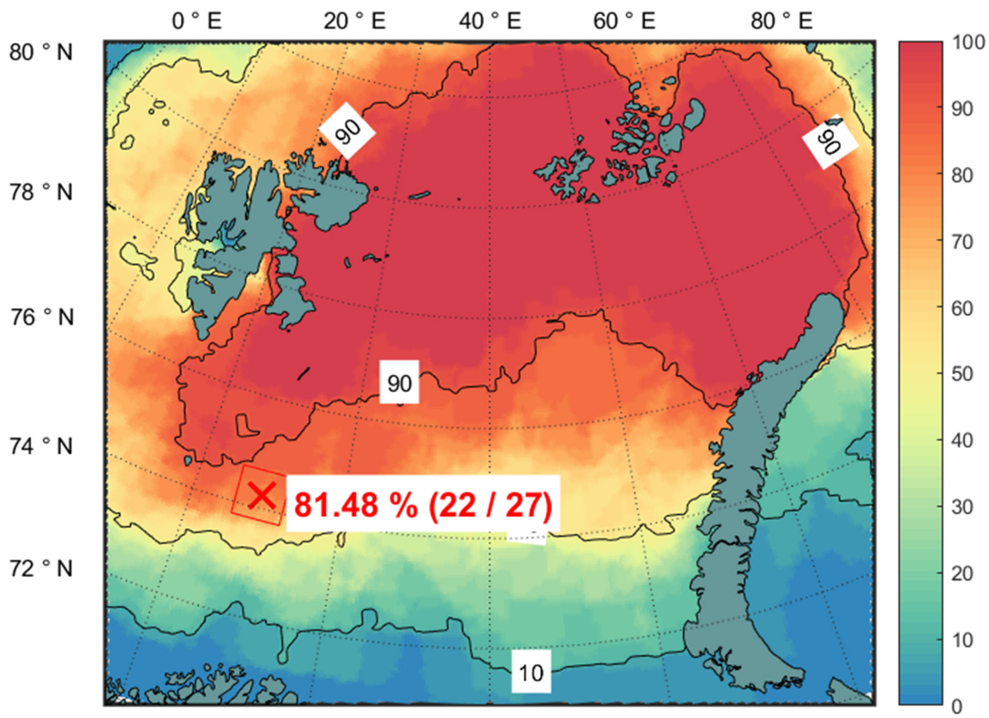

Figure B. 10. Yearly probability of iceberg occurrence in a 100 × 100 km box (i.e., at least one iceberg entering a box), for Simulation #2.

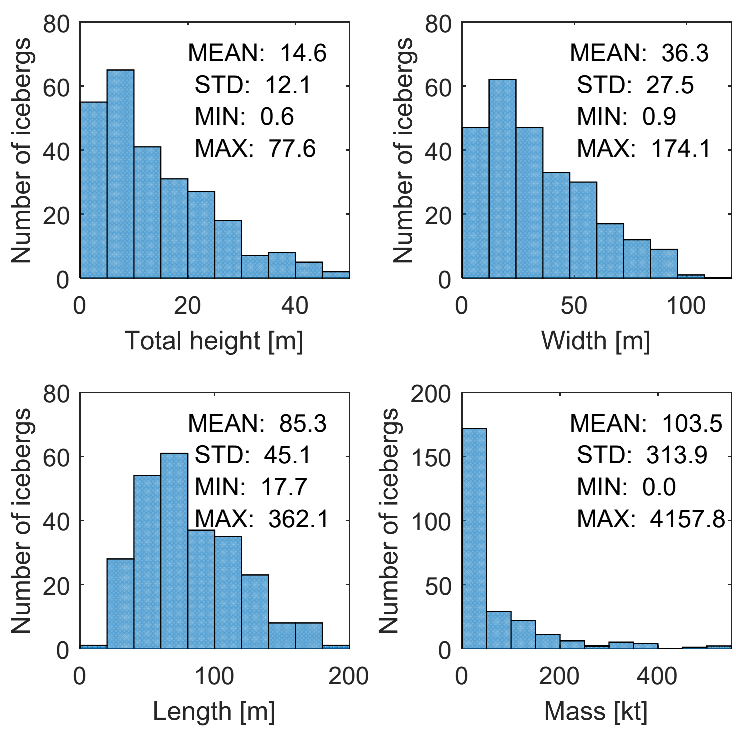

Figure B. 11. Histogram of dimensions and mass of icebergs as they enter the 100 × 100 km box at Block #7424 for Simulation #2.

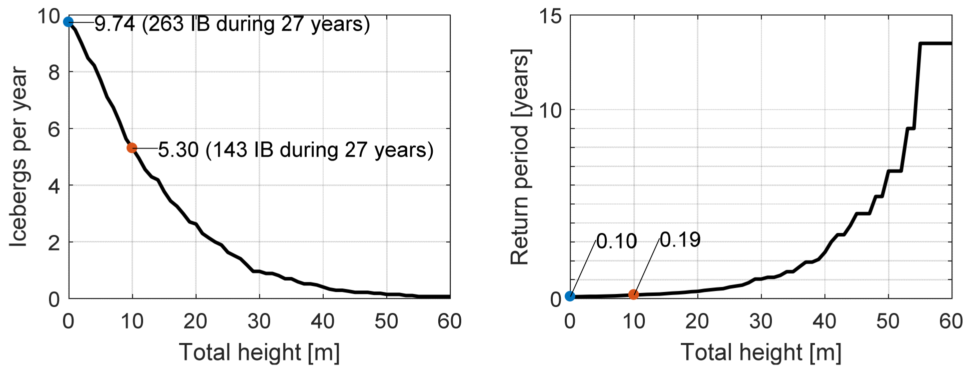

Figure B. 12. Effect of imposing a threshold for minimal total height of icebergs. Left: Number of icebergs entering Block #7424. Right: Return period (Expected average number of years for an iceberg of given height to enter Block #7424), for Simulation #2.

B.3. Results of Simulation #3

The results of Simulation #3 are presented in Figure B. 13, Figure B. 14, Figure B. 15, Figure B. 16, Figure B. 17 including all the icebergs, i.e., no threshold is applied on the iceberg total height. Figure B. 18 shows the effect of applying the threshold of 10 meter on the iceberg total height for the location of Block #7424.

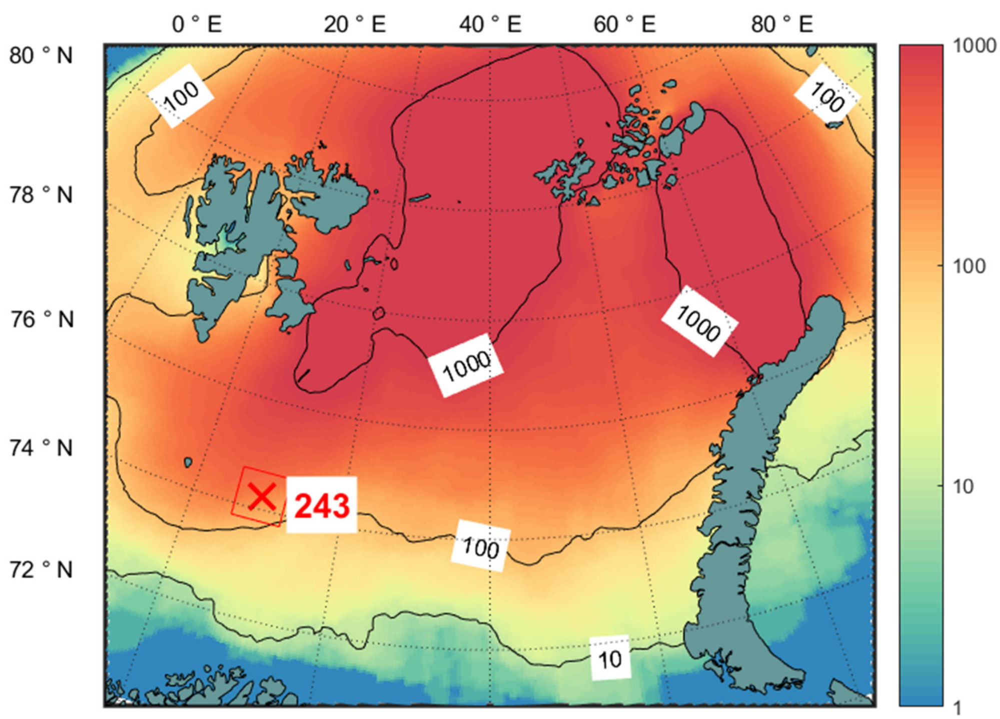

Figure B. 13. Total number of icebergs in a 100 × 100 km box during the simulated 27 years for Simulation #3.

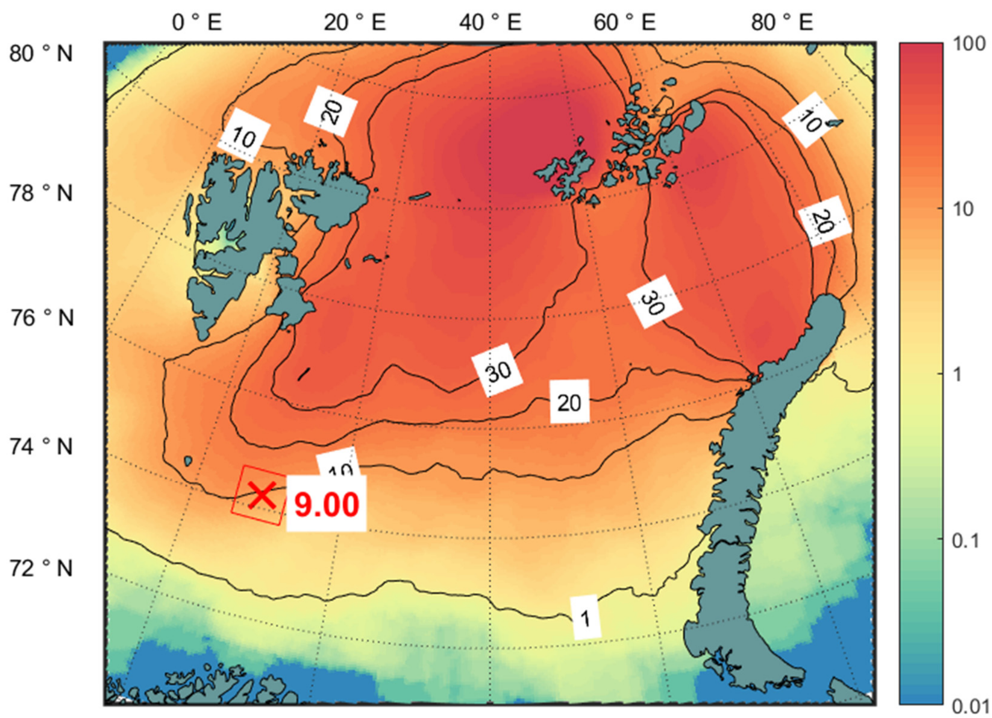

Figure B. 14. Expected number of icebergs per year in a 100 × 100 km box for Simulation #3.

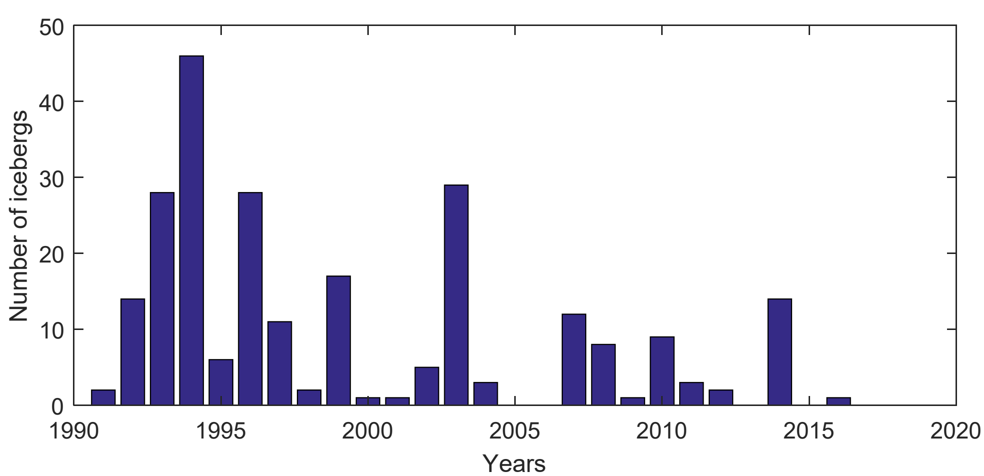

Figure B. 15. Number of icebergs entering the 100 × 100 km box at Block #7424 for Simulation #3.

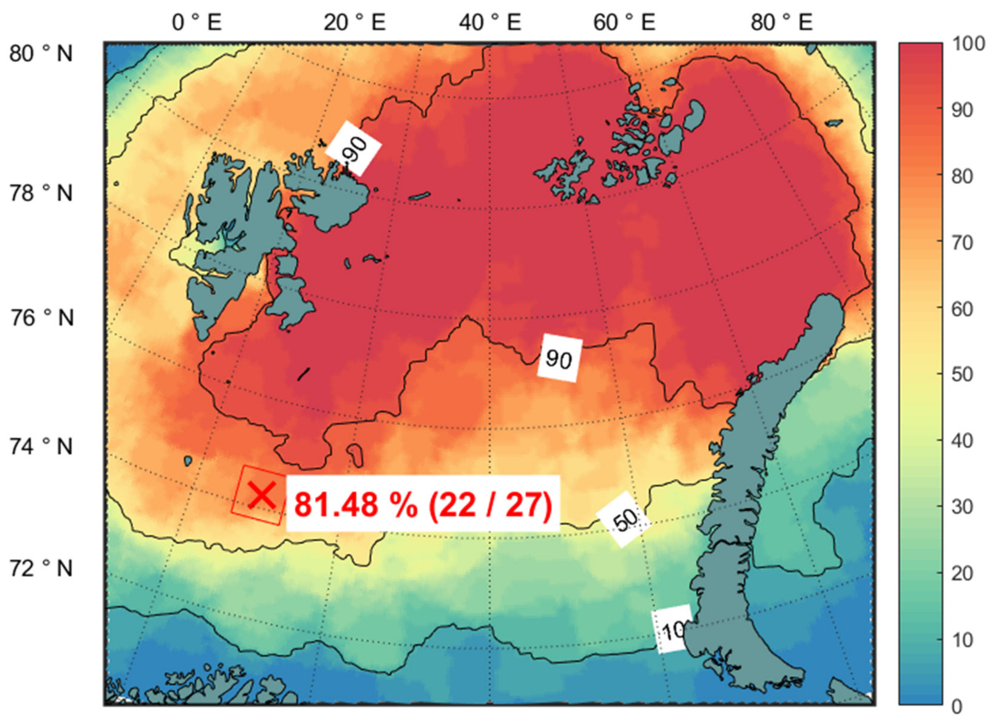

Figure B. 16. Yearly probability of iceberg occurrence in a 100 × 100 km box (i.e., at least one iceberg entering the box), for Simulation #3.

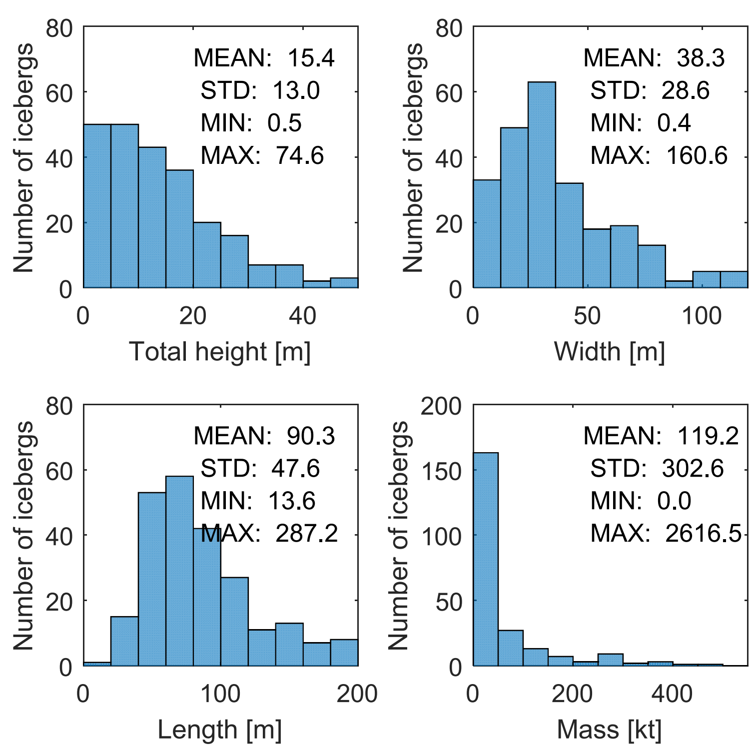

Figure B. 17. Histogram of dimensions and mass of icebergs as they enter the 100 × 100 km box at Block #7424 for Simulation #3.

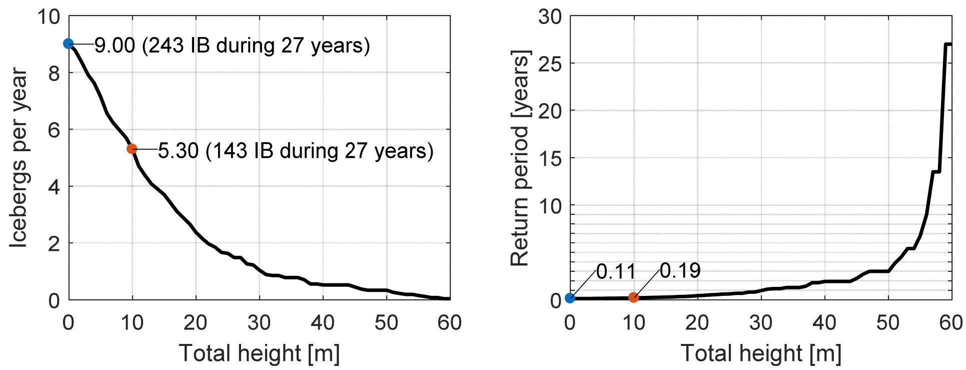

Figure B. 18. Effect of imposing a threshold for minimal total height of icebergs. Left: Number of icebergs entering Block #7424. Right: Return period (Expected average number of years for an iceberg of given height to enter Block #7424), for Simulation #3.

Appendix C

This appendix presents the simulation results of the conservative scenario once with half the number of the released icebergs (*less conservative scenario*) and once the twice the number of the released icebergs (*overly conservative scenario*). This is done to study the sensitivity of the results from the conservative scenario on the assumed number of icebergs released.

C.1. Less conservative scenario

The number of icebergs released from each location is provided in Table C. 1. The total number of icebergs released per year from the 5 sources is 164 icebergs per year. The results of the global analysis including all the icebergs are presented in Figure C. 1, Figure C. 2, Figure C. 3, Figure C. 4 and Figure C. 5 . The results of the global analysis excluding growlers (icebergs with a total height less than 10 m are excluded) are presented in Figure C. 6, Figure C. 7, Figure C. 8, Figure C. 9, Figure C. 10, Figure C. 11 Figure A. 6 and Table C. 2. The local probabilities and annual encounter frequencies are shown in

Table C. 3 and Table C. 4.

Table C. 1. Major iceberg calving locations and average iceberg production rates in the Barents Sea. The average number of icebergs is based on an average iceberg mass of 311000 tonnes.

Geographical area	Calving location	Number of icebergs released/year
Franz Josef Land (East)	80.5°N/62.8°E	38
Franz Josef Land (West)	81.0°N/48.7°E	85
Nordaustfonna	79.6°N/27.0°E	7
Edgeøya	77.7°N/25.0°E	9
Novaya Zemlya	76.4°N/63.0°E	25

C.1.1. Global analysis

C.1.1.1. Results including growlers

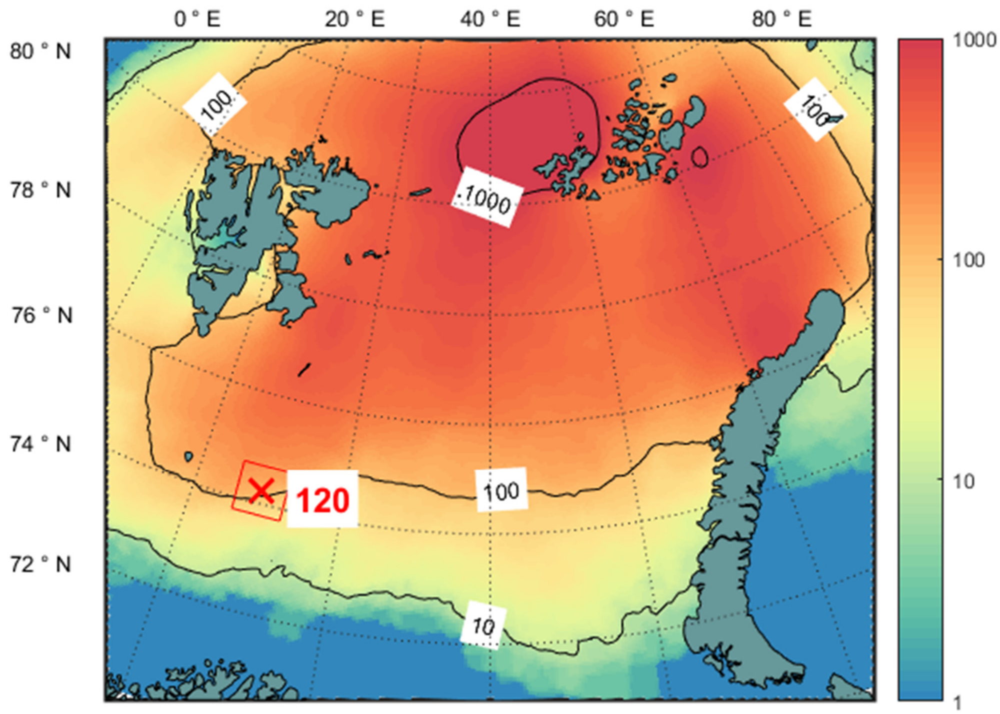

Figure C. 1. Total number of icebergs in a 100 × 100 km box during the simulated 27 years.

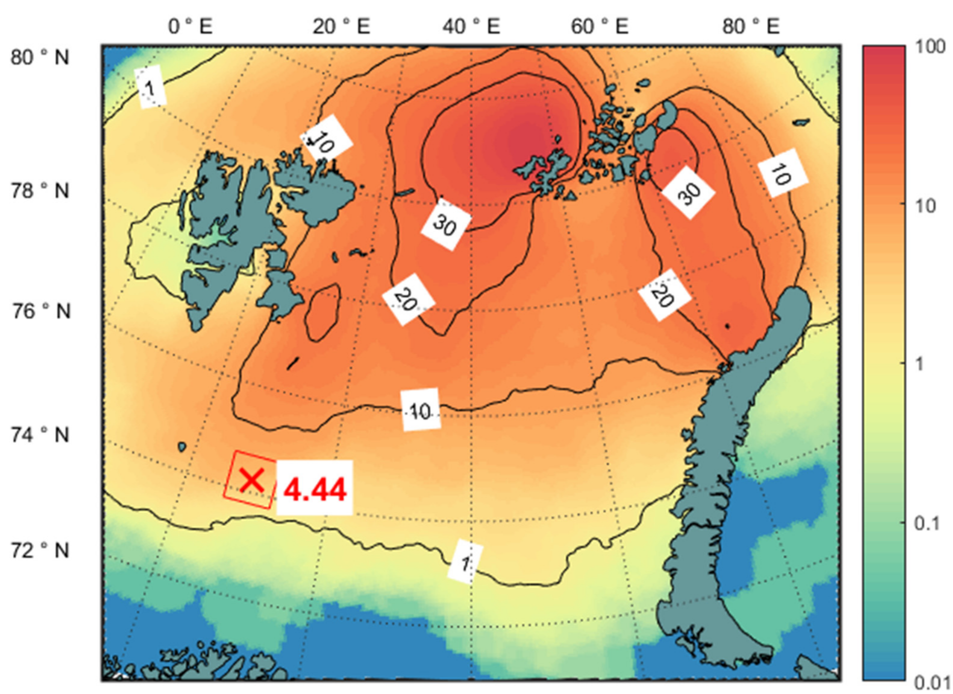

Figure C. 2. Expected number of icebergs per year in a 100 × 100 km box.

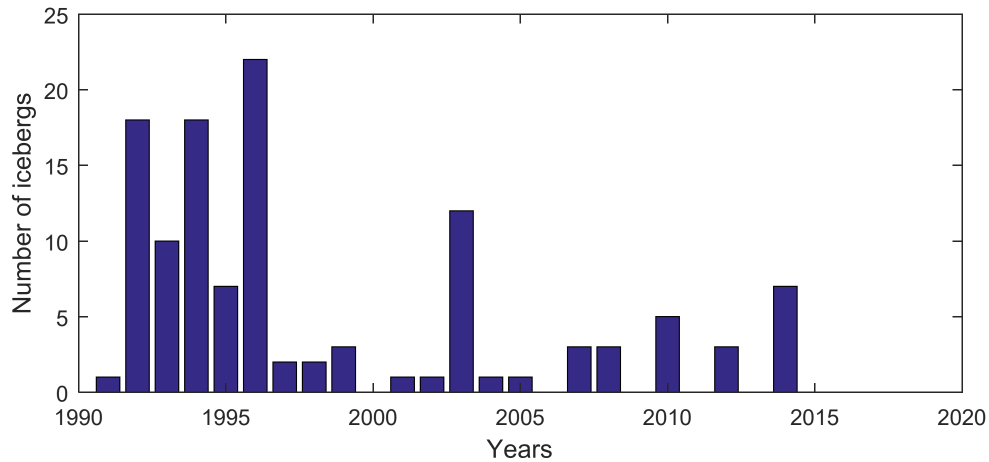

Figure C. 3. Number of icebergs entering the 100 × 100 km box at Block #7424.

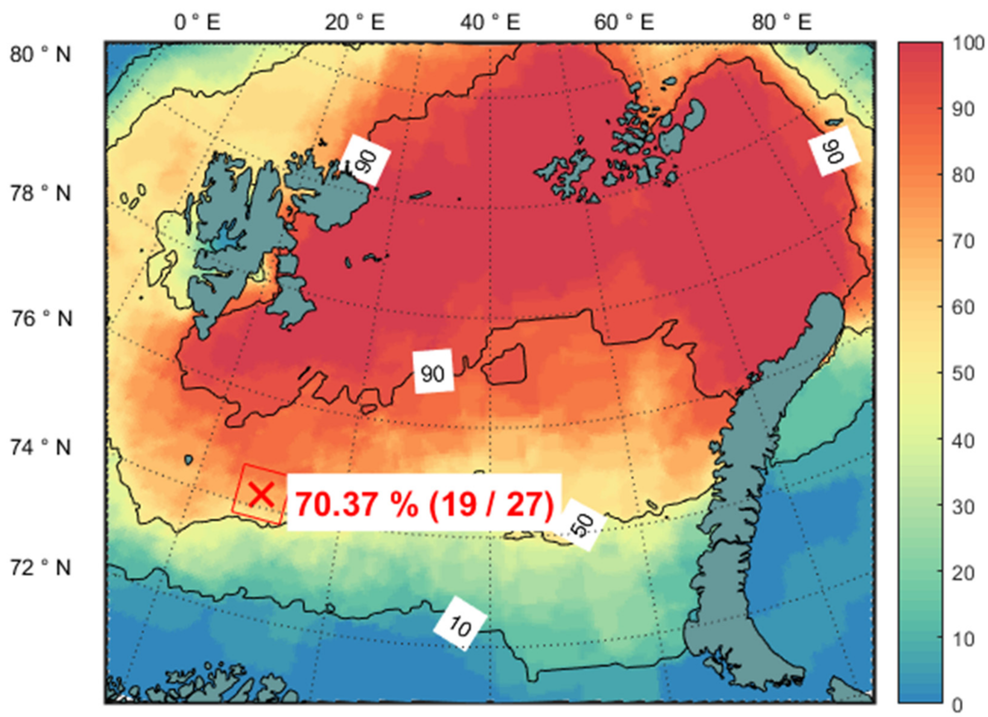

Figure C. 4. Yearly probability of iceberg occurrence in a 100 × 100 km box (i.e., at least one iceberg entering the box).

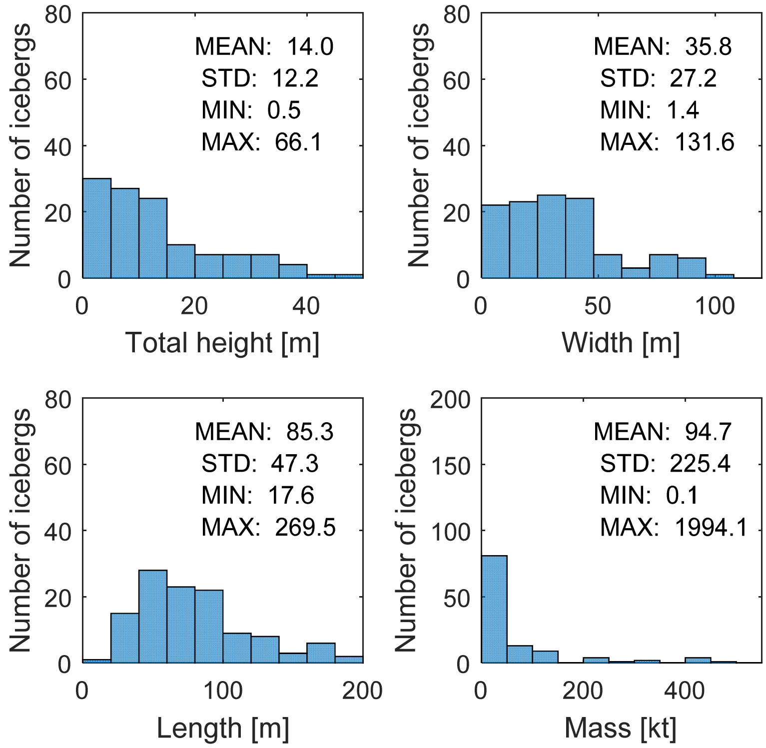

Figure C. 5. Histogram of dimensions and mass of icebergs as they enter the 100 × 100 km box at Block #7424.

C.1.1.2. Results excluding growlers

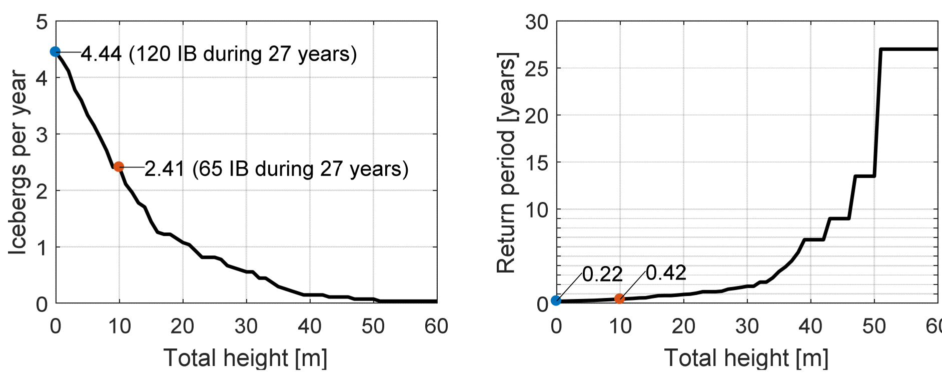

Figure C. 6. Effect of imposing a threshold for minimal total height of icebergs. Left: Number of icebergs entering Block #7424. Right: Return period (Expected average number of years for an iceberg of given height to enter Block #7424).

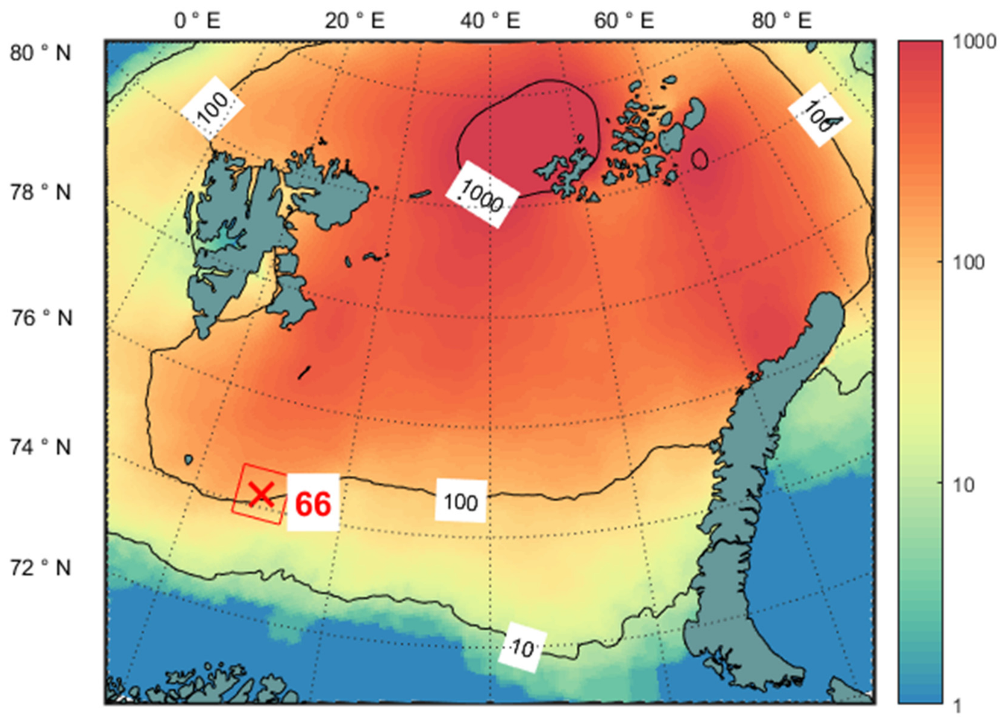

Figure C. 7. Updated total number of icebergs in a 100 × 100 km box during the simulated 27 years. Icebergs with total height less than 10 m are neglected.

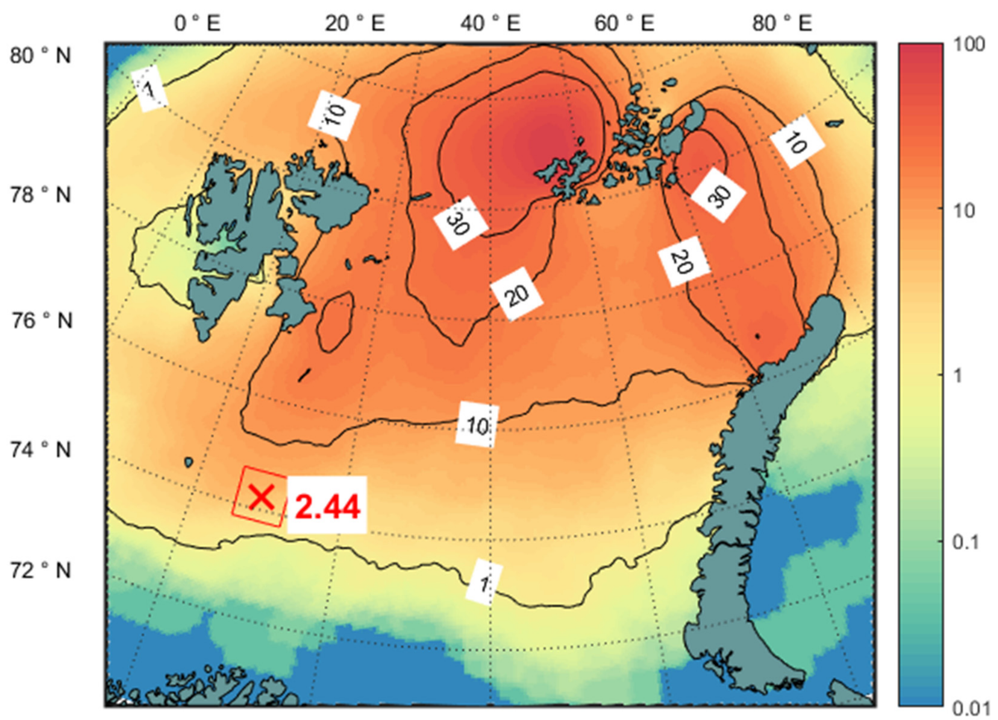

Figure C. 8. Updated expected number of icebergs per year in a 100 × 100 km box. Icebergs with total height less than 10 m are neglected.

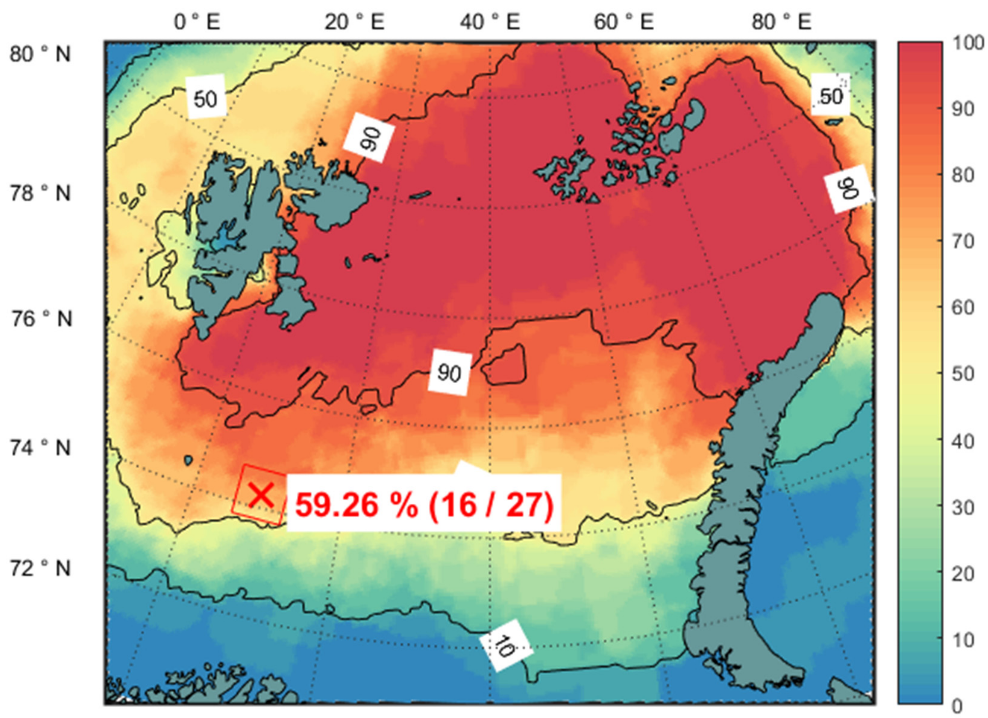

Figure C. 9. Updated yearly probability of iceberg occurrence in a 100 × 100 km box (i.e., at least one iceberg entering). Icebergs with total height less than 10 m are neglected.

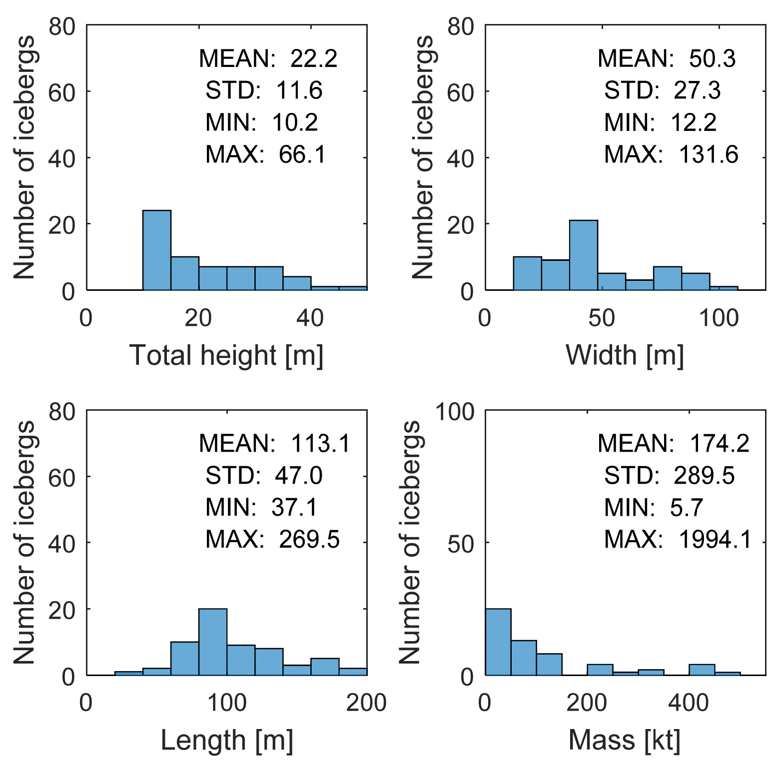

Figure C. 10. Updated histograms of dimensions and mass of icebergs as they enter the 100 x 100 km box at Block #7424. Icebergs with total height less than 10 m are neglected.

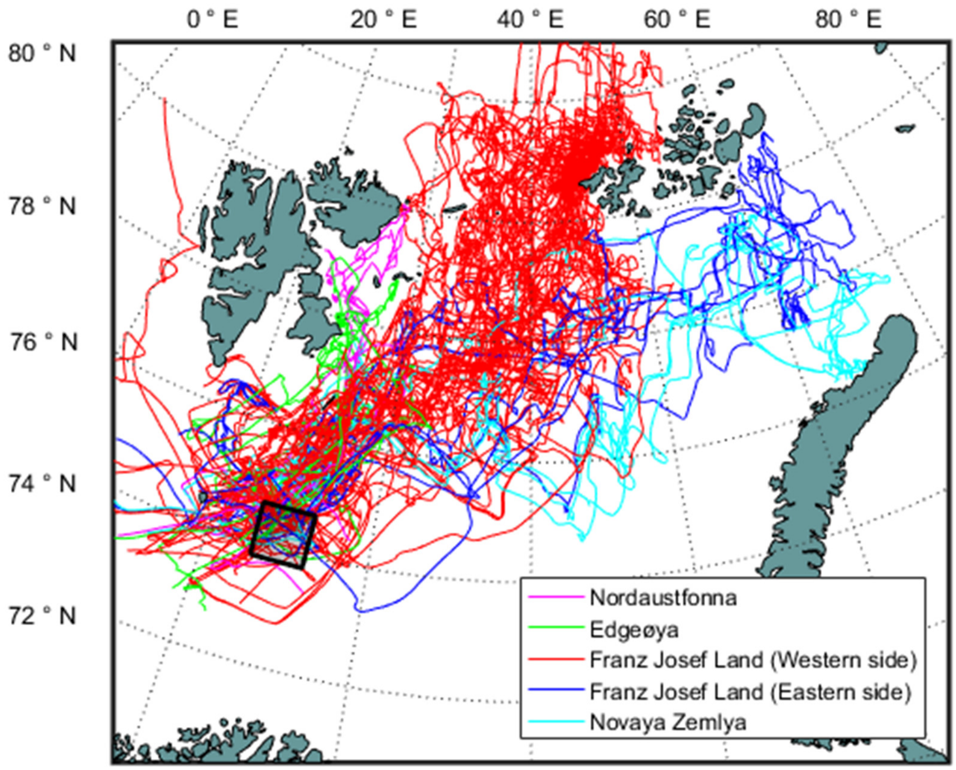

Figure C. 11. Trajectories of 66 icebergs that have entered the 100 × 100 km box at Block #7424. Trajectories are plotted from the origin of icebergs until the icebergs deteriorated to a total thickness smaller than 10 m.

Table C. 2. Origin of the 11 tracks that entered the 100 × 100 km box at Block #7424.

Origin of icebergs	Number	Percentage [%]
Nordaustfonna	3	4.55
Edgeøya	8	12.12
Franz Josef Land (Western side)	43	65.15
Franz Josef Land (Eastern side)	7	10.61
Novaya Zemlya	5	7.58

C.1.2. Local analysis

C.1.2.1 Results excluding growlers

Table C. 3. The local iceberg collision probability with structures of varying sizes.

	Structure size (l)		
	100 × 100 m	500 × 500 m	1000 × 1000 m
Local Probability (P_l)	0.000477	0.00241	0.00485

Table C. 4. The annual iceberg encounter frequency at Block #7424.

	Structure size (l)		
	100 × 100 m	500 × 500 m	1000 × 1000 m
Annual iceberg encounter frequency (E_N)	$1.64 \cdot 10^{-3}$	$5.88 \cdot 10^{-3}$	$1.18 \cdot 10^{-2}$

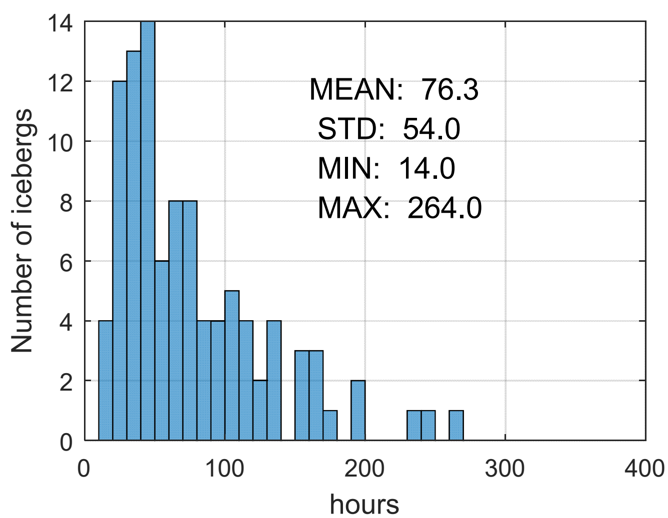

Figure C. 12. Histogram of the iceberg residence time within the 100 × 100 km box at Block #7424.

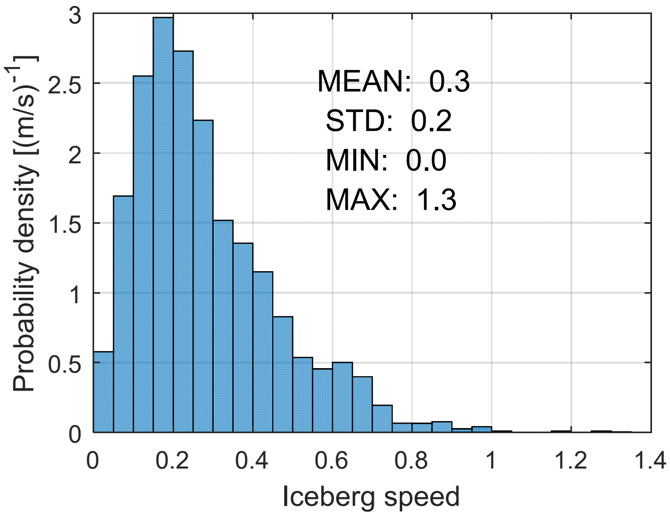

Figure C. 13. Histogram of the iceberg drift speed.

C.1.2.2 Results including growlers

Table C. 5. The local iceberg collision probability with structures of varying sizes.

	Structure size (l)		
	100 × 100 m	500 × 500 m	1000 × 1000 m
Local Probability (P_l)	0.000476	0.00241	0.00483

Table C. 6. The annual iceberg encounter frequency at Block #7424.

	Structure size (l)		
	100 × 100 m	500 × 500 m	1000 × 1000 m
Annual iceberg encounter frequency (E_N)	$2.11 \cdot 10^{-3}$	$1.07 \cdot 10^{-2}$	$2.14 \cdot 10^{-2}$

C.2. Overly conservative scenario

The number of icebergs released from each location is provided in Table C. 7. The total number of icebergs released per year from the 5 sources is 750 icebergs per year. The results of the global analysis including all the icebergs are presented in Figure C. 14, Figure C. 15, Figure C. 16, Figure C. 17 and Figure C. 18. The results of the global analysis excluding growlers (icebergs with a total height less than 10 m are excluded) are presented in Figure C. 19, Figure C. 20, Figure C. 21, Figure C. 22, Figure C. 23, Figure C. 24 and Table C. 8. The local probabilities and annual encounter frequencies are shown in Table C. 9 and Table C. 10.

Table C. 7. Major iceberg calving locations and average iceberg production rates in the Barents Sea. The average number of icebergs is based on an average iceberg mass of 311000 tonnes.

Geographical area	Calving location	Number of icebergs released/year
Franz Josef Land (East)	80.5°N/62.8°E	152
Franz Josef Land (West)	81.0°N/48.7°E	338
Nordaustfonna	79.6°N/27.0°E	28
Edgeøya	77.7°N/25.0°E	34
Novaya Zemlya	76.4°N/63.0°E	98

C.2.1. Global analysis

C.2.1.1. Results including growlers

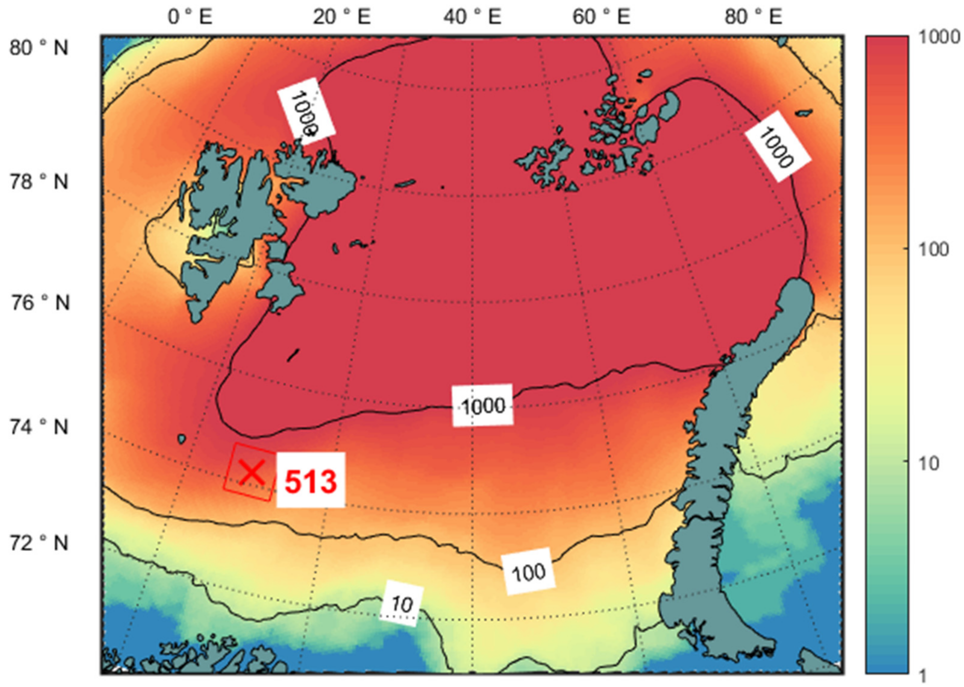

Figure C. 14. Total number of icebergs in a 100 × 100 km box during the simulated 27 years.

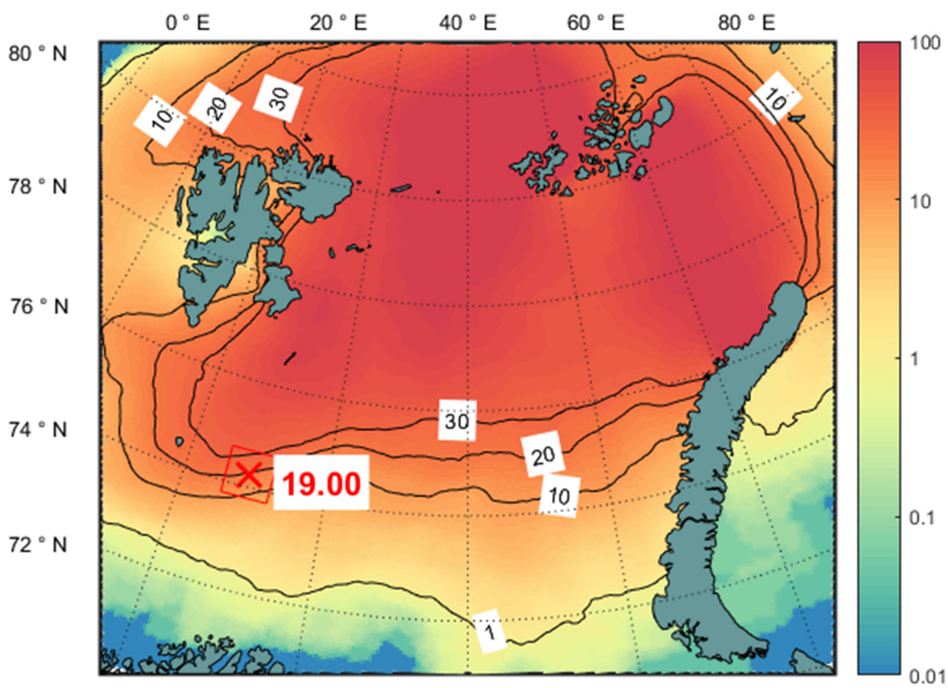

Figure C. 15. Expected number of icebergs per year in a 100 x 100 km box.

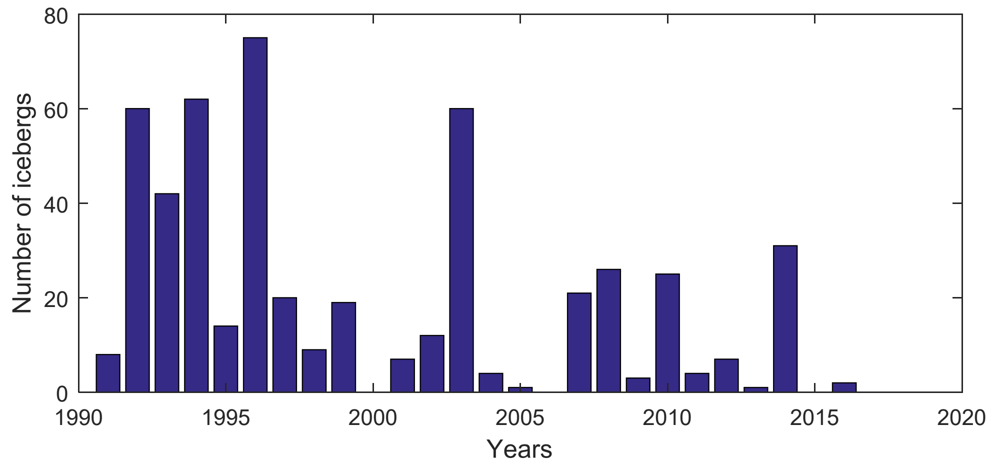

Figure C. 16. Number of icebergs entering the 100 × 100 km box at Block #7424.

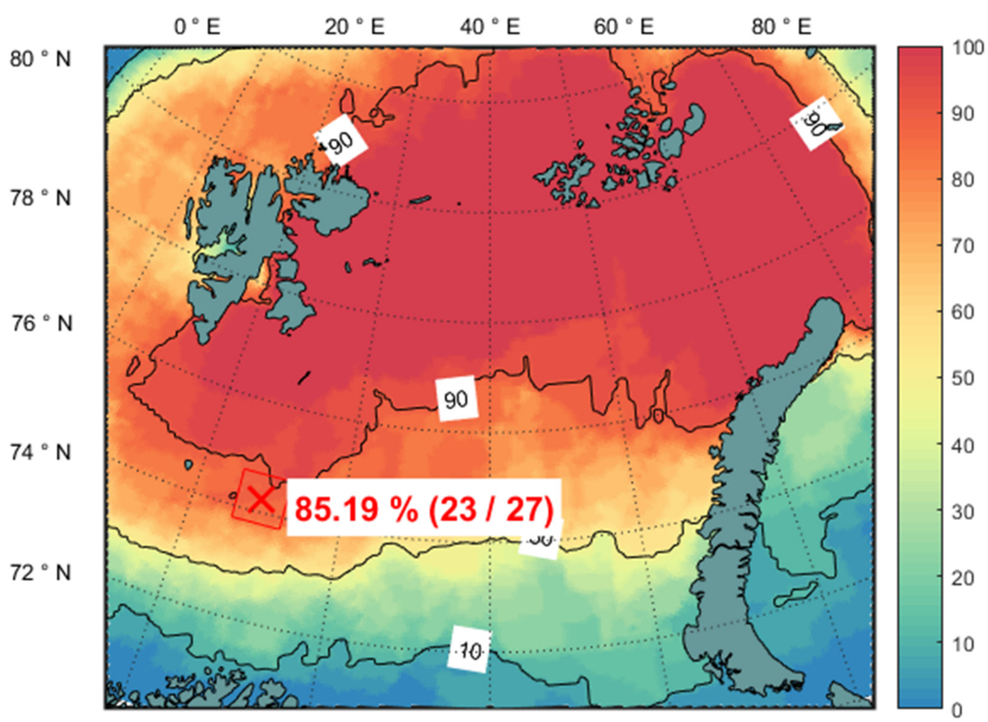

Figure C. 17. Yearly probability of iceberg occurrence in a 100 × 100 km box (i.e., at least one iceberg entering the box).

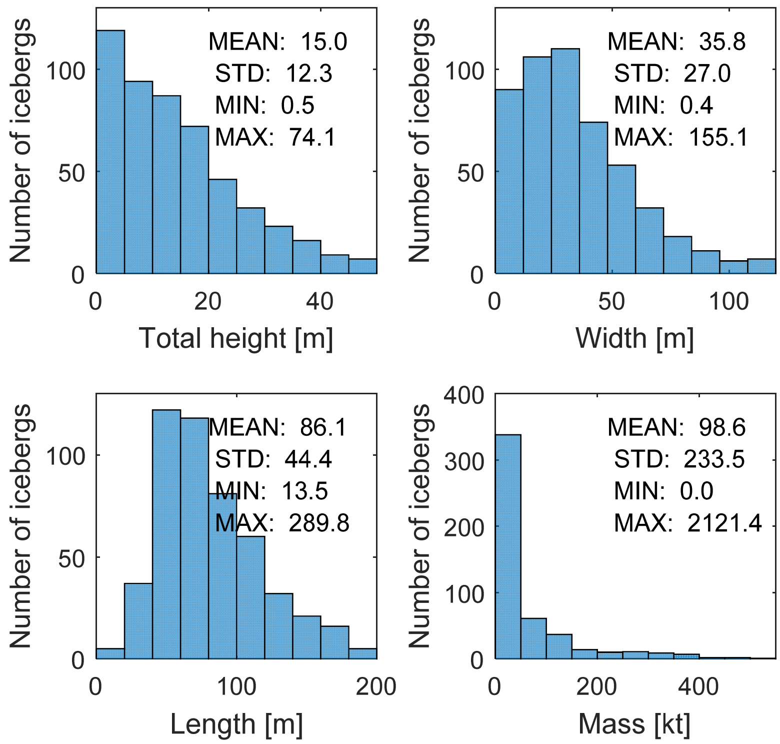

Figure C. 18. Histogram of dimensions and mass of icebergs as they enter the 100 × 100 km box at Block #7424.

C.2.1.1. Icebergs excluding growlers

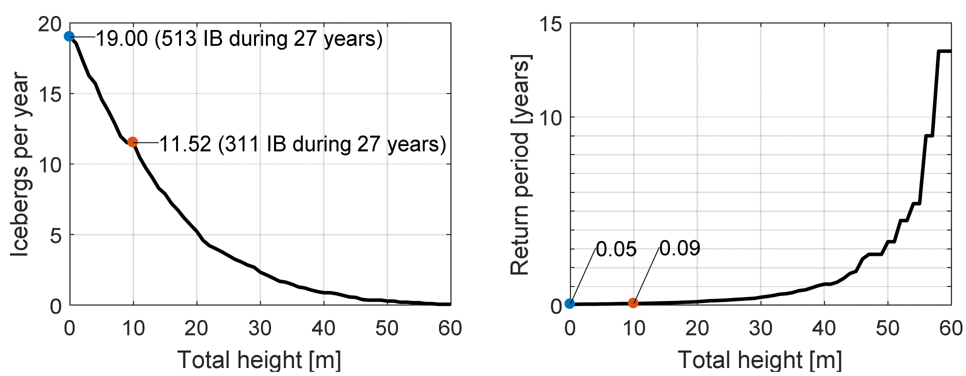

Figure C. 19. Effect of imposing a threshold for minimal total height of icebergs. Left: Number of icebergs entering Block #7424. Right: Return period (Expected average number of years for an iceberg of given height to enter Block #7424).

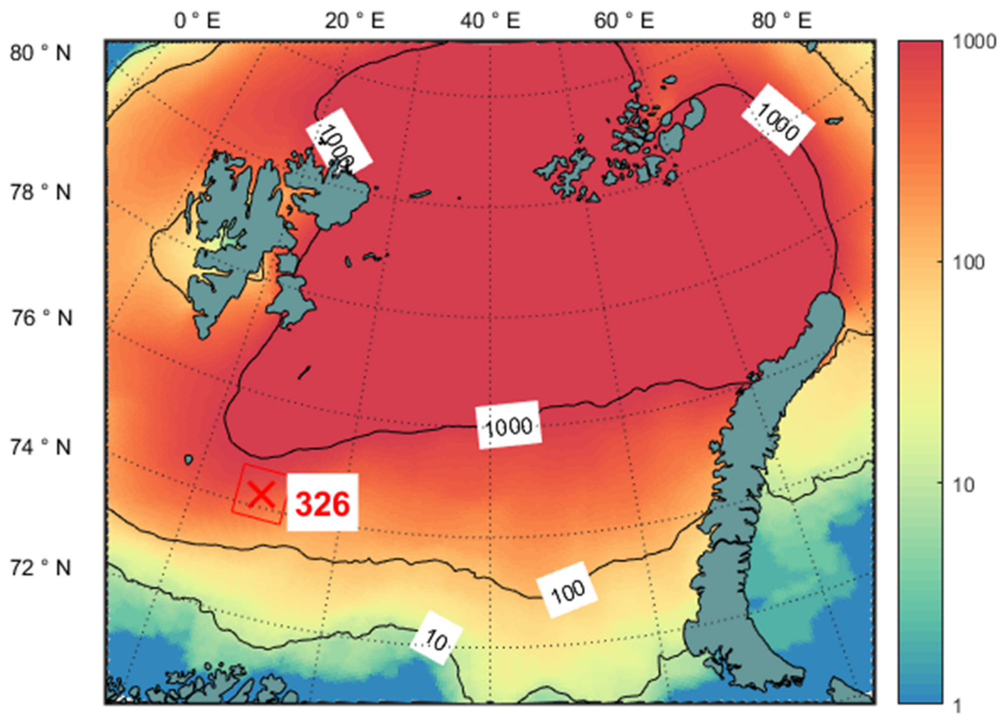

Figure C. 20. Updated total number of icebergs in a 100 × 100 km box during the simulated 27 years. Icebergs with total height less than 10 m are neglected.

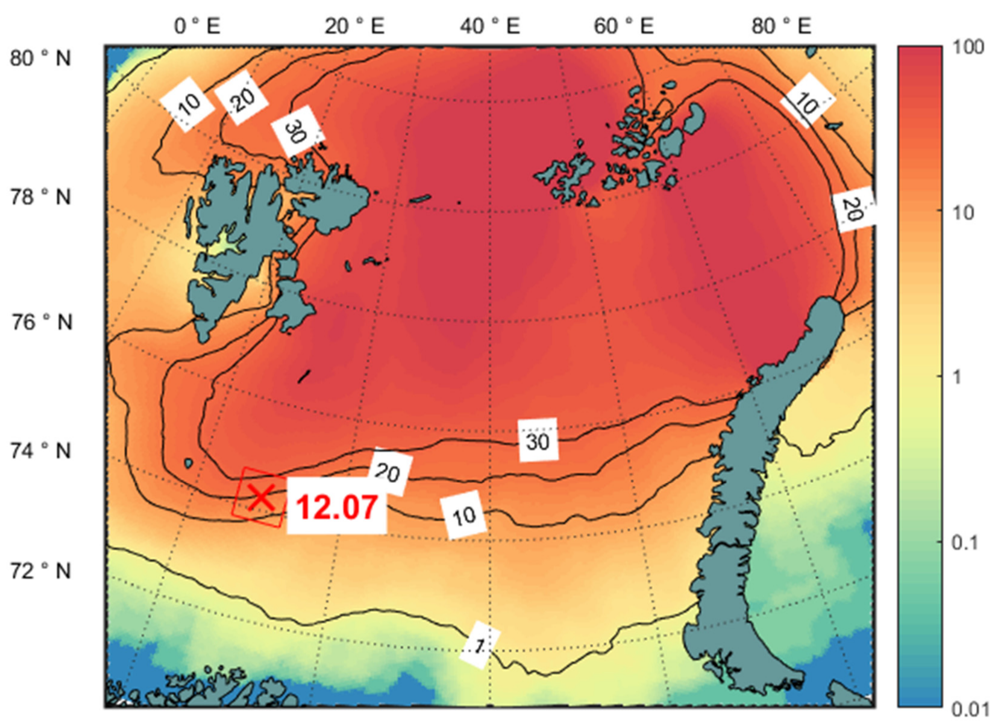

Figure C. 21. Updated expected number of icebergs per year in a 100 × 100 km box. Icebergs with total height less than 10 m are neglected.

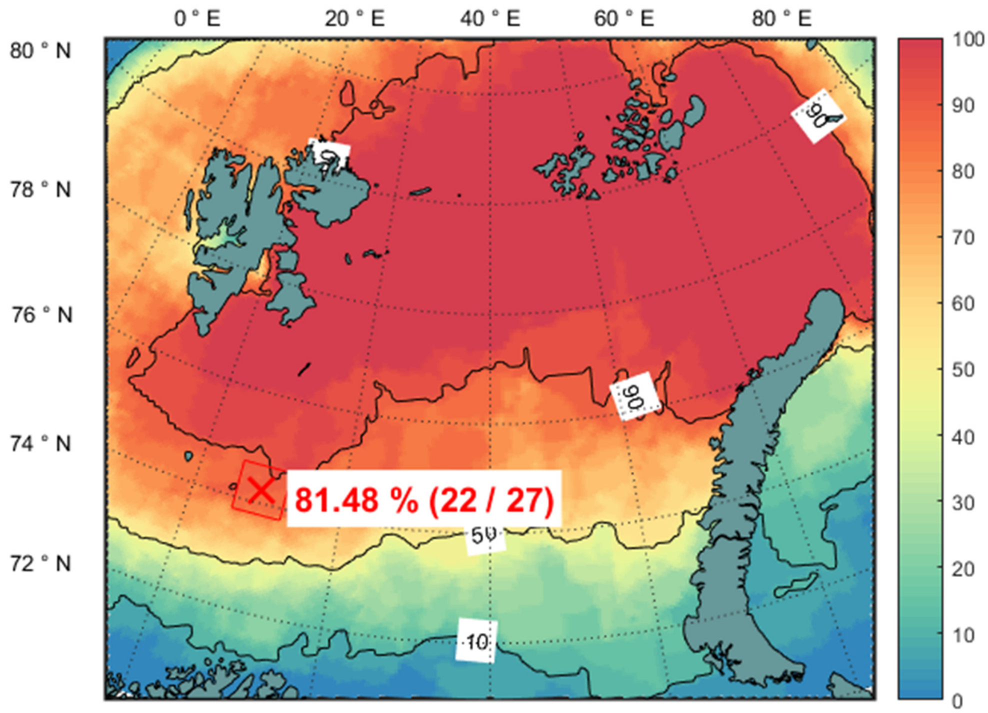

Figure C. 22. Updated yearly probability of iceberg occurrence in a 100 × 100 km box (i.e., at least one iceberg entering). Icebergs with total height less than 10 m are neglected.

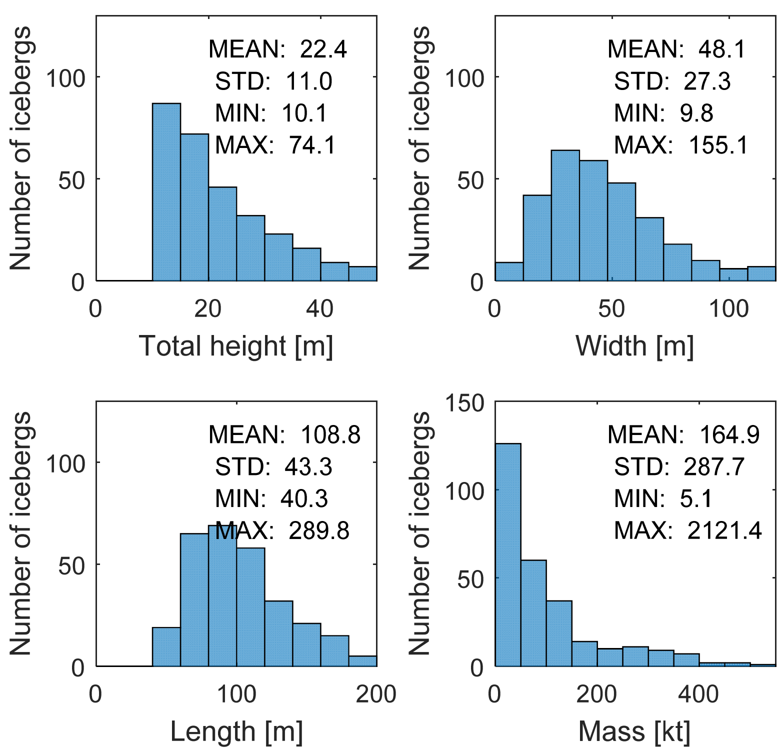

Figure C. 23. Updated histograms of dimensions and mass of icebergs as they enter the 100 x 100 km box at Block #7424. Icebergs with total height less than 10 m are neglected.

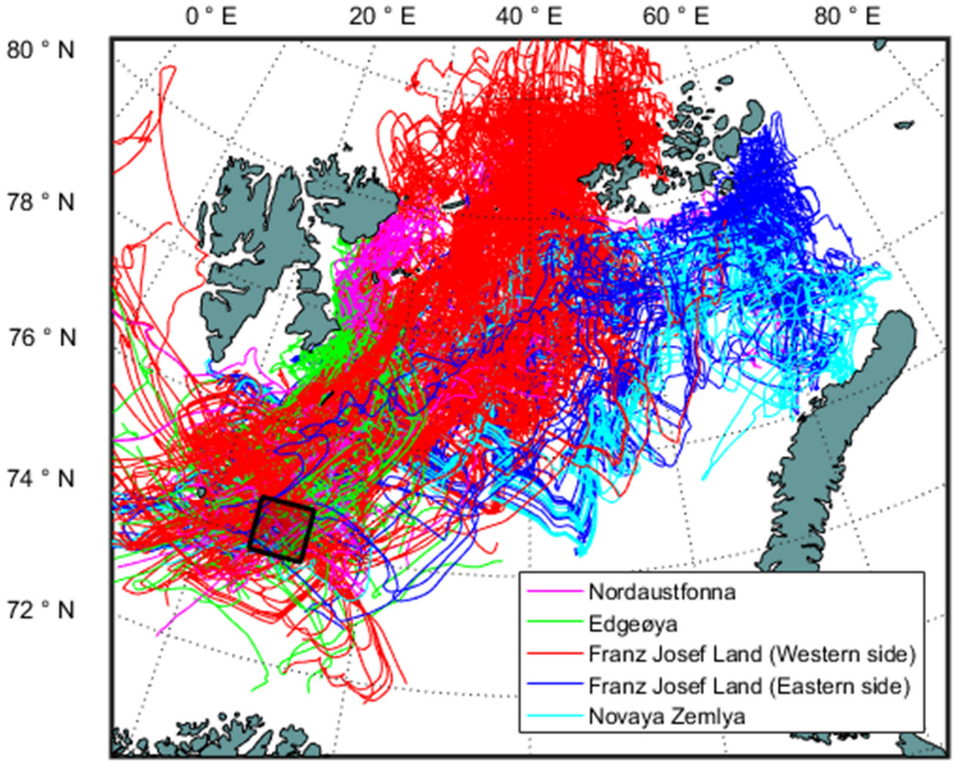

Figure C. 24. Trajectories of 326 icebergs that have entered the 100 × 100 km box at Block #7424. Trajectories are plotted from the origin of icebergs until the icebergs deteriorated to a total thickness smaller than 10 m.

Table C. 8. Origin of the 77 tracks that entered the 100 × 100 km box at Block #7424.

Origin of icebergs	Number	Percentage [%]
Nordaustfonna	25	7.67
Edgeøya	47	14.42
Franz Josef Land (Western side)	196	60.12
Franz Josef Land (Eastern side)	40	12.27
Novaya Zemlya	18	5.52

C.2.2. Local analysis

C.2.2.1 Results excluding growlers

Table C. 9. The local iceberg collision probability with structures of varying sizes.

	Structure size (l)		
	100 × 100 m	500 × 500 m	1000 × 1000 m
Local Probability (P_l)	0.000478	0.00241	0.00485

Table C. 10. The annual iceberg encounter frequency at Block #7424.

	Structure size (l)		
	100 × 100 m	500 × 500 m	1000 × 1000 m
Annual iceberg encounter frequency (E_N)	$5.77 \cdot 10^{-3}$	$2.91 \cdot 10^{-2}$	$5.85 \cdot 10^{-2}$

C.2.2.2 Results including growlers

Table C. 11. The local iceberg collision probability with structures of varying sizes.

	Structure size (l)		
	100 × 100 m	500 × 500 m	1000 × 1000 m
Local Probability (P_l)	0.000477	0.00240	0.00484

Table C. 12. The annual iceberg encounter frequency at Block #7424.

	Structure size (l)		
	100 × 100 m	500 × 500 m	1000 × 1000 m
Annual iceberg encounter frequency (E_N)	$9.06 \cdot 10^{-3}$	$4.56 \cdot 10^{-2}$	$9.20 \cdot 10^{-2}$

Appendix D

Assuming that the Coriolis force acting on the sea waters will be balanced by the surface tilt ($\nabla\xi$) of the sea (in the absence of wind), one gets:

$$m \cdot (1 + C_m) \frac{d(V_g + V_t)}{dt} = -m \cdot f \times (V_g + V_t) - m \cdot g \cdot \nabla\xi \tag{D.1}$$

$$-m \cdot g \cdot \nabla\xi = m \cdot (1 + C_m) \frac{d(V_g + V_t)}{dt} + m \cdot f \times (V_g + V_t) \times (V_g + V_t) \tag{D.2}$$

Examine Eq. (5.25)

$$m \cdot (1 + C_m) \frac{d}{dt}(V_i - V_g - V_t) = F_a + F_w + F_c + F_{wd} + F_{si}$$

Expand terms

$$m \cdot (1 + C_m) \frac{d(V_i - V_g - V_t)}{dt} = F_a + F_w + -m \cdot f \times (V_i - V_g - V_t) + F_{wd} + F_{si} \tag{D.3}$$

$$\begin{aligned} m \cdot (1 + C_m) \left(\frac{d(V_i)}{dt} - \frac{d(V_g + V_t)}{dt} \right) \\ = F_a + F_w + -m \cdot fk \times V_i + m \cdot f \times (V_g + V_t) + F_{wd} + F_{si} \end{aligned} \tag{D.4}$$

$$\begin{aligned} m \cdot (1 + C_m) \left(\frac{d(V_i)}{dt} - \frac{d(V_g + V_t)}{dt} \right) \\ = F_a + F_w + -m \cdot fk \times V_i + m \cdot f \times (V_g + V_t) + F_{wd} + F_{si} \end{aligned} \tag{D.5}$$

Rearrange terms yield

$$\begin{aligned} m \cdot (1 + C_m) \left(\frac{d(V_i)}{dt} \right) \\ = F_a + F_w - m \cdot f \times V_i + m \cdot f \times (V_g + V_t) + m \cdot (1 + C_A) \frac{d(V_g + V_t)}{dt} \\ + F_{wd} + F_{si} \end{aligned} \tag{D.6}$$

By substitute Equation (D.2) into Equation (D.6), one gets:

$$m \cdot (1 + C_m) \left(\frac{d(V_i)}{dt} \right) = F_a + F_w - m \cdot f \times V_i - m \cdot g \cdot \nabla\xi + F_{wd} + F_{si} \tag{D.7}$$

Equation D.7 is the equation of motion of an iceberg under the influence of drag forces from wind (F_a) and current (F_w), Coriolis force ($-m \cdot f \times V_i$), force due to sea surface tilt ($-m \cdot g \cdot \nabla\xi$), wave force ($F_{wd}$) and forces from sea ice (F_{si}).

Appendix E

For the local analysis, described in Section 5.3, we generated 100 icebergs in the centre of the spatial domain. In order to examine the effect of the number of icebergs used in the local model, one shows here the calculated local probability of collision between icebergs and a structure of 100 × 100 m as a function of the number of icebergs used, see Figure E. 1. We observe that the local probability changes only marginally when using a number icebergs higher than 100. Therefore, it was deemed unnecessary to use more than 100 icebergs for our simulations.

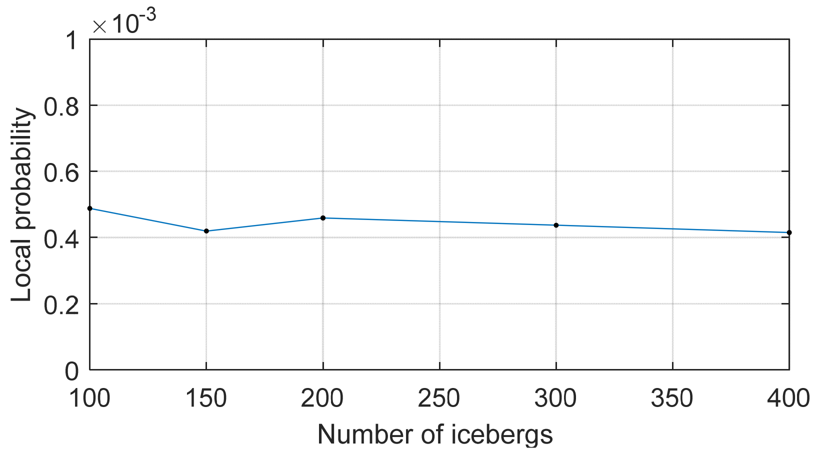

Figure E. 1. Local probability of collision with the structure of 100 × 100 m as function of the number of icebergs generated.

Appendix F

This appendix compares the results of our 'conservative scenario' with the results of the report from Dezecot and Eik (2015). In their report they determined, among others, the annual probability of iceberg occurrence for Block "A", shown in Figure F. 1. The results obtained from our simulations are in reasonable agreement with Dezecot and Eik (2015).

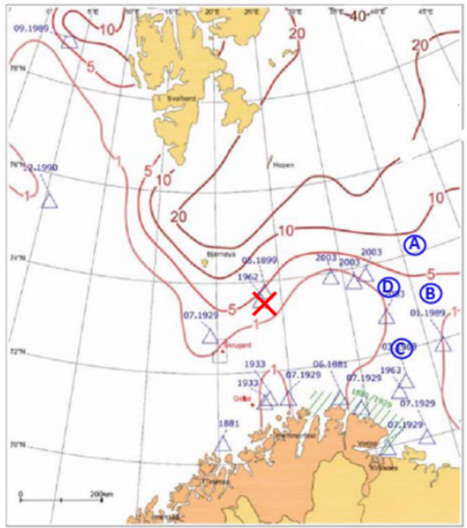

Figure F. 1. Results from the Atlas of Arctic Icebergs as presented in Dezecot and Eik (2015).

F.1. Global analysis

F.1.1. Results including growlers

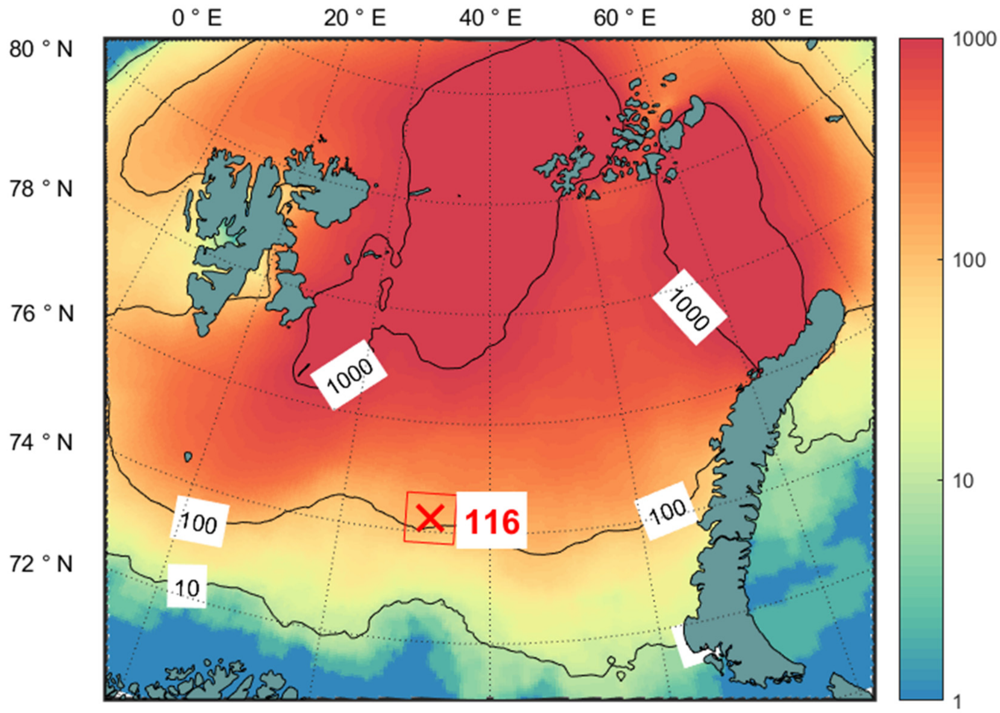

Figure F. 2. Total number of icebergs in a 100 × 100 km box during the simulated 27 years.

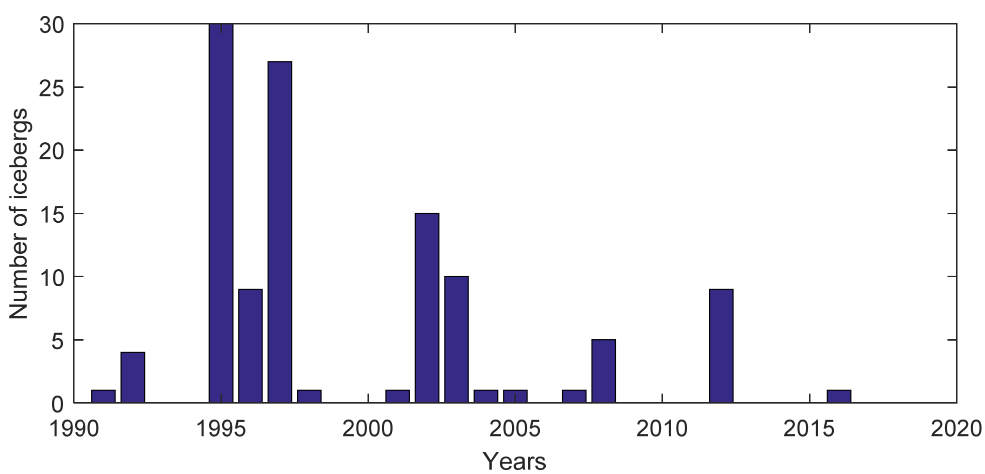

Figure F. 3. Number of icebergs entering the 100 × 100 km box at Block A.

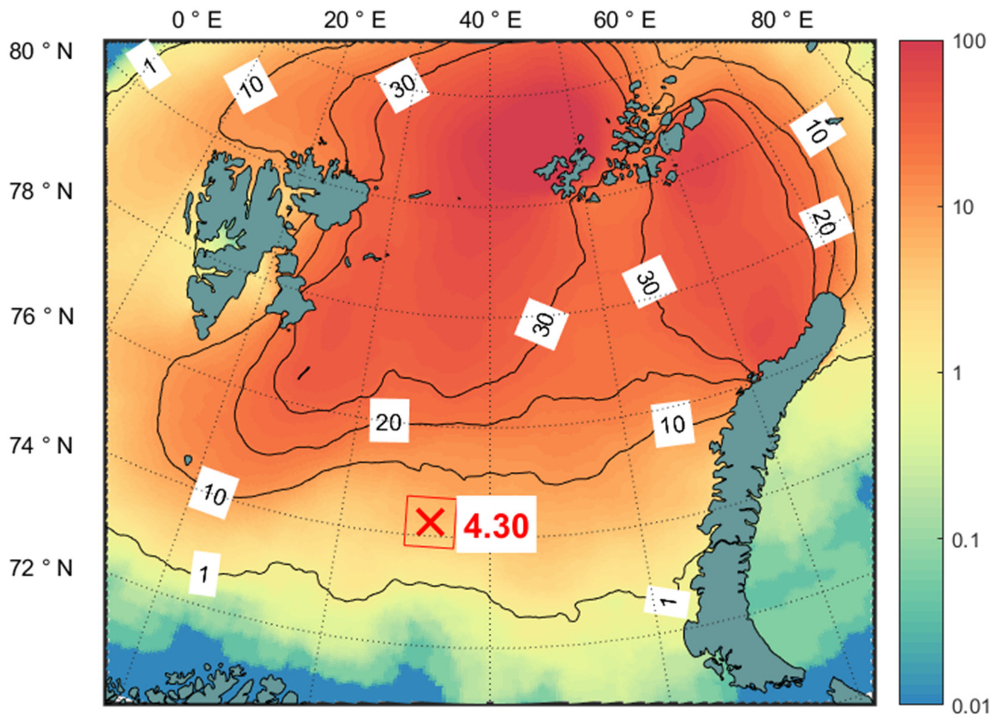

Figure F. 4. Expected number of icebergs per year in a 100 x 100 km box.

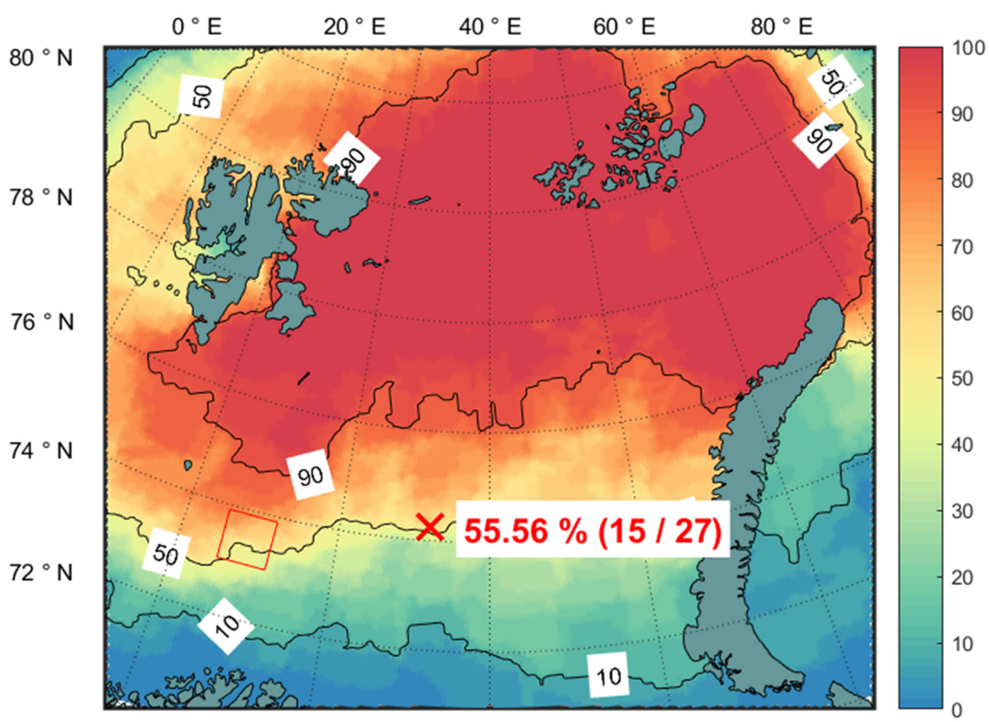

Figure F. 5. Yearly probability of iceberg occurrence in a 100 × 100 km box (i.e., at least one iceberg entering the box).

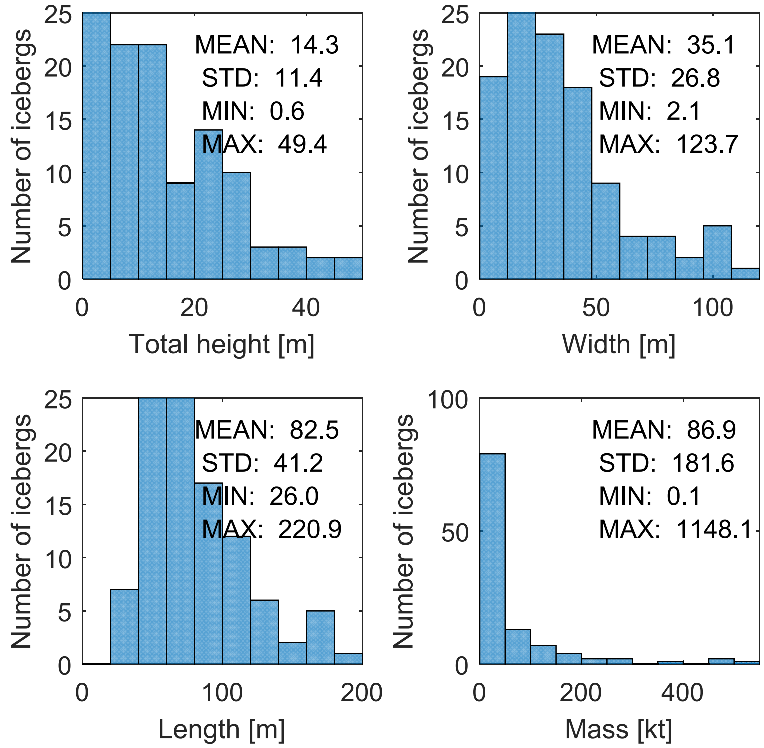

Figure F. 6. Histogram of dimensions and mass of icebergs as they enter the 100 × 100 km box at Block A.

F.1.2. Results excluding growlers

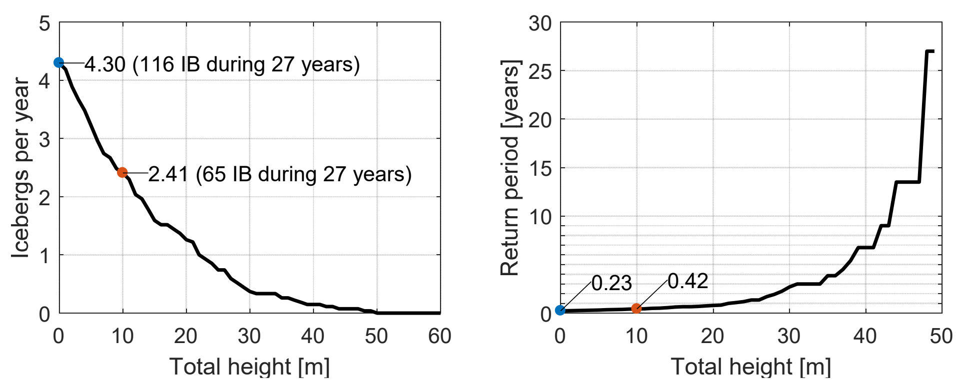

Figure F. 7. Effect of imposing a threshold for minimal total height of icebergs. Left: Number of icebergs entering Block A. Right: Return period (Expected average number of years for an iceberg of given height to Block A).

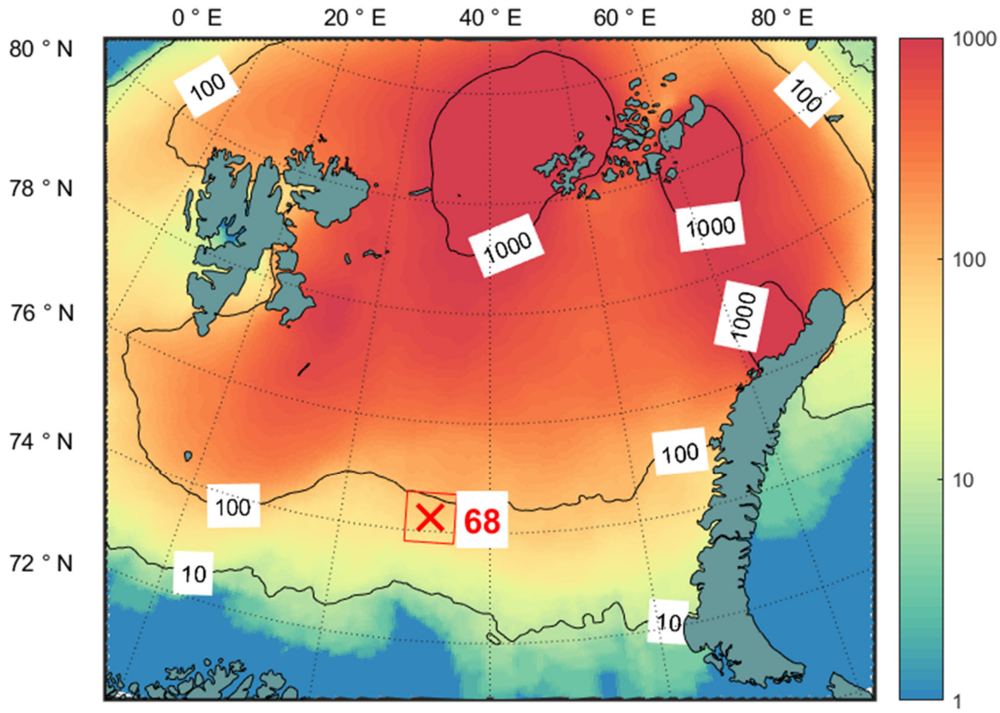

Figure F. 8. Updated total number of icebergs in a100 × 100 km box during the simulated 27 years. Icebergs with total height less than 10 m are neglected.

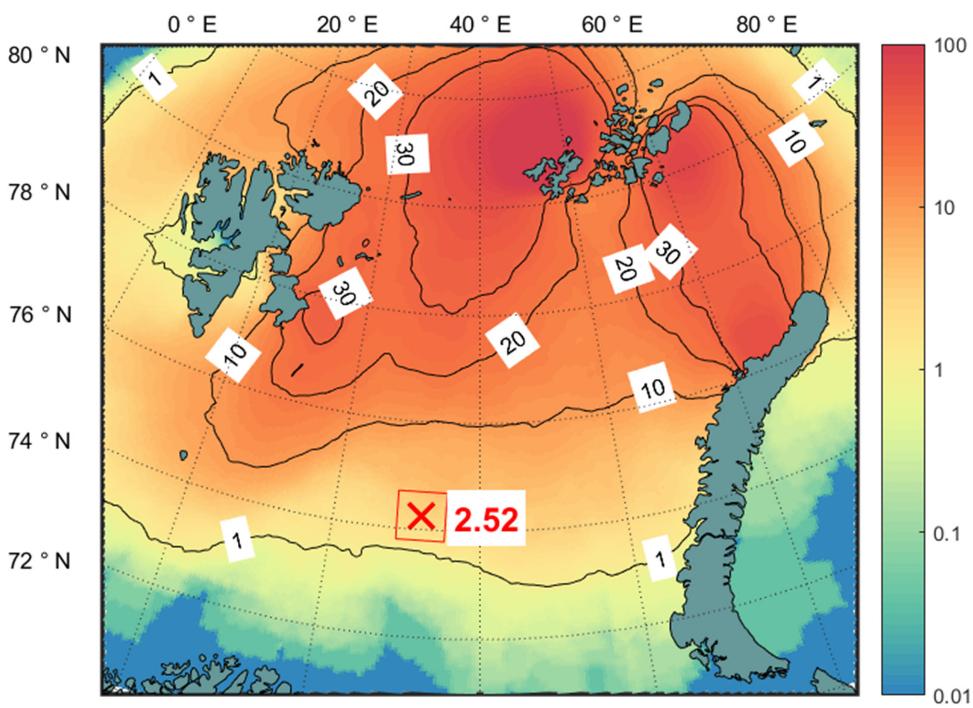

Figure F. 9. Updated expected number of icebergs per year in a 100 × 100 km box. Icebergs with total height less than 10 m are neglected.

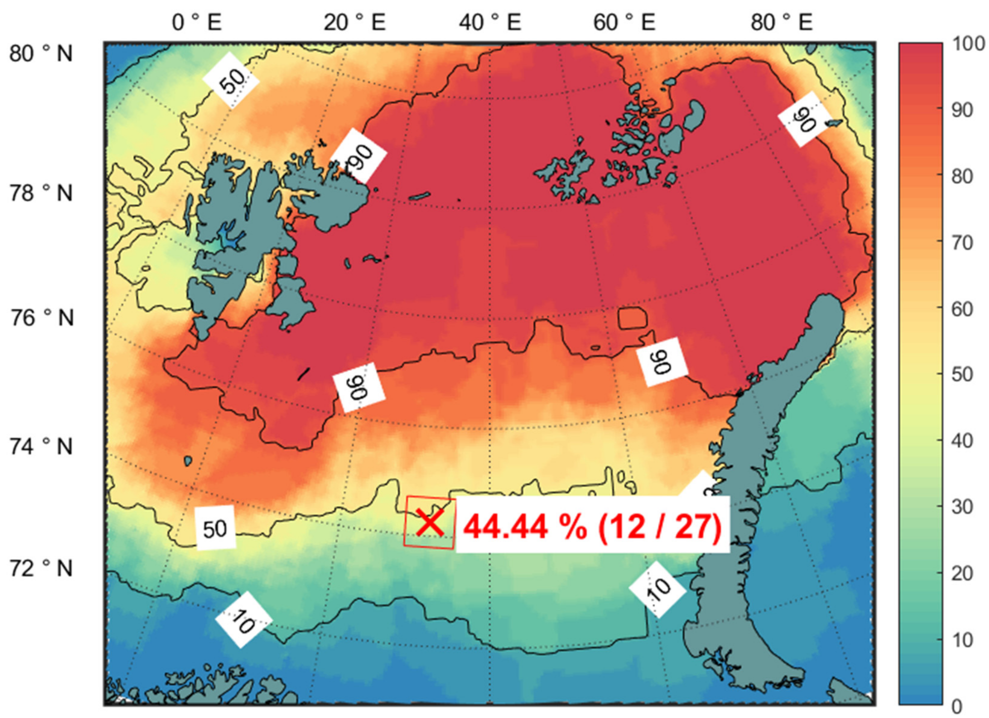

Figure F. 10. Updated yearly probability of iceberg occurrence in a 100 × 100 km box (i.e., at least one iceberg entering). Icebergs with total height less than 10 m are neglected.

F.2. Local analysis

Table F. 1. The local iceberg collision probability with structures of varying sizes.

	Structure size (l)		
	100 × 100 m	500 × 500 m	1000 × 1000 m
Local Probability (P_l)	0.000436	0.00224	0.00453

Table F. 2. The annual iceberg encounter frequency at Block A.

	Structure size (l)		
	100 × 100 m	500 × 500 m	1000 × 1000 m
Annual iceberg encounter frequency (E_N)	$1.10 \cdot 10^{-3}$	$5.65 \cdot 10^{-3}$	$1.14 \cdot 10^{-2}$